High-Temperature Oxidation Mechanisms of Titanium and Titanium Alloys

by

Thomas C. Valenza

A dissertation submitted in partial fulfillment
of the requirements for the degree of
Doctor of Philosophy
(Materials Science and Engineering)
in the University of Michigan
2024

Doctoral Committee:

Professor Emmanuelle A. Marquis, Chair
Assistant Professor Ashley N. Bucsek
Associate Professor Liang Qi
Professor Alan I. Taub

Thomas C. Valenza

tvalenz@umich.edu

ORCID iD: 0000-0002-2994-1109

Dedication

To my nonna,
Mary Joan Valenza,
who has filled my life
with delicious food
and much love.

Acknowledgments

I want to express my gratitude to all the people who helped me during my PhD. I especially want to thank my advisor, Professor Emmanuelle Marquis, who continually challenged me to become a better scientific researcher, storyteller, and writer and whom I am grateful to call a mentor and friend. I also want to thank my dissertation committee members, Professors Ashley Bucsek, Liang Qi, and Alan Taub, for their helpful insights and suggestions on this thesis.

I am very appreciative of my lab mates in the Marquis Group for their continual encouragement and technical help, especially Kathleen Chou for training and mentoring me as I joined the group and Anshul Kamboj for his friendship through the years. I want to extend my thanks to all the staff in the University of Michigan in the Materials Science & Engineering Department, Michigan Center for Materials Characterization, and Robert B. Mitchell Electron Microbeam Analysis Lab. In particular, I want to thank Allen Hunter, Bobby Kerns, Tao Ma, and Haiping Sun for their persistent help with characterization techniques and experiments, Owen Neill for performing WDS measurements, Peter Weber and Christina Ramon at Lawrence Livermore National Laboratory for performing nanoSIMS experiments, and Mayela Aldaz-Cervantes and Carlos Levi at UC Santa Barbara for providing Ti-0.8Si and Ti-2Nb materials used in this thesis. I want to thank Owen Neill and Peter Weber for their invaluable feedback on the final drafts of the publications reproduced in this thesis. Finally, I want to thank Roy Wentz at the University of Michigan glassblowing shop and Aaron Ward at Swagelok Michigan for their extensive advice and support that contributed to the tracer oxidation setup used in this thesis.

I am extremely grateful to my friends and family for their constant interest and support. I want to give a special thanks to my friends Anshul, Emily, Ethan, Jing, Kevin, Maria, Mark, Nina, Vishwas, and Zed and to my family, especially my mom, aunts and uncles, and nonna. Additionally, I want to thank my many teachers, from elementary school to college, who made learning interesting, challenging, and human and contributed to my desire to pursue a PhD: Mary Beth Ryan, Paula Hernandez, Chivaz Pruitt, Sallie Bryant, Roger Crider, Richard McHugh,

Betsy Morris, Paige Stanley, Jackie Bixler, Annie Hesp, Maureen Julian, Richard Phillips, and others.

This work was supported by the U.S. National Science Foundation (NSF) through grants CMMI-1729166 and DMR-1436154. Funding at Lawrence Livermore National Laboratory (LLNL) was provided by LLNL Laboratory Directed Research and Development project 20-SI-004. Work at LLNL was performed under the auspices of the U.S. Department of Energy, Contract DE-AC52-07NA27344.

Table of Contents

List of Tables

List of Figures

List of Appendices

List of Abbreviations

APT	Atom-probe tomography
BCC	Body-centered cubic
BSE	Backscattered electron
EDS	Energy-dispersive spectroscopy
EPMA	Electron-probe microanalyzer
FIB	Focused ion beam
HAADF	High-angle annular dark field
HCP	Hexagonal close packed
LEAP	Local electrode atom probe
NSF	National Science Foundation
SAED	Selected-area electron diffraction
SCCM	Standard cubic centimeter(s) per minute
SEM	Scanning electron microscopy
SIMS	Secondary-ion mass spectrometry
STEM	Scanning transmission electron microscopy
TEM	Transmission electron microscopy
WDS	Wavelength-dispersive spectroscopy
XRD	X-ray diffraction

Abstract

To help combat climate change, we need to develop durable, lightweight structural materials for transportation, especially in aerospace where minor weight reductions can dramatically reduce fuel consumption and CO_2 emissions. Among candidate materials, titanium alloys are particularly promising because of their high strength-to-weight ratio, fracture toughness, and resistance to fatigue and creep. Although widely used for aircraft structural components, titanium alloys remain poorly suited to the hottest areas in jet engines because they oxidize rapidly above 550 °C. During oxidation, oxygen reacts with titanium, readily diffusing into the metal and also forming (rutile TiO_2) oxide scale. Both phenomena are undesirable, with oxygen embrittling the metal and oxide growth reflecting a loss of load-bearing metal.

The oxidation behavior of titanium can be improved by alloying it with small amounts of other elements. In particular, Si and Nb are known to be beneficial. Additionally, nitrogen found in air can also influence the oxidation behavior, typically with positive effects of reducing overall oxidation rates, oxide thickness, and the amount of oxygen dissolved in the metal. Similarly to oxygen, nitrogen diffuses into the metal and can form nitride phases at the oxide-metal interface. Despite the known benefits of Si and Nb alloying additions and nitrogen, their influence on the oxidation mechanisms remains poorly understood. Notably, it remains challenging to distinguish the role of nitrogen from potential synergy with alloying additions.

Therefore, this thesis investigates the mechanisms by which Si, Nb, and atmospheric nitrogen influence the oxidation response of titanium. To this end, I systematically characterized and compared the behavior of pure titanium and titanium alloys containing Si (0.8 at.%) or Nb (2 at.%) during oxidation at 800 °C for up to 100 h in O_2 or N_2-O_2 atmospheres. Without atmospheric nitrogen, Si and Nb had no effect on oxygen dissolution in the metal. Instead, they slowed oxide scale growth via two different mechanisms previously unidentified in the literature. Si initially formed a protective Ti_5Si_3 layer at the scale-metal interface that prevented inward oxide growth. In contrast, Nb doped the oxide grain boundaries, slowing outward oxide growth presumably by slowing outward Ti transport along the oxide grain boundaries. With atmospheric

nitrogen, nitrogen in the surface of the metal can play a key role in reducing oxygen concentrations throughout the metal, as evidenced using thermodynamic calculations and diffusion simulations. Notably, the mechanistic role of nitrogen in the metal appears to be the same independent of alloying elements in the metal. Synergistically with alloying, nitrogen helps the oxide scales remain compact and protective over extended oxidation time.

In this thesis, I discredited many mechanisms repeated throughout the literature, evidenced distinct and previously unidentified mechanisms by which Si and Nb influence scale growth, and conclusively demonstrated the beneficial role of nitrogen in the metal in reducing oxygen concentrations in the metal. For the first time in the titanium oxidation literature, I showed that oxygen transport through the oxide primarily takes place along oxide grain boundaries, rather than through the lattice as previously assumed. Finally, I demonstrated a null effect of alloying additions on the behavior of O and N in the metal, suggesting in contrast to the literature that dilute alloying is ineffective for influencing O and N solubilities or diffusivities in the metal. These new findings provide a critical scientific basis for engineering long-lasting, oxidation-resistant titanium alloys.

Chapter 1: Introduction

1.1 Background and Motivation

Climate change is one of the most pressing issues of our time. Combating climate change will require fundamental shifts in society, widespread adoption of green technology, and continued incremental improvements to existing technology. For transportation specifically, we need to develop increasingly durable and lightweight structural materials. This need is especially pressing in aerospace, where minor weight reductions can dramatically reduce fuel consumption and CO_2 emissions. Among candidate structural materials for aerospace applications, titanium alloys are particularly promising because they are lightweight yet strong, with good fracture toughness and resistance to fatigue and creep [1]. For these reasons, titanium alloys are currently used in a variety of airframe components — landing gear beams, fuselage frames and panels, and engine support mountings — and engine components — fan blades, spacers, and afterburner cowlings. Nevertheless, titanium alloys are not suitable for the hottest areas in jet engines because they oxidize rapidly above 550 °C [1], [2].

In the context of structural aerospace applications, oxidation is typically detrimental to mechanical properties and overall performance. For titanium alloys specifically, oxidation leads to reduced load-bearing capability, as metal transforms to oxide, and reduced ductility and fatigue life due to hardening of the outermost, oxygen-enriched metal [2], [3]. At the high temperatures considered here, the oxide phase is often exclusively rutile TiO_2 [4], [5], [6], [7]. The extensive enrichment of oxygen in the metal is a phenomenon somewhat unique to Ti, along with other group IV elements, and arises from the moderate diffusivity and high solubility of oxygen in the metal at the high temperatures.

In general, two approaches to mitigate oxidation and its detrimental effects include applying protective coatings and alloying. Alloying is a particularly elegant option, as it is relatively simple in practice and can help a material natively form an oxide scale that acts as a protective coating. Additionally, since alloying additions are typically present for other purposes such as enhancing mechanical properties, understanding their role in oxidation is critical.

Alloying was the focus of an early study on the oxidation of titanium, from the 1950s, which showed that small additions of other elements — particularly Si and Nb — could significantly slow oxidation in air [8].

Although the fact that Si [9], [10], [11], [12], [13] and Nb [14], [15], [16], [17], [18] alloying additions can improve the oxidation behavior is now well established, how these elements influence the oxidation mechanisms remains poorly understood. For example, it was suggested that Si and Nb may influence oxygen diffusivity in the oxide [11], [14], [16], [19] , oxygen diffusivity in the metal [11], [14], [15], and oxygen solubility [9], [14], [15] in the metal. However, these effects remain unverified, and alternative potential roles of the alloying elements remain unexplored. One contribution to this situation is the use of different oxidation atmospheres, some containing nitrogen that is known to influence the oxidation behavior of titanium alloys.

In nitrogen-containing atmospheres such as air, nitrogen can also play a role in the oxidation process. Similarly to oxygen, nitrogen diffuses into the metal and can form nitride phases at the oxide-metal interface. Nitrogen has been linked to numerous positive effects on the oxidation response such as reducing mass gain [9], [10], [11], [20], [21], [22], oxide thickness [9], [14], [16], [21], [22], [23], and the amount of oxygen dissolved in the metal [9], [10], [11], [16], [21], [22], [24]. These benefits were reported for Ti [10] and numerous alloys — Ti-Si [9], [11], Ti-Nb [14], [16], Ti-Ta [20], [24], and Ti6242S [21], [22], [23] — oxidized over a large temperature range (500-1400 °C). Many studies generally attribute the benefits of nitrogen to the formation of nitride phases, oxynitride phases, and/or nitrogen dissolution in the metal, with one or more acting as a barrier to oxygen [14], [20], [22], [23], [25], [26]. However, the origin of the reduced amount of oxygen dissolved in the metal has not been conclusively established. Additionally, as many studies use alloys, it remains challenging to distinguish the role of nitrogen from potential synergy with alloying additions and whether the role of nitrogen depends on alloy composition. Indeed, synergy between alloying and nitrogen is generally expected, for example, based on evidence that alloying titanium with small amounts of Si [10] or Nb [14], [15] more strongly reduces the oxidation rates in air than in oxygen.

This thesis clarifies how Si, Nb, and atmospheric nitrogen influence the oxidation mechanisms of titanium, with a focus on unraveling the anticipated synergy between the alloying additions and nitrogen. To this end, we systematically compare the behavior of pure titanium and titanium containing small amounts of Si (0.8 at.%) or Nb (2 at.%) oxidized in O_2 and N_2-O_2

atmospheres. We employ an array of characterization techniques traversing length scales — from thermogravimetry to understand the macroscopic oxidation response to atom-probe tomography to access atomic-scale microstructure and chemistry. Notably, our two-stage oxidation experiments using isotopically labeled atmospheres and subsequent analysis with nanoSIMS provide convincing support for the oxidation mechanisms that we discuss. Our findings deepen the foundational knowledge and contribute to the scientific basis necessary for designing durable titanium alloys resistant to the adverse effects of high-temperature oxidation.

1.2 Thesis Structure

This thesis has six main chapters. After this introduction, **Chapter 2** reviews the literature, first providing background on titanium metallurgy and then the current understanding of the oxidation behavior and mechanisms of pure titanium alone, with alloying additions, and with atmospheric nitrogen. **Chapter 3** and **Chapter 4** discuss how Si and Nb, respectively, influence the high-temperature oxidation response and oxidation mechanisms of titanium in nitrogen-free atmospheres. Extending this work, **Chapter 5** examines how nitrogen alone and synergistically with Si or Nb modifies the oxidation response and the oxidation mechanisms of titanium. In **Chapter 6**, we summarize our main conclusions and recommend future studies. **Appendices** provide additional details for various experimental procedures and supplementary content. We note that Chapter 3 and Chapter 4 are based on work previously published in [27] and [28], respectively.

Chapter 2: Literature Review

This chapter introduces the metallurgy of titanium along with the relevant binary and ternary systems, i.e. Ti with Si, Nb, O, and/or N (Section 2.1). We then present diffusivity information in titanium for all the relevant species. This is followed by a review of the oxidation behavior of pure titanium (Section 2.2) and titanium with dilute Si (Section 2.3) and Nb (Section 2.4) additions, along with the current understanding of the oxidation mechanisms. In each of those sections, we briefly discuss the influence of nitrogen on the overall oxidation behavior, without discussing the mechanisms. Finally, we summarize the effects of nitrogen more generally for titanium alloys and the current understanding of how it influences the oxidation mechanisms (Section 2.5).

2.1 Metallurgy of Titanium

At ambient pressure, the crystal structure of pure titanium is hexagonal close-packed (α phase) below 882 °C and body-centered cubic (β) above this temperature. The relative stability of each phase is strongly affected by both interstitial and substitutional elements [2], [3], which are classified as α stabilizers if they raise the α-to-β transformation temperature or β stabilizers if they lower it. Alpha stabilizers include interstitial C, N, and O and the substitutional element Al [2]. Beta stabilizers include interstitial H [2], [3] and the substitutional elements Si and Nb [2].

Both oxygen and nitrogen are highly soluble in titanium, especially in the α phase. According to the historical Ti-O and Ti-N phase diagrams, the maximum solubility of oxygen is about 33.3% in the α phase and 7% in β (Figure 2.1), and the maximum solubility of nitrogen is about 25% in α and 6% in β (Figure 2.2). Recent first-principles calculations [29], [30] reproduced the high-temperature solubilities of oxygen and nitrogen in α titanium and suggested that titanium suboxides may also be stable at lower temperatures.

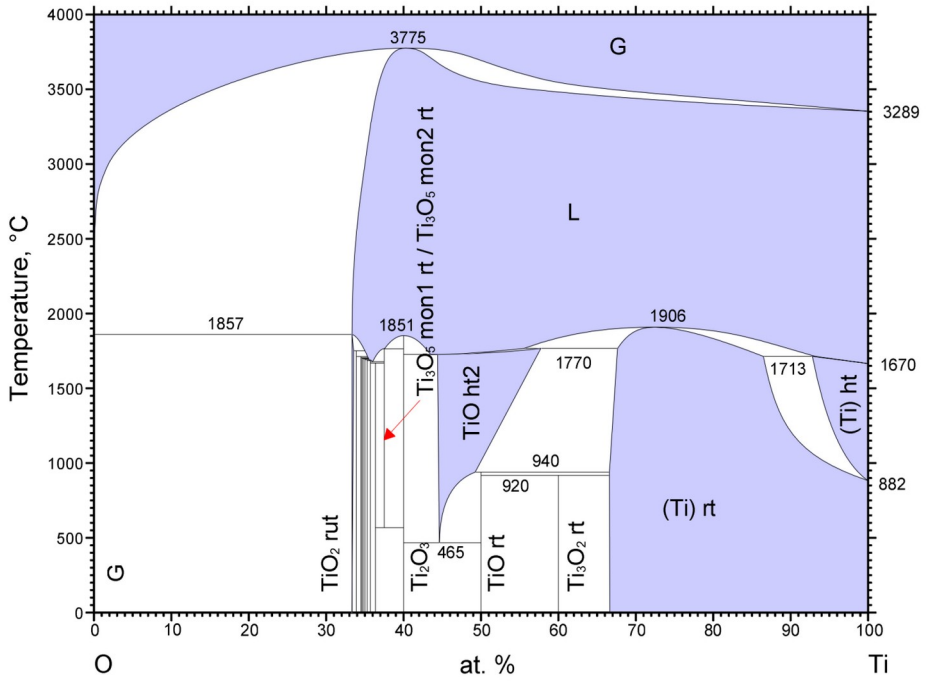

Figure 2.1: O-Ti phase diagram, adapted from the ASM Alloy Phase Diagram Database [31].

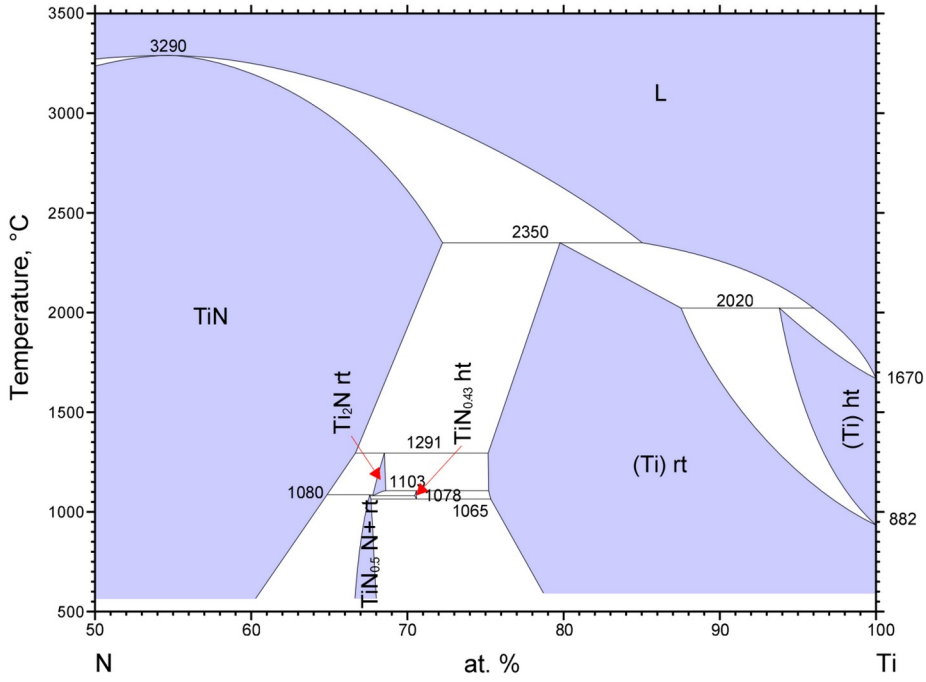

Figure 2.2: N-Ti phase diagram, from the ASM Alloy Phase Diagram Database [32].

Commercial titanium alloys are classified as α, near-α, α-β, or β [33]. The α alloys include unalloyed titanium, which has excellent corrosion resistance and weldability but lower strength compared to the alloys [3], [33]. Unalloyed titanium has four grades (1-4), which differ mostly in impurity levels of oxygen and iron [3]. Increasing grade numbers correspond to higher levels of oxygen and consequently higher tensile strengths, since oxygen acts as a strong solid-solution strengthener [33]. Near-α alloys typically contain Al, Sn, and Zr and small amounts of β stabilizers such as Mo or Nb (<2 wt.%) and Si (up to 0.5 wt.%) [33]. These alloys cannot be strengthened via heat treatments but have good creep strength, making them suited to high-temperature applications [33]. Common near-α alloys include Ti6242S (Ti-6Al-2Sn-4Zr-2Mo+Si) and IMI834 (Ti-5.8Al-4Sn-3.5Zr-0.5Mo-0.7Nb-0.35Si-0.06C) (compositions in wt.%). These alloys, respectively, can be used up to 540 °C and 600 °C [33]. At these temperatures, the main limitation is oxygen dissolution in the metal causing embrittlement and early fatigue crack initiation [33]. Considering this limitation and that these alloys contain small amounts of Si and/or Nb, the scope of this thesis is extremely relevant. The α-β alloys, which contain higher concentrations of β stabilizers than near-α alloys, are the most commonly used for structural applications [33]. Notably, the widely known Ti-6Al-4V, or Ti-6-4, alloy is an α-β alloy. These alloys can be strengthened via solution treating and subsequent aging, to precipitate fine α platelets within the β phase [3]. Finally, the β alloys contain the highest concentrations of β stabilizers. Like α-β alloys, β alloys can be solution treated and aged. In the solutionized state, β alloys are ductile, tough, and highly formable [3]. In the aged states, their strengths can match or exceed that of α-β alloys; however, β alloys typically have higher density (associated with the dense β stabilizers), lower creep strength, and lower tensile ductility than comparable α-β alloys [3].

2.1.1 Titanium-Niobium Alloys

Niobium is typically added to titanium and titanium alloys to tailor magnetic [34], mechanical [35], [36], [37], oxidation [14], [15], [17], [38], [39], and corrosion [40] properties. Nb-rich alloys (e.g. Ti-31 at.% Nb) have been employed as superconductor magnets [34]. They are also being studied as materials for biomedical implants because of their low modulus of elasticity

approaching that of bone [35], [36], [41], high deformability [42], shape memory and superelasticity [42], [43], corrosion resistance [40], and biocompatibility [41].

Niobium is β isomorphous, meaning it is similar to β Ti and does not form intermetallic compounds with titanium (Figure 2.2) [3], [42]. In sufficient quantity, niobium can stabilize the high-temperature β phase at room temperature [3]. Ti-Nb alloys exhibits considerable metastability and are highly sensitive to prior thermal processing [42], [44]. In typical commercial thermal processing, alloys are heated into the β phase field, quenched, and may be aged [42]. As a result, they may contain α, β, and/or non-equilibrium phases: hexagonal α' ($P6_3/mmc$) or orthorhombic α" (C*mcm*) martensites and hexagonal ω ($P6/mmm$) [42]. The structure and lattice parameters of α' are identical to those of α Ti [45]. The type of martensite is a function of Nb content, where α' forms in alloys with low Nb content and α" in those with higher Nb content [45]. If present, martensite forms upon quenching. Depending on alloy composition, ω can form as a result of slow quenching from β (athermal ω) or aging heat treatment (isothermal ω) [42], [45], [46]. The martensitic transformation between β and α" accounts for shape memory and superelasticity in Ti-Nb alloys [41], [42]. After quenching, the state of the alloy can be further modified via thermal and/or mechanical processing to adjust properties such as elastic modulus (e.g. by phase fractions, since the elastic modulus of ω > α' > α" > β [35], [36]), strength (e.g. via precipitation of ω or α [42]), and shape memory or superelasticity.

Limited data is available for the ternary Ti-Nb-O and Ti-Nb-N systems, as shown in Figure 2.4. The Ti-Nb-O phase diagram (Figure 2.4, left) suggests that the Nb does not influence the solubility of O in α Ti at 800 °C. The Ti-Nb-N phase diagram (Figure 2.4, right) suggests some Nb solubility in Ti_2N and TiN nitrides at high temperatures.

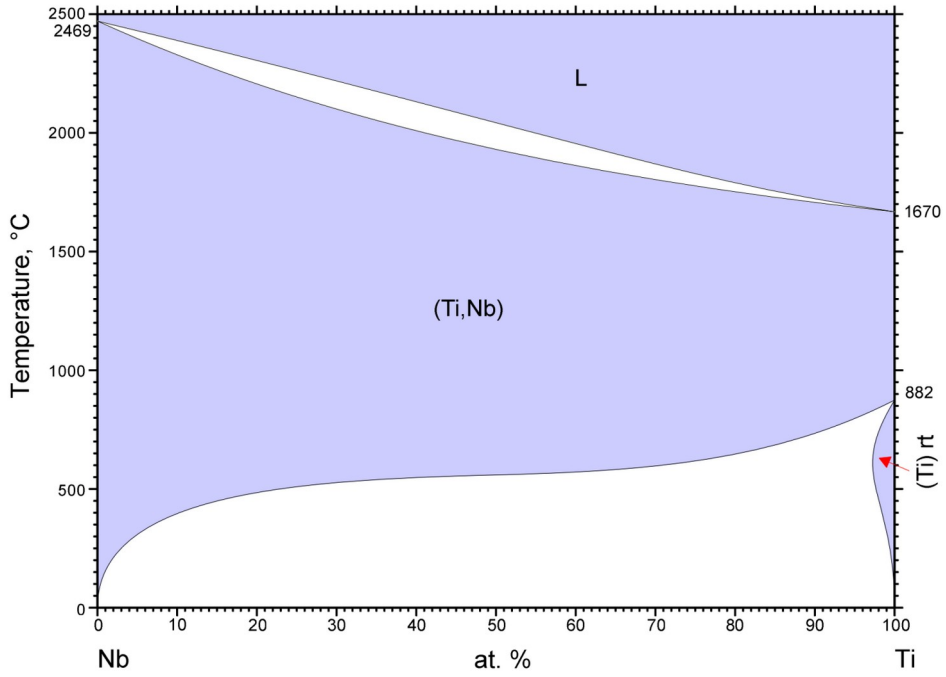

Figure 2.3: Nb-Ti phase diagram, from the ASM Alloy Phase Diagram Database [47].

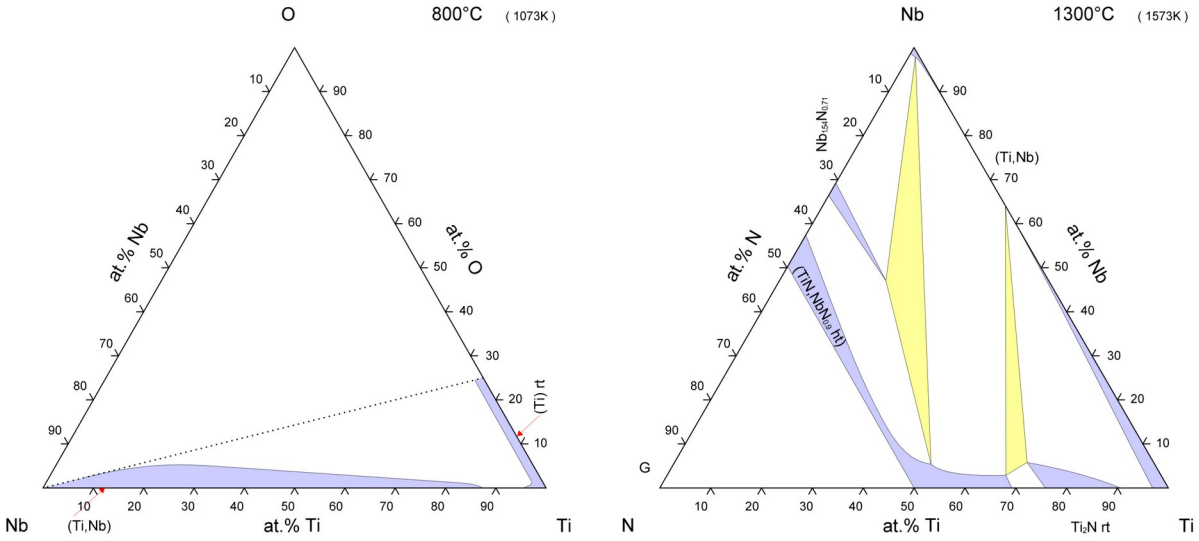

Figure 2.4: Ti-Nb-O (left) [48] Ti-Nb-N (right) [49] ternary phase diagrams, from the ASM Alloy Phase Diagram Database. For Ti-Nb-O, data is only shown in the region enclosed by the dotted line.

2.1.2 Titanium-Silicon Alloys

Additions of silicon to titanium can increase resistance to high-temperature creep [50], [51], [52] and oxidation [11]. One example of a commercial Ti-Si alloy with enhanced oxidation resistance is Timet Exhaust HT (Ti-0.8 at.% Si), which has been positioned as a weight-saving alternative to stainless steel for exhaust pipes in automobiles or motorcycles [53]. While silicon content is typically low (0.1-0.5 at.% [2]) in commercial alloys, silicon-rich binary Ti-Si alloys, especially the eutectic Ti-13.7 at.% Si, are also considered promising for high-temperature structural applications [12].

Silicon is a β stabilizer with limited solubility in titanium, less than 1 at.% in the α phase and at most about 4 at.% in the β phase (Figure 2.5). With greater silicon concentration, silicon and titanium react to form intermetallic silicides, which are typically brittle and reduce ductility [44]. Ti-Si alloys can contain a mixture of α Ti, β Ti, and different silicides with varied microstructures. Notably, lamellar microstructures of α Ti + silicide or β Ti + silicide can form directly from cooling: α Ti + silicide at the eutectoid point (about 1.3 at.% Si, 864 °C) and β Ti + silicide from about 4-38 at.% Si, where there is a eutectic reaction. The microstructure can be modified via heat treatments in the α and/or β phase fields, particularly to refine the morphology of silicides and to influence mechanical properties such as ductility and strength [44].

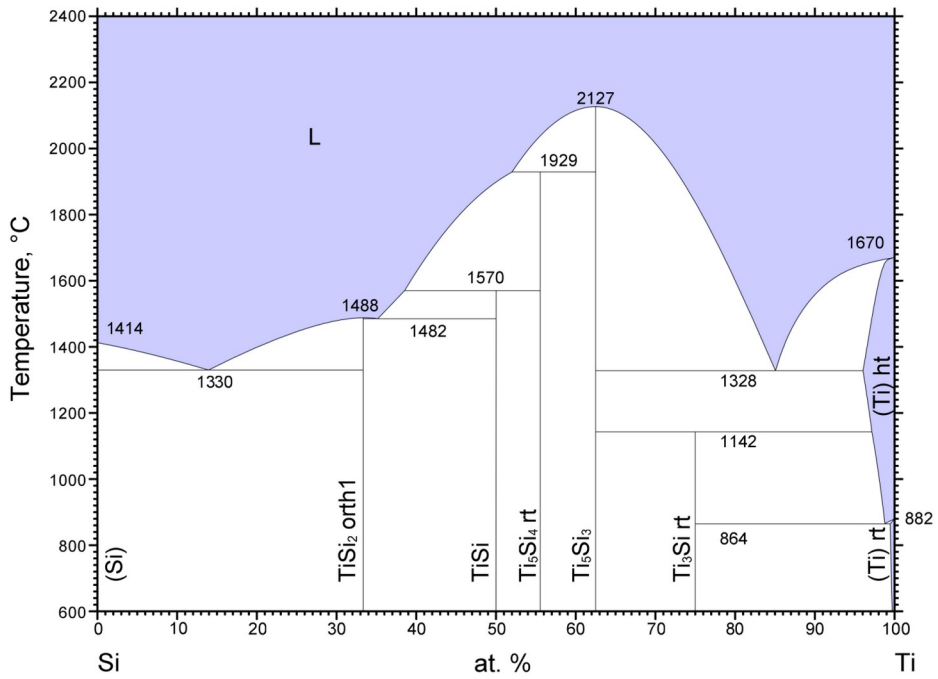

Figure 2.5: Si-Ti phase diagram, from the ASM Alloy Phase Diagram Database [54].

The use of refractory metal silicides in integrated circuits has driven interest in the ternary Ti-Si-O and Ti-Si-N systems [55], [56]. However, the phase diagrams for ternary Ti-Si-O and Ti-Si-N systems are scarce. The ternary phase diagrams shown in Figure 2.6 are only approximate, as they span a temperature range (700-1000 °C), omit certain compounds present in the binary diagrams, and show compounds to be stoichiometric. The Ti-Si-O phase diagram (Figure 2.6, left) lacks some titanium suboxides (e.g. Ti_3O_2 and Magnéli phases) and shows Ti_5Si_3 having no oxygen solubility, in disagreement with experimental measurements [57]. Similarly, the Ti-Si-N phase diagram (Figure 2.6, right) lacks certain titanium silicides (i.e. Ti_3Si, Ti_5Si_4) and, in contrast to the binary Ti-N phase diagram (Figure 2.2), shows titanium nitrides as stoichiometric.

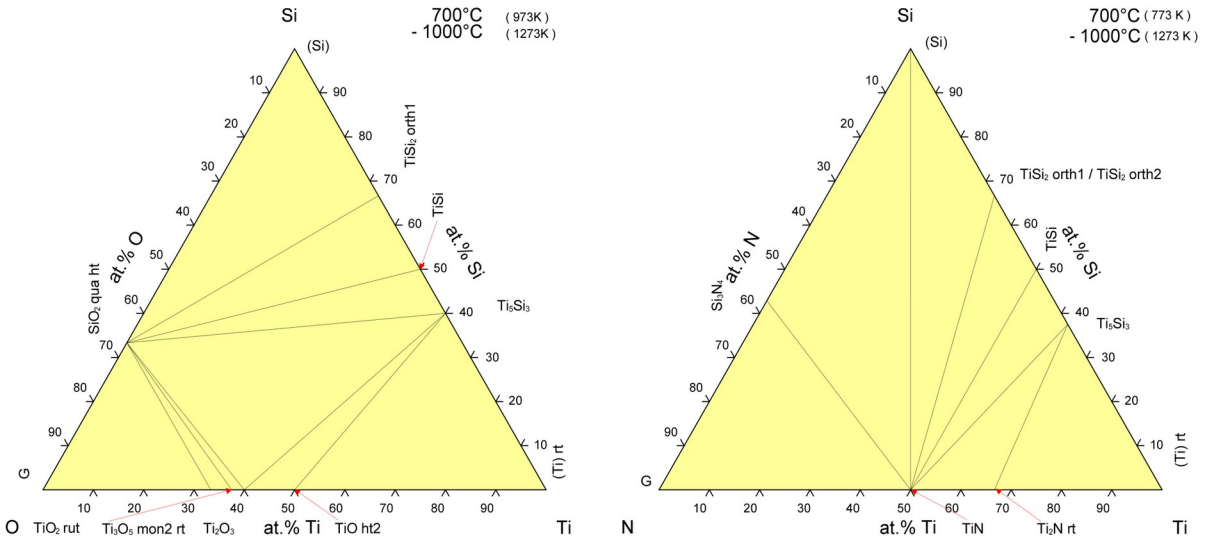

Figure 2.6: Ti-Si-O (left) and Ti-Si-N (right) ternary phase diagrams, from the ASM Alloy Phase Diagram Database [56].

2.1.3 Diffusion in Titanium

Diffusion data is important for understanding the relative mobilities of different species. Here we review the diffusivities of the substitutional elements Ti, Si, and Nb (Figure 2.7, left) and the interstitial elements O and N (Figure 2.7, right) in α and β titanium. Diffusivity, D, typically obeys an Arrhenius equation of the form

$$D = D_0 \exp\left(\frac{-Q}{RT}\right), \tag{1}$$

where D_0 is the frequency factor, Q is the activation energy, R is the gas constant, and T is the absolute temperature. D_0 and Q are typically considered constants.

Diffusivity data for the substitutional elements is scarce (Figure 2.7, left). In α Ti, diffusion measurements are commonly performed using single crystals to eliminate the contribution from diffusion along grain boundaries, which can be significant at the lower temperatures where α Ti is stable [58]. Because of the anisotropy of the HCP structure, diffusivity values in α Ti can depend on crystallographic orientation. For example, $D_{\parallel \text{ to c}} / D_{\perp \text{ to c}}$ for self-diffusion is about 0.5 [59], which is consistent with self-diffusion data in HCP alloys

with $c/a > 1$ [60]. Self-diffusion in α Ti is highly sensitive to the presence of Fe, Ni, and Co impurities (e.g. just 40 ppm in wt.% [58]), which can accelerate self-diffusion [59]. Impurity-enhanced self-diffusion (upper line) is contrasted with normal self-diffusion (lower line) measured in ultrapure titanium, with the difference in diffusivities being most pronounced at lower temperatures. It is believed that these impurities enhance self-diffusion by dissolving interstitially, diffusing rapidly, and forming extremely mobile impurity-vacancy pairs [59], [60]. Compared to self-diffusivity, the diffusivity of Si in α Ti is much greater (e.g. $D_{Si}^{\alpha} / D_{Ti}^{\alpha} > 100$ at 800 °C). The diffusivity of Nb in α Ti could not be found.

At the α-to-β transformation at 882 °C, Ti self-diffusivity and Si diffusivity exhibit a discontinuous step upward, so that the diffusivities are much greater in β titanium than would be expected by extrapolating the values for α to higher temperatures. The diffusivities of Ti, Si, and Nb in β Ti are relatively similar in magnitude and $D_{Si}^{\beta} > D_{Ti}^{\beta} > D_{Nb}^{\beta}$. An interesting feature of substitutional diffusivity in β Ti is the upward curvature, which is typical for self-diffusion in group IV BCC metals and alloys [60] and has been observed for the diffusion of numerous other solutes (Mo, Cr, Mn, Fe, Ni, Co [61]) in β Ti. This curvature is believed to result from temperature dependence of the vacancy migration energy, due to certain phonon modes softening with temperature [60], [62]. Diffusivity can depend on alloy concentration as well; in concentrated β Ti-Nb alloys with less than ~36 at.% Nb, diffusivities of both Ti and Nb were shown to decrease as the concentration of the slower diffuser, Nb, increased [63]. As a note, we would not anticipate this behavior with Ti or Si in Ti-Si alloys because of the limited solubility of Si in Ti.

Compared to substitutional elements, interstitial O and N diffuse much more rapidly in Ti (Figure 2.7, right). In α Ti, O diffusivity is about at least an order of magnitude larger than that of N over the temperature range shown. In β Ti, it is difficult to compare the relative diffusivities of O and N considering the scatter in the O diffusivity values and singular reference for N diffusivity.

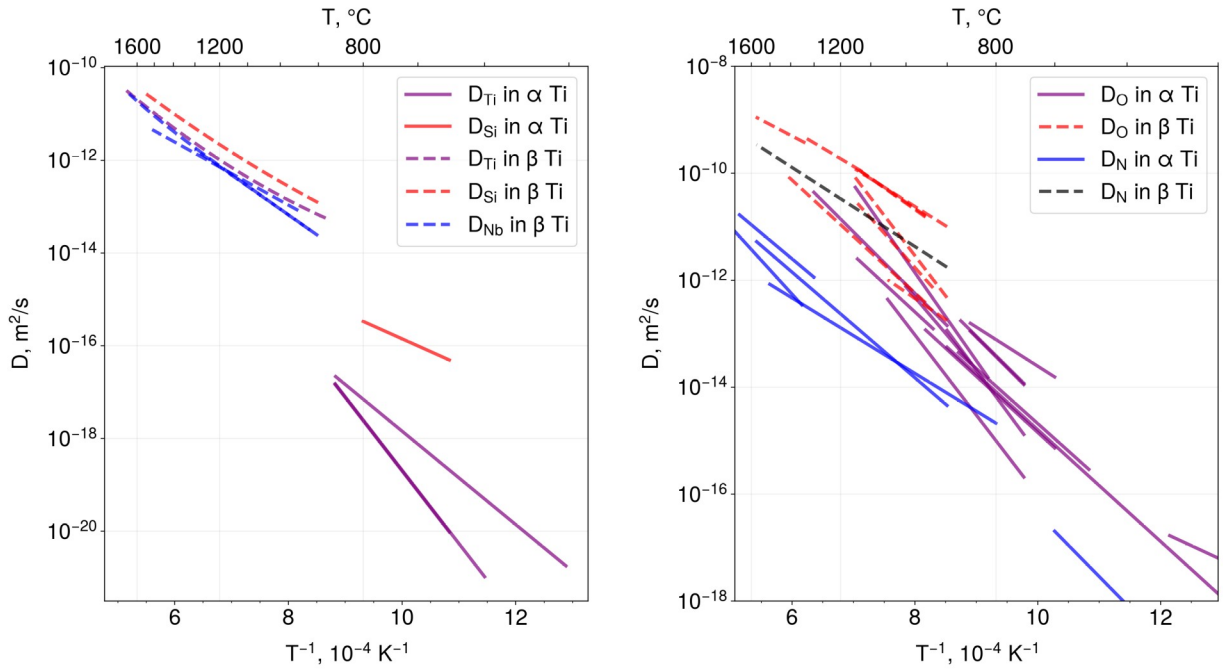

Figure 2.7: Diffusivities of substitutional (left) and interstitial (right) elements in Ti. Diffusivity values are from various references, as follows: D_{Ti}^{α} [59], [62], [64], D_{Si}^{α} [65], D_{Ti}^{β} [62], D_{Si}^{β} [66], D_{Nb}^{β} [61], [63], [67], D_O^{α} and D_O^{β} [68], D_N^{α} [69], D_N^{β} [70].

2.2 High-Temperature Oxidation Behavior of Pure Titanium

The behavior described in this section is relevant for oxidation in oxygen atmospheres at near-atmospheric pressure over the temperature range of 600-1100 °C, unless otherwise noted.

The oxide scale formed during oxidation of pure titanium is often exclusively rutile TiO_2 [4], [5], [6], [7], with different colors indicating differences in oxide scale stoichiometry and/or morphology. Rutile TiO_2 alone is not expected according to the phase diagram (Figure 2.1), which suggests a sequence of stable oxides between atmospheric oxygen and the Ti-O solid solution. While the exclusive formation of rutile is still not understood, one explanation is that it is kinetically favored [71]. The rutile scale usually appears gray [4], [5], [6], [72] or white [5], [6] in color, depending on the oxidation time and temperature. Other colors (yellow, brown) were also reported [4], [7], [73] and possibly related to contaminants in the low-purity raw materials. The gray scale is associated with shorter oxidation times [4], [5], [6] and lower temperatures [4], [7] and is reportedly thin and extremely adherent to the metal [4], [5]. In contrast, the white scale is associated with longer oxidation times [5] and higher temperatures [7]

and is reportedly thick [5] and detached from the metal [6]. The scale may not be exclusively gray or white, as scales of both colors have been found together (e.g. predominantly gray sample with white edges [4], both colors in cross section of scale [7], [72]. The scale color is thought to indicate stoichiometry, where gray is non-stoichiometric (oxygen deficient) rutile and white is stoichiometric [6], [71], [72]. This is generally supported by experiments [4], [73], which reported a change in color upon heating the rutile scale in vacuum or oxygen/air. The non-stoichiometry of rutile is typically written as $Ti_{1+y}O_{2-x}$ (x and y << 1) because the predominant defects are believed to be titanium interstitials (dominant at low oxygen activities and high temperatures) and oxygen vacancies (dominant at high oxygen activities and low temperatures) [71]. In addition to stoichiometry, scale morphology may also contribute to apparent colors, as suggested by evidence of light transmission through translucent rutile and subsequent reflection off the metal accounting for a gray appearance [7].

In cross section, the scale is typically lamellar (in both oxygen [4], [5], [6], [7], [72], [74] and air [72]) and porous [4], [72], [75]. Porosity is believed to facilitate oxygen transport through the scale [5], [6], [75]. Additionally, there are many reports of the scale consisting of two layers: an inner layer with variable microstructure and a monolithic, dense outer layer [5], [7], [75], [76]. In general, this two-layered scale microstructure may reflect scale growth mechanisms, with the inner layer growing by inward oxygen diffusion and the outer layer by outward titanium diffusion. Although inward oxygen diffusion is believed to be dominant [71], there is potential experimental support for both inward oxygen diffusion (by marker studies [4], [5] and observations of scale reabsorption [4]) and outward titanium diffusion (by changes in microstructure of the top surface [75] and marker studies [76]). The dense microstructure of the outer layer was attributed to its growth by outward titanium diffusion [75], [76] or to recrystallization of the scale at high temperature (at 900 °C [5] and 1000 °C [7]). Details about the grain morphology in the inner and outer layers are limited and sometimes inconsistent (e.g. shape is equiaxed (both) [7], [76] or columnar (outer) [76], and size is a combination of coarse and fine (inner) [76] or follows a continuous gradient (outer) [5]). Similarly, the microstructure of the top surface of the scale is poorly documented, and the descriptions available (e.g. of blisters [6], a ridge pattern [4], and aligned features [75]) do not show any obvious

commonalities. In general, the scale microstructure is difficult to interpret considering the differences in the experimental conditions, results, and descriptions.

Throughout the oxidation process, oxygen dissolves in titanium metal [4], [71], where it can influence lattice parameters and induce phase transformations. In α Ti, oxygen causes lattice parameters *a* and *c* to increase relatively linearly when present in concentrations of 0~26 at.% [77]. In β Ti, oxygen stabilizes the growth of a layer of α phase under the scale during oxidation [5], [71]. Oxygen dissolution is influenced by the solubility and diffusivity of oxygen in each phase. Oxygen solubility limits the concentration of oxygen in the metal at the scale-metal interface, or *oxygen surface concentration*. Oxygen diffusivity can influence the depth of oxygen penetration into the metal. In the range 600-1100 °C, oxygen solubility is much greater in α (33.3 at.%) than in β (3 at.% or less) [47], while oxygen diffusivity follows the opposite trend, being much less in α than in β ($D_O^{\alpha} \sim 1/10\ D_O^{\beta}$ or less, as shown in Figure 2.7, right) [68]. In α Ti, prior work suggested that oxygen surface concentration may change with time at lower oxidation temperatures (650-700 °C [78]) and be a function of temperature (12~18 at.% O at 650-800 °C [4], [78] and 26 at.% above 900 °C [4], [5]). In general, diffusivity of oxygen is often assumed constant but could be function of oxygen concentration.

Titanium typically gains mass due to the oxidation process. Mass gains are ideally measured continuously during oxidation (e.g. using thermogravimetry) but may alternatively be measured discontinuously by weighing samples before and after oxidation. Importantly, continuous measurements provide richer data and avoid potential artifacts that could influence mass gains, such as microstructural damage due to thermal cycling. In oxygen atmospheres, mass gain (X) has four possible contributions: oxygen fixed in oxide scale (O_{oxide}), oxygen dissolved in metal (O_{metal}), metal lost to sublimation, ($M_{sublimated}$), and oxide lost to sublimation ($Mo_{sublimated}$):

$$X = O_{oxide} + O_{metal} - M_{sublimated} - MO_{sublimated}, \tag{2}$$

where all quantities have units of mass per surface area, normalizing by the *initial* surface area of the sample. Because there is no sublimation of titanium metal [79] and oxides in this temperature and pressure range, the last two terms can be ignored. Therefore, the total mass gain only reflects oxygen uptake [5]:

$$X = O_{oxide} + O_{metal}. \quad (3)$$

The contribution of oxygen in the metal relative to total mass gain, $O_{metal} / (O_{scale} + O_{metal})$, can range greatly, for example, from 5-80% [4], [5], [6], and typically decreases with increasing oxidation time [4], [6]. This quantity may also be affected by impurity content [4].

Trends in mass gain with time, termed *oxidation kinetics*, can be understood by fitting mass gains to the rate equation

$$X^m = k_m t + C, \quad (4)$$

where m is the rate exponent, k_m is the rate constant, t is the time, and C is a constant. The value of the rate exponent, m, is used to classify the oxidation kinetics, with $m = 1$ termed *linear* and $m = 2$ termed parabolic (Figure 2.8). In the field of oxidation, parabolic kinetics ($m = 2$) is often considered ideal, as it indicates *protective* oxidation behavior in which a progressively thickening oxide scale slows the reaction rate by increasing the distance that reactants must diffuse (oxygen inward and/or metal outward, presumably through the oxide lattice) in order to react.

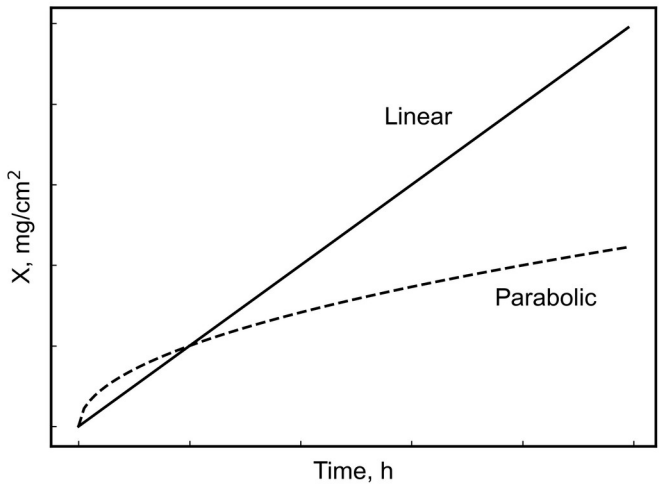

Figure 2.8: Schematic of linear and parabolic oxidation kinetics.

Oxidation kinetics of titanium are generally described as initially parabolic and then linear at longer times [5], [6], [7], [75], [80], with the transition to linear kinetics starting earlier with increasing temperature [5], [6], [7], [75], [80]. The parabolic kinetics are believed to result from simultaneous inward diffusion of oxygen through a compact growing scale and oxygen dissolution in the metal [6], [71], [80]. Because each of these processes has a parabolic contribution to mass gain, their sum is also parabolic [6], [71], [80]. Although the outward diffusion of titanium could also contribute without altering the parabolic rate, its potential contribution is somewhat neglected. The linear oxidation kinetics are thought to reflect periodic detachment and growth of oxide scale on the metal [6], [71], presumably with rapid O_2 transport through the previously detached scale. Since short-term oxidation kinetics are parabolic while the scale is adherent to the metal, the overall linear rate reflects averaging of the short, parabolic subperiods (as identified by [72], [75]) over time [6], [71]. Although the linear kinetics have alternatively been associated with inward diffusion of gaseous oxygen across a porous outer scale [75], this mechanism is less plausible. Detachment of the oxide scale during oxidation, which is generally supported by acoustic measurements [74], is likely due to mechanical stresses associated with expansion of the metal lattice with oxygen [5], [7], [75] and/or the large volume change as Ti oxidizes to rutile TiO_2 [72], [75] (for which the ratio of the volume of the metal atom in the oxide versus in the metal, or Pilling-Bedworth ratio, is 1.76 [16]). In general, oxidation kinetics appear insensitive to mechanical deformation prior to oxidation and considerable reductions in oxygen pressure (e.g. to $pO_2 = 0.05$ atm) [80].

Few studies ([10], [14], [15]) are available to provide insight into the influence of atmospheric nitrogen on the oxidation behavior of unalloyed titanium. While the benefit of reduced oxygen in the metal was observed in all cases, subtle differences in the behavior point to an effect of oxidation temperature. At intermediate temperatures of 550-700 °C, nitrogen resulted in reduced overall mass gain, a delayed transition from parabolic to linear oxidation kinetics, and reduced oxygen in the metal [10]. At the high temperature of 800 °C, only the last effect, reduced oxygen in the metal, was noted [14]. Moreover, this effect was only active initially, as oxygen in the metal increased at longer oxidation times. The benefit of parabolic oxidation kinetics with reduced overall mass gain noted at intermediate temperatures [10] was not realized at high

temperature [14], [15], where oxidation kinetics were linear with high mass gains regardless of the presence of atmospheric nitrogen. Nitrogen does not influence the phase of the oxide scale (rutile TiO_2). We note that we briefly summarize the effects of nitrogen synergistically with Si or Nb alloying additions in the following two sections but wait to discuss the mechanistic role of nitrogen until Section 2.5.

2.3 Effect of Silicon on the High-Temperature Oxidation Behavior of Titanium

Very few studies have investigated the oxidation behavior of titanium with small Si additions, as shown in Table 2.1. To isolate the effect of Si from atmospheric nitrogen, we first consider the oxidation response in oxygen atmospheres. Small Si additions reduced overall mass gain, promoted parabolic rather than linear oxidation kinetics, and reportedly reduced oxygen in the metal [11], [81]. Si helped maintain the parabolic kinetics at higher temperatures, where kinetics were instead linear for unalloyed Ti [11], However, at very high temperatures such as 1200 °C, oxidation kinetics were linear despite the Si [9]. Si had no apparent effect on the phase (rutile TiO_2, as identified by XRD) or layering of the oxide scale [11], [81]. The oxide scale consisted of two layers, an inner microcrystalline layer and outer layer with larger crystals, separated by pores [11], [81]. The number of pores reportedly decreased with increasing Si content [11], [81].

Adding nitrogen to the oxidation atmosphere for the Ti-Si alloys resulted in additional benefits of reducing mass gain [9], [11], thickness of the oxide scale [9], and oxygen in the metal [9], [11]. No changes were noted in the parabolic nature of the oxidation kinetics, the cross-sectional scale morphology, or the oxide phase. However, additional phases were detected: limited cristobalite SiO_2 in the oxide scale [11] and TiN near the scale-metal interface [11], [81].

Table 2.1: Summary of oxidation studies for titanium with dilute Si alloying additions.

Ref.	Si (at.%)	Atmosphere	Temperature (°C)	Time (h)	Oxide Phases
[9]	1.69	O_2	900-1200	≤12	TiO_2
		Air			
[11], [81]	0, 0.39, 0.73, 1.47	O_2	550-700	≤500 (O_2)	TiO_2
		Air		≤6500 (Air)	SiO_2

Four mechanisms have been proposed to account for the effects of Si independent of atmospheric nitrogen:

1. Si^{4+} ions dope rutile TiO_2, reducing the concentration of oxygen vacancies and therefore oxygen diffusivity in the oxide [11];
2. A fine dispersion of SiO_2 in the rutile oxide modifies the stress relaxation processes in the oxide, resulting in a dense oxide with reduced diffusion of oxygen through pores and cracks [11];
3. Si reduces oxygen diffusivity in the metal, reducing the depth of oxygen penetration [11]; and
4. Si influences oxygen solubility in the metal [9].

There is currently no experimental confirmation for the first mechanism, that Si^{4+} dopes the oxide and thereby reduces oxygen diffusivity in the oxide. Alternatively, some evidence suggests that reduced oxygen diffusivity in rutile could be due not to Si^{4+} doping but rather to an SiO_2 dispersion [82]. However, there is also no evidence of an SiO_2 dispersion in the oxide in [11], to account for reduced oxygen diffusivity or, per the second mechanism, densification of the oxide. The third mechanism is generally supported by experimental measurements of oxygen in the metal. While indirectly measured via hardness, the oxygen profile in the metal was shallower in a Ti-1.47Si alloy than in pure Ti [11], [81]. The fourth mechanism — that Si influences O solubility — was suggested after observing variations in hardness near the surface of the metal as a function of oxidation temperature for Ti-1.47Si [9]. Considering the limited evidence for the third and fourth mechanisms and that hardness is likely not proportional to oxygen content [83], quantitative measurements of oxygen in the metal are warranted. Although these mechanisms are not confirmed, mechanisms 1-3 in particular are repeated throughout the literature as if they are truth (e.g. in [12], [13], [84]).

2.4 Effect of Niobium on the High-Temperature Oxidation Behavior of Titanium

Since the early work linking Nb alloying in titanium with improved oxidation behavior [8], a limited number of follow-up studies have been performed examining the effects of small Nb additions (≤5 at.%), as shown in Table 2.1. Additionally, only two studies ([15], [16]) give insight into the oxidation behavior in nitrogen-free atmospheres.

Table 2.2: Summary of oxidation studies for titanium with dilute Nb alloying additions.

Ref.	Nb (at.%)	Atmosphere	Temperature (°C)	Time (h)	Oxide Phases
[8]	0, 0.52, 2.34	Dry air	650~980	50~300	Not tested
[16]	2.27	O_2	1000~1200	12~19	TiO_2
		Air			Ti_2O
[15]	0, 4	Dry/moist Ar-O_2	800	≤150	TiO_2
[14]	0, 4	Dry/moist N_2-O_2	800	≤150	TiO_2
					Ti_2O
[19]	0, 5	Dry air	900	24	TiO_2
[17]	0, 0.05, 0.26, 0.52, 1	Air	800	24-288	TiO_2
[39]	1, 5	Air	1000	1	TiO_2
[18]	0, 4	Dry/moist N_2-O_2	800	5	TiO_2

In oxygen atmospheres, Nb reduced mass gain, shifted oxidation kinetics closer to parabolic, reduced the thickness of the (lamellar) oxide scale and its degree of stratification, and reportedly increased oxygen in the metal [15]. As with Si, Nb had no apparent effect on the oxide phase (rutile TiO_2) [15], [16].

Adding nitrogen to the oxidation atmosphere for the Ti-Nb alloys reduced mass gain further [14], [15] and reportedly reduced oxygen in the metal [14], [15], [16]. Additionally, the thickness of the oxide scale was reduced, with stratification in the scale completely eliminated [14], [17]. While the (rutile TiO_2) phase of the dominant oxide remained the same, additional phases were sometimes noted at the scale-metal interface: Ti_2O [14], [16], TiN [16], and Ti_2N [14].

Various mechanisms have been proposed to account for the effects of Nb independent of atmospheric nitrogen, with four warranting discussion:

1. Nb^{5+} ions dope rutile TiO_2, reducing the concentration of oxygen vacancies and/or titanium interstitials and thereby reducing oxygen and/or titanium diffusivity in the oxide [14], [15], [16], [19];
2. Nb accumulates at the oxide-metal interface, forming a Nb-rich layer that slows oxygen and/or titanium diffusion [14], [15], [17];
3. Nb increases oxygen diffusivity in the metal [15]; and
4. Nb reduces oxygen solubility in the metal [14], [15].

Many of these mechanisms are very similar to those discussed for Si in Section 2.3. The first mechanism, that Nb dopes TiO_2, is very controversial. While it is alternately assumed to be important [16], [19] or not [14], [15], [17], there is little evidence to either support or refute this mechanism. As measurements typically showed little to no Nb content in the oxide scale [14], [15], [16], [17], more work is necessary to check for Nb in the scale and investigate its possible effects. There is no evidence for the second mechanism. Although it was claimed in one instance [17], experimental evidence was inconsistent; specifically, no Nb-rich layer was visible in SEM, and EDS composition profiles through the purported layer did not show Nb enrichment. The third mechanism (Nb increases oxygen diffusivity in the metal) is consistent with indirect measurements of oxygen in the metal, i.e. elevated hardness extending deeper into the metal for a Ti-4Nb alloy than for pure Ti [15]. However, this behavior could be explained by the non-negligible amount of β-phase titanium observed in the metal, which has much greater oxygen diffusivity than the predominant α phase (Figure 2.7). Therefore, additional work is necessary to determine if Nb influences diffusivity in α titanium. The fourth mechanism (Nb reduces oxygen solubility in the metal) does not appear to be supported by any evidence. As was the case for the Si, quantitative measurements of oxygen in the metal are needed to clarify the third and fourth mechanisms.

2.5 Effect of Nitrogen on the High-Temperature Oxidation Mechanisms of Titanium and Titanium Alloys

Although nitrogen can impact the oxidation behavior of titanium and titanium alloys, its influence on the oxidation mechanisms remains poorly understood. As discussed in the last three sections, for unalloyed titanium, the net effect of nitrogen can be positive [10] or null [14] depending on the oxidation conditions. In contrast, the effects of nitrogen with dilute Si or Nb alloying additions are typically positive. Similar positive effects of nitrogen — specifically, reducing mass gain [20], [21], [22], oxide thickness [21], [22], [23], and the amount of oxygen dissolved in the metal [21], [22], [24] — were also reported for other alloys (Ti-Ta [20], [24] and Ti6242S [21], [22], [23], oxidation at 800-1400 °C).

The general role of nitrogen during oxidation in air can be understood as follows. Upon initial oxidation, air reacts with titanium to form titanium oxide rather than nitride. This is due to the greater thermodynamic stability of oxides than nitrides at the high pO_2 (0.2) in the gas. As the oxide grows, nitrogen diffuses inward through the oxide and into the metal and can form nitride phases at the oxide-metal interface. The accumulation of nitrogen at the oxide-metal interface is possible because of its fast transport through the oxide scale and comparatively slow diffusion away, into the metal. Fast inward transport of nitrogen through the oxide scale is consistent with a report of diffusivity in rutile being greater for nitrogen than oxygen [10]. Furthermore, nitrogen remains strongly localized to the surface of the metal, in comparison to oxygen, because of its low diffusivity in the metal ($D_N/D_O \sim 1/300$ in α Ti at 800 ° [68], [69], Figure 2.7). Chaze and Coddet [10] proposed that the accumulation of nitrogen at the oxide-metal interface would:

1. Reduce the oxygen concentration at the interface and therefore decrease the diffusion rate of oxygen into the metal;
2. Reduce the growth rate of the TiO_2 at the internal interface, due to the reduced concentration of anionic vacancies there; and
3. Modify the stress accumulation in a way that promotes a compact, protective oxide scale (with oxidation kinetics remaining parabolic).

Thoroughly evaluating the first mechanism would require measurements of nitrogen near the scale-metal interface and, as with investigating the roles of Si and Nb, quantitative measurements of oxygen in the metal. Additionally, an alternative mechanism potentially accounting for the reduced oxygen in the metal is that the nitride layer itself, rather than nitrogen accumulation in the metal, limits the diffusion of oxygen into the metal. As oxide growth mechanisms are unconfirmed, as discussed in Section 2.2, the second mechanism is speculative. The third mechanism generally agrees with the observed behavior but is difficult to test. Despite these specific mechanisms, many studies simply broadly attribute the benefits of nitrogen to the formation of nitride phases, oxynitride phases, and/or nitrogen dissolution in the metal, with one or more acting as a barrier to oxygen [14], [20], [22], [23], [25], [26].

More work is needed to understand how atmospheric nitrogen alone and with alloying additions influences the oxidation mechanisms of titanium. Specifically, the origin of the reduced amount of oxygen dissolved in the metal needs to be resolved. It remains unclear if it arises from the nitride phase limiting the diffusion of oxygen or from nitrogen in the metal limiting the oxygen solubility near the surface (and therefore throughout the metal). Additionally, it is important to determine if, synergistically with nitrogen, alloying additions influence the behavior of oxygen in the metal, such as the oxygen concentrations.

2.6 Summary

After briefly summarizing relevant metallurgy and diffusivity data for titanium, this chapter reviewed the high-temperature oxidation behavior of pure titanium and titanium alloyed with small amounts of Si or Nb. Oxidation behavior was considered both with and without nitrogen in the oxidation atmosphere. In general, the oxidation behavior of pure titanium is poor. Contributing factors include the high oxygen solubility and diffusivity in the metal, which lead to extensive oxygen enrichment in the metal, and detachment of the oxide scale, which results in rapid oxidation and an overall non-protective scale. Despite numerous studies since the 1950s, some details about the oxidation of titanium remain unknown or unconfirmed, particularly the expected scale microstructure and dominant scale-growth direction (and therefore dominantly diffusing species, i.e. oxygen or titanium). Additionally, although alloying and atmospheric

nitrogen can potentially improve the oxidation behavior, the mechanisms remain unclear, as we explained in detail. The purpose of this thesis is to clarify these mechanisms. Bolstering this foundational knowledge will help us design oxidation-resistant titanium alloys for use in increasingly demanding high-temperature environments.

Chapter 3: Role of Silicon in the High-Temperature Oxidation of Titanium

3.1 Introduction

For titanium-based alloys, employing silicon either in coatings (e.g. via laser surface alloying or solid-, liquid-, or vapor-based siliconizing) [57], [76], [84], [85], [86], [87] or as an alloying addition [9], [10], [11], [12], [13] can be particularly effective at limiting oxidation. For example, alloying with silicon is used to improve high-temperature oxidation resistance, along with strength, in the binary commercial alloy Timet Exhaust HT, which has the same composition of the alloy used in this thesis (Ti-0.8 at.% Si) and is marketed as a weight-saving alternative to stainless steel for exhaust pipes in cars and motorcycles [53].

Despite the well-known empirical benefit of silicon, as an alloying addition, its influence on oxidation mechanisms is not well understood. Specifically, the potential influence of silicon on oxygen diffusivity [11] or stress relaxation [11] in the oxide scale and on oxygen diffusivity [11] or solubility in the metal [9] remain unclear or unverified. Through a systematic comparison and detailed characterization of the oxidation response of pure titanium and a dilute Ti-Si alloy oxidized in Ar-O_2 or O_2, we clarify the role of silicon in the oxidation of titanium.

The effect of silicon stemmed from differences in oxide growth rather than oxygen dissolution in the metal. Initially, silicon reduced outward oxide growth and completely eliminated inward growth, which we attributed to the continuous Ti_5Si_3 layer formed at the oxide-metal interface. After breakdown of the Ti_5Si_3 layer, the oxide — containing silicon — became lamellar but remained more compact and possibly slower growing than the oxide on pure titanium.

3.2 Experimental Methods

The materials used in this study were pure (99.999%) titanium plate purchased from Alfa Aesar (Lot M31E035; Tewksbury, MA) and Ti-0.8 at.% Si (‘‘Ti-0.8Si’’) prepared via arc melting raw materials on a water-cooled Cu crucible under gettered Ar. The arc-melted button was flipped

and remelted three times to enhance chemical homogeneity. Grains were small and equiaxed in pure Ti and larger and irregular in shape in Ti-0.8Si, as shown in Appendix Figure A.1. The specific silicon content of 0.8 at.% in the Ti-Si alloy was selected to promote the formation of single-phase α-Ti solid solution at the isothermal oxidation temperature (800 °C) while avoiding titanium silicides present at higher silicon concentrations [54].

For oxidation studies, specimens were ground and subsequently polished with 9 μm diamond suspension. This final polishing step was intended to minimize deformation. Before oxidation, specimens were cleaned ultrasonically in acetone and then methanol.

Oxidation studies were performed under flowing Ar-20% O_2 for 8 h or 32 h in a tube furnace (Lindberg/Blue M; Thermo Fisher Scientific; Waltham, MA) or for 100 h in a thermogravimetric analyzer (STA 449 F3 Jupiter; NETZSCH Instruments North America, LLC; Burlington, MA). Nominal gas purity was 99.999% for Ar and 99.993% for O_2. The tube furnace was flushed with flowing Ar (40 SCCM, for 20 min) while heating to 800 °C. Specimens were then inserted into the hot zone. After the temperature equilibrated (8 min), gas flows were adjusted to 16 SCCM Ar – 4 SCCM O_2. After the oxidation time elapsed, specimens were pulled from the hot zone and cooled to room temperature under flowing Ar (40 SCCM). For thermogravimetric studies, the two largest faces of rectangular plate-shaped specimens were polished with 9 μm diamond suspension, while the four smaller faces were only ground with 30 μm alumina lapping film. The furnace was flushed with flowing Ar (40 SCCM) during heating (20 °C/min) to 800 °C. The specimen equilibrated for 10 min before O_2 flow (10 SCCM) was initiated. After 100 h, O_2 flow was terminated, and the specimen was cooled to room temperature under flowing Ar (40 SCCM). Mass gain was recorded during heating and isothermal oxidation and subsequently background corrected, by subtracting mass gain measured under identical conditions with no sample present. Two trials were conducted for each material to ensure that the measurements were repeatable.

Two-stage tracer oxidation experiments were performed using the setup in Figure 3.1, which consisted of the aforementioned tube furnace on a sliding track and a quartz oxidation chamber connected to a mass spectrometer (PrismaPro QMG 250 F1, 1–100 μ; Pfeiffer Vacuum GmbH; Asslar, Germany), a diaphragm vacuum pump (MD 1C; Vacuubrand Inc.; Essex, CT), and oxygen gas sources. Pure Ti was oxidized for 12 h in $^{16}O_2$ followed by 4 h in $^{18}O_2$. Ti-0.8Si was oxidized for 28 h in $^{16}O_2$ followed by 4 h in $^{18}O_2$. Given differences in scale growth rates, different durations of the initial ($^{16}O_2$) oxidation stage were used to achieve compact oxide scales

of thicknesses suitable for subsequent nanoSIMS analysis. Nominal purity and isotopic purity of ^{18}O was at least 99.00% (Sigma-Aldrich; St. Louis, MO). Composition of the exposure atmosphere was continuously monitored using the mass spectrometer. Specimens were sealed in the oxidation chamber, which was then evacuated with the vacuum pump (nominally rated to 2 mbar) for 1 min and backfilled with $^{16}O_2$ to atmospheric pressure. This purging process was repeated three more times, with the final backfill to approximately 0.2 atm $^{16}O_2$ for pure Ti and 1 atm for Ti-0.8Si (at room temperature). After heating to 800 °C, the furnace was moved over the specimens and equilibrated in temperature for 8 min. For the second oxidation exposure, i.e. after 12 h for pure Ti or 28 h for Ti-0.8Si, the atmosphere was replaced (at high temperature) by evacuating the system for 1 min and backfilling to approximately 0.2 atm $^{18}O_2$ within 1 min. After 4 h, the furnace was moved off the specimens, which then cooled to room temperature (in $^{18}O_2$).

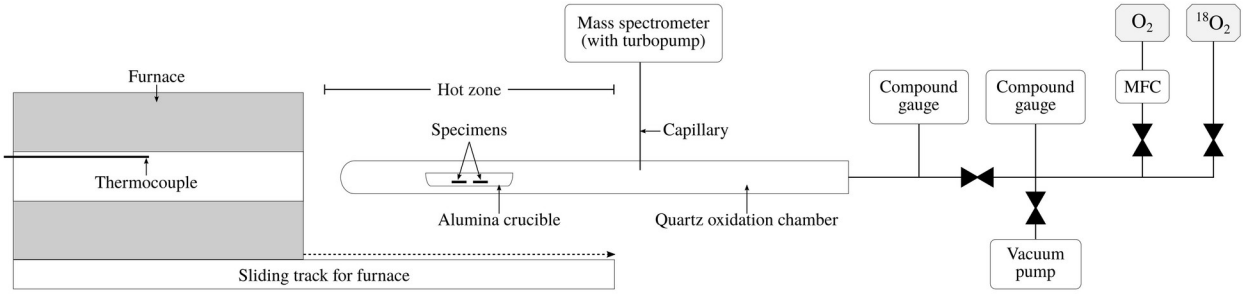

Figure 3.1: Schematic of the experimental setup for two-stage tracer oxidation experiments.

After oxidation, specimens were imaged in plan view using an optical microscope (AZ100; Nikon Metrology, Inc; Brighton, MI). Bulk cross sections were prepared by mounting specimens in low-shrinkage epoxy, sectioning the mount in half perpendicular to the oxidized surface, remounting one half, grinding with SiC papers, and polishing with colloidal silica. Mounted specimens were carbon coated and then imaged in a Thermo Fisher Scientific Helios 650 Nanolab SEM equipped with a directional BSE detector. This microscope, with its integrated Ga FIB, was also used to prepare all cross-sectional lamellae and APT tips. Standard FIB techniques were used, including depositing a protective Pt cap before milling and using a final low-voltage cleaning step (5 kV for lamellae, 2 kV for APT tips). Lamellae were characterized with TEM, STEM, and EDS in STEM using a Thermo Fisher Scientific Talos F200X G2 equipped with a Super-X detector and operating at 200 kV. Net-intensity EDS maps

were prepared using Velox 3.1.0.919 (FEI Company; Hillsboro, OR), with a post-processing Gaussian blur to enhance contrast.

Quantitative oxygen concentration in the metal was measured on bulk cross sections using WDS in a Cameca SX100 EPMA with a beam voltage of 15 kV and current of 40 nA. Ti, O, and Si signals were collected using Kα X-rays and quantified using Probe For EPMA (Probe Software, Inc.; Eugene, OR). A correction was applied to O to account for the interference of Ti Lβ on O Kα [88]. For each specimen, two profiles consisting of points spaced 5 μm apart were collected, spatially calibrated for angle and offset to the oxide-metal interface, and combined into a single dataset. Points outside of physical ranges were discarded, and points below the detection limit of oxygen (about 0.1 wt.% or, in pure Ti, 0.3 at.%) were set to zero.

For nanoSIMS studies, lamellae were prepared from tracer-oxidized pure Ti and Ti-0.8Si. The distributions of ^{16}O and ^{18}O in the oxide and underlying metal were analyzed using a Cameca NanoSIMS 50 (Gennevilliers, France) with a focused Cs^+ beam (0.2 pA current, ~50 nm spot size) at a mass-resolving power of ~3000 (corrected after [89]). $^{16}O^-$, $^{18}O^-$, and (to mark the Pt cap) $^{12}C^-$ were detected simultaneously using pulse counting on electron multipliers. Data was processed with L'image (Carnegie Institution of Washington; Washington, DC) [90] to correct for dead time (44 ns), automatically align scan frames to compensate for drift, and generate isotope maps.

APT was used to characterize ^{18}O-rich oxide grain boundaries observed in nanoSIMS. One needle-shaped tip was prepared from the oxide on tracer-oxidized Ti-0.8Si; additional details are in the Appendix, Section 3.6.1. The tip was analyzed in a Cameca LEAP 5000 HR using a specimen temperature of 50 K, detection rate of 0.25%, laser-assisted mode with a laser pulse energy of 60 pJ, and auto pulse-rate control with a minimum m/q range (Da) of 150. The tip was reconstructed using Cameca AP Suite version 6.1.0.35 using a k factor of 3.3, an evaporation field of 32 V/nm, an image compression factor of 1.65, and fixed-shank radius evolution. The evaporation field was estimated using the aforementioned k factor, final voltage, and final tip radius. Tip radius and shank angle were measured using STEM. For accurate compositional analysis, AtomProbeLab version 0.2.4 [91] was used for statistically informed selection of appropriate ions [92] and for resolving peak overlaps, particularly those due to ^{18}O replacing ^{16}O in various Ti-O ions; additional details, including the mass spectrum (Figure 3.10) are in the Appendix, Section 3.6.2.

3.3 Results

Mass gain was always lower for Ti-0.8Si than for pure Ti (Figure 3.2). However, both alloys exhibited similar rate laws according to the analysis of the mass gain fitted to Equation 4, discussed previously in Section 2.2. For both materials, mass gain, while initially approximately parabolic ($m \sim 1.7$ from 0 to 10 h for both materials), was overall approximately linear ($m \sim 1.2$ for pure Ti and $m \sim 1.3$ for Ti-0.8Si from 0 to 100 h, with k_m for Ti-0.8Si about half that of pure Ti).

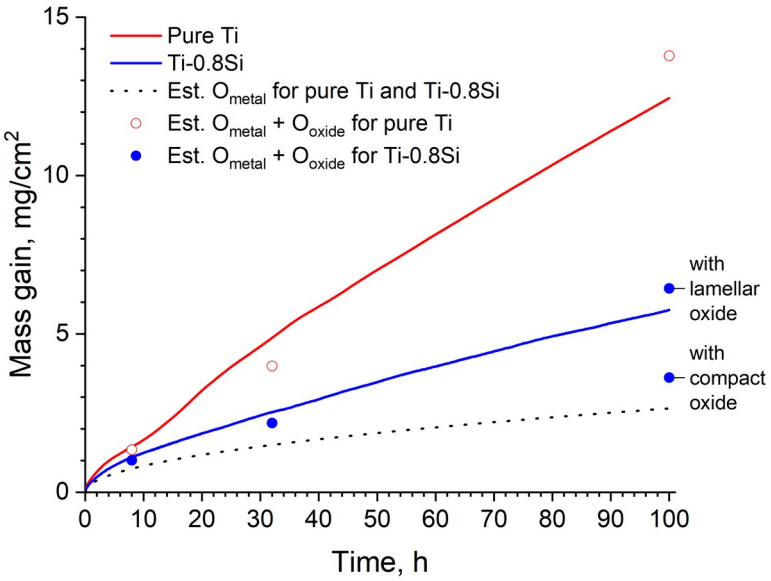

Figure 3.2: Mass gain of pure Ti and Ti-0.8Si during isothermal oxidation at 800 °C in Ar-O_2 with estimates of oxygen in the metal (O_{metal}) and oxide (O_{oxide}). O_{metal} was estimated using integration of Equation 5 with $C_s = 26$ at.%, $C_0 = 0.0$ at.%, and $D = 1.0 \times 10^{-14}$ m^2/s. O_{oxide} was calculated using the density of rutile TiO_2 and measurements of oxide thickness (corrected for cracks and porosity).

Optically, the oxidized surfaces on both materials ranged in color from dark gray to white, with edges typically white (Figure 3.1). All oxide was presumed to be rutile TiO_2, in accordance with the literature [4], [5], [6], [7], and because no observations indicated otherwise (e.g. the oxide exhibited uniform contrast in BSE SEM and STEM (not shown) and had a composition corresponding to TiO_2 in APT). For pure Ti, the surface was initially grayish white (8 h, Figure 3.1a) and, with increasing oxidation time, became white locally (32 h, Figure 3.1b) and then over the entire surface (100 h, Figure 3.1c). For Ti-0.8Si, the surface was initially dark gray with white along the edges and along ridges in the center of the sample (8 h, Figure 3.1d).

With increasing oxidation time, the white areas along the edges widened. After 100 h, the surface of Ti-0.8Si varied, appearing either predominantly dark gray (Figure 3.1f) or completely white (Figure 3.1g); the undersides of these specimens exhibited similar colors, with darker shades typically near the center of sample surfaces (Figure 3.13 in the Appendix).

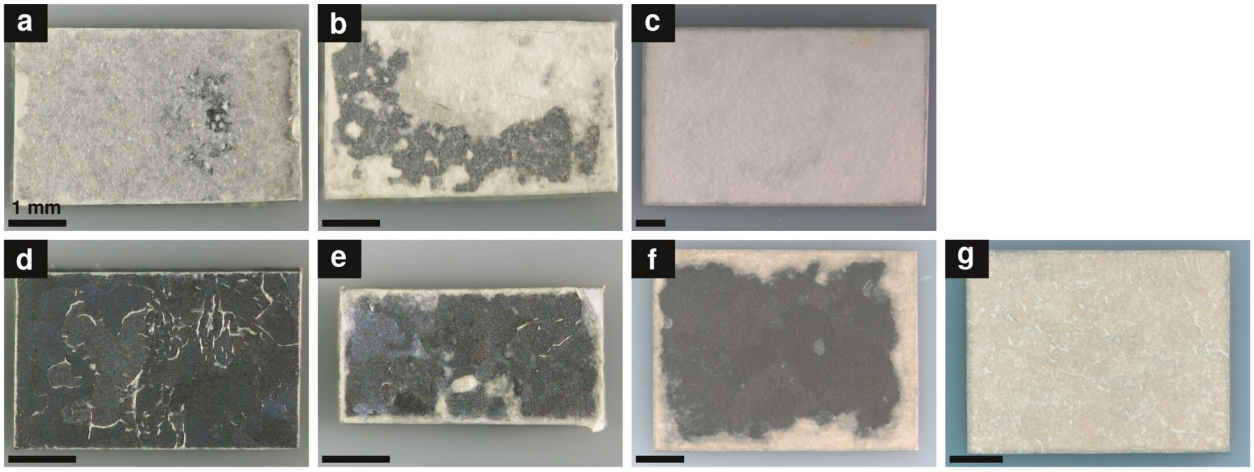

Figure 3.3: Plan-view optical images of (a-c) pure Ti and (d-g) Ti-0.8Si oxidized for (a, d) 8 h, (b, e) 32 h, and (c, f, g) 100 h (800 °C, Ar-O_2). For Ti-0.8Si at 100 h, two images are shown to emphasize the variability in oxide color across the sample surface, i.e. predominantly gray (f) or white (g). All scale bars are 1 mm.

Using SEM, the oxidized surface of each sample was examined in two locations and found to be consistent (Figure 3.4). The surface of pure Ti (Figure 3.4a-c) consisted of faceted, equiaxed crystals — which grew from 8 to 32 to 100 h (Figure 3.4a-c) — and acicular/plate-like protrusions (falling arrows in Figure 3.4a and 3.4c). The surface of Ti-0.8Si (Figure 3.4d-g) consisted of faceted, equiaxed crystals like those on pure Ti (Figure 3.4a). The equiaxed crystals progressively grew with time more so in gray regions (Figure 3.4d-f) than in white regions (Figure 3.4g). On both materials, fine ridges (rising arrows in Figure 3.4) were present along some boundaries between crystals — at 8 h in pure Ti (Figure 3.4a) and at both 8 and 32 h in Ti-0.8Si (Figure 3.4d and 3.4e).

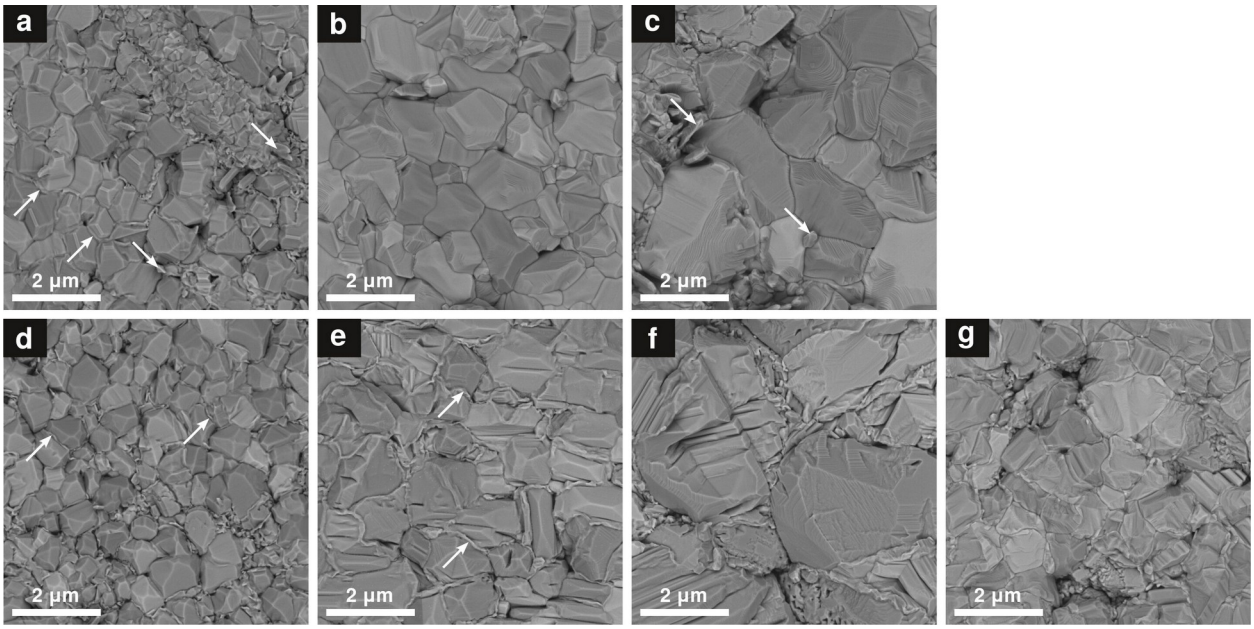

Figure 3.4: Plan-view, BSE-mode SEM of (a-c) pure Ti and (d-g) Ti-0.8Si oxidized for (a, d) 8 h, (b, e) 32 h, and (c, f, g) 100 h (800 °C, Ar-O_2). The two images for Ti-0.8Si at 100 h correspond to oxide optically appearing gray (f) and white (g). Rising arrows point to ridges along boundaries between equiaxed crystals in both materials (also observed in cross section, Figure 3.14 in the Appendix). Falling arrows point to acicular/plate-like protrusions (in pure Ti).

In polished cross sections obtained after oxidation for 100 h (Figure 3.5), the oxide on both materials was uniform across the sample surface with distinct corners. For pure Ti, the oxide in the center of the sample was lamellar, with layers of irregular thickness separated by voids (Figure 3.5a); toward the corners, the oxide gradually thinned and became dense (Figure 3.5b). For Ti-0.8Si, the oxide in the center of the sample consisted of a dense outer layer and thinner inner lamellar layer (Figure 3.5c); as in pure Ti, the oxide at the corners was dense (Figure 3.5d). Compared to pure Ti, Ti-0.8Si exhibited significantly thinner oxide with less porosity. Note that the cross-sectional micrographs of Ti-0.8Si were taken from a sample with all white oxide, as in Figure 3.1g. Cracks and chips in the oxide and metal indicated by arrows in Figure 3.5d reflected damage from metallographic preparation.

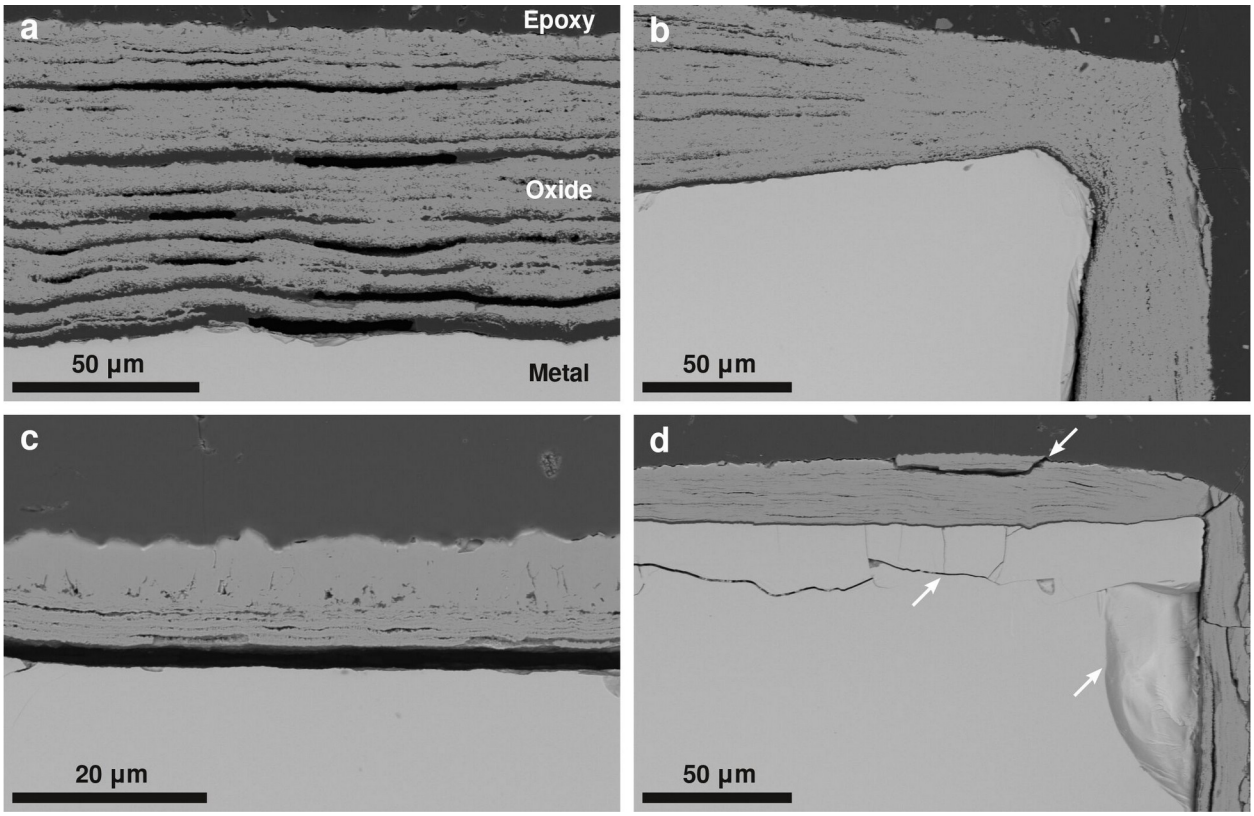

Figure 3.5: BSE-mode SEM of polished cross sections of (a, b) pure Ti and (c, d) Ti-0.8Si oxidized for 100 h (800 °C, Ar-O_2) showing oxide on flat surfaces far from corners (a, c) and near the corners (b, d). Arrows in (d) point to presumed damage from metallographic preparation.

Microstructure and local chemistry in cross section were examined using SEM, TEM, and STEM. At early times, the oxide on both materials was relatively compact but exhibited differences in porosity and chemistry near the oxide-metal interface. The oxide on pure Ti oxidized for 8 h (Figure 3.6a) exhibited two layers: a dense outer layer (about 1.5 µm thick) with large columnar grains and a porous inner layer (about 2 µm thick) with finer, equiaxed grains. For Ti-0.8Si, we first consider the oxide from gray regions (Figure 3.6b-d), which consisted of a single layer of large, columnar grains that thickened with increasing oxidation time. Porosity in the oxide tended to be fine (tens of nm in size) and faceted. Below the oxide, EDS showed a continuous Si-rich layer about 30–40 nm thick, which within error did not appreciably thicken from 8 to 100 h (Figure 3.7a-c). This layer was identified as Ti_5Si_3 ($P6_3/mcm$ [93]) using nanobeam diffraction, as shown in Figure 3.15. In white regions, the oxide (Figure 3.8) was lamellar with a dense outer layer (above Region 1) resembling the oxide in gray regions. Region 1 and Region 2, located below, both contained bands of grains tens of nanometers and hundreds

of nanometers in size. The finer grains, which appeared internally layered, were richer in Si than the coarser grains (Figure 3.8d, 3.8e, 3.8h, and 3.8i).

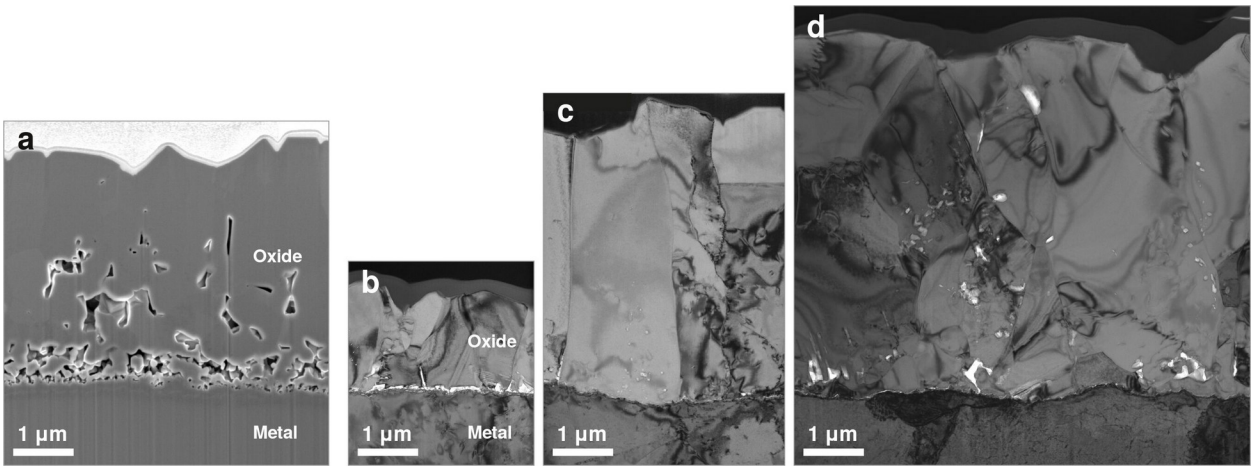

Figure 3.6: Cross sections of (a) pure Ti oxidized for 8 h (SE-mode SEM) and, from regions appearing gray, Ti-0.8Si oxidized for (b) 8 h, (c) 32 h, and (d) 100 h (bright-field TEM) (800 °C, Ar-O_2).

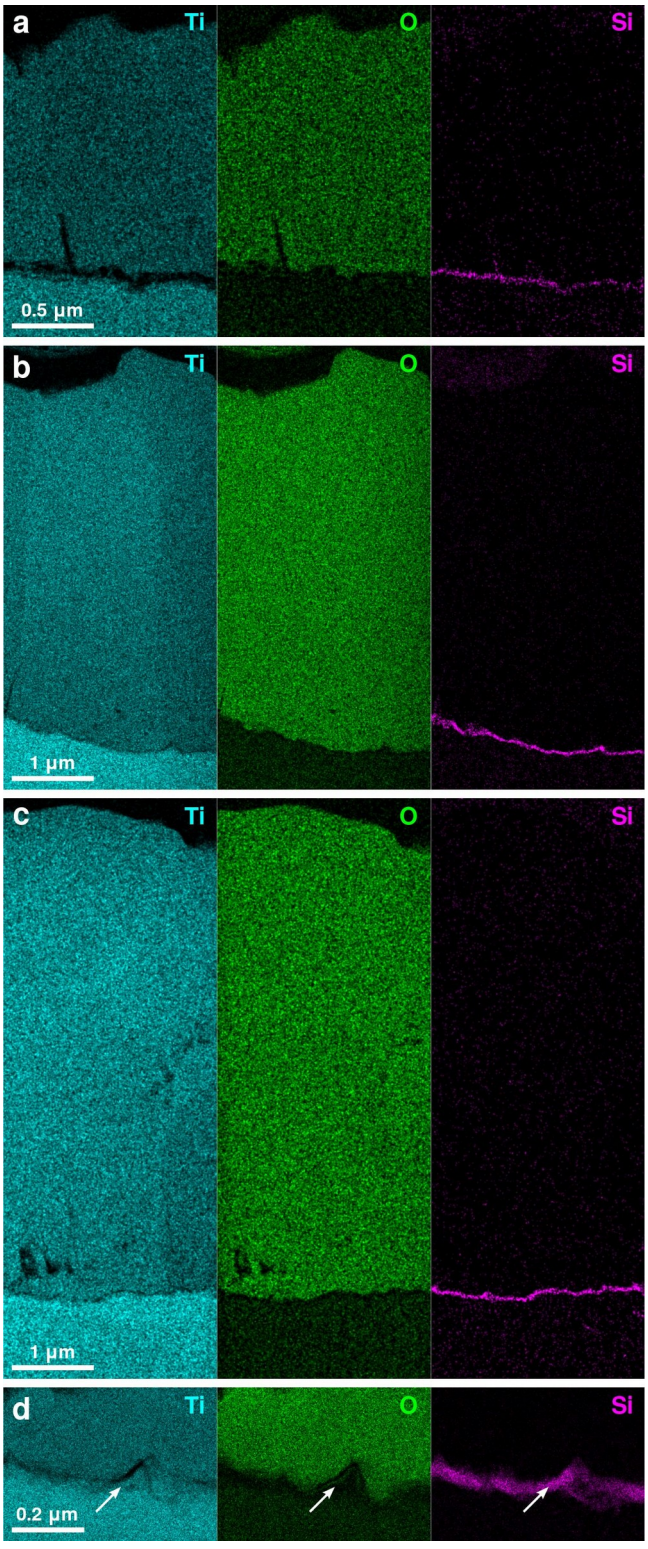

Figure 3.7: Net-intensity EDS maps on cross sections of Ti-0.8Si oxidized for (a) 8 h, (b) 32 h, and (c) 100 h (800 °C, Ar-O_2), showing Ti, O, and Si. Cross sections are from regions appearing gray. (d) shows the Ti- and Si-rich layer at the oxide-metal interface at 100 h.

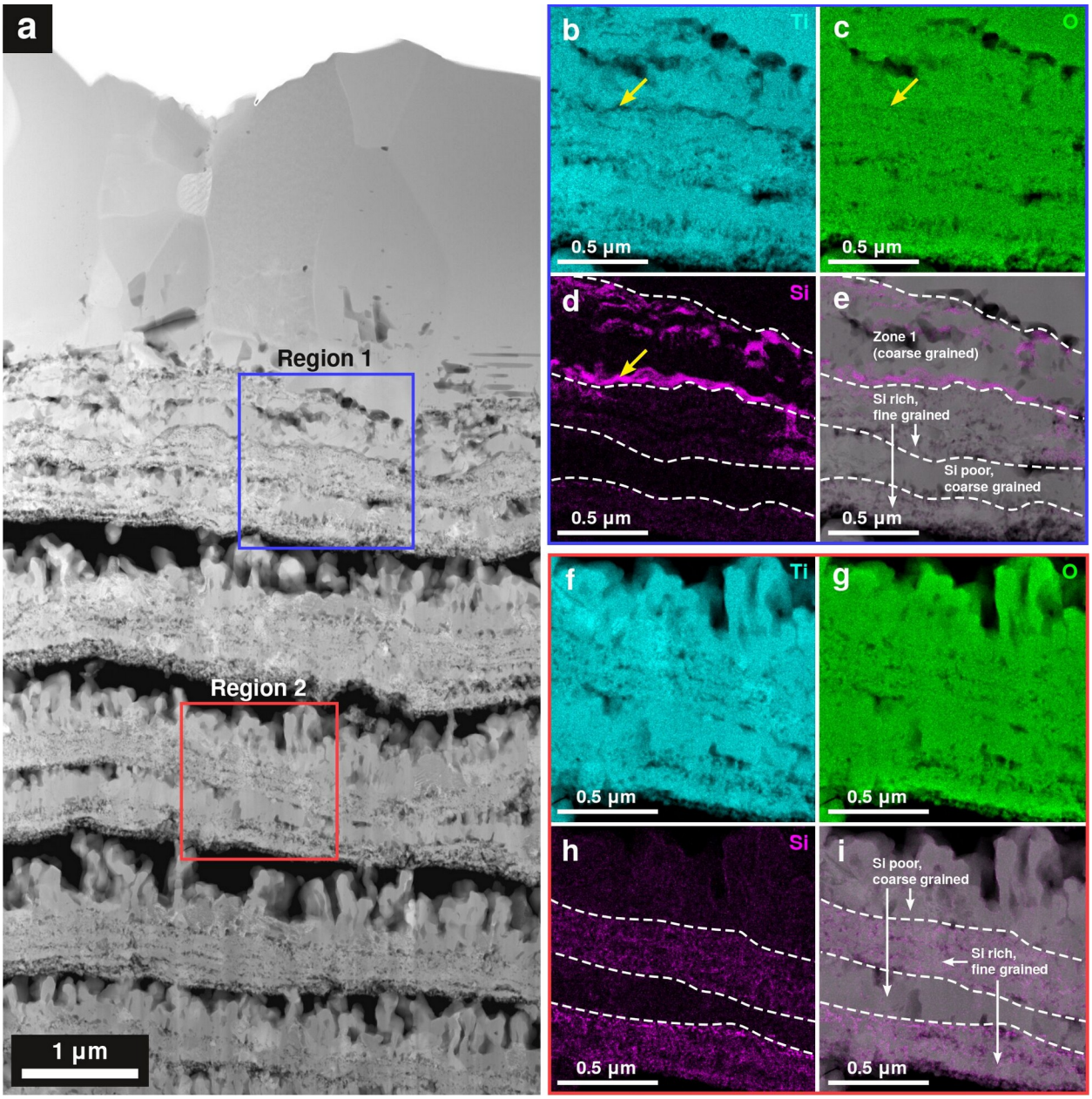

Figure 3.8: In the upper portion of the oxide from a white region on Ti-0.8Si oxidized for 100 h (800 °C, Ar-O_2), (a) HAADF STEM with corresponding net-intensity EDS maps in Region 1 (b-e) and Region 2 (f-i). Maps show Ti (b, f), O (c, g), Si (d, h), and Si overlaid on HAADF STEM (e, i). Note that contrast in (d) was enhanced.

To understand the contribution of oxygen dissolution in the metal to oxidation, oxygen concentration in the metal was measured on polished cross sections. Concentration profiles were fitted to the equation for diffusion in a semi-infinite slab with fixed surface concentration:

$$C(x) = \mathrm{erfc}\left(\frac{x}{2\sqrt{(Dt)}}\right)(C_s - C_0) + C_0, \quad (5)$$

Where $C(x)$ is the concentration at a distance x from the oxide-metal interface, D is oxygen diffusivity in the metal, t is oxidation time, C_s is oxygen surface concentration, and C_0 is initial oxygen concentration in the metal. At each oxidation time (8 h, 32 h), the oxygen concentration profiles for pure Ti and Ti-0.8Si were the same (Figure 3.9). With increasing oxidation time, the oxygen penetration depth increased. Average parameter values from fitting the four datasets were C_s = 26.1 at.% (SD 0.4), C_0 = 0.0 at.%, and $D = 0.98 \times 10^{-14}$ m^2/s (SD 0.02).

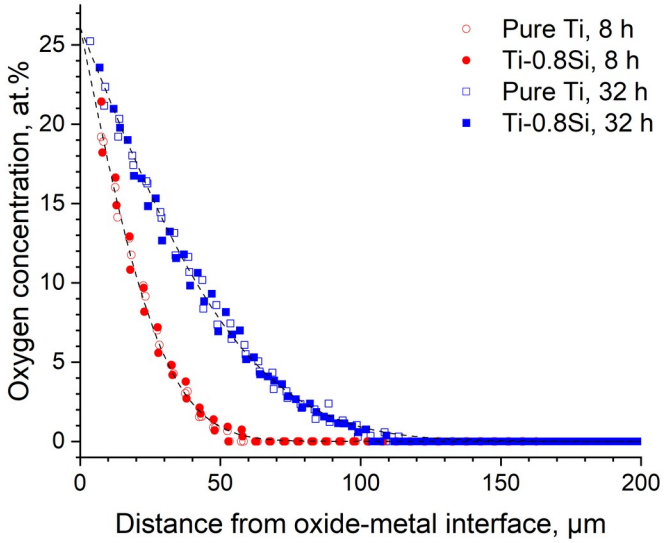

Figure 3.9: WDS profiles of oxygen concentration in the metal for pure Ti and Ti-0.8Si oxidized for 8 h and 32 h (800 °C, Ar-O_2). Dashed lines show oxygen concentration at 8 h and 32 h calculated using Equation 5 with the average parameter values.

To investigate oxide-growth mechanisms at shorter times, we used two-stage tracer oxidation experiments, with the first stage in $^{16}O_2$ and the second stage in $^{18}O_2$. Cross sections prepared from pure Ti oxidized for 16 h (12 h in $^{16}O_2$ followed by 4 h in $^{18}O_2$) and Ti-0.8Si oxidized for 32 h (28 h in $^{16}O_2$ followed by 4 h in $^{18}O_2$) were analyzed using nanoSIMS (Figure 3.10). In pure Ti (Figure 3.10a and 3.10b), ^{18}O isotopic concentration, i.e. $^{18}O/(^{16}O + {}^{18}O)$, was elevated and uniform in the top 2 μm of oxide (~70%), moderate and non-uniform in the 3–4 μm thick region below (10~30%), dilute (1%) in the remaining majority of oxide, and slightly elevated (~4%) just above the oxide-metal interface. Within the region of moderate ^{18}O

enrichment and a few microns below it, ^{18}O was concentrated along grain boundaries (dotted in Figure 3.10b), with ^{18}O isotopic concentration progressively decreasing deeper into the oxide (profiles *b2*-*b4* in Figure 3.10f). In Ti- 0.8Si (Figure 3.10c and 3.10d), ^{18}O enrichment was present in the top 1 μm of oxide, along oxide grain boundaries (dotted in Figure 3.10d), and in the metal underneath strongly ^{18}O-enriched oxide grain boundaries (arrows in Figure 3.10d). Compared to that in pure Ti, the ^{18}O isotopic concentration was similar in the top ^{18}O-rich oxide (~70%) but 5–10 times lower in the rest of the oxide and in the metal (Figure 3.10e). As in pure Ti, ^{18}O isotopic concentration across oxide grain boundaries progressively decreased deeper into the oxide (profiles *d2* and *d3* in Figure 3.10f). The extent of lateral ^{18}O enrichment away from oxide grain boundaries at comparable depths was reduced in Ti-0.8Si compared to pure Ti, per arrows in Figure 3.10f.

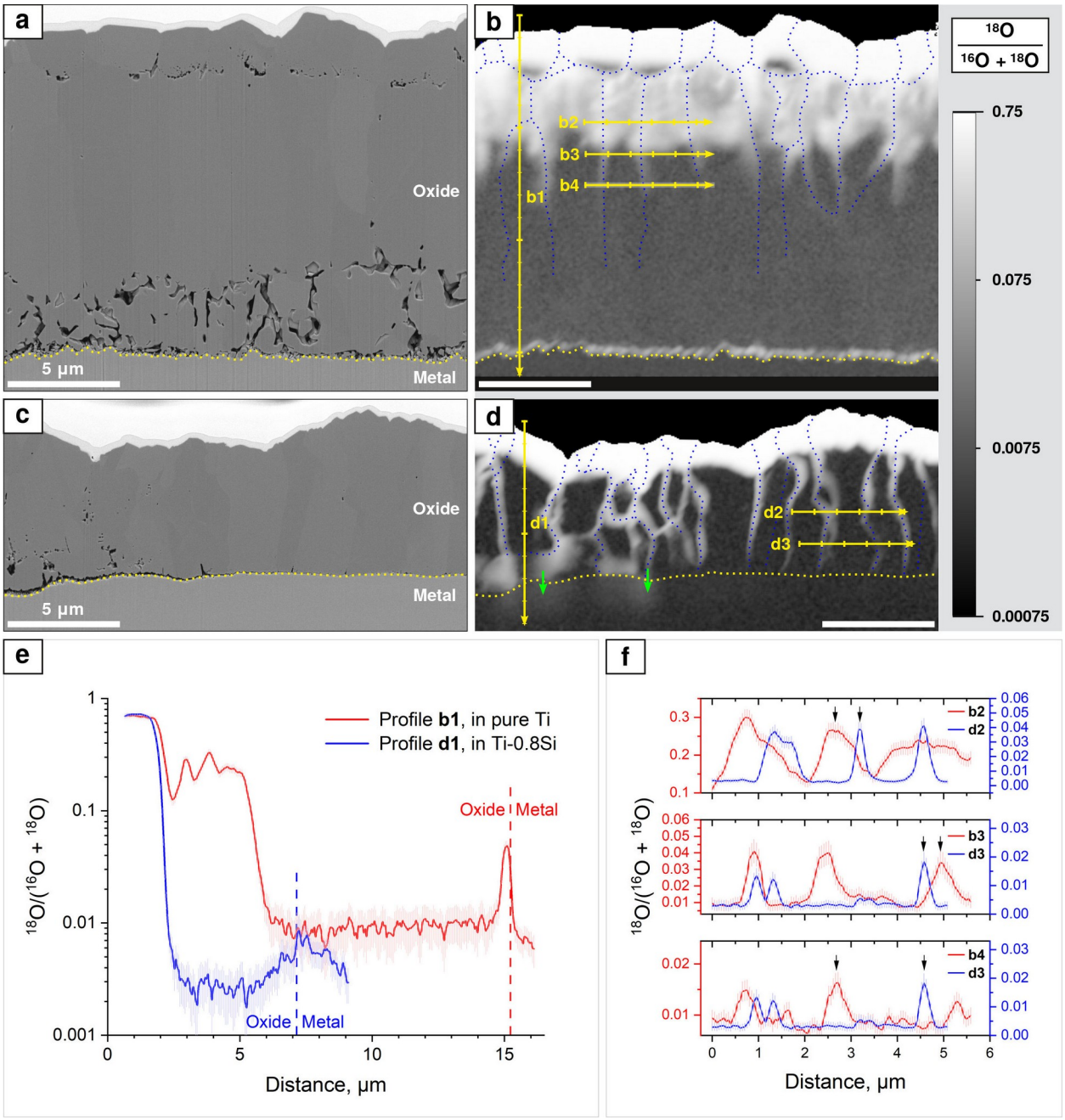

Figure 3.10: BSE-mode SEM with a corresponding nanoSIMS map of the logarithm of ^{18}O isotopic concentration, $\log_{10}(^{18}O/(^{16}O + ^{18}O))$, for (a, b) pure Ti oxidized for 12 h in $^{16}O_2$ followed by 4 h in $^{18}O_2$ and (c, d) Ti-0.8Si oxidized for 28 h in $^{16}O_2$ followed by 4 h in $^{18}O_2$ (800 °C). Additional nanoSIMS maps are in the Appendix, Figure 3.16. ^{18}O isotopic concentration along yellow profiles is plotted (e) through the cross sections (profiles *b1* and *d1*) and (f) across oxide grain boundaries at comparable depths in the oxide (profiles *b2-b4*, *d2*, *d3*). Yellow dotted lines mark the oxide-metal interface in (a-d), whereas blue dotted lines in nanoSIMS maps (b, d) mark all oxide grain boundaries clearly perceptible in SEM. In (b, d), profiles have 1 µm tick spacing and widths less than or equal to those drawn. In (d), green arrows point to ^{18}O enrichment in the metal observed underneath some oxide grain boundaries.

To understand the nature of ^{18}O enrichment along oxide grain boundaries in nanoSIMS, an APT specimen was prepared from the oxide on tracer-oxidized Ti-0.8Si, avoiding the top ^{18}O-rich oxide in order to capture an ^{18}O-rich grain boundary within the ^{16}O-rich oxide. Composition approximately corresponded to TiO_2, with low detectable Si concentration at <0.05 at.%. An additional nanoSIMS experiment was unable to confirm the presence of Si in the oxide, as shown in Figure 3.17. In the full reconstruction (Figure 3.11a) and 20 nm thick slice (Figure 3.11b), a decreasing ^{18}O gradient was observed under the grain boundary, which was marked by Ga contamination from FIB milling and showed no measurable Si segregation. A quantitative composition profile (Figure 3.11c) generated using AtomProbeLab (additional details in the Appendix, Section 3.6.2) showed ^{18}O gradients extending less than 10 nm to the left and more than 100 nm to the right of the ^{18}O peak. ^{18}O isotopic concentration ranged from a baseline of 0.3~1% to a maximum of ~40% (at the grain boundary). These values were within the range of 0.3~70% ^{18}O obtained from nanoSIMS.

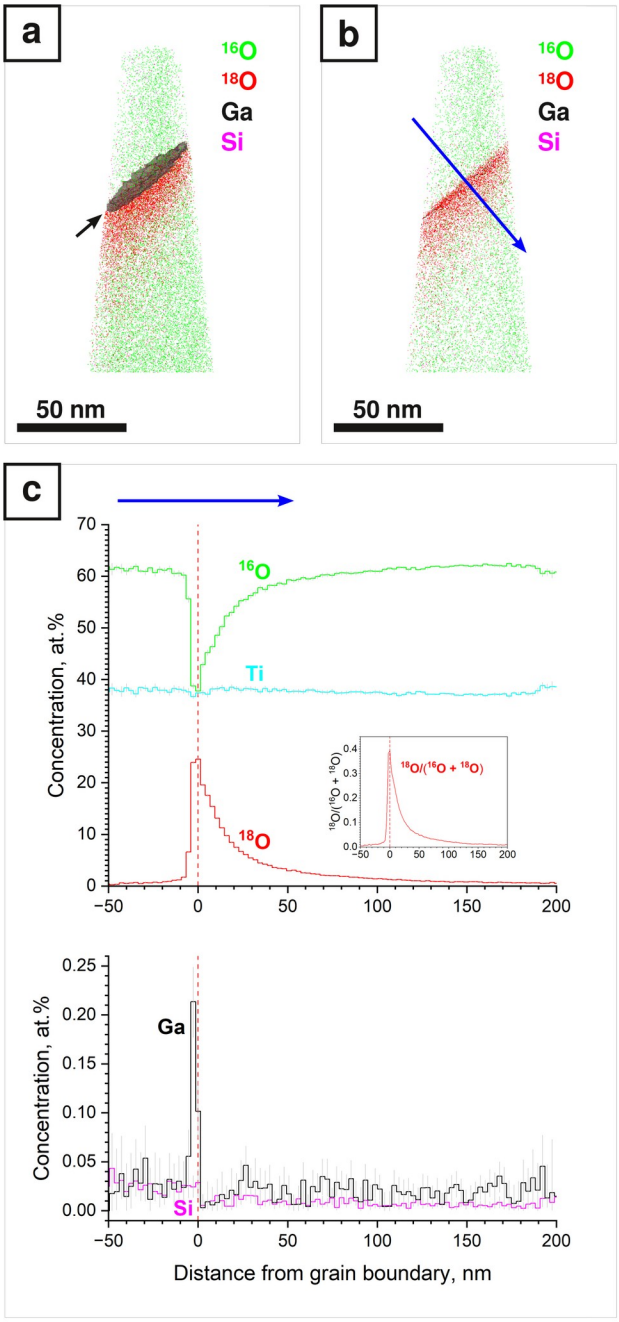

Figure 3.11: APT reconstruction and corresponding concentration profiles across a grain boundary in the oxide on Ti-0.8Si oxidized for 28 h in $^{16}O_2$ followed by 4 h in $^{18}O_2$ (800 °C). (a) the full reconstruction and (b) a 20 nm thick slice (after rotation around the vertical axis) showing ^{16}O ($^{16}O^+$ at 16.0 Da), ^{18}O ($^{18}O_2^+$ at 36.0 Da), Ga (Ga^+ at 68.9 Da), and Si (Si^+ at 28.0, 29.0, 30.0 Da) ions; Ti is omitted for clarity. In (a), a Ga isosurface, indicated by the black arrow, highlights the grain boundary. In (b), the blue arrow denotes the approximate position and direction of the concentration profile in (c). In (c), bin width (~3 nm) reflects the thickness of volumetric slices used to generate the profile; error bars show the 95% confidence interval; and C and H, which were included in the analysis and totaled less than 0.5 at.% in any slice, were not plotted for clarity.

3.4 Discussion

The positive effect of silicon on the oxidation behavior of titanium — expected from literature on titanium alloys coated [57], [76], [84], [85], [86] or alloyed with silicon [9], [10], [11], [12], [13] and oxidized in various atmospheres — was demonstrated by the significantly lower mass gain of Ti-0.8Si compared to pure Ti at a given time (Figure 3.2). Since mass gain reflects the sum of oxygen fixed in the oxide and dissolved in the metal (Equation 3), the addition of silicon must reduce oxygen fixed in the oxide and/or dissolved in the metal. WDS measurements of oxygen in the metal unambiguously showed that silicon had no effect on oxygen dissolution (Figure 3.9). Furthermore, values for oxygen diffusivity and surface concentration matched those reported in literature for α Ti: D of 0.98×10^{-14} m^2/s, within the expected range of $0.10–7.8 \times 10^{-14}$ m^2/s at 800 °C [68], and C_s of ~26 at.% [4], [5]. Therefore, differences in mass gain were linked to the oxide, which was always thinner for Ti-0.8Si. Per Figure 3.2, the estimated contributions of oxygen in the metal and oxide agreed well with total mass gain measured via thermogravimetry. For both materials, the relative contribution of dissolved oxygen to total mass gain, i.e. $O_{metal}/(O_{metal} + O_{oxide})$, decreased in time, as noted previously for pure Ti [4], [6]. Estimates of $O_{metal}/(O_{metal} + O_{oxide})$ in this study fall within the range of 5–80% reported for pure Ti oxidized over a range of times and temperatures in oxygen atmospheres [4], [5], [6].

As discussed in Section 2.2, both oxide scale morphology and stoichiometry can likely influence the apparent oxide color. Although the interpretation of oxide color remains uncertain in this study, the transition from gray to white oxide — which was generally restricted in extent and delayed for Ti-0.8Si compared to pure Ti (Figure 3.1) — was most obviously correlated with thickening and layering of the oxide.

Because of the complicating effects of geometry on oxidation, this study focused on flat surfaces far from corners. For both materials, oxide-growth mechanisms evolved in time, differing for the initial thin, compact oxide scales and subsequent thick, lamellar scales. First, we discuss the growth of the compact oxide scale and then the lamellar scale on pure Ti. Next, we consider the same for Ti-0.8Si.

The compact oxide scale on pure Ti, per Figure 3.10b, was confirmed to growth in both directions, with limited inward growth at the oxide-metal interface and dominant outward growth on the outermost surface. In the new oxide, ^{18}O isotopic concentration — about ~70% in the outer oxide and up to 5% in the inner oxide (Figure 3.10e) — was lower than the isotopic gas

purity of 99%, as observed previously in Ni-Al [94]. This lower concentration, particularly in the outer oxide, was likely due in part to the presence of residual $^{16}O_2$ from the first exposure, which was detected by mass spectrometry. The further decrease in ^{18}O isotopic concentration in the inner oxide relative to the outer oxide reflected ^{18}O diffusion and exchange with ^{16}O as ^{18}O diffused inward. The presence of ^{18}O enrichment at grain boundaries in the ^{16}O-rich oxide pointed to inward O transport predominantly occurring along oxide grain boundaries rather than through the lattice. Diffuse ^{18}O enrichment surrounding grain boundaries (profile *b2* in Figure 3.10b and 3.10f) likely reflected ^{18}O at grain boundaries diffusing into the bulk. This interpretation is consistent with APT on a comparable grain boundary in Ti-0.8Si (Figure 3.11) showing similar maximum ^{18}O isotopic concentration at the grain boundary and decreasing ^{18}O gradients to either side.

The origins and evolution of porosity prominent in the inner oxide on pure Ti are not well understood. Oxide dissolution, known to occur upon heating in vacuum [4], could plausibly occur when inward O flux through the oxide and into the metal is not sufficient to maintain saturation in the surface of the metal. Because of enhanced O transport along oxide grain boundaries, oxide dissolution may preferentially occur along oxide grain boundaries located near the metal (e.g. accounting for large pores intersecting oxide grain boundaries in Figure 3.6a and 3.10a).

At longer times, the oxide on pure Ti became much thicker and lamellar (Figure 3.5a). As discussed in Section 2.2, the mechanism for lamellar oxide growth is believed to be detachment of the initial adherent layer of oxide followed by repetitive growth and detachment of new oxide underneath this. Rather than distinct parabolic-like subperiods, our experiments showed slight oscillations within the approximately linear oxidation kinetics, perhaps because of limited mass sensitivity or non-uniform detachment across the sample surface. Because oxide detachment would disrupt outward Ti transport to the surface, Ti transport was not expected to contribute to growth of oxide grains on the surface. Therefore, the qualitative increase in oxide grain size from 32 to 100 h (Figure 3.4b-c) may instead be due to grain growth in the detached oxide.

The compact (gray) oxide on Ti-0.8Si grew primarily via outward Ti diffusion, consistent with the progressive increase in surface grain size from 8 to 32 to 100 h (Figure 3.4d-f) and new outer oxide in tracer oxidation experiments (Figure 3.10d). As in pure Ti, there was rapid inward O transport along oxide grain boundaries, sometimes leading to localized enrichment in the metal (arrows in Figure 3.10d). However, three key differences were noted in Ti-0.8Si compared to

pure Ti. First, the thinner outer ^{18}O-rich oxide in Ti-0.8Si indicated reduced outward Ti flux, despite the thinner initial oxide (i.e. shorter lattice diffusion path) in Ti-0.8Si. This may be due to slow Ti transport through the Ti_5Si_3 layer near the oxide-metal interface or through the oxide, though the specific mechanism is not known. Second, the reduced lateral extent of ^{18}O enrichment away from oxide grain boundaries at comparable depths suggested reduced lattice O diffusivity in the oxide. Reduced lattice O diffusivity, by limiting isotope exchange, could also explain the lower baseline isotopic ^{18}O concentration in the ^{16}O-rich oxide in Ti-0.8Si. We note that the asymmetry of the isotopic ^{18}O peak in APT (Figure 3.11c), which reflected diffusivity values differing by about one order of magnitude, was consistent with the high anisotropy of O diffusivity in TiO_2 [95], [96]. Third, the lack of ^{18}O enrichment at the oxide-metal interface indicated no inward oxide growth in Ti-0.8Si.

We attribute the lack of inward oxide growth in Ti-0.8Si to the presence of the continuous Ti_5Si_3 silicide layer between the oxide and metal (Figure 3.7), which was previously observed in oxidized Si-coated Ti [57] and is known to be stabilized over the more Ti-rich Ti_3Si by oxygen [97]. While Ti_5Si_3 is known for its good oxidation resistance in bulk form [98], [99], [100] and as a coating on pure Ti [86], [101], the present study demonstrated its positive effect when formed *during* oxidation of Si-alloyed titanium: The Ti_5Si_3 layer, together with the compact TiO_2 oxide, prevented the inward-growing TiO_2 front at the metal. The Ti_5Si_3 layer did not limit the amount of O dissolved in the metal, as indicated by the equivalent O concentration profiles in pure Ti and Ti-0.8Si. Considering the reduced outward Ti flux in Ti-0.8Si, it may have acted as a barrier to outward Ti transport. However, no values for Ti diffusivity in Ti_5Si_3 could be found in literature to support this. Formation of the Ti_5Si_3 layer required silicon accumulation below the oxide. However, because silicon should be more mobile in the metal (e.g. 1.6 μm 1D mean displacement in 1 h at 800 °C, using diffusivity from [65]) than the oxide-metal interface, accumulation was not expected. This may indicate reduced Si diffusivity in α Ti, possibly due to oxygen in solid solution. If all Si remaining after selective oxidation of Ti in the alloy were incorporated into the Ti_5Si_3 layer, the layer should thicken predictably with the TiO_2 oxide, i.e. giving about 15, 35, and 50 nm of Ti_5Si_3 at 8, 32, and 100 h, respectively. However, measured layer thicknesses (about 35 nm at 8 h, 40 nm at 32 and 100 h), while reasonably close to expectations, did not clearly increase in time, possibly because of limited spatial resolution (e.g. since S/TEM lamellae were thicker than the layer) or because some Si diffused away.

The departure from a compact, outward-growing (gray) oxide in Ti- 0.8Si to a lamellar (white) oxide similar to that on pure Ti was linked to the breakdown of the Ti_5Si_3 layer, which occurred non-uniformly across the sample surface (as early as 32 h and sometimes later than 100 h per Figure 3.1e, 3.3f, and 3.3g). Ti_5Si_3 oxidized to TiO_2 and SiO_2 (in Zone 1 in Figure 3.8e), in agreement with [57], [98], [100]. Breakdown of the Ti_5Si_3 layer enabled inward oxide growth and incorporation of Si in the TiO_2, forming the Si-rich, fine-grained oxide in Region 1 in Figure 3.8a. After detachment of the monolithic oxide from the substrate, a new adherent layer of oxide grew below. As described for pure Ti, repetitive growth and detachment of an adherent oxide layer led to the lamellar scale microstructure. Each adherent layer of oxide grew simultaneously via outward Ti diffusion, forming outer (Si-poor) coarse-grained oxide, and via inward O diffusion, forming inner (Si-rich) fine-grained oxide, consistent with the bilayer structure observed in Region 2 (Figure 3.8a).

The disruption of Ti flux to the outermost surface due to oxide detachment was consistent with surface grains of the white (detached) oxide (Figure 3.4g) being smaller than those on the gray (adherent) oxide (Figure 3.4f) at 100 h. The lack of any bands containing Si underneath those in Figure 3.8e (e.g. in Figure 3.8i) suggested no redevelopment of a thick Ti_5Si_3 layer after its initial breakdown. At longer times, the lower linear oxidation rate in Ti-0.8Si compared to pure Ti was attributed solely to slower oxide growth, due partly to the persistence of slow-growing compact (gray) oxide in some areas (e.g. in Figure 3.1f) and also possibly to slower growth of lamellar oxide. Nevertheless, the mechanics of lamellar oxide growth and detachment may be important to oxidation rate and warrant further investigation.

As discussed in Section 2.3, early studies proposed four mechanisms to account for the role of silicon in the high-temperature oxidation of titanium. In the context of this study, the first two mechanisms have some merit. For the compact (gray) oxide on Ti-0.8Si, the first mechanism, Si^{4+} doping of the TiO_2, was consistent with evidence of dilute Si in the oxide (per Figure 3.11c and Si^{+} peaks in Figure 3.10) and could account for the observed reduction in lattice O diffusivity in the oxide relative to that on pure Ti. However, since inward O transport occurred primarily along oxide grain boundaries, reduced lattice O diffusivity may not play a significant role. The second mechanism, densification of the oxide by an SiO_2 dispersion leading to less diffusion through pores and cracks, may apply to the lamellar (white) oxide, since it contained Si (per EDS, Figure 3.8) — possibly in the form of an SiO_2 dispersion — and was more compact than the lamellar oxide on pure Ti. As mentioned previously in Section 2.3, experiments on bulk

rutile TiO_2 [82] suggested that reduced O lattice diffusivity may be due to the presence of an SiO_2 dispersion. However, this potential alternative mechanism did not apply to our results, since reduced lattice O diffusivity — only evidenced for the compact oxide — was not accompanied by an SiO_2 dispersion. Considering the general evidence of Si in the lamellar oxide on Ti-0.8Si and inward O transport along oxide grain boundaries in both materials, we hypothesize that the presence of Si in the lamellar oxide, particularly at the grain boundaries, may slow inward O transport along oxide grain boundaries. We note that Si, in addition to possibly affecting O transport, may also influence Ti transport via the initial formation of a Ti_5Si_3 layer. The third and fourth mechanisms, regarding Si influencing oxygen diffusivity or solubility as inferred from hardness measurements [9], [11], [81], were inconsistent with our WDS measurements (Figure 3.9). Si did not influence O diffusivity or solubility in the metal.

3.5 Conclusions

We investigated the oxidation of pure Ti and Ti-0.8Si at 800 °C in Ar-O_2 and in two-stage exposures of $^{16}O_2$ followed by $^{18}O_2$ to understand the mechanisms responsible for the improved oxidation resistance of titanium alloyed with Si. For the conditions used in this study, we reached the following conclusions:

1. The beneficial impact of Si alloying on lowering mass gain reflected reductions in oxide thickness but not in oxygen dissolved in the metal. Contrary to prior suggestions, Si had no effect on oxygen diffusivity or solubility in α Ti.
2. The initial compact oxide scale on pure Ti grew both outward and inward, as confirmed using isotopic oxygen. Alloying with Si eliminated inward oxide growth, leading to a compact oxide scale growing only by outward Ti diffusion. To the best of our knowledge, our use of isotopic oxygen for the first time unambiguously revealed that oxygen diffusion primarily takes place along TiO_2 grain boundaries.
3. In Ti-0.8Si, the initial lack of inward oxide growth was attributed to the formation of a continuous Ti_5Si_3 silicide layer between the oxide scale and metal.
4. Breakdown of the Ti_5Si_3 layer enabled fast inward oxide growth, ultimately resulting in a Si-containing lamellar oxide.

3.6 Appendix

3.6.1 Preparation of APT tips containing an oxide grain boundary

APT tips were prepared from the oxide on tracer-oxidized Ti-0.8Si using a Thermo Fisher Scientific Helios 650 Nanolab SEM/FIB. Two strategies were employed to facilitate capturing a grain boundary in the sharpened atom-probe tips. First, the FIB lift-out, taken from the plan-view oxidized surface, was rotated 90° before attachment to posts. This made oxide grain boundaries approximately horizontal. They could then be targeted by controlling milling depth. Second, the position of the grain boundary in the tip was periodically examined during the low-voltage (2 kV) milling step in the same microscope, using transmission Kikuchi diffraction (TKD) and/or scanning transmission electron microscopy (STEM). To allow switching between FIB milling, TKD, and STEM, it was necessary to attach specimens to a (Mo) TEM grid held in a custom holder. Fingers on the TEM grid were previously milled into posts suitable for APT using a Thermo Fisher Scientific Helios G4 PFIB UXe DualBeam Xe-FIB/SEM.

3.6.2 APT data processing with AtomProbeLab

AtomProbeLab version 0.2.4 (https://sourceforge.net/projects/atomprobelab/) was used to create a quantitative composition profile through the ^{18}O-rich grain boundary in the oxide on tracer-oxidized Ti-0.8Si. First, it was necessary to modify the isotopes definition file, by adding standalone ^{18}O as "Q" and zeroing the abundance of ^{71}Ga, which was absent in the monoisotopic FIB source. Second, appropriate ions were determined using the *ionFitTester* function on the entire APT dataset. Candidate ions, approximately in order of increasing mass-to-charge ratio, were **O^+**, OH^+, Q^+, QH^+, **Ti^{++}**, TiH^{++}, TiH_2^{++}, *N_2^+*, Si^+, *CO^+*, **TiO^{++}**, **O_2^+**, TiQ^{++}, OQ^+, Q_2^+, TiO_2^{++}, GaC^{++}, $Ti_2O_2^{+++}$, TiQ_2^{++}, *Ti_2OQ^{+++}*, $Ti_2Q_2^{+++}$, **SiO^+**, **Ti^+**, **TiO^+**, TiQ^+, **Ga^+**, $Ti_2O_3^{++}$, *Ti_3^{++}*, $Ti_2O_2Q^{++}$, $Ti_2OQ_2^{++}$, $Ti_2Q_3^{++}$, **TiO_2^+**, GaC^+, $TiOQ^+$, TiQ_2^+, **TiO_3^+**, TiO_2Q^+, $TiOQ_2^+$, TiQ_3^+, and **$Ti_4O_2^{++}$**. Bolded ions were set as mandatory, whereas red, italicized ions were eliminated based on the results of *ionFitTester*. Selected ions are overlaid on the mass spectrum in Figure 3.10. Although various additional H-containing Ti-O/Ti-Q ions could be included as candidate ions, this would introduce rank deficiency in the overlap problems. Moreover, omission of H-containing Ti-O/Ti-Q ions was justified by the minimal estimated H content, about 1 at.% (using a portion of the dataset lacking ^{18}O and the resulting overlap with Ti-O-H ions). Third, as a check, selected ions

were used to calculate bulk decomposition (about 37% Ti, 60% O, and 2.3% ^{18}O and 0.7% combined Si, H, C, and Ga). Finally, a line profile was generated normal to the grain boundary. One hundred bins were used, giving volumetric slices ~3 nm thick. The normal direction was determined visually in AP Suite.

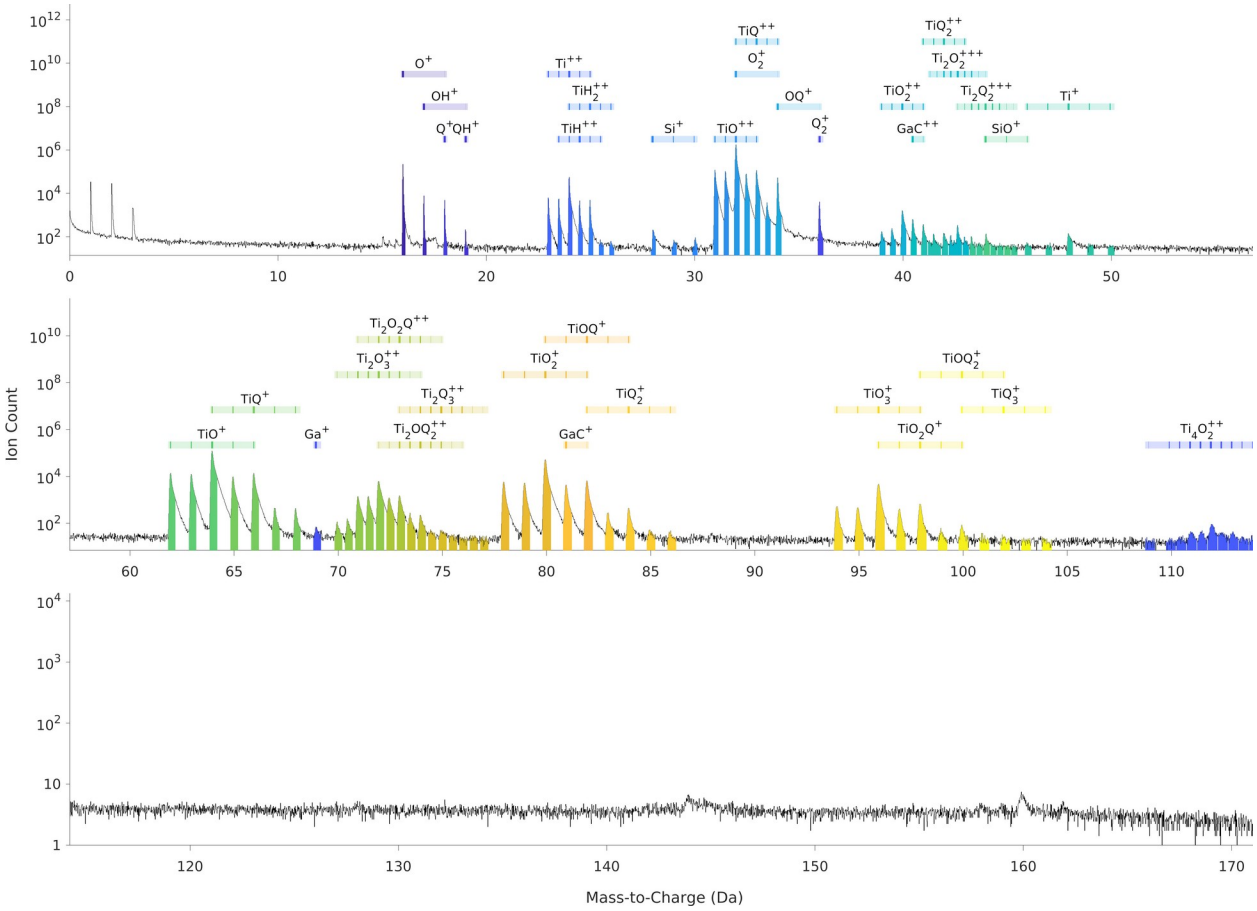

Figure 3.12: Mass spectrum of the APT tip shown in Figure 3.11a with selected ions overlaid. Note the presence of Si^+ peaks (at 28.0, 29.0, 30.0 Da). "Q" denotes ^{18}O.

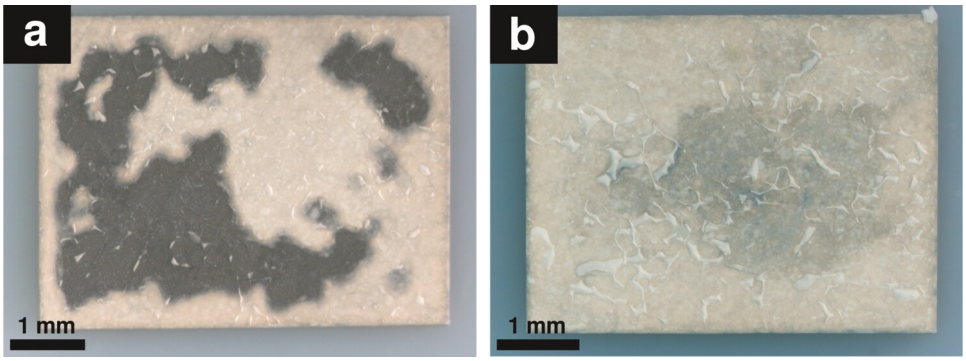

Figure 3.13: Plan-view optical images of Ti-0.8Si oxidized for 100 h in thermogravimetric studies (800 °C, Ar-O_2); (a) and (b) show the undersides of samples shown in Figure 3.1f and Figure 3.1g, respectively. The undersides, which were polished before oxidation, contacted the alumina pan during oxidation.

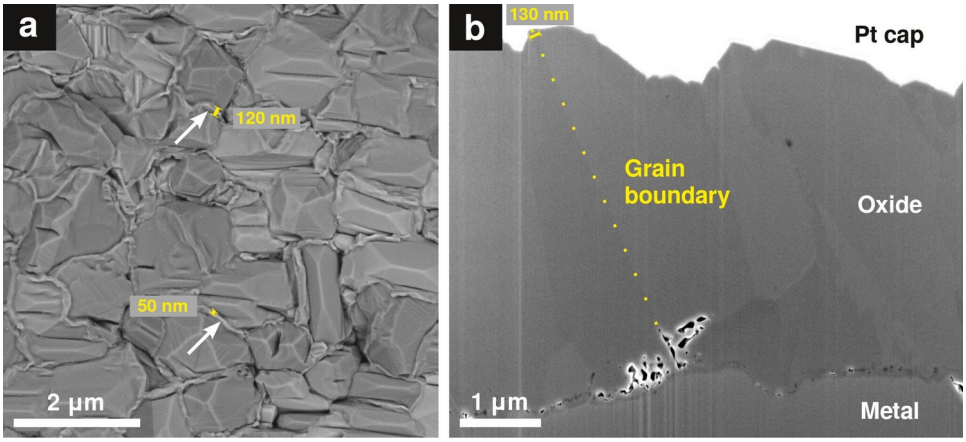

Figure 3.14: From regions with compact (optically gray) oxide, Ti-0.8Si oxidized for 32 h (800 °C, Ar-O_2) in (a) plan view with BSE-mode SEM and (b) cross section with SE-mode SEM. Ridges along boundaries between equiaxed crystals, marked by arrows in plan view (a), were visible and similar in size in cross section (b).

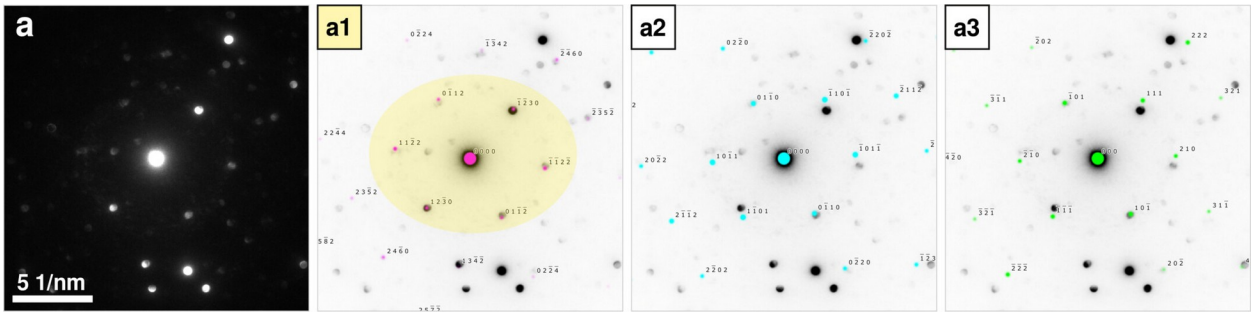

Figure 3.15: From a region with compact (gray) oxide on Ti-0.8Si oxidized for 100 h (800 °C, Ar-O_2), i.e. the cross section shown in Figure 3.7c, (a) nanobeam diffraction pattern of the Ti- and Si-rich layer formed at the oxide-metal interface, showing good correspondence to (a1) Ti_5Si_3 ($P6_3/mcm$) [93] along $[1\bar{0}823]$. The diffraction pattern was also compared to other phases known to be present nearby, α Ti and rutile TiO_2, but did not match either of these phases: (a2)

shows poor correspondence for α Ti ($P6_3/mmc$) along the best fit direction, $[\bar{2}113]$, while (a3) shows poor correspondence for rutile TiO_2 ($P4_2/mnm$) along the best fit direction, $[\bar{1}21]$. Diffraction patterns were matched using SingleCrystal 4.1.7 (CrystalMaker Software Ltd.; Oxfordshire, UK) with physical distances.

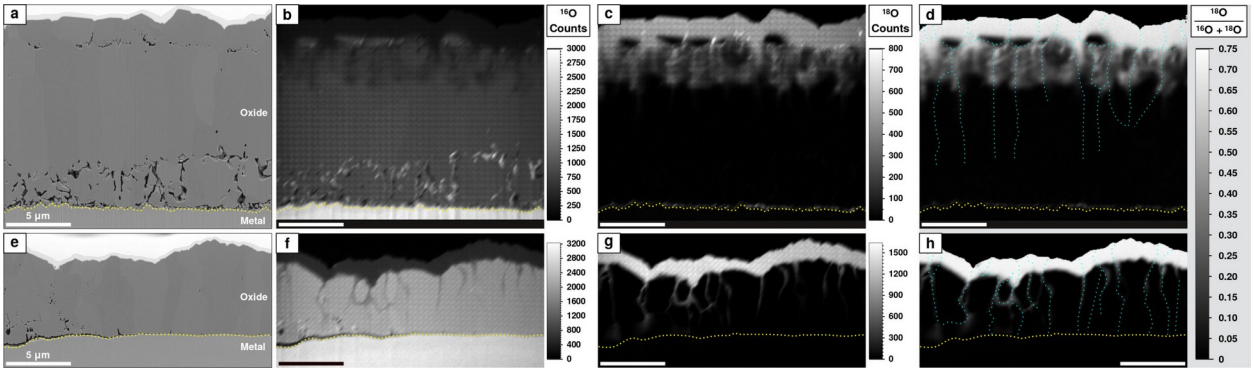

Figure 3.16: BSE-mode SEM with corresponding nanoSIMS isotope maps for (a-d) pure Ti oxidized for 12 h in $^{16}O_2$ followed by 4 h in $^{18}O_2$ and (e-h) Ti-0.8Si oxidized for 28 h in $^{16}O_2$ followed by 4 h in $^{18}O_2$ (800 °C). Isotope maps show (b, f) $^{16}O^-$ counts, (c, g) $^{18}O^-$ counts, and (d, h) the ^{18}O isotopic concentration, $^{18}O/(^{16}O + {}^{18}O)$. Yellow dotted lines mark the oxide-metal interface, whereas blue dotted lines in (d, h) mark all oxide grain boundaries clearly perceptible in SEM. The apparent grid pattern in (b, c, f, g) was due to insufficient sputtering density in nanoSIMS before analysis. The high intensity of ^{16}O or ^{18}O in pores reflected increased net ion yields, likely due to the non-planar topography rather than relative enrichment in that isotope per (d, h).

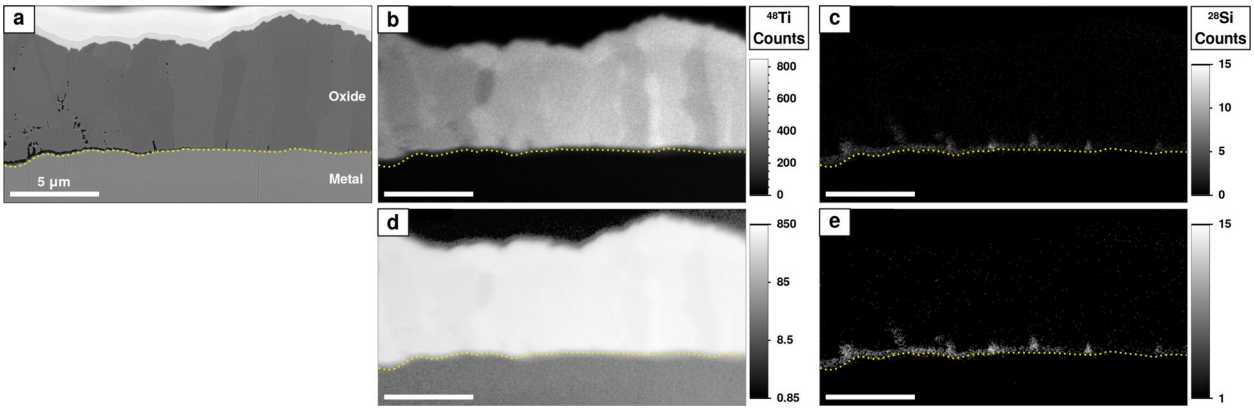

Figure 3.17: On the lamella prepared from Ti-0.8Si oxidized for 28 h in $^{16}O_2$ followed by 4 h in $^{18}O_2$ (800 °C), (a) BSE-mode SEM and (b-e) corresponding nanoSIMS maps from an additional nanoSIMS experiment intended to measure Si in the oxide. NanoSIMS maps show (b) $^{48}Ti^+$ counts, (c) $^{28}Si^+$ counts, (d) $\log_{10}(^{48}Ti^+$ counts), and (e) $\log_{10}(^{28}Si^+$ counts). $^{48}Ti^+$ and $^{28}Si^+$ were detected simultaneously. The yellow dotted line marks the oxide-metal interface. We note that this experiment used a focused O^- beam (0.8 pA, ~100 nm spot size), and $^{48}Ti^+$ counts were used to align frames. In (b, d), $^{48}Ti^+$ counts are greater in the oxide than in the metal due to oxygen enhancing the yield of positive secondary ions.

Chapter 4: Role of Niobium in the High-Temperature Oxidation of Titanium

4.1 Introduction

In early efforts to improve the oxidation resistance of titanium, Maynor et al. [8] showed that alloying with small amounts of niobium could significantly slow oxidation in air. More recent work by Pérez et al. [14], [15] additionally highlighted synergies between niobium and atmospheric nitrogen — i.e. the slowest oxidation rate was obtained by alloying with Nb while oxidizing in air as opposed to Ar-O_2. Because relevant studies (i.e. [14], [15], [16], [17], [18]) are scarce and sometimes complicated by the use of nitrogen (e.g. [17], [18]), the role of Nb alloying on the high-temperature oxidation of titanium remains poorly understood. Specifically, it remains unclear if Nb influences diffusion in the oxide scale [14], [16], [19], accumulates at the scale-metal interface [14], [17], or influences O diffusivity or solubility in the α-Ti metal [14], [15].

By systematically comparing the oxidation response of pure Ti and Ti-2 at.% Nb in Ar-O_2 atmospheres and in two-stage exposures of $^{16}O_2$ followed by $^{18}O_2$, we clarify the role of niobium independent of atmospheric nitrogen. The findings for pure Ti discussed in the previous chapter are reproduced in this chapter for comparison purposes. Niobium had no effect on the amount of oxygen dissolved in the metal or on oxygen diffusion in the metal. Instead, niobium enhanced oxidation resistance by segregating to TiO_2 grain boundaries, where it presumably slowed outward Ti diffusion. These findings spotlight doping of TiO_2 grain boundaries as a strategy for improving the oxidation resistance of titanium-based alloys and, more generally, TiO_2-forming alloys.

4.2 Experimental Methods

Although many of the materials and methods are identical to those used in the previous chapter (Section 3.2), they are reproduced here for completeness. This study used pure (99.999%) titanium plate purchased from Alfa Aesar and Ti-2 at.% Nb ("Ti-2Nb") prepared by arc melting

under Ar, with flipping and remelting at least three times to enhance homogeneity. Grains were small and equiaxed in pure Ti and larger and irregular in shape in Ti-2Nb, as shown in Appendix Figure A.1. Niobium content was limited to a few percent to promote single-phase α Ti at the isothermal oxidation temperature of 800 °C [47].

Specimens to be oxidized were ground, polished with 9 μm diamond suspension, and ultrasonically cleaned in methanol just before oxidation. Nominal gas purity was 99.999% for Ar, 99.993% for O_2, and ≥ 99.00% for $^{18}O_2$.

Oxidation was performed in Ar-20% O_2 for 8 or 32 h using a tube furnace or for 100 h using a NETZSCH STA 449 F3 Jupiter thermogravimetric analyzer. The furnace chamber was flushed with flowing Ar before oxidation exposures. Specimens then equilibrated in temperature (for 8-10 minutes), were exposed to Ar-20% O_2 for the desired time, and cooled to room temperature under flowing Ar. For thermogravimetric studies, rectangular plate-shaped specimens were prepared, with the two largest faces polished and the four smaller faces only ground (with 30 μm alumina lapping film). Polished surfaces accounted for 69~77% of the total surface area. To ensure reproducibility, two thermogravimetric experiments were conducted for each material.

Two-stage tracer oxidation experiments were performed using the setup and methods described previously in Section 3.2, which included continuously monitoring the exposure atmosphere using a mass spectrometer. Pure Ti was exposed to $^{16}O_2$ for 12 h and then $^{18}O_2$ for 4 h. Ti-2Nb was exposed to $^{16}O_2$ for 20 h and then $^{18}O_2$ for 4 h. For each exposure, the amount of oxygen used was equivalent to that giving 0.2 atm absolute pressure in the oxidation chamber as measured at room temperature. Given differences in scale growth rates, different durations of the initial ($^{16}O_2$) oxidation stage were used to achieve compact oxide scales with thicknesses suitable for nanoSIMS analysis. The exposure atmosphere was switched while at 800 °C. Isotopic purity was ≥ 99.00% for $^{18}O_2$ (Sigma-Aldrich; St. Louis, MO).

Oxidized specimens were imaged using a Nikon AZ100 optical microscope. To prepare bulk cross sections, specimens were mounted in epoxy, polished, and carbon coated. A Thermo Fisher Scientific Helios 650 Nanolab FIB-SEM was used to image bulk cross sections, prepare cross-sectional lamellae, and prepare APT tips. Using a Thermo Fisher Scientific Talos F200X G2 operating at 200 kV, lamellae were characterized with TEM, STEM, and EDS. Net-intensity EDS maps were produced with Velox 3.1.0.919.

Oxygen dissolution in the metal was characterized using WDS on bulk cross sections in a Cameca SX100 EPMA (operating at 15 kV, 40 nA; Gennevilliers, France). X-rays for Ti, O, and Nb (Kα for Ti and O, Lα for Nb) were quantified using Probe For EPMA (Probe Software, Inc.; Eugene, OR), with O corrected after [88] to account for the interference of Ti Lβ on O Kα. Two profiles were collected for each specimen and combined into a single dataset. O concentration values were discarded if outside of physical ranges and set to zero if below the detection limit (about 0.1 wt.% or, in pure Ti, 0.3 at.%).

Lamella from tracer-oxidized pure Ti and Ti-2Nb were characterized using nanoSIMS. $^{16}O^-$ and $^{18}O^-$ ions were measured concurrently using a Cameca NanoSIMS 50 with a ~50 nm, 0.2 pA focused Cs^+ beam at a mass-resolving power of ~3000 (corrected after [89]). Isotope maps were generated using L'image [90].

One APT analysis of the oxide formed on tracer-oxidized Ti-2Nb was performed using a Cameca LEAP 5000 HR operating at 50 K in laser-assisted mode (60 pJ) with auto pulse-rate control (150 Da minimum). Detection rate ranged from 0.25-0.75%. Cameca AP Suite version 6.1.0.35 was used to reconstruct the tip using the default image compression factor (1.65) and k factor (3.3), an evaporation field of 32 V/nm, and voltage radius evolution. AtomProbeLab version 0.2.4 [91] was used to select appropriate ions, resolve overlapping peaks (especially in O-containing ions), and thereby accurately characterize composition; additional information is provided in the Appendix, Section 4.6.1.

4.3 Results

Per continuous thermogravimetry, the mass gain of Ti-2Nb was initially similar to that of pure Ti for the first few hours but became noticeably lower thereafter (Figure 4.1). The mass gain data were fitted to Equation 4. Rate exponents and rate constants are listed in Table 4.1 in the Appendix. Rate exponents were similar for both materials: $m \sim 1.7$ for pure Ti and $m \sim 2.0$ for Ti-2Nb from 0 to 10 h — indicating initial approximately parabolic kinetics — and $m \sim 1.2$ for pure Ti and $m \sim 1.1$ for Ti-2Nb from 0 to 100 h — indicating overall approximately linear kinetics. The overall rate constant, k_m, of Ti-2Nb was on average about half that of pure Ti. We note that mass gains measured via thermogravimetry matched well with the estimated sum of

oxygen dissolved in the metal and oxygen fixed in the oxide scale; more details are provided in the Appendix, Figure 4.12.

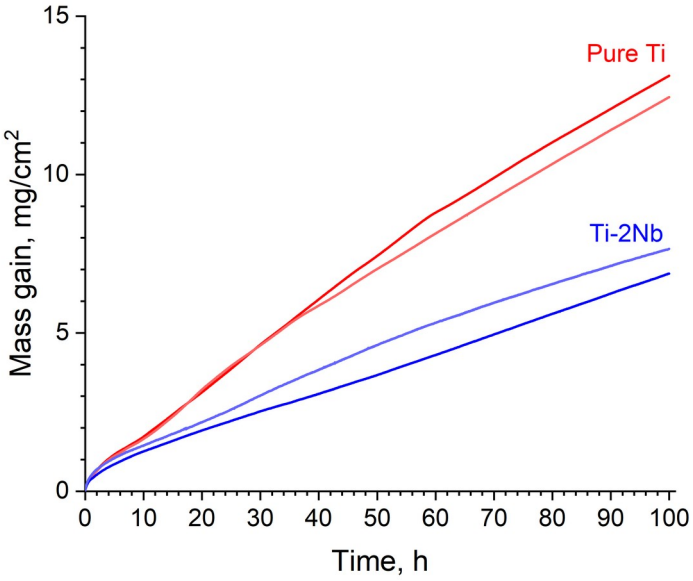

Figure 4.1: Mass gains for pure Ti and Ti-2Nb oxidized isothermally at 800 °C in Ar-O_2, as measured using continuous thermogravimetry. Two trials are shown for each material.

For both materials, the oxidized surfaces optically ranged in color from dark gray to whitish gray initially and progressively turned white with increasing oxidation time (Figure 4.2). No oxide spallation was observed. The appearance of the surfaces differed most notably at 8 h, when pure Ti appeared uniformly whitish gray (Figure 4.2a), whereas Ti-2Nb appeared dark gray with whitish patches (Figure 4.2d). Subsequent FIB cross sections (in Figure 4.5 and Figure 4.9) were prepared from darker areas, where the oxide scale was presumed to be more compact. The oxide scale was presumed to be rutile TiO_2 based on the literature [4], [5], [6], [7], [15].

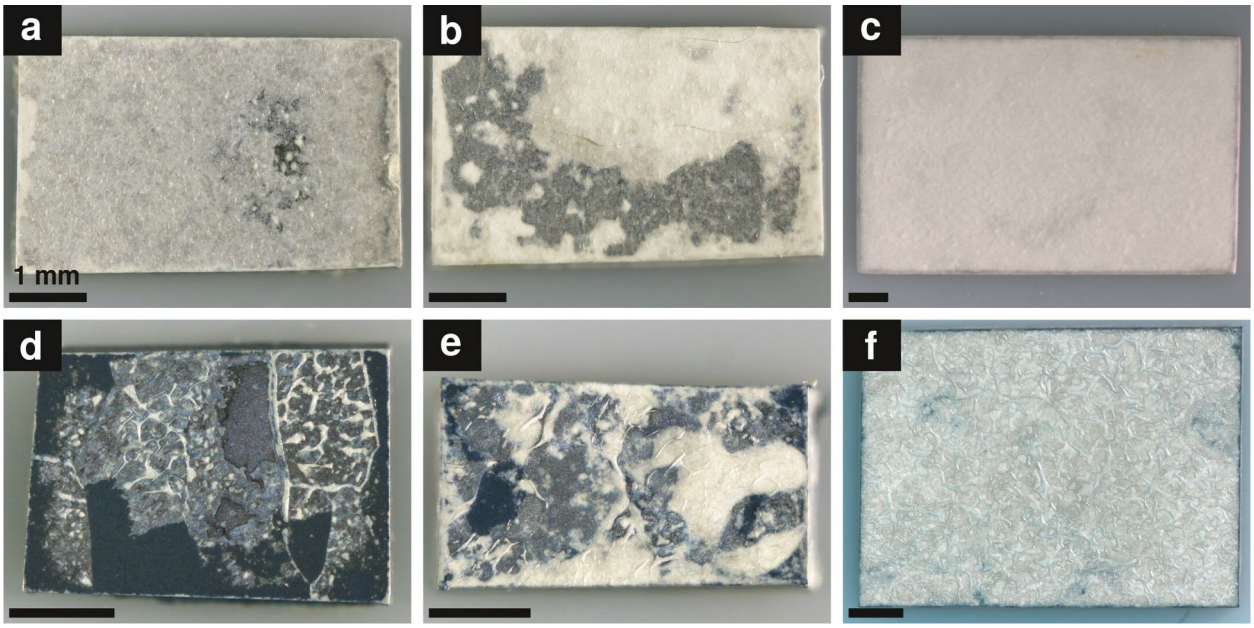

Figure 4.2: Optical images of (a-c) pure Ti and (d-f) Ti-2Nb specimens oxidized for (a, d) 8 h, (b, e) 32 h, and (c, f) 100 h (800 °C, Ar-O_2). All scale bars are 1 mm. (a-c) are reproduced from Figure 3.1.

SEM observations of the oxidized surfaces on pure Ti consistently revealed a mixture of smaller and larger equiaxed oxide crystals that grew from 8 to 32 to 100 h (Figure 4.2a-c). In contrast, Ti-2Nb exhibited pronounced local variations, particularly in the size of faceted oxide crystals (e.g. in Figure 4.2g and 4.3i). The crystals did not obviously grow in time. The oxidized surface on Ti-2Nb was much less dense than that on pure Ti, as the large cavities observed on Ti-2Nb (e.g. in Figure 4.2f) were absent on pure Ti.

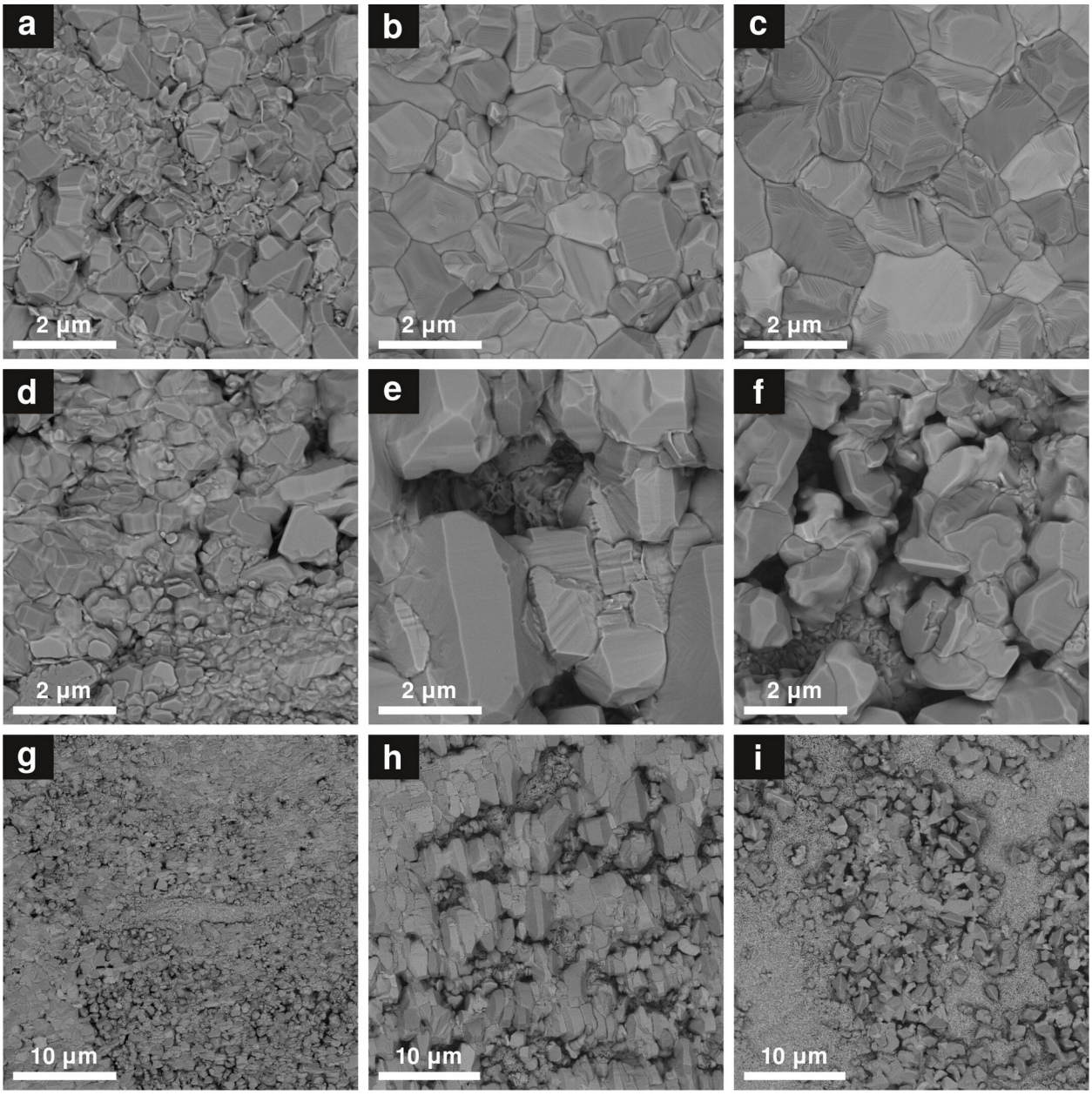

Figure 4.3: BSE-mode SEM of the surface on (a-c) pure Ti and (d-i) Ti-2Nb oxidized for (a, d, g) 8 h, (b, e, h) 32 h, and (c, f, i) 100 h. Lower-magnification images for Ti-2Nb (g-i) are included to show the local microstructural variability, which was not observed for pure Ti.

The oxide scales at 100 h were generally lamellar but dense at corners, as shown in the polished cross sections (Figure 4.3). For pure Ti, the lamellar oxide scale had uniform thickness across the surface and consisted of thick, irregular layers separated by large cracks (Figure 4.3a). On Ti-2Nb, the scale was more compact with a higher density of thinner, regular layers (Figure 4.3c1). In limited areas, the scale on Ti-2Nb was significantly thinner and compact rather than

lamellar (Figure 4.3c2). Furthermore, an additional layer was typically observed between the oxide scale and metal, as indicated by blue arrows in Figure 4.3c1 and 4.4c2. This layer was thin (~1 μm) in areas with lamellar scale (Figure 4.3c1) but potentially much thicker (e.g. ~11 μm) with columnar grains in areas with compact scale (Figure 4.3c2). The thickness of this layer appeared to correlate with the grains in the metal substrate, as shown in Figure 4.13 in the Appendix. We note that cracks and chips indicated by yellow arrows in Figure 4.3b and 4.4d likely originated from metallographic preparation.

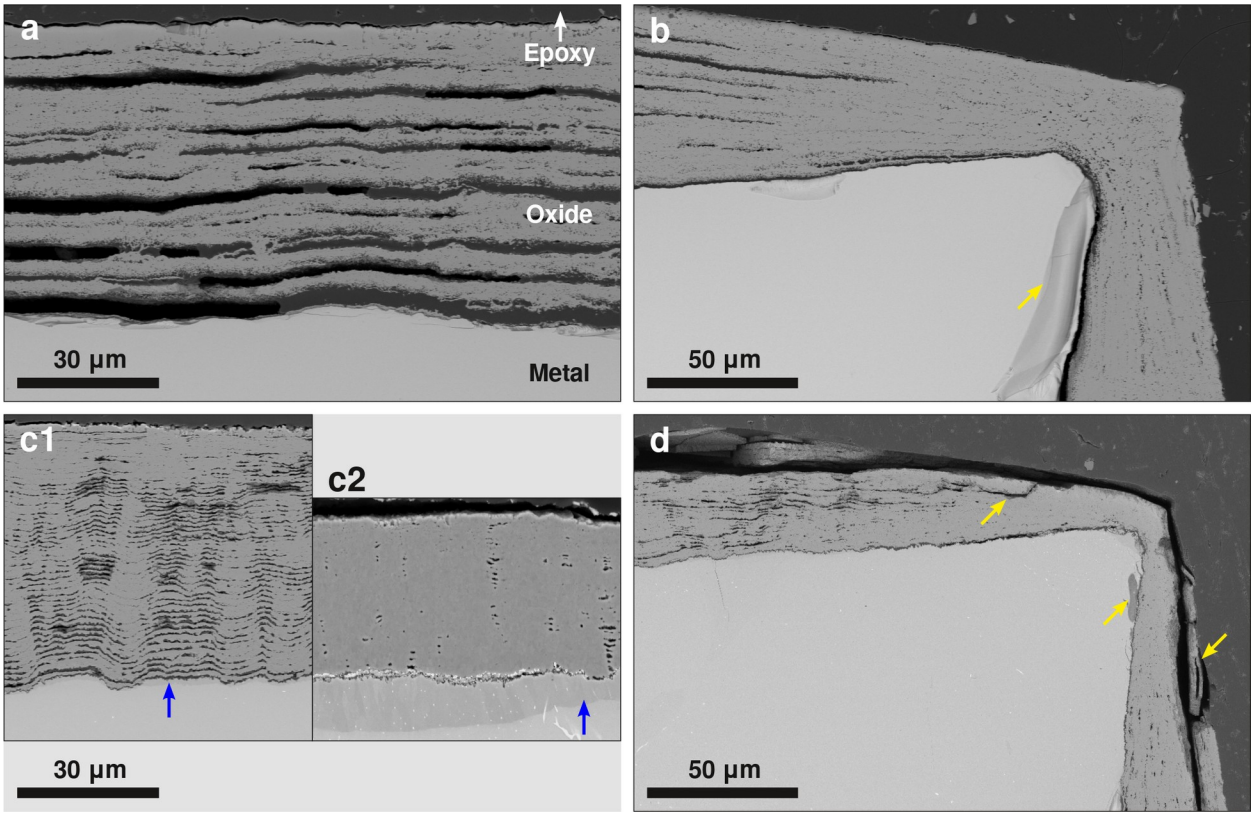

Figure 4.4: BSE-mode SEM of polished cross sections of (a, b) pure Ti and (c, d) Ti-2Nb oxidized for 100 h (800 °C, Ar-O_2), showing the oxide scale formed centrally on specimens (a, c) and near the corners (b, d). On Ti-2Nb, both lamellar oxide scale (c1) and compact oxide scale (c2) were observed; blue arrows point to the additional layer observed between the oxide scale and the metal. In (b, d), yellow arrows point to cracks or chips presumed to be damage from metallographic preparation.

Microstructure and local chemistry were examined using SEM and S/TEM on cross sections from specimens oxidized for different times. We note that cross sections were prepared from darker areas (as shown in Figure 4.2), where the oxide scale was presumed to be more

compact. The oxide scales formed on pure Ti at 8 h and Ti-2Nb at 8 h and 32 h were compact with similar microstructures (Figure 4.5). The scales consisted predominantly of larger (sometimes columnar) outer grains and finer inner grains. Grain size ranged from ~100 nm to ~3 μm. Pores present throughout the scale were typically tens to hundreds of nanometers in size and sometimes faceted. Compared to the scale on pure Ti, the scale on Ti-2Nb was thin and contained light-colored Nb-rich precipitates and lateral pores/cracks, as indicated by yellow circles and arrows in Figure 4.5b and 4.5c. Additionally, Nb segregation was observed along the TiO_2 grain boundaries (Figure 4.6). We note that the crack at the scale-metal interface in each Ti-2Nb cross section (Figure 4.5b and 4.5c) likely resulted from cooling and/or sample preparation and therefore is not believed to have been present or formed during oxidation at 800 °C. The layer previously noted at the scale-metal interface at 100 h (in Figure 4.3c) had an estimated O concentration of ~40 at.%, according to EDS analysis, and was identified as Ti_2O (*P6/mmm*) suboxide using selected-area TEM diffraction (Figure 4.7). The Ti_2O layer consisted of micron-sized grains.

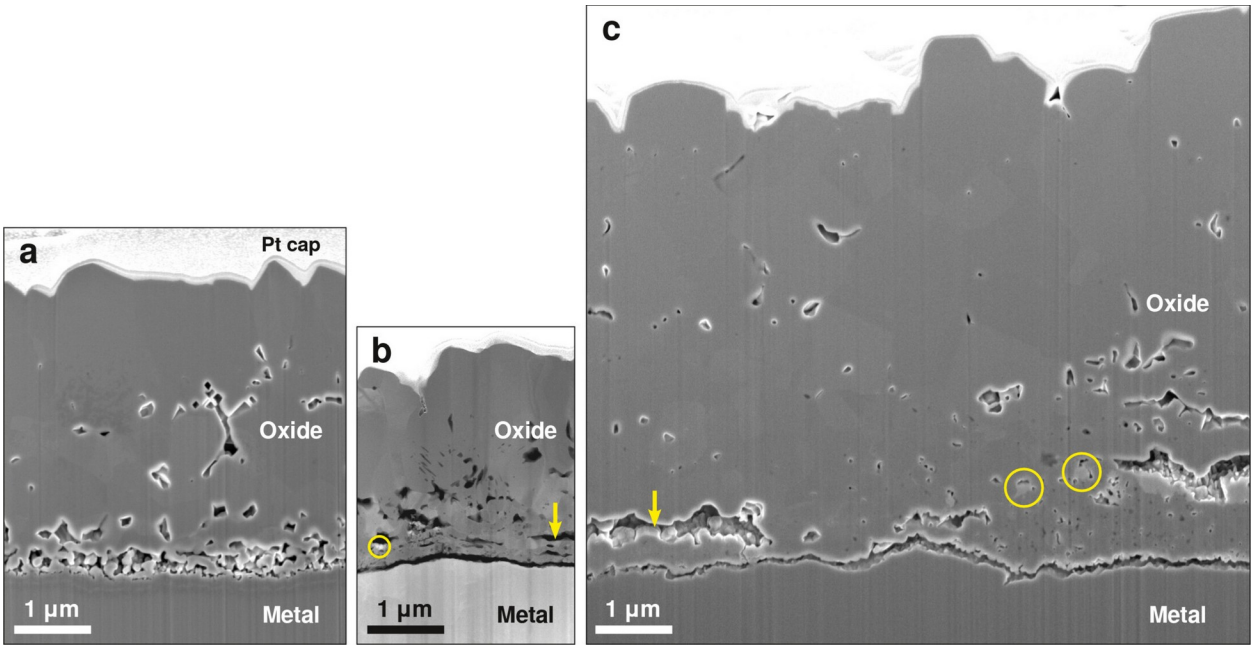

Figure 4.5: Cross sections of (a) pure Ti oxidized for 8 h and Ti-2Nb oxidized for (b) 8 h and (c) 32 h (800 °C, Ar-O_2). The cross sections were prepared from darker areas such as those shown in Figure 4.2. In (b, c), circles enclose light-colored, Nb-rich particles, while arrows point to lateral pores/cracks. (a, c) are SE-mode SEM, whereas (b) is HAADF STEM.

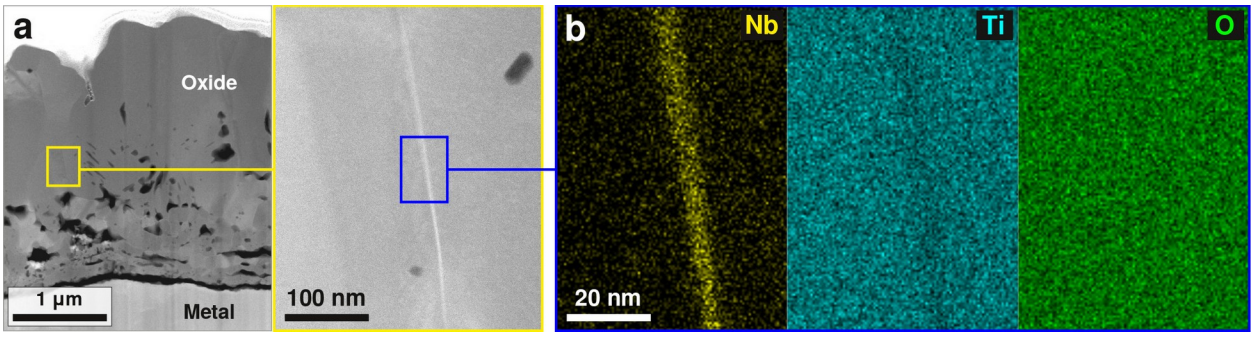

Figure 4.6: (a) HAADF STEM of the cross section of Ti-2Nb oxidized for 8 h (800 °C, Ar-O_2) with (b) corresponding net-intensity EDS maps showing a Nb-rich grain boundary in the TiO_2 oxide.

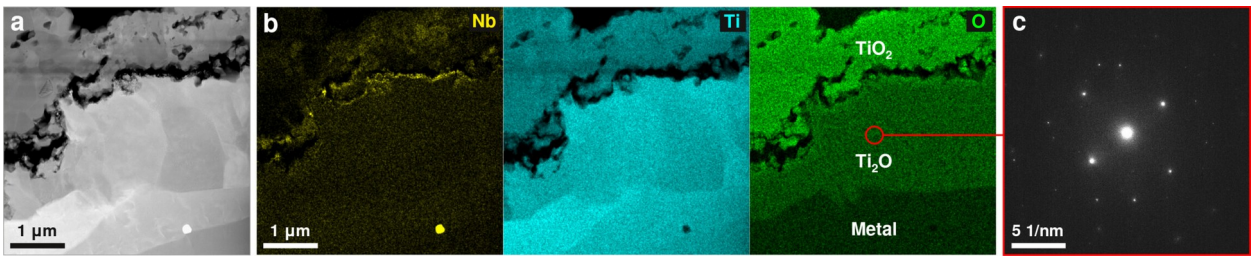

Figure 4.7: At the scale-metal interface of Ti-2Nb oxidized for 100 h (800 °C, Ar-O_2), (a) HAADF STEM and (b) net-intensity EDS maps with (c) selected-area TEM diffraction showing Ti_2O (*P6/mmm*) suboxide along the $[\bar{4}5\bar{1}\bar{3}]$ zone axis.

Oxygen dissolution in the metal was measured on polished cross sections to assess its contribution to the measured mass gains. As shown in Figure 4.8a, oxygen concentration profiles were the same for pure Ti and Ti-2Nb at a given oxidation time (8 h, 32 h) and extended to greater depth with increasing oxidation time. Profiles were fitted to Equation 5. As shown in Figure 4.8b, within error, the fitted values did not differ by material or by oxidation time. C_s ranged from 22~26 at.%, C_0 was 0.0 at.% (not shown), and D was on the order of 1.0×10^{-14} m^2/s.

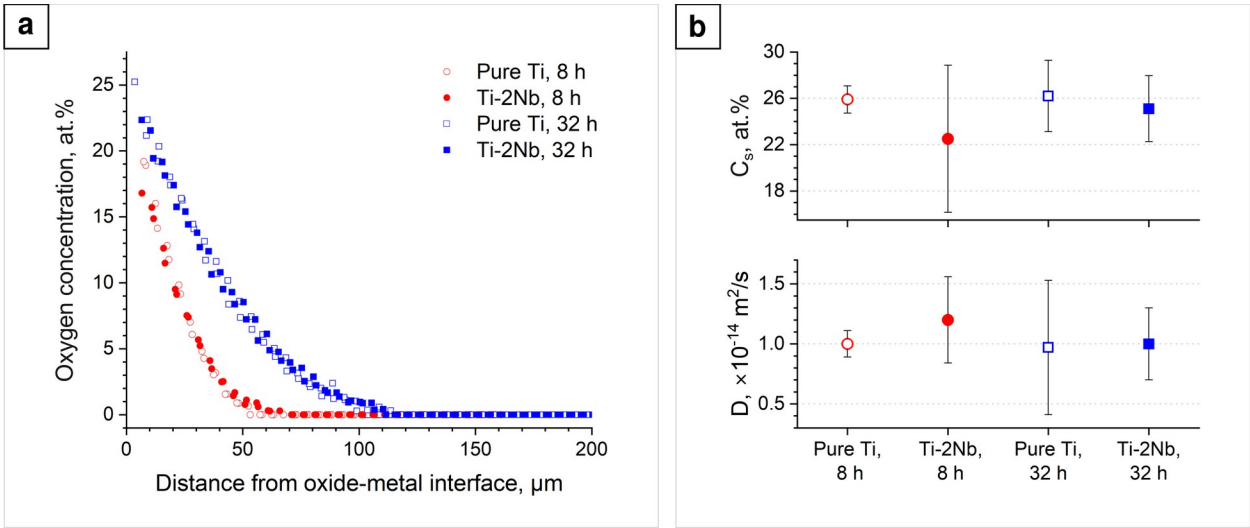

Figure 4.8: (a) WDS measurements of oxygen concentration in the metal for pure Ti and Ti-2Nb oxidized for 8 h and 32 h (800 °C, Ar-O_2). (b) average values for oxygen surface concentration (C_s, top) and oxygen diffusivity (D, bottom) obtained from fitting the two profiles for each specimen to Equation 5; error bars indicate the 90% confidence interval.

Oxide-growth mechanisms at shorter times were investigated using two-stage tracer oxidation experiments and nanoSIMS analyses (Figure 4.9). As for those in Figure 4.5, cross sections were prepared from darker areas. For both materials, ^{18}O enrichment was observed along the top surface of the oxide scale, along oxide grain boundaries (dotted in blue), and in the layer above the scale-metal interface (dotted in yellow) (Figure 4.9b and 4.9d). In comparison to pure Ti (Figure 4.9b), in Ti-2Nb (Figure 4.9d), ^{18}O enrichment was thinner and less uniform along the top surface, more uniformly distributed along oxide grain boundaries throughout the scale, and qualitatively thicker near the scale-metal interface. Additionally, Ti-2Nb lacked a region with diffuse ^{18}O enrichment like the one observed near the top surface of the oxide in pure Ti. As shown in Figure 4.9e, the relative ^{18}O isotopic concentration, $^{18}O/(^{16}O + {}^{18}O)$, was similar for both materials in the top band (~70%) and in the ^{18}O-poor oxide (~1%) but higher for Ti-2Nb both in the layer just above the scale-metal interface (~40% v. 5% in pure Ti) and in the metal (~2% v. <1% in pure Ti).

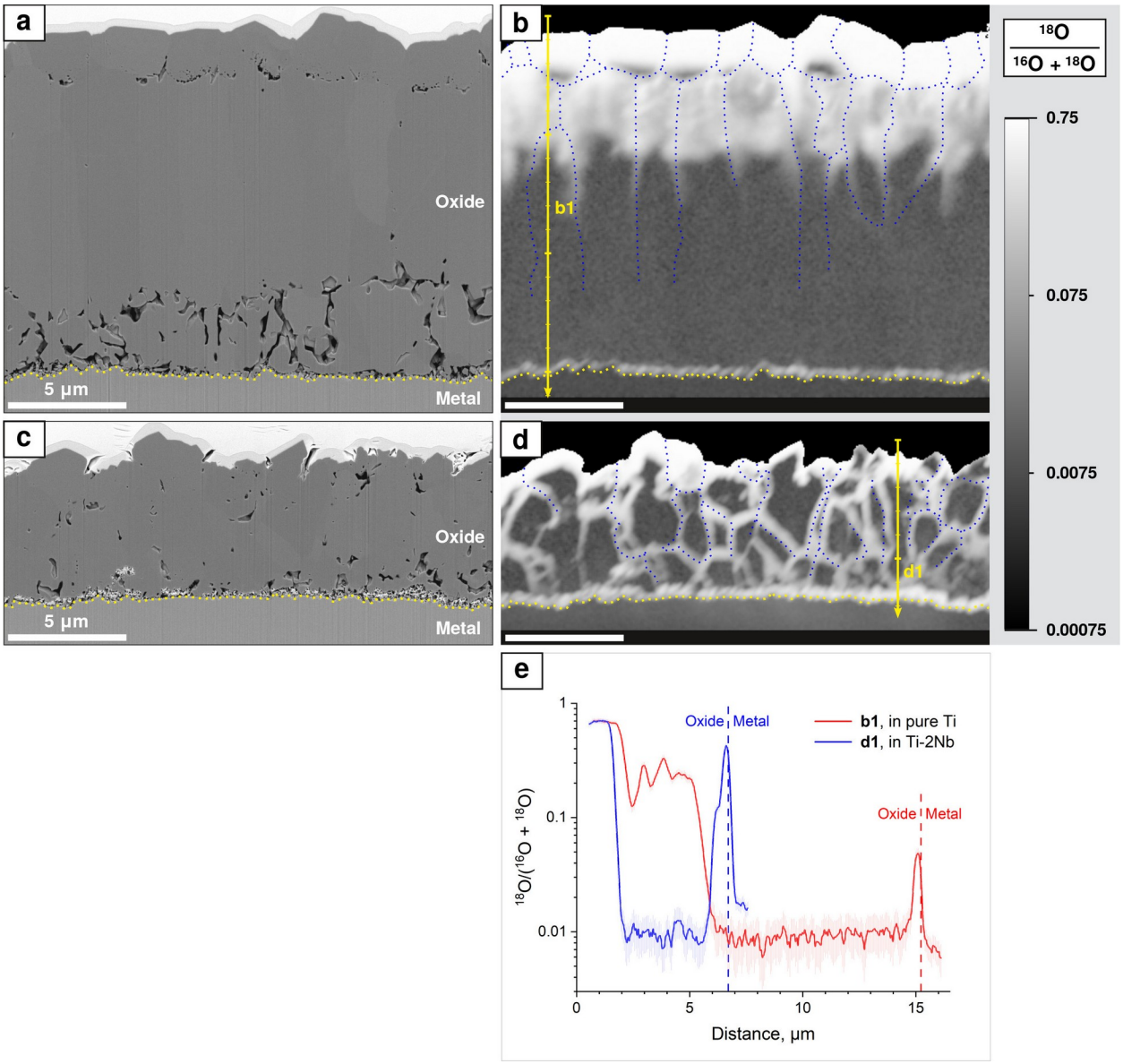

Figure 4.9: BSE-mode SEM with a corresponding nanoSIMS map of the logarithm of ^{18}O isotopic concentration, $\log_{10}(^{18}O/(^{16}O + ^{18}O))$, for (a, b) pure Ti oxidized for 12 h in $^{16}O_2$ followed by 4 h in $^{18}O_2$ and (c, d) Ti-2Nb oxidized for 20 h in $^{16}O_2$ followed by 4 h in $^{18}O_2$ (800 °C). Cross sections were prepared from darker areas. Yellow dotted lines denote the scale-metal interface. NanoSIMS maps (b, d) include blue dotted lines marking all oxide grain boundaries clearly perceptible in SEM and yellow profiles through the thickness of the oxide scale, for which ^{18}O isotopic concentration is plotted in (e). Additional nanoSIMS maps are provided in the Appendix, Figure 4.14. Figures (a, b) and the corresponding profile in (e) are reproduced from Figure 3.10.

To clarify the nature of the ^{18}O enrichment along oxide grain boundaries observed with nanoSIMS, APT was performed on a specimen prepared from the oxide formed on the tracer-

oxidized Ti-2Nb specimen (Figure 4.10). The analysis captured a triple junction. The oxide composition matched the stoichiometry of TiO_2 (Figure 4.10b). Grain boundaries were decorated with ^{18}O and Nb, as illustrated in Figure 4.10a. As shown in Figure 4.10b, a quantitative composition profile across one of the grain boundaries (generated using AtomProbeLab as described in the Appendix, Section 4.6.1) showed coincident peaks of ^{18}O and Nb, with gradients extending about ~4 nm on either side. The ^{18}O isotopic concentration ranged from a baseline of ~1.5% away from the grain boundary to a maximum of ~26% at the grain boundary (Figure 4.10b, bottom), consistent with the ^{18}O concentrations obtained using nanoSIMS. Nb concentration ranged from a low detectable ~0.1 at.% throughout the oxide to a maximum of ~1.6 at.% at the grain boundary. The presence of Nb in the bulk oxide was confirmed in the mass spectrum, as shown in Figure 4.15 in the Appendix.

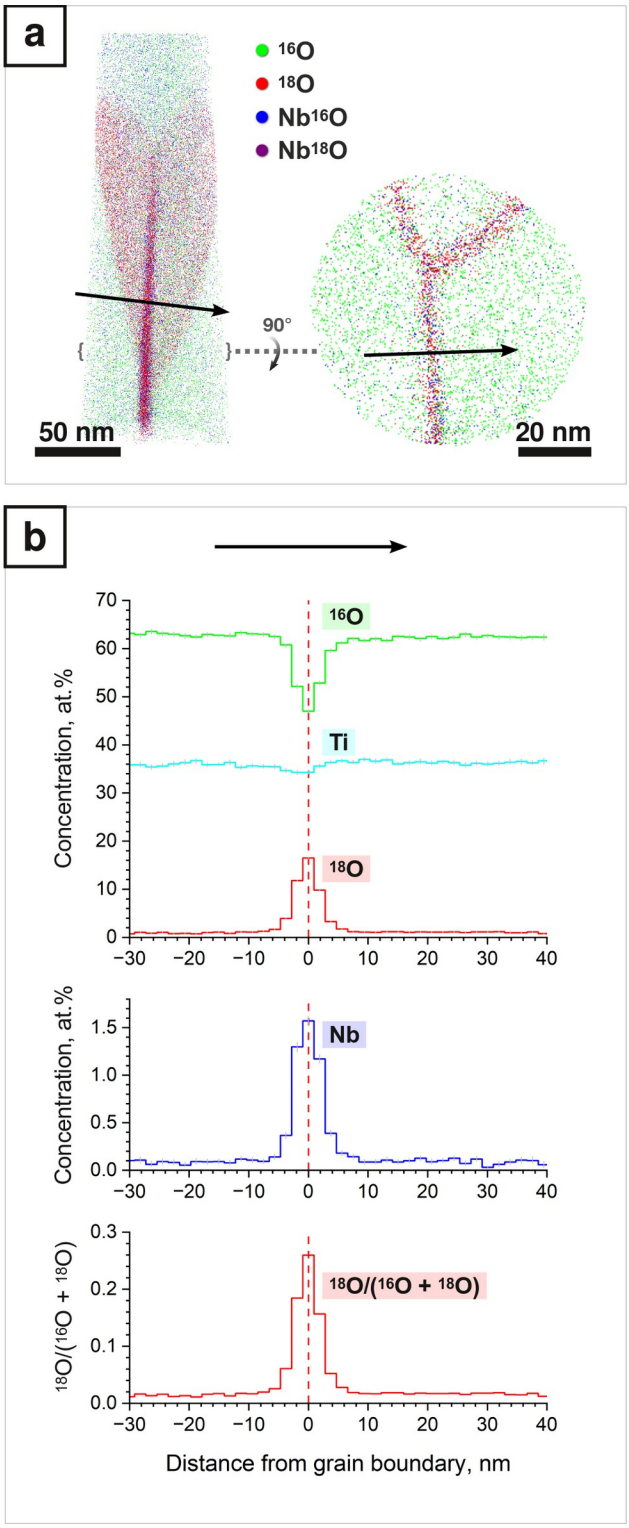

Figure 4.10: (a) APT reconstruction and (b) corresponding concentration profiles across a grain boundary in the TiO_2 formed on Ti-2Nb oxidized for 20 h in $^{16}O_2$ followed by 4 h in $^{18}O_2$ (800 °C). (a) the 3D reconstruction (left) and 10 nm thick slice (right) show ^{16}O ($^{16}O^+$ at 16.0 Da), ^{18}O ($^{18}O_2^+$ at 36.0 Da), $Nb^{16}O$ ($Nb^{16}O_2^{++}$ at 62.5 Da and $Nb^{16}O_2^+$ at 124.9 Da), and $Nb^{18}O$ ($Nb^{18}O_2^+$ at 128.9 Da) ions; Ti is omitted for clarity. The black arrow in (a) marks the direction of the

concentration profile in (b). In (b), bin width (~2 nm) corresponds to the thickness of volumetric slices used to generate the profile; error bars indicate the 95% confidence interval; and H, C, and Ga — which were included in the analysis and totaled at most 0.7 at.% in any slice — were not plotted for clarity.

4.4 Discussion

The present results confirmed the beneficial impact of Nb alloying on the oxidation of titanium that was previously noted in the literature [15]. Additionally, these results revealed that the positive effect of Nb in the absence of nitrogen is due solely to reduced oxide formation, and not to differences in the behavior of oxygen in the metal. Similar to our observations on the influence of Si on the oxidation of titanium discussed in Chapter 3 and in contrast to previous suggestions [14], [15], Nb had no effect on O solubility or diffusivity in the metal, as shown by the comparable O surface concentrations at the oxide-metal interface and comparable diffusivities in Ti-2Nb and pure Ti samples (Figure 4.8b). O surface concentrations and O diffusivities agreed well with the literature values of ~26 at.% [4], [5] and (at 800 °C in α Ti) 0.10-7.8 × 10^{-14} m^2/s [68]. Since we discussed the oxidation mechanisms of pure Ti in Section 2.2 and in Section 3.4 in the context of Si alloying, we will therefore focus on discussing and comparing the oxidation of Ti-2Nb.

Slower growth of the initially compact oxide scale on Ti-2Nb was partly due to slowed outward Ti transport, as shown by the reduced thickness of the new oxide along the top surface of Ti-2Nb compared to pure Ti (Figure 4.9). In principle, slowed inward O transport — by slowing inward oxide growth at the scale-metal interface — could have also contributed to slower overall oxide growth. However, differences in inward O transport rates between materials could not be inferred from nanoSIMS results in Figure 4.9, because the thicker new oxide at the scale-metal interface in Ti-2Nb could have been a consequence of its initially thinner oxide scale. As indicated by ^{18}O enrichment along oxide grain boundaries in nanoSIMS (Figure 4.9) and APT (Figure 4.10), inward O transport through the compact scale occurred predominantly via diffusion along the oxide grain boundaries. This ^{18}O enrichment along oxide grain boundaries reflected ^{18}O diffusion and exchange with ^{16}O rather than the formation of new oxide. This interpretation is consistent with the thin ^{18}O layer (~8 nm) and moderate ^{18}O isotopic concentration (<40%), as shown in Figure 4.10b and as we observed previously for Ti-0.8 at.% Si (Figure 3.10 and Figure 3.11). In contrast, the formation of new oxide along oxide grain

boundaries would entail thicker, step-like ^{18}O enrichment, e.g. as observed in a tracer-oxidized Ni-Al alloy in [94].

The measured mass-gain kinetics generally correlated with the oxide-scale morphology, i.e. the initial parabolic kinetics with the compact scales and linear kinetics with scales being mainly or exclusively lamellar. Notably both alloys transitioned from compact to lamellar scales at similar times.

The lamellar oxide scale on Ti-2Nb appeared to form in the same way as that on pure Ti, as evidenced by our nanoSIMS analysis on an additional lamella prepared from tracer-oxidized Ti-2Nb (Figure 2.4 in the Appendix). This analysis showed ^{18}O-rich oxide formed during the second oxidation exposure located on the metal underneath a continuous crack in the oxide scale, thereby confirming that cracking was followed by growth of new oxide on the metal. Furthermore, the high relative ^{18}O isotopic concentration in the new oxide and underlying metal (up to ~80%) pointed to rapid $^{18}O_2$ access through the detached oxide layer. The formation of thinner, more densely packed layers in the lamellar scale on Ti-2Nb may reflect a more uniform and reproducible oxide-detachment process through, for example, a reduced ability to accommodate strains, possibly due to the added presence of the Ti_2O suboxide at the scale-metal interface. However, the exact mechanism remains unclear.

The eventual formation of Ti_2O suboxide under the oxide scale on Ti-2Nb at some time between 32 and 100 h indicated the establishment of a gradient in oxygen chemical potential through the adherent oxide layer and metal. This would be consistent with the lower standard Gibbs free energies of formation per mole of O_2 of titanium suboxides compared to TiO_2 [102] and with reports of titanium suboxides forming on Ti oxidized in very low oxygen pressures (e.g. at ~10^{-6} atm [79] but not at 10^{-2} atm at 800 °C [103]. The low thickness of the suboxide under the lamellar oxide scale (Figure 4.3c1) compared to under the compact one (Figure 4.3c2) can be explained by periodic oxide detachment disrupting the compact oxide-suboxide-metal microstructure and gradient in oxygen chemical potential, thereby permitting oxidation of the suboxide. We note that the suboxide formation was not an artifact of the slow cooling rate typically used after 100 h oxidation treatments, as evidenced in Figure 4.17 in the Appendix.

The formation of the suboxide on Ti-2Nb may point to slowed inward O transport in comparison to pure Ti. Indeed, the fact that the Ti_2O suboxide only appeared after some time suggests that its formation is to some extent a kinetic effect. Slowed inward O transport could

simply be due to the differences in the oxide scale morphologies. For example, on Ti-2Nb, the thick, densely packed lamellar oxide scale that developed at longer oxidation times (Figure 4.3c1) may to some extent limit the penetration of molecular O_2, and the compact oxide scale (Figure 4.3c2) may limit inward O diffusion by its progressive thickening. Furthermore, chemical differences in the oxide scale — namely Nb segregation at the oxide grain boundaries — could slow inward O diffusion along oxide grain boundaries, as we hypothesized for outward Ti diffusion. Further work is needed to clarify the significance of the suboxide formation.

In prior literature, the positive role of Nb has typically been attributed to Nb^{5+} ions doping rutile TiO_2 and thereby slowing O and/or Ti diffusion through the oxide lattice [14], [15], [16], [19] (the first mechanism discussed in Section 2.4). Indeed, a low but measurable Nb concentration was found in the present study using APT (Figure 4.10b and Figure 4.15). However, we found that *oxide grain boundaries* are the main transport pathway for O and — as we hypothesize — Ti. Therefore in contrast to suggestions in prior literature, any effect of Nb^{5+} doping on O or Ti diffusion through the oxide *lattice* can only have a minor effect on scale-growth kinetics.

It was also previously suggested that the presence of Nb at the scale-metal interface influences O and/or Ti transport [14], [15], [17] (the second mechanism discussed in Section 2.4). No Nb segregation was observed at the oxide-metal interface in the present study at 8 h or 32 h, as shown in Figure 4.18 in the Appendix. Although a very thin layer of Nb was present between the oxide and suboxide at 100 h (Figure 4.7b), it cannot explain the slowed oxide growth of Ti-2Nb observed at earlier oxidation times. The presence of Nb-rich, BCC β precipitates in the alloy was due to the limited Nb solubility (about 1~2 at.% Nb in α Ti at the oxidation temperature [47]. During oxidation, these precipitates were incorporated into the scale by the inward-growing oxide front and oxidized, ultimately forming the Nb-rich oxide particles within TiO_2.

The present study highlights the importance of TiO_2 grain boundary chemistry on oxidation behavior. Grain boundaries are the primary pathway for inward O diffusion and likely outward Ti diffusion in rutile TiO_2. Although the possible benefits of doping of oxide grain boundaries is well known, particularly for Cr_2O_3- and Al_2O_3-forming alloys (i.e. the reactive-element effect) [94], [104], [105], [106], to our knowledge, the present study is the first to report a similar phenomenon in TiO_2-forming/titanium-based alloys. Interestingly, comparing to the

previous study on Si, Nb and Si slowed oxide growth via different mechanisms. Unlike Nb, Si was not detected at oxide grain boundaries and instead formed a protective Ti_5Si_3 layer at the scale-metal interface that prevented inward oxide growth. Therefore, the present work points to an additional, distinct mechanism — doping of TiO_2 grain boundaries — as a tool for engineering oxidation-resistant titanium alloys. This mechanism may apply to more complex titanium-based alloys such as TiAl- and Ti_3Al-based intermetallics known to benefit from Nb [14] and more broadly to any TiO_2-forming alloys such as Ti-containing multi-principal-element alloys.

4.5 Conclusions

To clarify how Nb alloying improves the oxidation resistance of titanium, we investigated the oxidation of pure Ti and Ti-2Nb at 800 °C in Ar-O_2 or in two-stage exposures of $^{16}O_2$ followed by $^{18}O_2$. Under these experimental conditions, we reached the following conclusions:

1. Ti-2Nb exhibited less mass gain than pure Ti, which was due to its thinner oxide scale rather than to differences in oxygen dissolved in the metal.
2. Nb alloying significantly reduced outward TiO_2 growth.
3. The eventual formation of a Ti_2O suboxide layer at the scale-metal interface in Ti-2Nb indicated the development of a decreasing gradient in oxygen chemical potential through the compact oxide-suboxide-metal microstructure.
4. Nb segregation to the (rutile TiO_2) oxide grain boundaries is believed to contribute to the differences noted in scale-growth kinetics and scale morphologies.

This study spotlights doping of rutile TiO_2 oxide grain boundaries as a relevant phenomenon influencing the oxidation behavior of titanium alloys and as a potential strategy for improving their oxidation resistance.

4.6 Appendix

4.6.1 APT data processing with AtomProbeLab

AtomProbeLab 0.2.4 was used to analyze the composition across the ^{18}O- and Nb-rich grain boundary in the oxide formed on tracer-oxidized Ti-2Nb. The volume of interest containing the grain boundary (perpendicular to the black arrow in Figure 4.10a) and the surrounding oxide was extracted using the cube ROI tool in AP Suite, with the *x* axis of the cube visually aligned normal to the grain boundary. In AtomProbeLab, the isotopes definition file was modified by adding standalone ^{18}O as "Q" and zeroing the ^{71}Ga abundance. Prospective ions were explored using the *ionFitTester* function on the cube dataset. These ions, approximately in order of increasing Da, were **O^+**, OH^+, Q^+, QH^+, QH_2^+, **Ti^{++}**, TiH^{++}, TiH_2^{++}, *N_2^+*, CO^+, **TiO^{++}**, **O_2^+**, TiQ^{++}, OQ^+, Q_2^+, NbO^{+++}, NbQ^{+++}, **TiO_2^{++}**, GaC^{++}, TiQ_2^{++}, $Ti_2O_2^{+++}$, *Ti_2OQ^{+++}*, $Ti_2Q_2^{+++}$, NbO_2^{+++}, $NbOQ^{++}$, NbQ_2^{+++}, Ti^+, NbO^{++}, NbQ^{++}, **TiO^+**, NbO_2^{++}, $NbOQ^{++}$, NbQ_2^{++}, TiQ^+, Ga^+, Ti_3^{++}, $Ti_2O_3^{++}$, $Ti_2O_2Q^+$, $Ti_2OQ_2^{++}$, *$Ti_2Q_3^{++}$*, **TiO_2^+**, $TiOQ^+$, GaC^+, TiQ_2^+, **TiO_3^+**, TiO_2Q^+, $TiOQ_2^+$, TiQ_3^+, NbO_2^+, $NbOQ^+$, and NbQ_2^+. Ions in bold were set as mandatory, whereas those in red italics were removed based on the results of *ionFitTester*. Selected ions, which are labeled on the mass spectrum in Figure 4.9, were then used to generate the concentration profile across the grain boundary in Figure 4.10b.

4.6.2 Figures

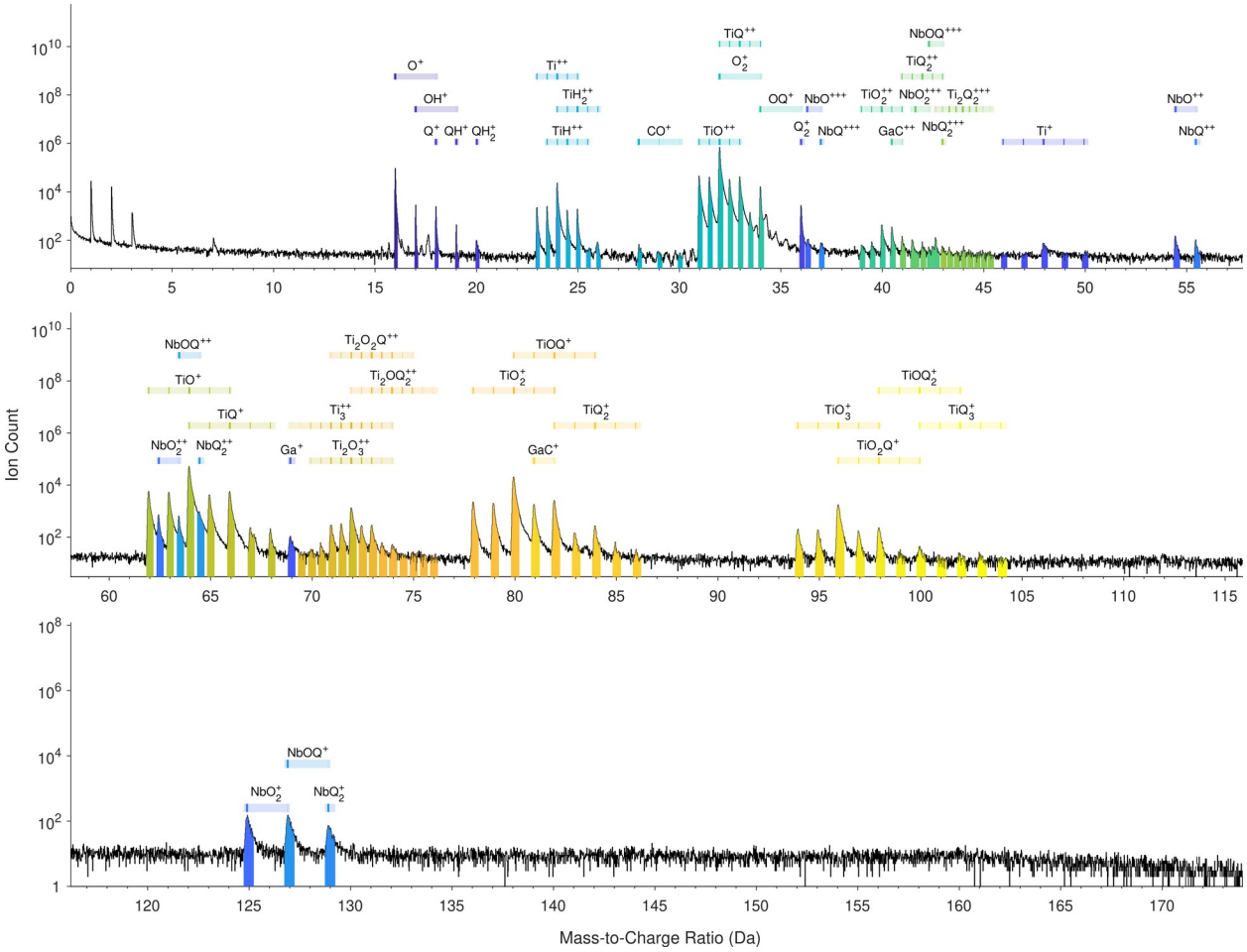

Figure 4.11: For the APT tip shown in Figure 4.10a, the mass spectrum of the cube enclosing the grain boundary of interest and the surrounding TiO_2. Labels show selected ions, with "Q" denoting ^{18}O.

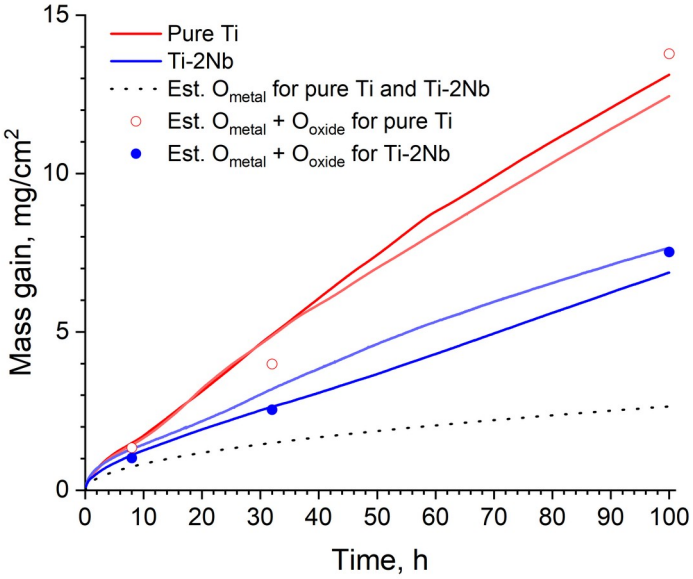

Figure 4.12: For pure Ti and Ti-2Nb oxidized isothermally at 800 °C in Ar-O_2, mass gains measured via thermogravimetry (solid lines) matched well with the estimated sum of oxygen dissolved in the metal (O_{metal}) and oxygen in the oxide scale (O_{oxide}). O_{metal} was estimated using integration of Equation 5 with $D = 1.0 \times 10^{-14}$ m^2/s, $C_s = 26$ at.%, and $C_0 = 0.0$ at.%. O_{oxide} was calculated using measurements of the rutile TiO_2 oxide scale thickness (corrected to account for cracks and porosity) and the density of TiO_2.

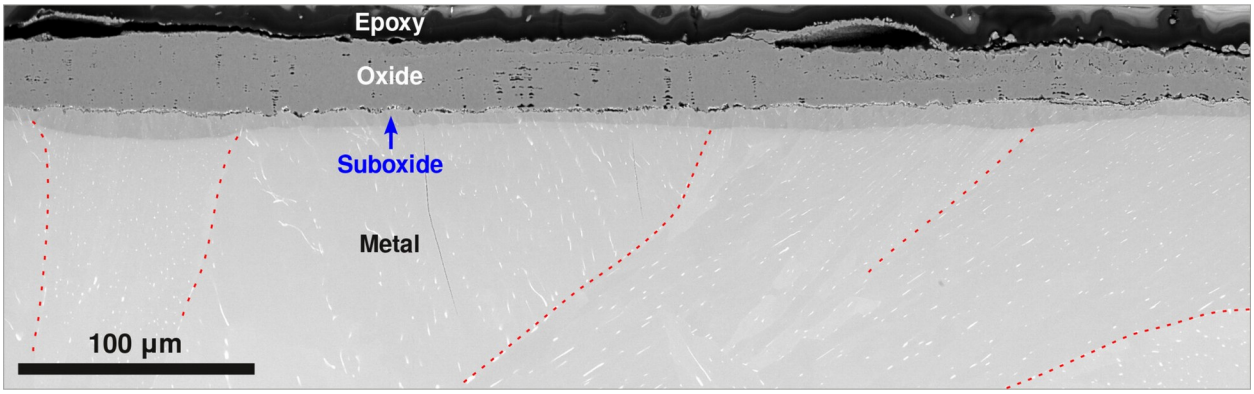

Figure 4.13: BSE-mode SEM of the polished cross section of Ti-2Nb oxidized for 100 h (800 °C, Ar-O_2) showing a possible correlation between the suboxide thickness and grains in the metal substrate. Clearly identifiable grain boundaries in the metal substrate are marked with red dashes.

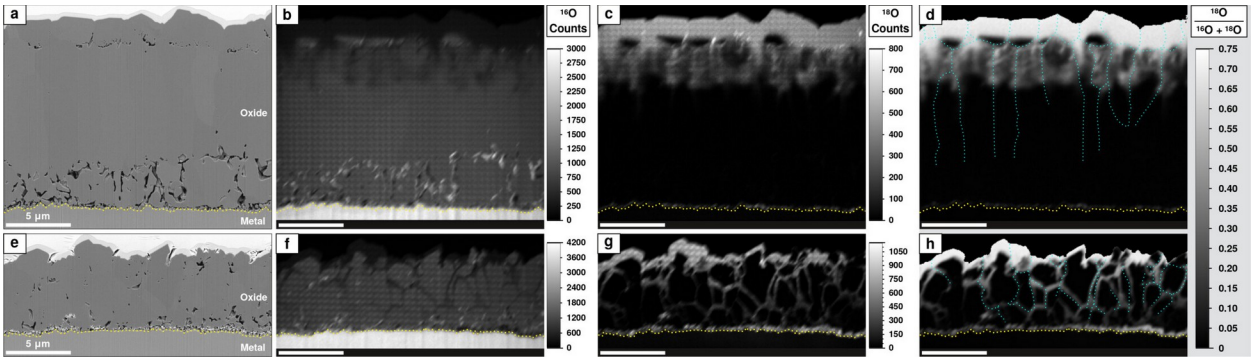

Figure 4.14: BSE-mode SEM for (a) pure Ti oxidized for 12 h in $^{16}O_2$ followed by 4 h in $^{18}O_2$ and (e) Ti-2Nb oxidized for 20 h in $^{16}O_2$ followed by 4 h in $^{18}O_2$ (800 °C) with corresponding nanoSIMS maps of (b, f) $^{16}O^-$ counts, (c, g) $^{18}O^-$ counts, and (d, h) the ^{18}O isotopic concentration, $^{18}O/(^{16}O + {}^{18}O)$. Yellow dotted lines mark the scale-metal interface. In (d, h), additional blue dotted lines mark the TiO_2 oxide grain boundaries that were clearly perceptible in SEM. In (b, c, f, g), the subtle grid pattern reflected insufficient sputtering density in nanoSIMS before analysis; additionally, high $^{16}O^-$ or $^{18}O^-$ counts in pores was likely an artifact of non-planar topography and, per (d, h), did not reflect any differences in ^{18}O isotopic concentration.

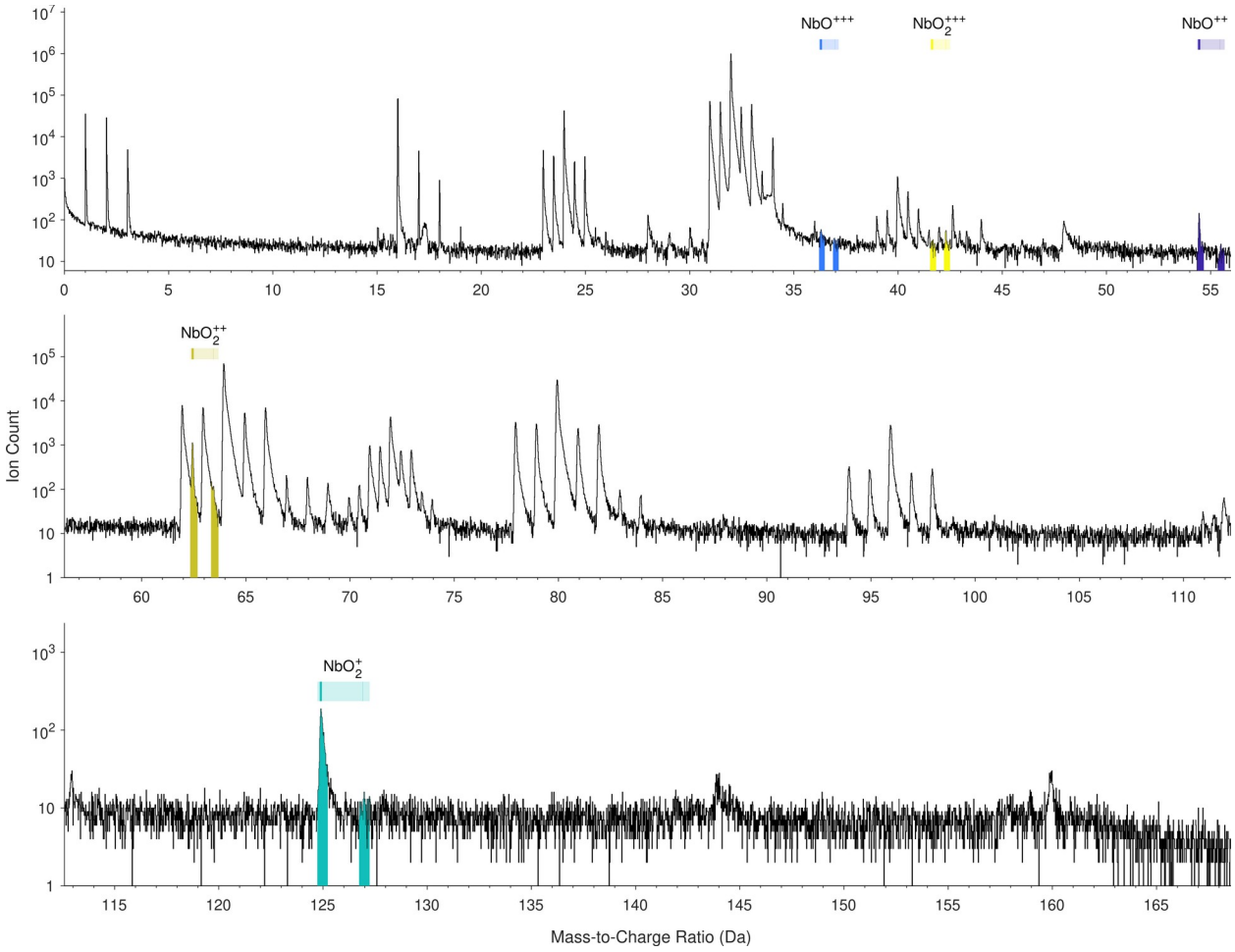

Figure 4.15: For the APT tip shown in Figure 4.10a, the mass spectrum showing NbO ions detected in the bulk, grain-boundary-free TiO_2.

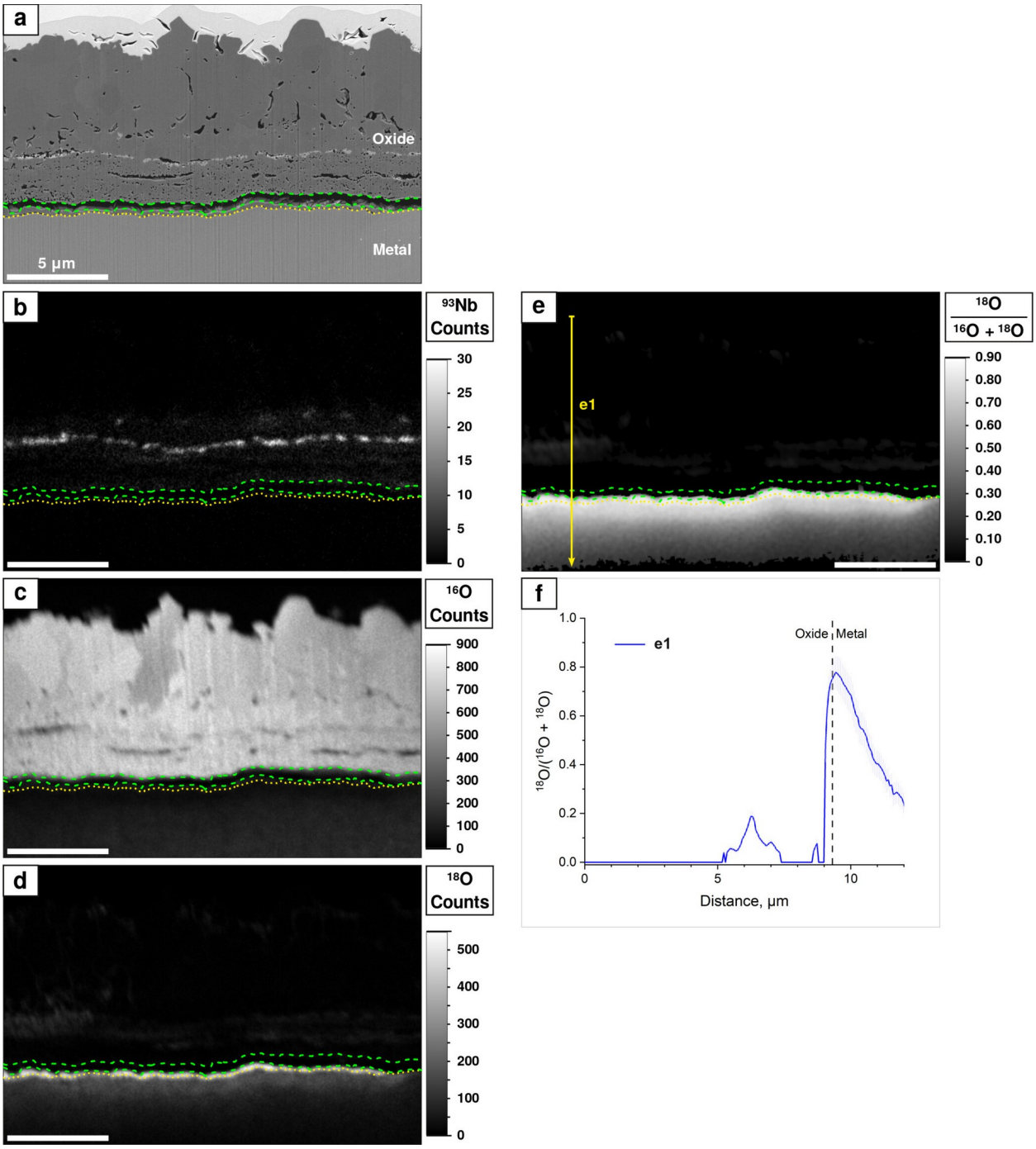

Figure 4.16: (a) BSE-mode SEM with (b-e) corresponding nanoSIMS maps for an additional lamella prepared from Ti-2Nb oxidized for 20 h in $^{16}O_2$ followed by 4 h in $^{18}O_2$ (800 °C). NanoSIMS maps show (b) $^{93}Nb^+$ counts, (c) $^{16}O^-$ counts, (d) $^{18}O^-$ counts, and (e) ^{18}O isotopic concentration, $^{18}O/(^{16}O + ^{18}O)$. ^{18}O isotopic concentration through the thickness of the oxide scale and metal, i.e. along profile *e1* drawn in (e), is plotted in (f). We note that $^{93}Nb^+$ ions were detected using a distinct experiment with a focused O^-, rather than Cs^+, beam. In (a-e), yellow dotted lines mark the scale-metal interface, while the green dashed lines enclose a continuous crack in the (TiO_2) oxide scale.

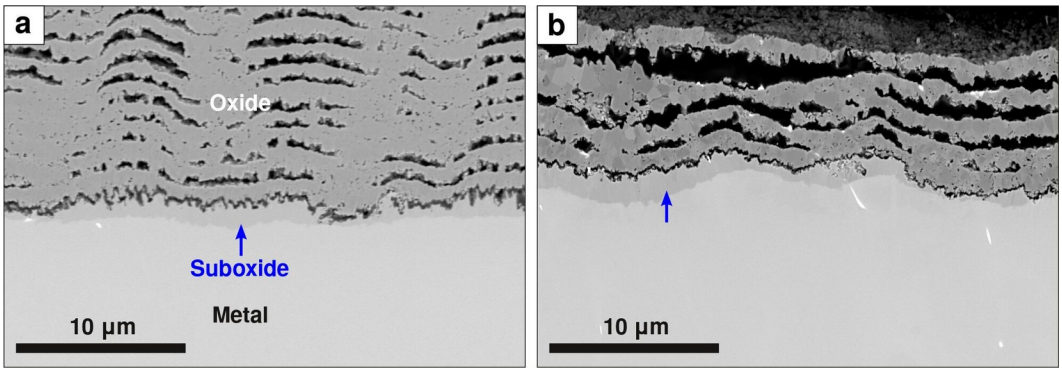

Figure 4.17: BSE-mode SEM from polished cross sections of Ti-2Nb oxidized for 100 h (800 °C, Ar-O_2) and then cooled to room temperature at different rates, (a) slow (20 °C/min, in a thermogravimetric analyzer) and (b) fast (averaging ~100 °C/min, in a tube furnace). The (Ti_2O) suboxide morphology was the same regardless of the cooling rate.

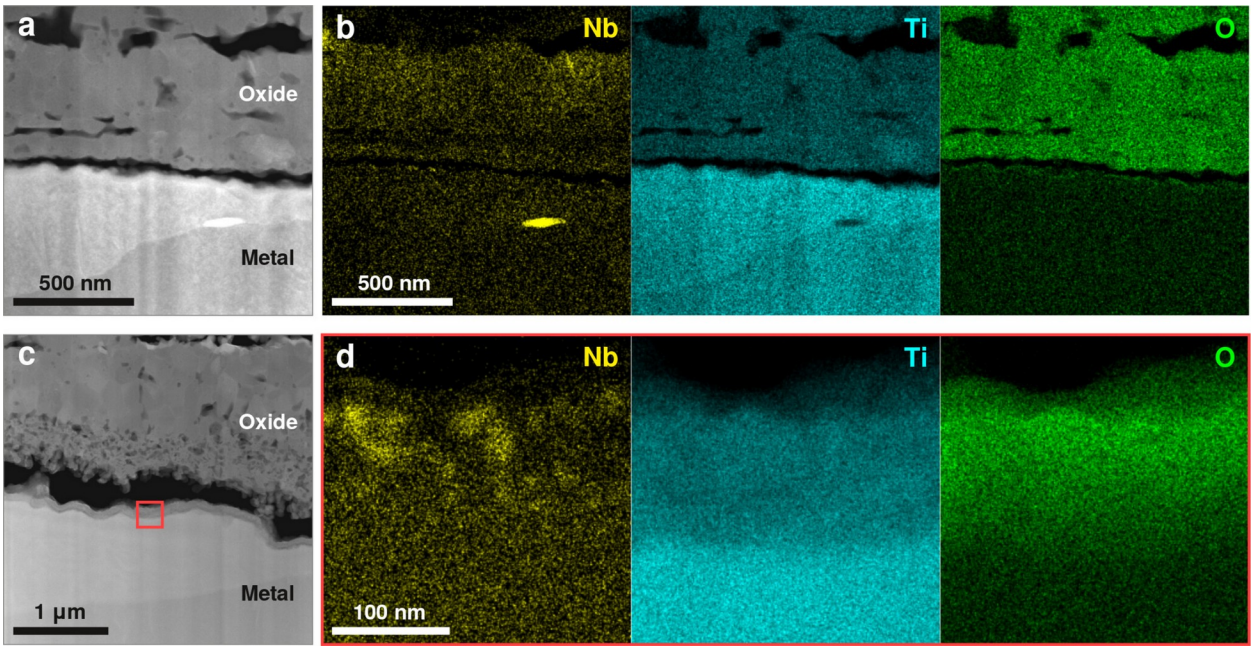

Figure 4.18: HAADF STEM with net-intensity EDS maps of the oxide-metal interface of Ti-2Nb oxidized for (a, b) 8 h and (c, d) 32 h (800 °C, Ar-O_2). EDS in (b) corresponds to the full area of (a), whereas EDS in (d) corresponds to the small, boxed region in (c). Nb did not obviously segregate along the oxide-metal interface.

4.6.3 Tables

Table 4.1: Values from fitting Equation 4 to mass gain data for pure Ti and Ti-2Nb oxidized isothermally at 800 °C in Ar-O_2. Mass gains were measured using continuous thermogravimetry. In Figure 4.1 and Figure 4.12, for each material, the dark line corresponds to trial 1, and the light line corresponds to trial 2.

	0–10 h		**0–100 h**	
Sample	***m***	***k_m****	***m***	***k_m****
Pure Ti, trial 1	1.73	0.25	1.16	0.20
Pure Ti, trial 2	1.74	0.24	1.20	0.20
Ti-2Nb, trial 1	1.86	0.15	1.03	0.067
Ti-2Nb, trial 2	2.16	0.22	1.26	0.13

*The units of k_m are $mg^m\ cm^{-2m}\ h^{-1}$ and therefore depend on the value of m.

Chapter 5: Role of Atmospheric Nitrogen in the High-Temperature Oxidation of Titanium Alloys

5.1 Introduction

Because nitrogen is known to influence the high-temperature oxidation behavior of titanium alloys, understanding its influence on the oxidation mechanisms is important for typical applications in nitrogen-containing air. Nitrogen has been linked to numerous positive effects on the oxidation response such as reducing mass gain [9], [10], [11], [21], [22], oxide thickness [9], [14], [16], [21], [22], [23], and the amount of oxygen dissolved in the metal [9], [10], [11], [16], [21], [22], [24]. Although many studies generally attribute the benefits of nitrogen to the formation of nitride phases, oxynitride phases, and/or nitrogen in the metal acting as a barrier to oxygen [14], [20], [22], [23], [25], [26], some unknowns remain. In particular, the origin of the reduced amount of oxygen dissolved in the metal has not been conclusively determined. Additionally, distinguishing the role of nitrogen from expected synergy with alloying additions remains challenging.

Extending the work in the previous two chapters, this chapter clarifies the role of nitrogen alone and synergistically with the alloying elements Si and Nb. To this end, we systematically characterize the oxidation responses of pure Ti, Ti-0.8Si, and Ti-2Nb at 800 °C in N_2-20% O_2 and in sequential isotopically labeled N_2-20% O_2 atmospheres. We find that the alloys always exhibit a nitride layer beneath a compact oxide scale with localized nitrogen concentrations in the underlying metal. Using Thermo-Calc simulations in agreement with our experiments, we demonstrate how nitrogen in the metal limits the oxygen concentrations in the metal. Notably, alloying additions do not influence the behavior of N or O in the metal. This finding is important because it suggests that alloying is not an effective method for influencing the solubilities or diffusivities of N and O in the metal, in contrast to recent suggestions in [107]. For the alloys, the synergy between alloying and nitrogen helps maintain compact oxide scales over long oxidation periods, preventing the formation of the lamellar scales observed during oxidation in nitrogen-free atmosphere and during the oxidation of pure Ti regardless of the atmosphere.

5.2 Experimental Methods

Many of the methods are similar to those used in the previous two chapters (Sections 3.2 and 4.2). The materials used in this study were pure titanium plate (99.999%; Lot M31E035; Alfa Aesar; Tewksbury, MA), Ti-0.8 at.% Si ("Ti-0.8Si"), and Ti-2 at.% Nb ("Ti-2Nb"). Ti-0.8Si and Ti-2Nb were prepared by arc melting the aforementioned titanium plate with high-purity Si (99.999%; Lot M21H026; Alfa Aesar) or Nb (99.95%; Lot M03F046Y; Alfa Aesar) under inert Ar, with flipping and remelting the ingots at least three times to enhance homogeneity. Ingots were then encapsulated in Ar-filled quartz tubes and heat treated for homogenization. Ti-0.8Si was held at 850 °C for 24 h. Ti-2Nb was held at 900 °C for 23 h, cooled to 800 °C over ~10 minutes, and held for an additional 50 minutes. Ingots were then quenched in water.

Specimens for oxidization studies were ground, polished with 9 μm polycrystalline diamond suspension, and sonicated in methanol immediately before oxidation. All oxidation experiments were carried out at 800 °C.

Standard oxidation experiments were performed in N_2-20% O_2 using a tube furnace for the 8 h and 32 h exposures and a thermogravimetric analyzer for the 100 h exposure (STA 449 F3 Jupiter; NETZSCH Instruments North America, LLC; Burlington, MA). Before oxidation exposures, the furnace chamber was flushed with Ar. Specimens were then equilibrated at 800 °C (for ~10 minutes), exposed to N_2-O_2 for the desired time, and cooled to room temperature under flowing Ar. For thermogravimetric studies, specimens were plate shaped, with the two largest faces polished (with 9 μm diamond abrasives) and the four smaller faces only ground (with 30 μm alumina lapping film or P1200 alumina paper). To ensure the reproducibility of thermogravimetric data, two trials were conducted per material. We note that specimen cooling rates differed in the tube furnace (averaging ~100 °C/min) and the thermogravimetric analyzer (20 °C/min for pure Ti and 40 °C/min for the alloys).

Specialized two-stage tracer oxidation experiments were performed using the setup in Figure 5.1. This setup consisted of the aforementioned tube furnace and a quartz oxidation chamber connected (from right to left) to gas sources, a diaphragm vacuum pump (MD 1C; Vacuubrand Inc.; Essex, CT), a mass spectrometer (PrismaPro QMG 250 F1, 1-100 μ; Pfeiffer Vacuum GmbH; Asslar, Germany), and a bubbler filled with mineral oil. In contrast to the setup

used in the two previous chapters (Figure 3.1), this setup allowed for atmosphere exchange at high temperature by flowing gases rather than by pulling vacuum.

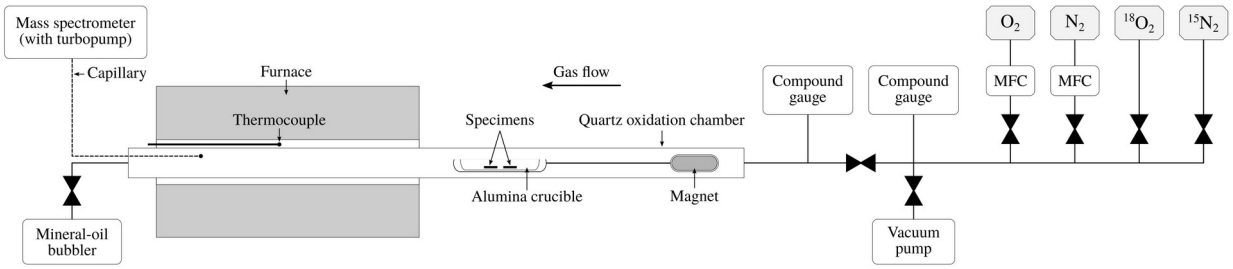

Figure 5.1: Schematic of the experimental setup for two-stage tracer oxidation experiments, based on the setup used in Figure 3.1.

For two-stage tracer oxidation experiments, specimens were oxidized first in stagnant $^{15}N_2$-20% $^{18}O_2$ (Sigma-Aldrich; St. Louis, MO) and then in flowing N_2-20% O_2. The $^{15}N_2$-20% $^{18}O_2$ atmosphere was stagnant to conserve the costly $^{15}N_2$ and $^{18}O_2$ gases. The order of the atmospheres — i.e. isotopically enriched followed by standard — was reversed compared to that in the previous two chapters to accommodate the atmosphere exchange by flowing gases (rather than by pulling vacuum) while conserving the costly isotopically enriched gases. Pure Ti was oxidized for 12 h in $^{15}N_2$-$^{18}O_2$ followed by 4 h in N_2-O_2. Both Ti-0.8Si and Ti-2Nb were oxidized for 18 h in $^{15}N_2$-$^{18}O_2$ followed by 4 h in N_2-O_2. Different durations were used for the first oxidation stage to account for differences in scale growth rates, while the same duration was used for the second stage to maximize the interpretability. Specimens were loaded into the oxidation chamber, which was evacuated using the vacuum pump and then backfilled with Ar to atmospheric pressure. This process was repeated at least three times before filling the evacuated chamber with $^{18}O_2$ to 0.2 atm and then with $^{15}N_2$ up to ambient pressure (at room temperature). After a 24 h waiting period to allow gases to thoroughly mix, the furnace was heated to 800 °C. Specimens were inserted into the hot zone and equilibrated in temperature for 8 minutes before the oxidation time was started. After the first oxidation stage was complete (12 h for pure Ti and 18 h for Ti-0.8Si and Ti-2Nb), N_2-O_2 flow (40 SCCM – 10 SCCM) was initiated. This new atmosphere stabilized within ~3 minutes. After the second oxidation stage (4 h), the specimens were removed from the hot zone and cooled to room temperature under the flowing N_2-O_2.

For all oxidation experiments, nominal gas purity was 99.999% for Ar and N_2, 99.993% for O_2, ≥ 99.00% for $^{18}O_2$, and ≥ 99.0% for $^{15}N_2$. Isotopic purity was ≥ 99.00% for $^{18}O_2$ and ≥

98.0% for $^{15}N_2$ and presumably the natural abundance for O_2 (99.76% ^{16}O) and N_2 (99.64% ^{14}N). A pre-mixed N_2-O_2 supply nominally containing 19.5-23.5% O_2 (PurityPlus Ultra Zero Air; PurityPlus; Indianapolis, IN) was used for thermogravimetric studies.

Oxidized specimens were photographed using a low-magnification Nikon AZ100 optical microscope. To characterize the bulk cross sections, specimens were mounted in low-shrinkage epoxy, polished, carbon coated, and imaged using a Thermo Fisher Scientific Helios 650 Nanolab FIB-SEM. This FIB-SEM was also used to prepare cross-sectional lamellae and APT tips. FIB damage was minimized by depositing a protective Pt cap on the region of interest before milling and by using a final low-voltage (5 kV) cleaning step. Cross-sectional lamellae were characterized with TEM, STEM, and EDS using a Thermo Fisher Scientific Talos F200X G2 operating at 200 kV. Net-intensity EDS maps and compositional estimates were generated using Velox 3.1, as discussed in more detail in the Appendix, Section 5.6.2.

Using bulk cross sections, oxygen concentration versus depth in the metal was characterized using WDS in a Cameca SX100 EPMA operating at 15 kV, 40 nA. Probe For EPMA (Probe Software, Inc.; Eugene, OR) was used to quantify X-rays for Ti, O, Si, and Nb (Kα for Ti, O, and Si; Lα for Nb), with O Kα corrected after [88] to account for interference from Ti Lβ. Two profiles were collected for each specimen, spatially calibrated for angle and offset to the oxide-substrate interface, and combined into a single dataset. Points with O concentration values outside of physical ranges were discarded. O concentration values below the detection limit (about 0.1-0.2 wt.% or, in pure Ti, 0.3 at.%) were set to zero.

Lamella from tracer-oxidized Ti, Ti-0.8Si, and Ti-2Nb were characterized with nanoSIMS using a Cameca NanoSIMS 50. $^{16}O^-$, $^{18}O^-$, $^{12}C^{14}N^-$, and $^{12}C^{15}N^-$ ions were measured concurrently using a ~50 nm, 0.2 pA focused Cs^+ beam at a mass-resolving power of ~7000 (corrected after [89]). N was detected as CN^-, which relied on residual surface C, because N does not yield sufficient N^- (or N^+) counts. Samples were sputtered to a depth of ~50 nm before data were collected, resulting in negligible background CN^- counts. TiN^- did not yield sufficient counts. Isotope maps were generated using L'image (Carnegie Institution of Washington; Washington, DC) [90].

APT was used to characterize the oxide formed on Ti-0.8Si, the oxide formed on tracer-oxidized Ti-0.8Si, and the region near the nitride-metal interface in tracer-oxidized Ti-2Nb. Specimens were analyzed using a Cameca LEAP 5000 HR operating in laser-assisted mode with auto pulse-rate control. Detection rate was either fixed or controlled by constant field. Specific

analysis parameters for each dataset are listed in Table 5.1 in the Appendix. Cameca AP Suite version 6.1.0.35 was used to reconstruct and visualize the data. Reconstructions were created using the default image compression factor of 1.65 and k factor of 3.3, an evaporation field of 32 V/nm for oxide tips and 26 V/nm for nitride or metal tips, and radius evolution by fixed shank or tip profile, using measurements from SEM images. AtomProbeLab version 0.2.4 [91] was used to select appropriate ions and to accurately quantify composition, as described in more detail in the Appendix, Section 5.6.1.

5.3 Results

Mass gains and rate exponents differed between pure Ti, Ti-2Nb, and Ti-0.8Si. As shown in Figure 5.2, the overall mass gain after 100 h was greatest for pure Ti (~14 mg/cm^2) and significantly lower for Ti-2Nb (~3 mg/cm^2) and Ti-0.8Si (~2 mg/cm^2). Mass gain data were fitted to Equation 4. The oxidation rate exponent was approximately linear for pure Ti (m ~ 1.2), between parabolic and cubic for Ti-2Nb (m ~ 2.6), and parabolic for Ti-0.8Si (m ~ 2.0).

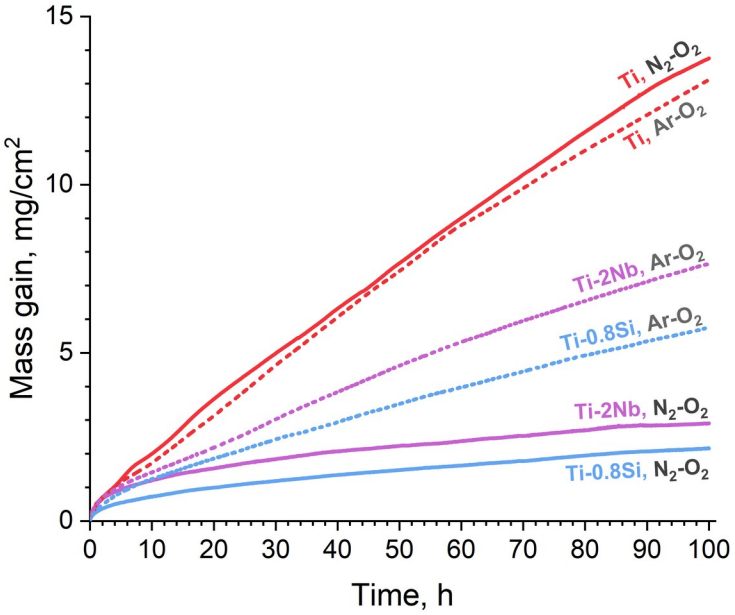

Figure 5.2: Mass gains for pure Ti, Ti-2Nb, and Ti-0.8Si oxidized isothermally at 800 °C in N_2-20% O_2 (solid lines) or in Ar-20% O_2 (dashed lines, reproduced from the two previous chapters).

Optically, the oxidized specimens appeared relatively smooth and uniform, as shown in Figure 5.3. All oxide was presumed to be rutile TiO_2, in accordance with the literature for pure Ti [14], Ti-Si [9], [11], and Ti-Nb alloys [14], [16], [18] oxidized in air. Specimen color ranged from dark gray to white and typically varied locally to a small extent. At a given oxidation time, the color was darkest for Ti-2Nb (Figure 5.3g-i), whiter for Ti-0.8Si (Figure 5.3d-f), and whitest for pure Ti (Figure 5.3a-c). Specimen color tended towards white with increasing oxidation time.

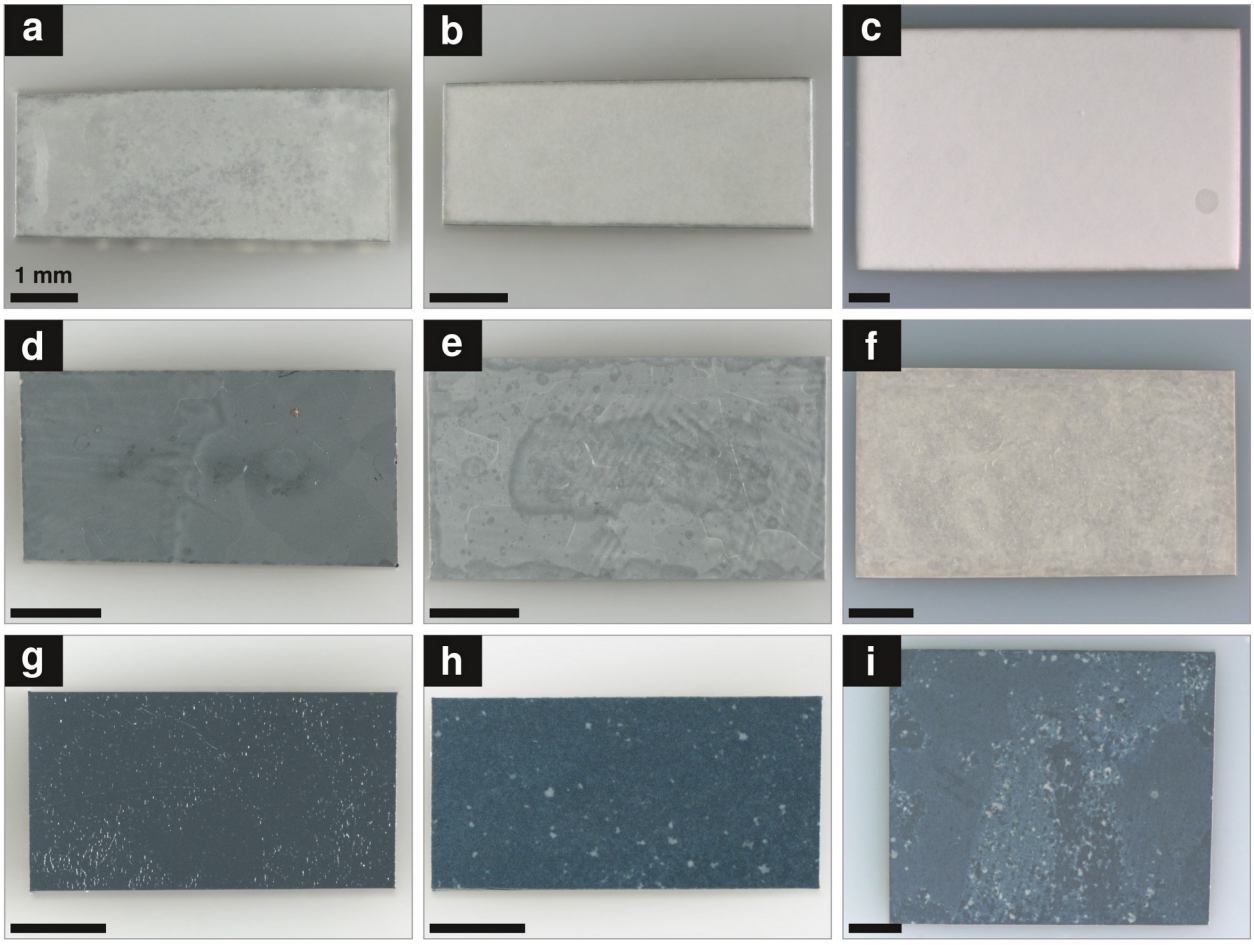

Figure 5.3: Plan-view optical images of (a-c) pure Ti, (d-f) Ti-0.8Si, and (g-i) Ti-2Nb oxidized for (a, d, g) 8 h, (b, e, h) 32 h, and (c, f, i) 100 h (800 °C, N_2-O_2). All scale bars are 1 mm.

SEM on the oxidized surfaces of Ti (Figure 5.4a-c), Ti-0.8Si (Figure 5.4d-f), and Ti-2Nb (Figure 5.4g-i) revealed distinct surface morphologies for each material. Oxide grains, which were on the order of 0.1~1 μm in size, qualitatively coarsened with time for Ti-0.8Si and Ti-2Nb, but not for pure Ti. At all times, pure Ti exhibited small equiaxed grains with pores of approximately the same size distributed across the surface. Additional plate-like protrusions, as

indicated by arrows, were first noted at 32 h (Figure 5.4b) and became more numerous at 100 h (Figure 5.4c). Ti-0.8Si exhibited smaller, loosely packed acicular grains, which coarsened most noticeably from 32 to 100 h (Figure 5.4e and Figure 5.4f). Ti-2Nb exhibited angular, shard-like grains that coarsened from 8 to 32 to 100 h (Figure 5.4g-i).

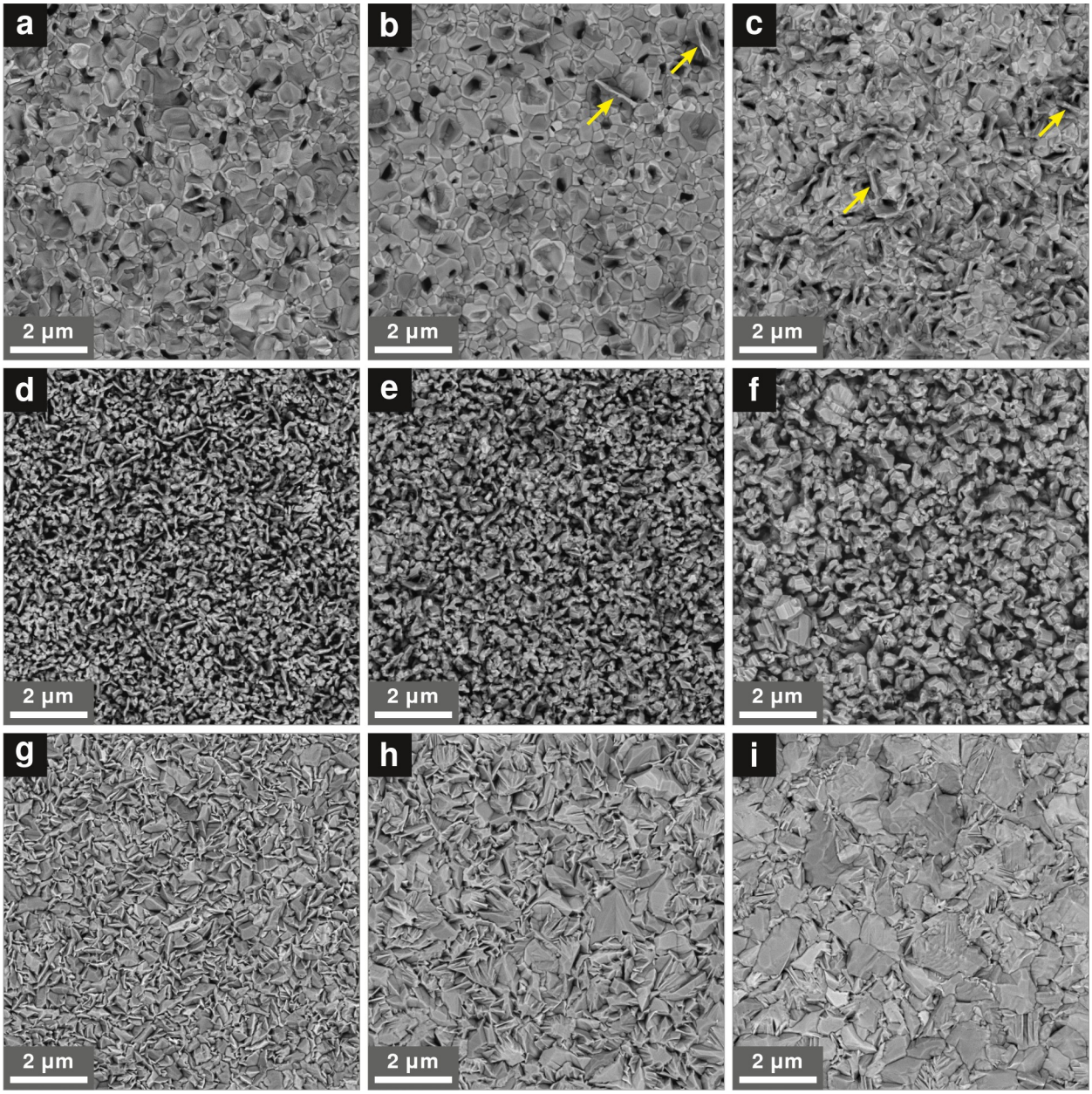

Figure 5.4: BSE-mode SEM of the surface on (a-c) pure Ti, (d-i) Ti-0.8Si, and (g-i) Ti-2Nb oxidized for (a, d, g) 8 h, (b, e, h) 32 h, and (c, f, i) 100 h. Arrows indicate plate-like protrusions.

Cross sections of samples oxidized for 8 h were examined using SEM and TEM (Figure 5.5), with local chemical analysis using STEM EDS (Figure 5.6). The oxides scales exhibited differences in thickness, layering, porosity, and chemistry. On pure Ti (Figure 5.5a), the oxide was thick (~12 μm), lamellar, and porous. Oxide grains were relatively equiaxed and ~1 μm or less in diameter. On Ti-0.8Si (Figure 5.5b), the oxide was thin (~3 μm) and compact, with two apparent layers. The outer layer (~1 μm) contained larger, columnar grains, while the inner layer (~2 μm) contained a mixture of fine (<100 nm) and coarser (~300 nm) equiaxed grains and was slightly more enriched with Si (~0.7 at.%, versus ~0.3 at.% in the outer layer). Porosity was minimal and concentrated near the oxide-substrate interface. On Ti-2Nb (Fib. 5c), the oxide was relatively thin (~5 μm) and compact with dilute Nb enrichment (~1.1 at.%). Porosity was moderate and particularly concentrated in the inner two-thirds of the oxide scale. Among the three materials, both the size and the number of pores in the oxide scale was greatest for pure Ti, intermediate for Ti-2Nb, and lowest for Ti-0.8Si.

A layer of titanium nitride(s) was observed below the oxide scale on all the materials, as shown in Figure 5.6. The nitride layer — enclosed by dashed lines in Figure 5.5) — was significantly thinner than the oxide scales and contained about 30~40 at.% N per EDS estimates. Ti_2N ($P4_2/mnm$) and TiN ($Fm\bar{3}m$) phases were identified using TEM selected-area diffraction, as shown in Figure 5.20 in the Appendix. Ti_2N was found on all materials, whereas TiN was only detected on Ti-2Nb, where it was located between the oxide and Ti_2N (i.e. the ~200 nm layer with enhanced N signal in Figure 5.6c). As for the oxide on Ti-2Nb, both nitride phases on Ti-2Nb contained Nb (~1.7 at.%). In Ti-0.8Si and Ti-2Nb, Si and Nb precipitates were observed in the nitride layer and in the metal (Figure 5.6b and Figure 5.6c).

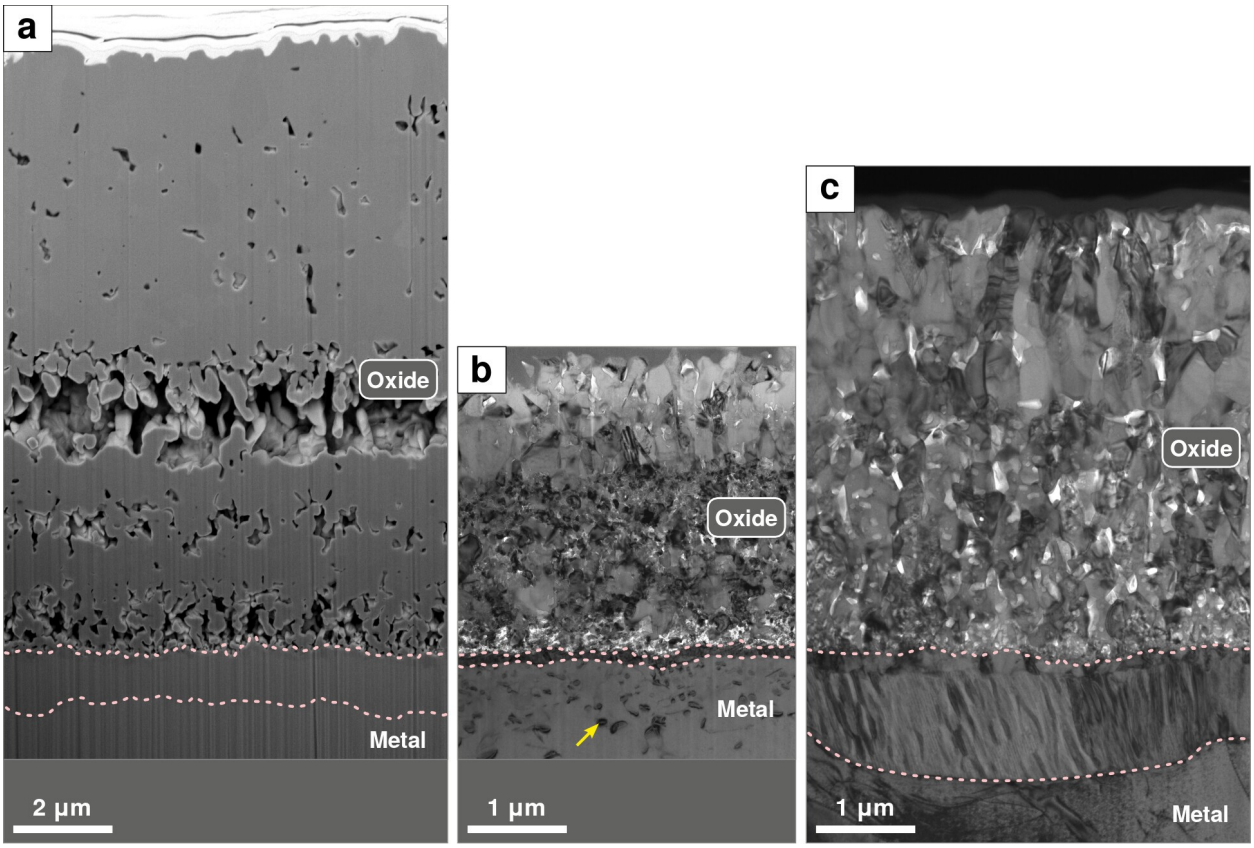

Figure 5.5: Cross sections of (a) pure Ti (b) Ti-0.8Si, and (c) Ti-2Nb oxidized for 8 h (800 °C, N_2-O_2). (a) is BSE-mode SEM, whereas (b, c) are bright-field TEM. We note that (b, c) are twice as magnified as (a). Dashed lines enclose the layer of titanium nitride(s). In (b), the yellow arrow points to a precipitate in the metal.

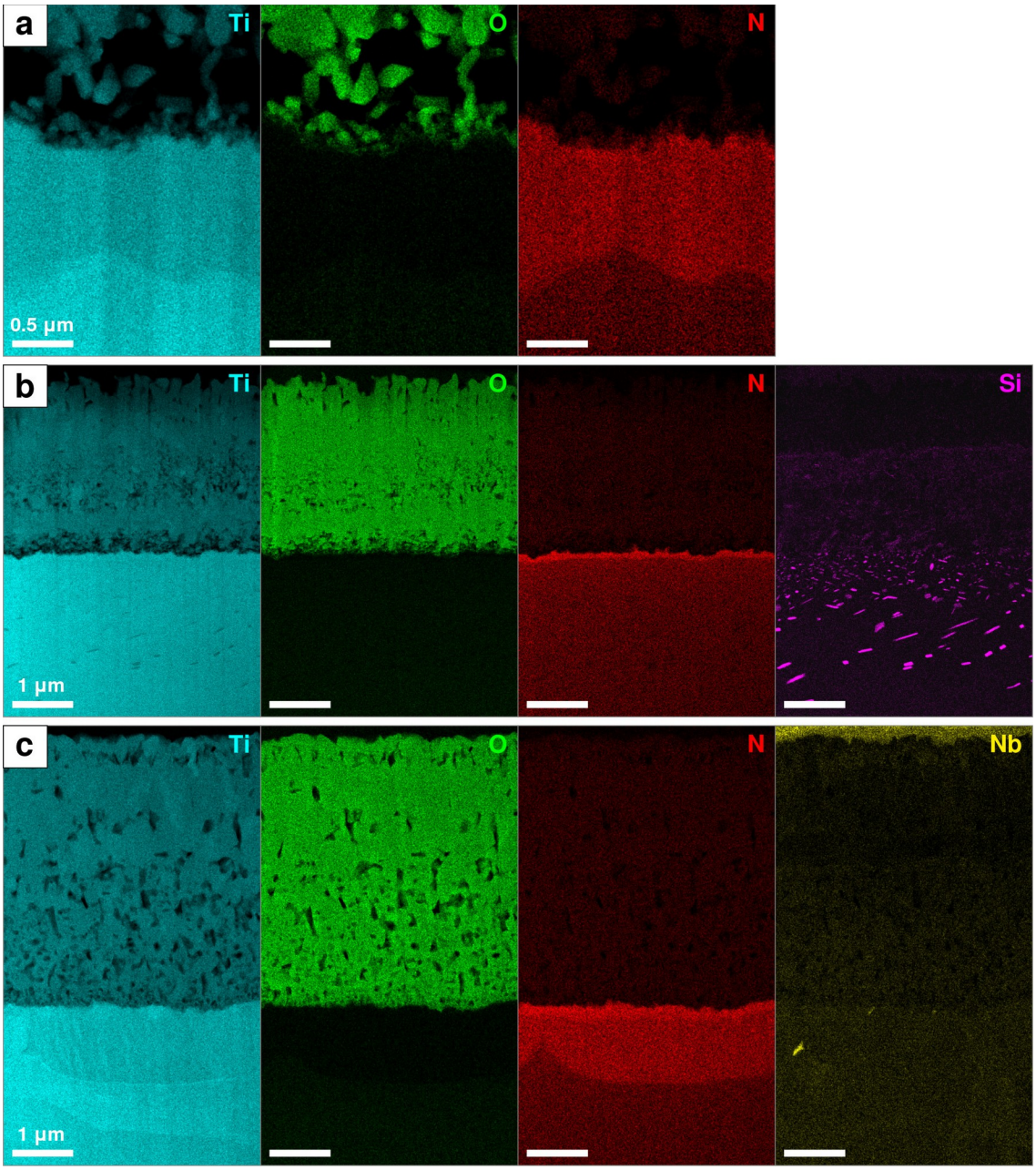

Figure 5.6: Net-intensity EDS maps on cross sections of (a) pure Ti, (b) Ti-0.8Si, and (c) Ti-2Nb oxidized for 8 h (800 °C, N_2-O_2). (a) shows only the oxide-substrate interface, whereas (b, c) show the full thickness of the oxide. In (b), contrast in the Si map was increased to better show dilute Si enrichment in the inner layer of oxide.

To investigate the evolution of the early microstructure with longer oxidation time, polished cross sections of pure Ti, Ti-0.8Si, and Ti-2Nb oxidized for 100 h were characterized using SEM (Figure 5.6). While oxide scale morphology was similar to that at 8 h (Figure 5.5), differences in the oxide thickness at specimen corners and differences in the nitride layer were

noted among materials. The oxide scale was thick (~80 μm) and lamellar on pure Ti (Figure 5.6a) but thin (~10 μm) and compact on Ti-0.8Si (Figure 5.6b) and Ti-2Nb (Figure 5.6c). Pores in the oxide were large and interconnected for pure Ti, intermediate in size for Ti-2Nb, and very fine and numerous for Ti-0.8Si. For all materials, the pores appeared to exhibit some layering. The oxide scale morphology differed at specimen corners only for pure Ti (Figure 5.6b) — where the scale was thinner and dense — but not for Ti-0.8Si (Figure 5.6d) or Ti-2Nb (Figure 5.6f). All the materials exhibited a nitride layer (bounded by a dashed line in Figure 5.6) below the oxide scale. This layer was presumed to correspond predominantly to Ti_2N. On pure Ti, the nitride layer was infrequently observed and otherwise thin (~2 μm or less). In contrast, the nitride layer on Ti-0.8Si and on Ti-2Nb was typically evident and thicker (up to ~5 μm), with thickness varying locally despite the apparently uniform overlying oxide scale.

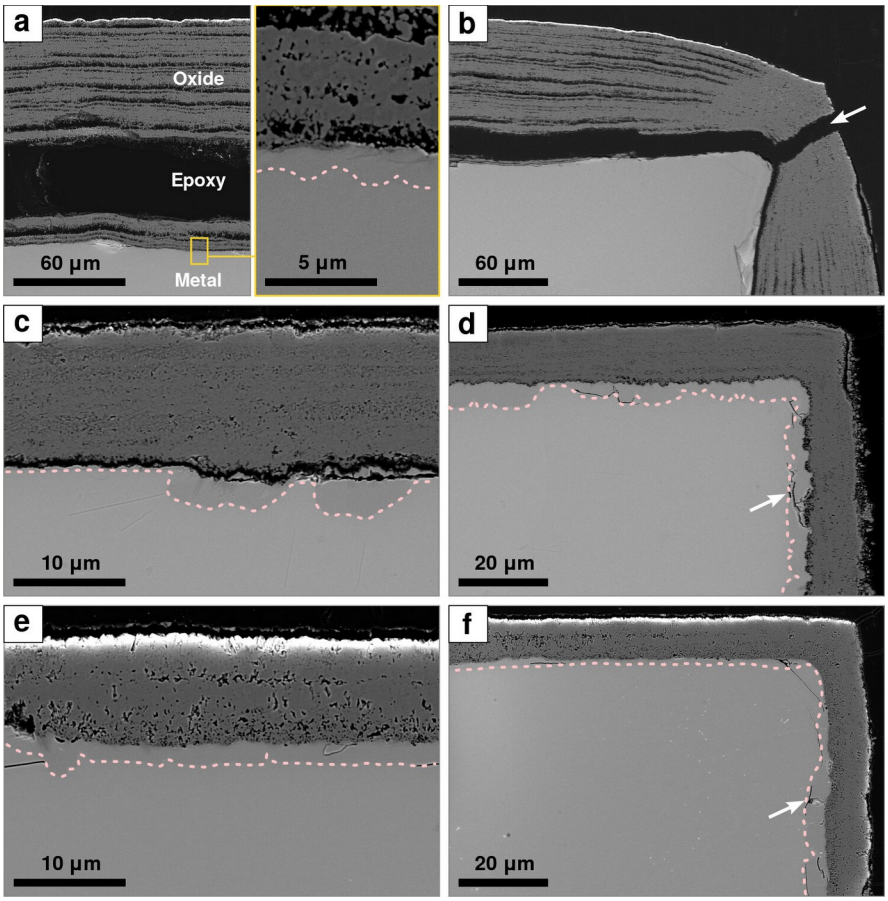

Figure 5.7: BSE-mode SEM of polished cross sections of (a, b) pure Ti, (c, d) Ti-0.8Si, and (e, f) Ti-2Nb oxidized for 100 h (800 °C, N_2-O_2). The microstructure is shown in areas located centrally on the specimen surface (a, c, e) and near the corners (b, d, f). The dashed line marks the interface between the nitride layer and the metal. In (b, d, f), arrows point to examples of damage presumably caused by metallographic preparation.

To assess the contribution of oxygen dissolved in the metal to the mass gains, O concentrations in the metal were measured on polished cross sections (Figure 5.8). Unique trends in O concentrations with time were noted in pure Ti compared to Ti-0.8Si and Ti-2Nb. Initially, at 8 h, O concentrations were similar in all the materials: 11~12 at.% near the surface and approaching zero about 60 µm into the metal. With increasing oxidation time, O concentration near the surface increased in pure Ti (to ~23 at.% at 32 h and 100 h) *but* remained low in Ti-0.8Si and Ti-2Nb. The thickness of the nitride layer did not appear to influence O concentrations at 100 h, as confirmed by additional measurements described in the Appendix, Section 5.6.3.

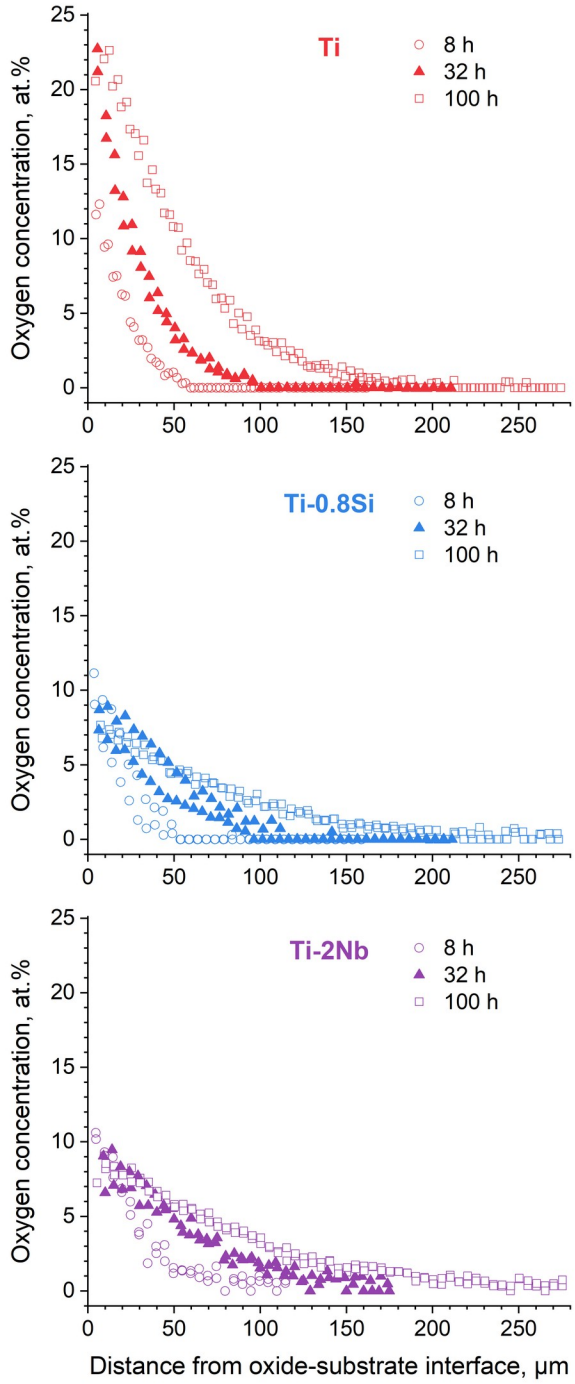

Figure 5.8: WDS measurements of oxygen concentrations in the metal for pure Ti, Ti-0.8Si, and Ti-2Nb oxidized for 8 h, 32 h, and 100 h (800 °C, N_2-O_2).

To further assess oxygen and nitrogen concentrations in the metal very close to the surface, O and N concentration profiles were estimated from STEM-EDS maps of cross-sectional lamellae, as shown in Figure 5.8. Data quantification is discussed in the Appendix,

Section 5.6.2. Initially, at 8 h, all the materials exhibited similar O concentration profiles and similar N concentration profiles (Figure 5.8a). O concentration was ~10 at.% at the nitride-metal interface and gradually *increased* with depth in the metal. In contrast, N concentration was higher (12~17 at.%) at the nitride-metal and gradually *decreased* with depth into the metal. With increasing oxidation time, the absolute concentrations at the interface and the trends changed for pure Ti but not for Ti-0.8Si (Figure 5.8b). Pure Ti at 100 h had high O (~30 at.%) and low N (3~6 at.%) concentrations at the interface and throughout the metal, giving flat concentration profiles over a distance of ~2 μm. In contrast, from 8 h to 32 h, Ti-0.8Si maintained similar O and N concentrations at the interface and the same trends in O and N in the metal, but with shallower concentration gradients. We note that the behavior in the metal discussed for Ti-0.8Si was also validated using APT, as discussed in the Appendix, Section 5.6.4.

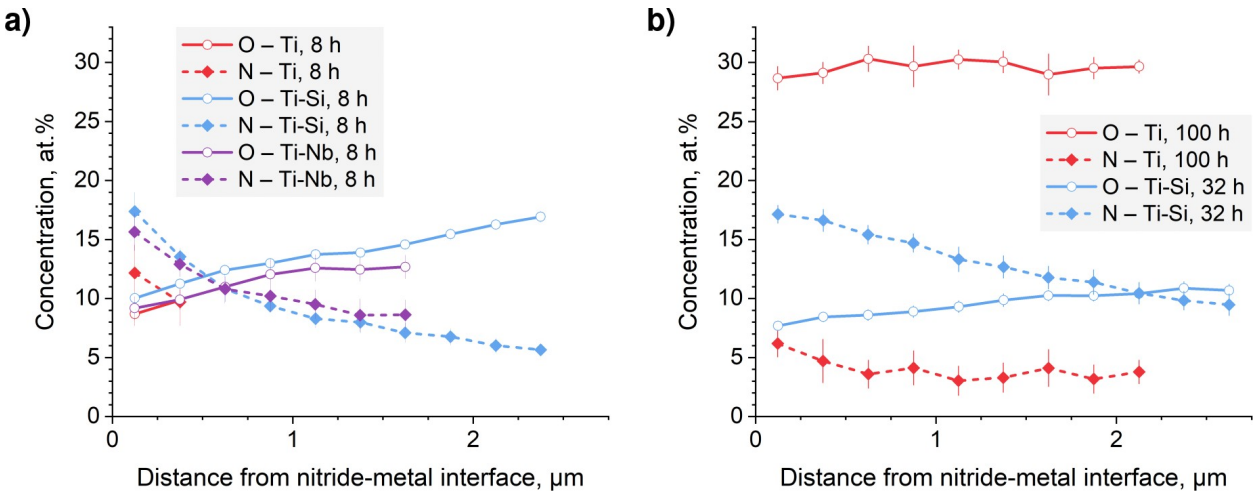

Figure 5.9: STEM-EDS concentration profiles of oxygen and nitrogen dissolved in the metal for (a) pure Ti, Ti-0.8Si, and Ti-2Nb oxidized for 8 h and (b) pure Ti and Ti-0.8Si oxidized, respectively, for 100 h and 32 h (800 °C, N_2-O_2). To reduce noise, data points were binned; plotted points and error bars indicate the average values and standard deviations, respectively.

The growth mechanisms of the oxide and nitride layer with time were investigated using two-stage tracer oxidation experiments. Cross sections were analyzed using nanoSIMS, as shown in Figure 5.9. Because the oxide scale on pure Ti was very thick and delaminated, only the bottommost portion was retained for nanoSIMS (Figure 5.9a-c). In contrast, the entire oxide scale was retained for Ti-0.8Si (Figure 5.9d-f) and Ti-2Nb (Figure 5.9g-i). Differences in local enrichment of ^{16}O and ^{14}N — assumed to originate from the second oxidation stage — were noted among the samples. For comparison purposes, we define *^{16}O isotopic concentration* as

$^{16}O/(^{16}O + ^{18}O)$ and *^{14}N isotopic concentration* as $^{14}N/(^{14}N + ^{15}N)$. These isotopic concentrations along profiles *a*, *d,* and *g* — i.e. through the oxidized microstructures — are plotted in Figure 5.9j. In the oxide scales, ^{16}O enrichment was most extensive for pure Ti as compared to the alloys. As shown in Figure 5.9b, the oxide on pure Ti showed high ^{16}O concentrations (50~90%) in a ~4 μm band along the bottom and in a ~1 μm band with irregular thickness near the top. Between these two layers, the distribution of ^{16}O enrichment matched with oxide grain boundaries (as indicated by the yellow arrow). For Ti-0.8Si (Figure 5.9e), ^{16}O isotopic concentration was greatest along the top of the oxide scale and progressively decreased toward the bottom of the oxide scale. In contrast to Ti-0.8Si, Ti-2Nb (Figure 5.9h) exhibited a thin top layer of nearly pure ^{16}O (~95% over 500 nm) with a more gradual decline in ^{16}O concentration toward the bottom of the oxide scale. In all the oxide scales, the minimum baseline ^{16}O concentration was similar at 10~15%. In the nitride layer, the ^{14}N distribution differed for each material. For pure Ti (Figure 5.9c), the nitride layer was highly enriched with ^{14}N (80~90%), with limited patches exhibiting lower concentration (~50%). For Ti-0.8Si (Figure 5.9f), the maximum ^{14}N concentration was moderate at ~65%, and the top of the thick nitride was more strongly enriched than bottom portions. In Ti-2Nb (Figure 5.9i), estimated ^{14}N concentration was low at <20%. In the metal, all materials exhibited similar ^{16}O isotopic concentration (60~80%).

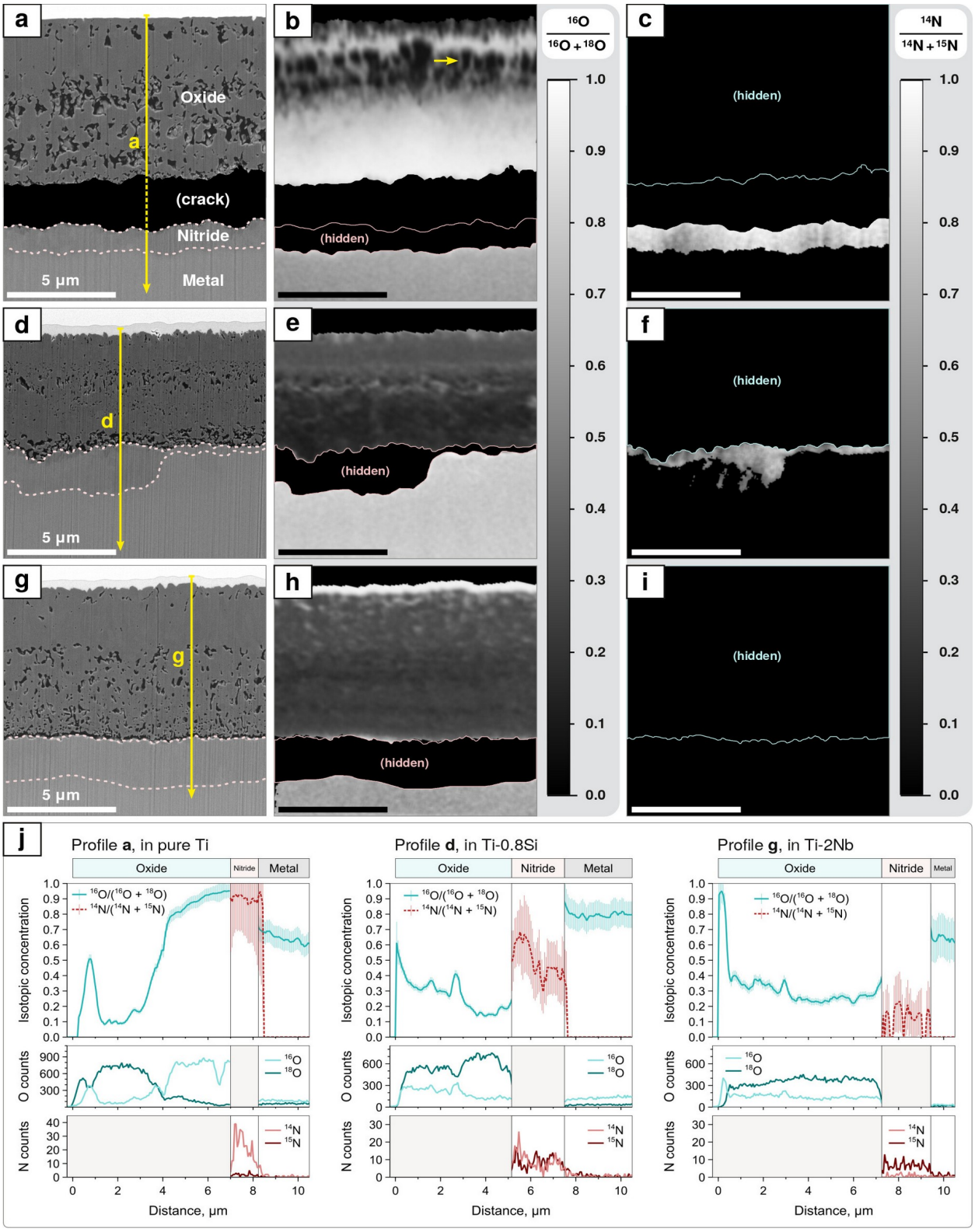

Figure 5.10: BSE-mode SEM with corresponding nanoSIMS maps of cross sections of (a-c) pure Ti, (d-f) Ti-0.8Si, and (g-i) Ti-2Nb oxidized in two stages, first in $^{15}N_2$-$^{18}O_2$ and then in N_2-O_2 (800 °C). The first stage was 12 h for pure Ti and 18 h for Ti-0.8Si and Ti-2Nb, while the second stage was 4 h for all the materials. To highlight species assumed to originate from the second

oxidation stage, nanoSIMS maps show ^{16}O isotopic concentration (b, e, h) and ^{14}N isotopic concentration (c, f, i). Isotopic concentrations and raw counts along profiles *a*, *d*, and *g* — i.e. through the oxidized microstructures — are plotted in (j). In SEM (a, d, g), dashed lines enclose the nitride layer. We note that, for pure Ti (a-c), only the bottommost portion of the oxide was retained. Certain areas are hidden from view in SEM and/or nanoSIMS maps as appropriate: the nitride layer in the isotopic ^{16}O concentration maps (b, e, h), and the oxide scale in the isotopic ^{14}N concentration maps (c, f, i). In (b), the yellow arrow points to ^{16}O enrichment along an oxide grain boundary. Additional nanoSIMS maps are provided in the Appendix, Figure 5.19.

APT was used to better understand the distribution of Si and O isotopes in the oxide formed on Ti-0.8Si, particularly at the oxide grain boundaries (Figure 5.11). Analyses were performed near the top of the oxide, within or just below the outer, Si-poor layer of oxide (as shown in EDS, Figure 5.6). The measured oxide composition agreed with the stoichiometry of TiO_2. Si was observed to segregate along grain boundaries and to form precipitates within grains (Figure 5.11a). In an analysis from a tracer-oxidized sample (Figure 5.11b), ^{16}O from the second oxidation stage was concentrated along the oxide grain boundary but also elevated throughout the oxide, with an ^{16}O isotopic concentration of ~ 40% at the grain boundary and baseline value of 24~26% in the bulk, in agreement with the nanoSIMS measurements. We note that the lack of clear ^{16}O enrichment at oxide grain boundaries in nanoSIMS maps (Figure 5.9) for Ti-0.8Si and Ti-2Nb, in contrast to pure Ti and despite being confirmed in APT (Figure 5.11b), simply reflected the small oxide grain size along with the limited spatial resolution of the nanoSIMS measurements.

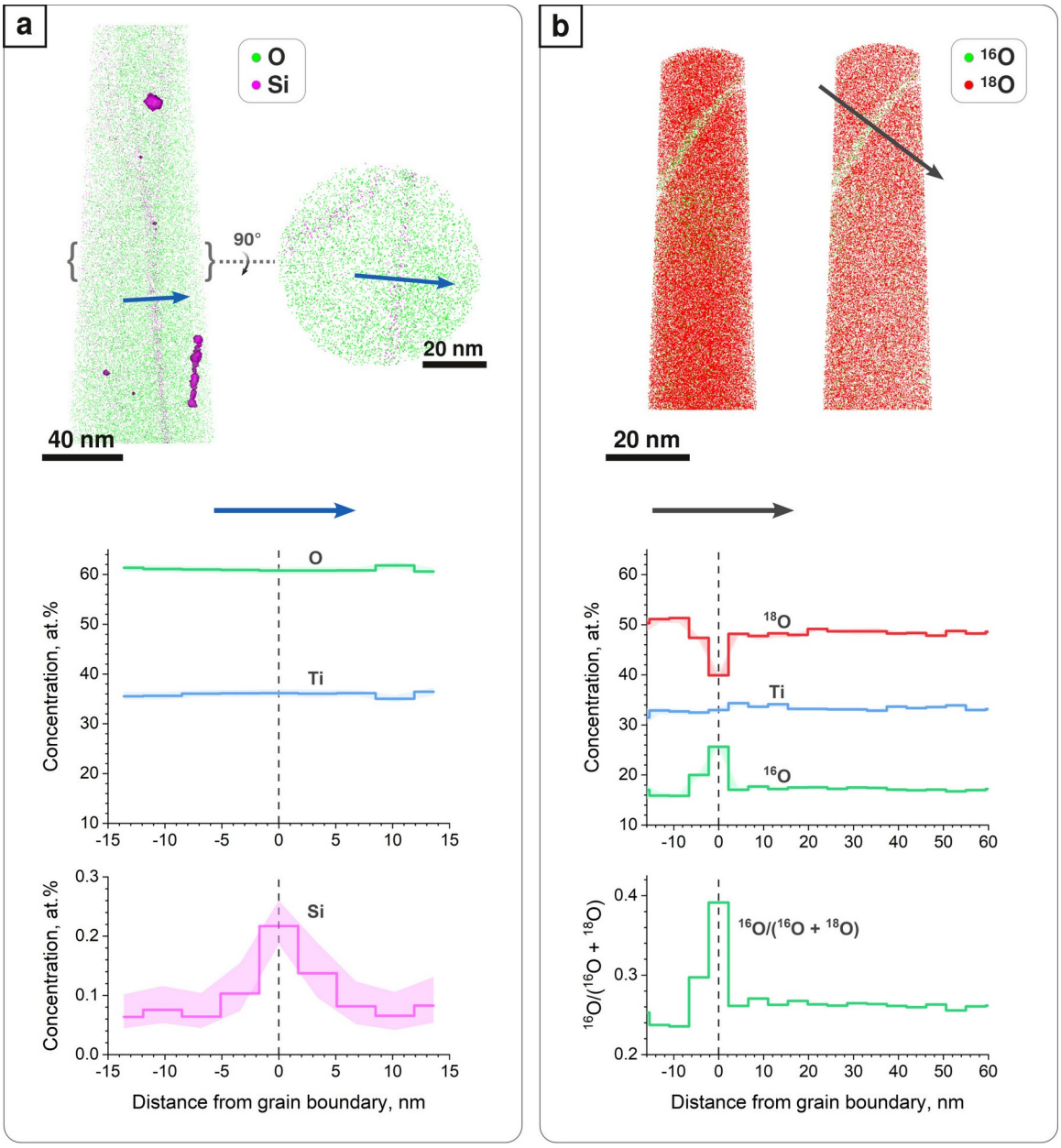

Figure 5.11: APT reconstruction with corresponding concentration profiles across a grain boundary in the TiO_2 formed on (a) Ti-0.8Si oxidized for 8 h in N_2-O_2 and (b) Ti-0.8Si oxidized for 18 h in $^{15}N_2$-$^{18}O_2$ followed by 4 h in N_2-O_2 (800 °C). In (a), the 3D reconstruction (top left) and circular slice (top right) show O (O^+ at 16.0 Da) and Si (SiO^+ at 44.0 Da and SiO_2^+ at 60.0 Da) ions; Si-rich precipitates are enclosed in pink isosurfaces. The circular slice in (a) corresponds to the (20 nm thick) volume enclosed by curly braces, with a 90° rotation toward the page to give a top view. In (b), the 3D reconstruction (top left) and 10 nm thick slice (top right) show ^{16}O ($^{16}O^+$ at 16.0 Da) and ^{18}O ($^{18}O^+$ at 18.0 Da and $^{18}O_2^+$ at 36.0 Da) ions. Ti ions are not shown for clarity. Arrows denote the position and direction of the plotted concentration profiles (bottom). In concentration profiles, step width corresponds to the thickness of volumetric slices used to generate the profile, and shading indicates the 95% confidence interval. Additional details on APT data processing and relevant mass spectra (Figure 5.14 and Figure 5.15) are in the Appendix, Section 5.6.1.

To explore the transport of O and N in the nitride and the metal, APT analyses were performed on the Ti_2N nitride phase and on the metal located within approximately 1 μm of the nitride-metal interface in tracer-oxidized Ti-2Nb (Figure 5.12). The reconstructions (not shown) were featureless. The nitride composition (Figure 5.12a) approximately matched the stoichiometry of Ti_2N, with small amounts of O (~2 at.%) and Nb (~1 at.%), while the metal (Figure 5.12b) contained about 10 at.% N, 6.5 at.% O, and 2 at.% Nb. In the nitride, the O concentration gradually decreased with depth, mainly due to the decrease in the ^{16}O concentration (Figure 5.12a). In the metal, the ^{16}O isotopic concentration was lower and also gradually decreased with depth (Figure 5.12d). ^{14}N isotopic concentration was low in both phases, ~2% in the nitride (Figure 5.12c) and ~1% in the metal (Figure 5.12d), without any notable trends with depth. The low values for ^{14}N isotopic concentration in the nitride agreed with nanoSIMS (Figure 5.9i). However, the values for ^{16}O isotopic concentration in the metal (~20%) were much lower than those obtained using nanoSIMS (60~80%). Therefore, the high ^{16}O concentrations detected using nanoSIMS may be an artifact from contamination of the lamellae with atmospheric oxygen.

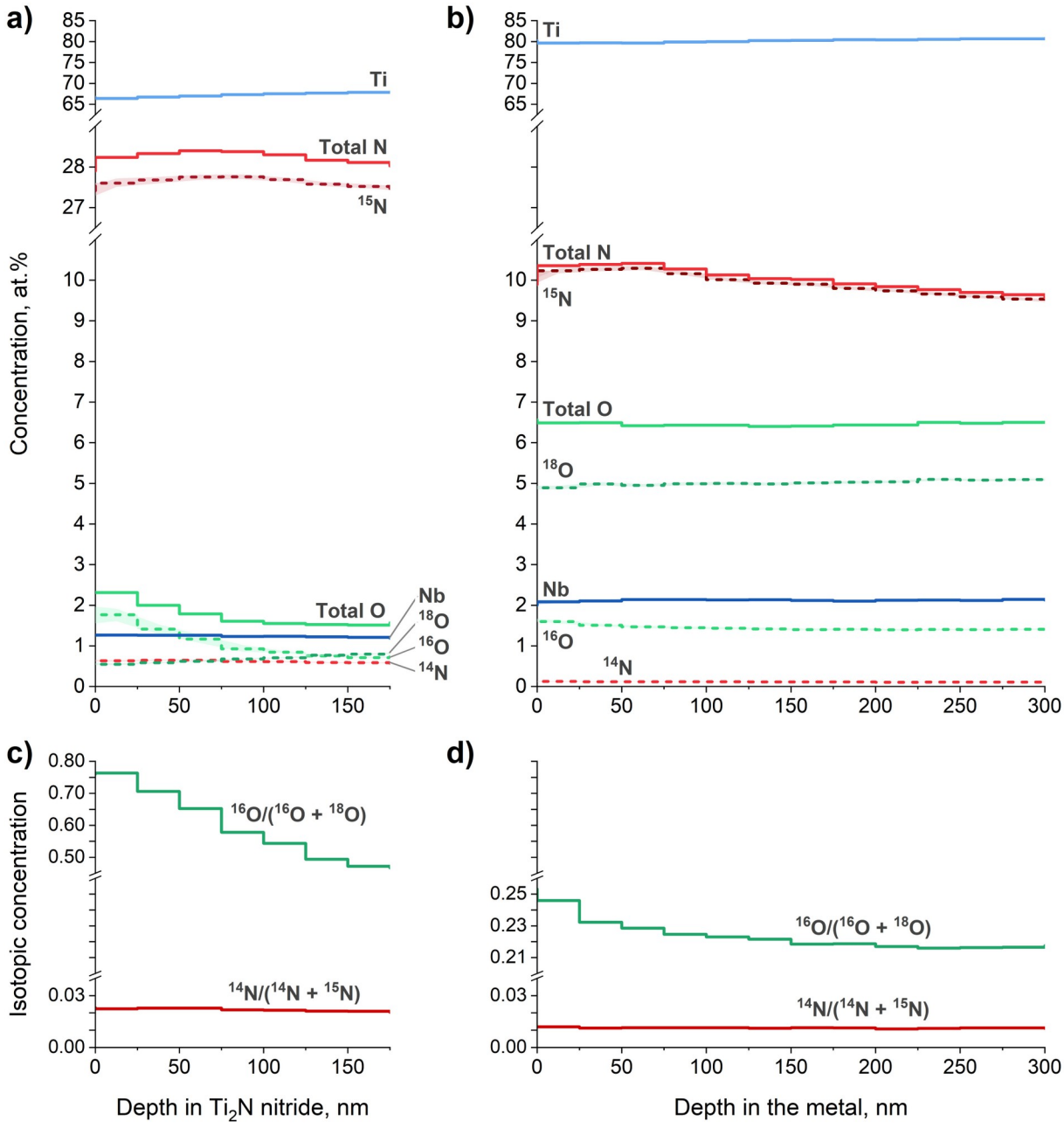

Figure 5.12: Compositional profiles as a function of depth obtained from APT analyses in the Ti_2N nitride (a, c) and metal (b, d) at approximately 1 µm from the nitride-metal interface in Ti-2Nb oxidized for 18 h in $^{15}N_2$-$^{18}O_2$ followed by 4 h in N_2-O_2 (800 °C). Step width corresponds to the thickness of volumetric slices used to generate the profiles, and shading indicates the 95% confidence interval. Additional details on APT data processing and relevant mass spectra (Figure 5.16 and Figure 5.17) are in the Appendix, Section 5.6.1.

5.4 Discussion

Since the oxidation behavior of pure Ti, Ti-0.8Si, and Ti-2Nb at 800 °C in Ar-20% O_2 and the effects of Si and Nb were described in the two previous chapters, this discussion focuses on the effects imparted by N_2 present in the oxidizing atmosphere. In general, the oxidation of the three materials in N_2-20% O_2 is similar to the oxidation in Ar-20% O_2 in that it entails growth of oxide scale and dissolution of oxygen in the metal. However, nitrogen brings the addition of a nitride layer at the oxide-metal interface and nitrogen dissolution in the metal.

Nitrogen did not impact the overall oxidation response or oxidation kinetics of pure Ti, as behavior was similar in N_2-O_2 and Ar-O_2. This null effect of nitrogen on the kinetics of pure Ti oxidized at 800 °C for up to 100 h is consistent with prior observations [14], [15]. The oxidation kinetics at long times are dominated by rapid repetitive growth and detachment of oxide layers, which forms a lamellar scale, regardless of the oxidizing environment. After 100 h in N_2-O_2, oxygen fixed in the oxide and in the metal, respectively, constituted ~85% and ~15% of the total mass gain, with essentially no contributions from nitrogen. In Ar-O_2, the contributions from oxygen were similar, with ~80% of oxygen fixed in the oxide and ~20% in the metal.

In contrast, nitrogen had a strong influence on the oxidation behavior of the Ti-0.8Si and Ti-2Nb alloys, confirming its beneficial synergistic effect with alloying elements. The alloys had reduced oxidation kinetics in N_2-O_2 versus Ar-O_2 (Figure 5.2), coming from reduced oxygen dissolution in the metal and from reduced scale thicknesses over long-term oxidation. Critically, the oxide scales formed on the alloys in N_2-O_2 remain compact both at thicknesses for which they would be lamellar in Ar-O_2 and over extended oxidation times. The parabolic oxidation rate of Ti-0.8Si and near-parabolic rate of Ti-2Nb were consistent with the compact, slow-growing oxide scales. Long-term mass gains in the alloys were dominated by contributions from oxygen, as noted for pure Ti. However, whereas nitrogen had essentially no contributions to mass gain in pure Ti, nitrogen (mostly in the nitrides) had small but non-negligible contributions to mass gains in the alloys, contributing up to ~12% of total mass gains at 100 h. These contributions of nitrogen compare favorably with recent measurements by Optasanu et al. [26].

The suppression of lamellar scale growth on the alloys in N_2-O_2 but not Ar-O_2 is probably related to differences in the accumulation of mechanical stresses in the oxidized microstructures, particularly since stress is thought to play a role in forming the lamellar oxide scale on pure Ti [5], [7], [72], [75]. Stress accumulation can be influenced by many parameters, including the

scale thickness, oxidation rate, scale growth directions, the substrate and its mechanical properties, and the scale or substrate microstructures [108]. Previous studies on unalloyed Ti [109] and various Ti-Al, Ti-Cr, and Ti-Si alloys [110] showed that atmospheric nitrogen always improved scale adherence. Here, the controlling mechanisms remain unclear. However, two factors potentially contributing to reducing stress accumulation for the alloys during oxidation in N_2-O_2 versus Ar-O_2 include the greatly reduced grain sizes in the initially forming oxide scales and the reduced O concentrations in the metal. While further work is needed to understand how nitrogen contributes to reducing grain sizes in the scale and suppressing lamellar scale growth, we now discuss the impact of nitrogen on oxygen ingress in the metal.

The presumed slow diffusion of nitrogen in the metal compared to its diffusion through the oxide scale enabled its accumulation at the oxide-metal interface, leading to the formation of a nitride layer. Titanium nitrides can be thermodynamically stable at these conditions, as shown in the ternary Ti-N-O phase diagram (Figure 5.12a). In contrast to prior claims that oxynitrides (not detected here) or nitrides are diffusion barriers for O [14], [20], [22], [23], [25], [26]), we find that nitrogen in the metal plays a key role in limiting oxygen in the metal. Additionally, this role is the *same* in all the materials. Because nitrogen diffuses in the metal more slowly than oxygen, nitrogen remains confined to a much narrower region of the metal below the nitride layer ($D_N/D_O \sim 1/300$ in α Ti at 800 °C [68], [69]). The presence of N in the metal thermodynamically limits the O concentration in the metal near the nitride-metal interface, with the limited combined N and O solubility presumably arising from N and O competing for interstitial sites. The reduction in O surface concentration controlled by nitrogen ultimately reduces O concentrations throughout the metal. We qualitatively reproduced the observed trends in N and O concentrations in the metal using Thermo-Calc, as shown in Figure 5.12b. The uphill diffusion of O in the presence of a concentration gradient of N is confirmed. Overall O penetration depth is unaffected by the presence of N, confirming that nitrogen does not impact the diffusivity of oxygen in the metal. As in our previous experiments in Ar-O_2, estimated O diffusivities in the metal are on the order of 1×10^{-14} m^2/s for all the materials. O diffusivities were estimated by fitting O concentration profiles in Figure 5.8 (ignoring the thin layer of N-enriched metal not captured using WDS) to Equation 5.

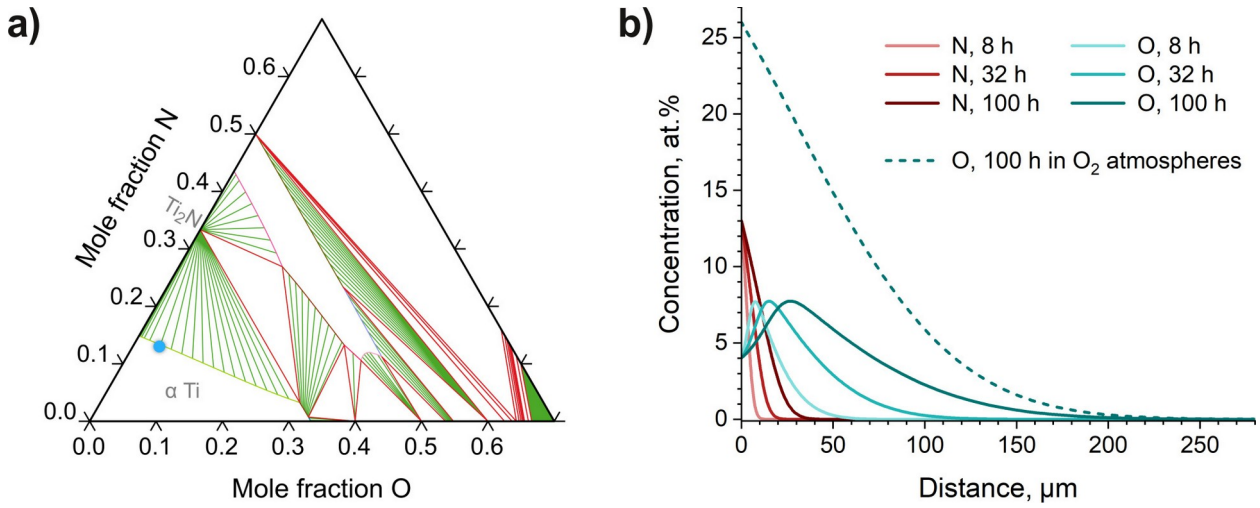

Figure 5.13: (a) ternary Ti-N-O phase diagram (800 °C, 1 atm) and (b) simulation of nitrogen and/or oxygen diffusion in the α-Ti metal at 800 °C, produced using Thermo-Calc 2023b with TCTI5.1 and MOBTI4.1 databases. In (b), solid lines depict simultaneous diffusion of nitrogen and oxygen after 8 h, 32 h, and 100 h. The surface concentration was fixed at 13 at.% N and 4 at. % O. This composition, marked by the blue dot in (a), falls within the α-Ti region near the phase boundary between α Ti and α Ti + Ti_2N and agreed reasonably with experimental measurements (e.g. 10.5 at.% N and 6.5 at.% O from APT on Ti-2Nb, Figure 5.12b). For comparison to the behavior of oxygen in O_2 atmospheres, in (b), the dashed line shows diffusion of oxygen alone after 100 h, with the surface concentration fixed at 26 at.%.

In contrast with recent suggestions in the literature that alloying elements (e.g. *Si*, *Nb*, Al, Mo, Sn, and/or Zr) influence N and O solubility in the metal [107], we find that Si and Nb did not significantly influence the solubilities or diffusivities of N and O in the metal, per the similar initial N and O metal concentrations in all the materials (Figure 5.8a). Instead, we propose that alloying impacts diffusivities of N and O in the oxide scales and nitrides, which may contribute to the varying nitride layer thicknesses noted in the present study for Ti-0.8Si and Ti-2Nb (Figure 5.6) and reported in the literature (e.g. in [23]). As previously noted for oxidation in Ar-O_2, inward O transport in TiO_2 primarily takes place along grain boundaries, as supported by the present nanoSIMS and APT data, and reduced oxygen transport along grain boundaries in the presence of segregating alloying elements such as Si and Nb is hypothesized. However, lattice O transport also appears to be enhanced in the presence of nitrogen given the high baseline second-stage O isotopic concentration in the bulk oxide (10~25%) compared to oxidation in Ar-O_2 (≤2%, Figure 3.10 and Figure 4.9). While the mechanistic link between nitrogen and oxide transport and growth remains to be established, the microstructures of the oxide scales on Ti-0.8Si and Ti-2Nb were suggestive of both outward growth (coarse-grained, outer layer) and

inward growth (fine-grained, inner layer), with outer and inner layers having comparable thicknesses. For Ti-0.8Si, this contrasts with the behavior in Ar-O_2 where inward growth was initially inhibited by the formation of a Ti_5Si_3 silicide layer at the oxide-metal interface, which does not form during oxidation with nitrogen. The presence of Si in the inner layer of oxide on Ti-0.8Si (Figure 5.6b) also reflected the inward growth mechanism, i.e. by oxidation of the substrate containing Si and Si-rich precipitates. Interestingly, for Ti-2Nb, the two-stage tracer oxidation experiment suggested that outward growth dominated (Figure 5.9h). Since accelerated inward scale growth would normally be expected with the enhanced inward O diffusion noted (in nanoSIMS and APT) but was not observed, we propose that the presence of a nitride phase that is enabled by fast nitrogen diffusion in the oxide compared to the metal limits inward oxide growth due to its slow oxidation kinetics. More work is needed to understand O and N transport through the oxide and nitrides and the thermodynamic and kinetic aspects of oxidation at the oxide-nitride interface.

In summary, the present study spotlights the beneficial role of nitrogen present in the metal near the nitride-metal interface in reducing O concentrations throughout the metal. This phenomenon presumably broadly applies to the oxidation of α-Ti alloys. Critically, this beneficial behavior requires sufficient N transport through the oxide scale and the nitrides to achieve a high N concentration in the metal (as ~4 at.% N or less will not limit O concentrations, per Figure 5.12a). We propose that alloying can enable this beneficial behavior by influencing the transport of N and O through the oxide scales and nitrides rather than by influencing the solubilities or diffusivities of N and O in the metal. In contrast to recent suggestions [107], we find that alloying elements have no influence on the behavior of N and O in the metal.

5.5 Conclusions

We investigated the oxidation of pure Ti, Ti-0.8Si, and Ti-2Nb at 800 °C in N_2-20% O_2 or in sequential isotopically labeled N_2-20% O_2 atmospheres to clarify how nitrogen influences the oxidation mechanisms of titanium and titanium alloys. For these conditions, the main conclusions are as follows:

1. The oxidation of the three materials in N_2-O_2 is similar to the oxidation in Ar-O_2 in that it entails growth of oxide scale and dissolution of oxygen in the metal. However, nitrogen

brings the addition of a nitride layer at the oxide-metal interface and nitrogen dissolution in the metal.

2. Adding nitrogen to the oxidation atmosphere has almost no effect on the oxidation rate of pure Ti but greatly reduces the oxidation rates of the Ti-0.8Si and Ti-2Nb alloys.
3. For the alloys, the reduced oxidation rates in N_2-O_2 compared to Ar-O_2 initially come from reduced oxygen dissolution in the metal. At longer oxidation times, reduced scale thicknesses also contribute and become the dominant factor in reducing the mass gains.
4. For the alloys, nitrogen completely suppresses the formation of lamellar oxide scales for up to 100 h.
5. Si and Nb detected in the oxide and Nb detected in the nitrides likely influence the transport of one or more of the reactive species (N, O, and Ti) through those phases.
6. For all the materials, inward O transport in the compact oxide scales primarily takes place along oxide grain boundaries, with additional O transport through the lattice.
7. The presence of nitrogen in the metal near the nitride-metal interface can contribute to reducing O concentrations throughout the metal.
8. Si or Nb alloying additions do not significantly influence the behavior of N and O in the metal.

5.6 Appendix

Table 5.1: Summary of experimental analysis parameters for atom-probe tips.

				Constant Field Control			
Specimen	**Region**	**T (K)**	**Detection Rate (%)**	**Field Estimate (V/nm)**	**Target Areal Evaporation (%/μm²)**	**Laser Pulse Energy (pJ)**	**Auto Pulse-Rate Control (Da)**
Ti-0.8Si, 8h	Oxide (TiO_2)	50	0.5	-	-	60	150
Tracer-oxidized Ti-0.8Si (22 h)	Oxide (TiO_2)	50	0.25 → 0.5	-	-	50	150
Tracer-oxidized Ti-2Nb (22 h)	Ti_2N nitride	30	-	26	80	25	180
	Metal	30	-	26	70	30	150

5.6.1 APT data processing with AtomProbeLab

AtomProbeLab 0.2.4 (https://sourceforge.net/projects/atomprobelab/) was used to analyze the composition for all atom-probe tips in the present study. A similar procedure was used for all analyses. First, the isotopes definition file was modified by zeroing the ^{71}Ga abundance and — for tracer-oxidized specimens only — adding standalone ^{18}O as "Q" and standalone ^{15}N as "Nn." The *ionFitTester* function was used to explore candidate ions (with certain ions set as mandatory) and eliminate unlikely ions, as summarized in Table 5.2. The selected ions were then used when generating concentration profiles along a given direction. For analyses across grain boundaries, the profile direction was determined visually using AP Suite. Figure 5.14-5.17 show the mass spectrum for each analysis with the selected ions labeled. We note that the minor presumed contaminants H, C, and Ga were sometimes included in the final analyses but were not plotted in Figure 5.11 or Figure 5.12 for clarity and because their concentrations were very low. Similarly, standalone ^{15}N, a potentially real dopant in the oxide on tracer-oxidized Ti-0.8Si, was included in the analysis but not plotted in Figure 5.11b.

Table 5.2: Summary of ions used for compositional analysis of atom-probe tips with AtomProbeLab. Bolded ions were set as mandatory, whereas red, italicized ions were eliminated based on the results of *ionFitTester*. Ions are listed approximately in order of increasing mass-to-charge ratio, from top to bottom in each column and then from left to right. "Q" denotes standalone ^{18}O, and "Nn" denotes standalone ^{15}N.

Specimen	Region	Ions					
Ti-0.8Si, 8h	Oxide (TiO_2)	Si^{++} *N^{+}* SiH_2^{++} **O^{+}** OH^{+} OH_2^{+}	SiO_2^{+++} **Ti^{++}** *N_2^{+}* Si^{+} *SiO_2^{++}* **TiO^{++}**	**O_2^{+}** $TiOH_2^{++}$ $O_2H_2^{+}$ Ga^{++} TiO_2^{++} $Ti_2O_2^{+++}$	SiO^{+} Ti^{+} SiO_2^{+} **TiO^{+}** $TiOH^{+}$ $TiOH_2^{+}$	Ga^{+} $Ti_2O_3^{++}$ *$Ti_2O_3H^{++}$* *Ti_3^{++}* TiO_2^{+} TiO_2H^{+}	$TiO_2H_2^{+}$ Si_3^{+} TiO_3^{+}
Tracer-oxidized Ti-0.8Si (22 h)	Oxide (TiO_2)	Si^{++} *N^{+}* Nn^{+} O^{+} OQ^{++} **Q^{+}**	**Ti^{++}** Si^{+} NNn^{+} *Nn_2^{+}* TiO^{++} **TiQ^{++}**	O_2^{+} OQ^{+} **Q_2^{+}** *TiO_2^{++}* $TiOQ^{++}$ TiQ_2^{++}	SiO^{+} *SiQ^{+}* Ti^{+} TiO^{+} **TiQ^{+}** Ga^{+}	*Ti_3^{++}* $Ti_2O_3^{++}$ $Ti_2O_2Q^{++}$ $Ti_2OQ_2^{++}$ $Ti_2Q_3^{++}$ TiO_2^{+}	$TiOQ^{+}$ TiQ_2^{+} Si_3^{+} TiO_2Q^{+} $TiOQ_2^{+}$ TiQ_3^{+}
Tracer-oxidized Ti-2Nb (22 h)	Ti_2N nitride	C^{++} Nn^{++} C^{+} N^{+} *NNn^{++}* **Nn^{+}**	**Ti^{+++}** TiH^{+++} O^{+} *OQ^{++}* Q^{+} **Ti^{++}**	TiH^{++} CNn^{+} NNn^{+} Nn_2^{+} *TiN^{++}* Nb^{+++}	**$TiNn^{++}$** TiO^{++} TiQ^{++} *O_2^{+}* *OQ^{+}* Ga^{++}	*NbN^{+++}* $NbNn^{+++}$ Nb^{++} *NbN^{++}* **$NbNn^{++}$** Ga^{+}	
	Metal	C^{+} **N^{+}** *NNn^{++}* **Nn^{+}** **Ti^{+++}** TiH^{+++}	*O^{+}* *OQ^{++}* Q^{+} **Ti^{++}** TiH^{++} *NNn^{+}*	Nn_2^{+} *TiN^{++}* Nb^{+++} $TiNn^{++}$ TiO^{++} TiQ^{++}	*O_2^{+}* OQ^{+} Ga^{++} *NbN^{+++}* $NbNn^{+++}$ NbO^{+++}	NbQ^{+++} Nb^{++} NbH^{++} *NbN^{++}* **$NbNn^{++}$** NbO^{++}	NbQ^{++}

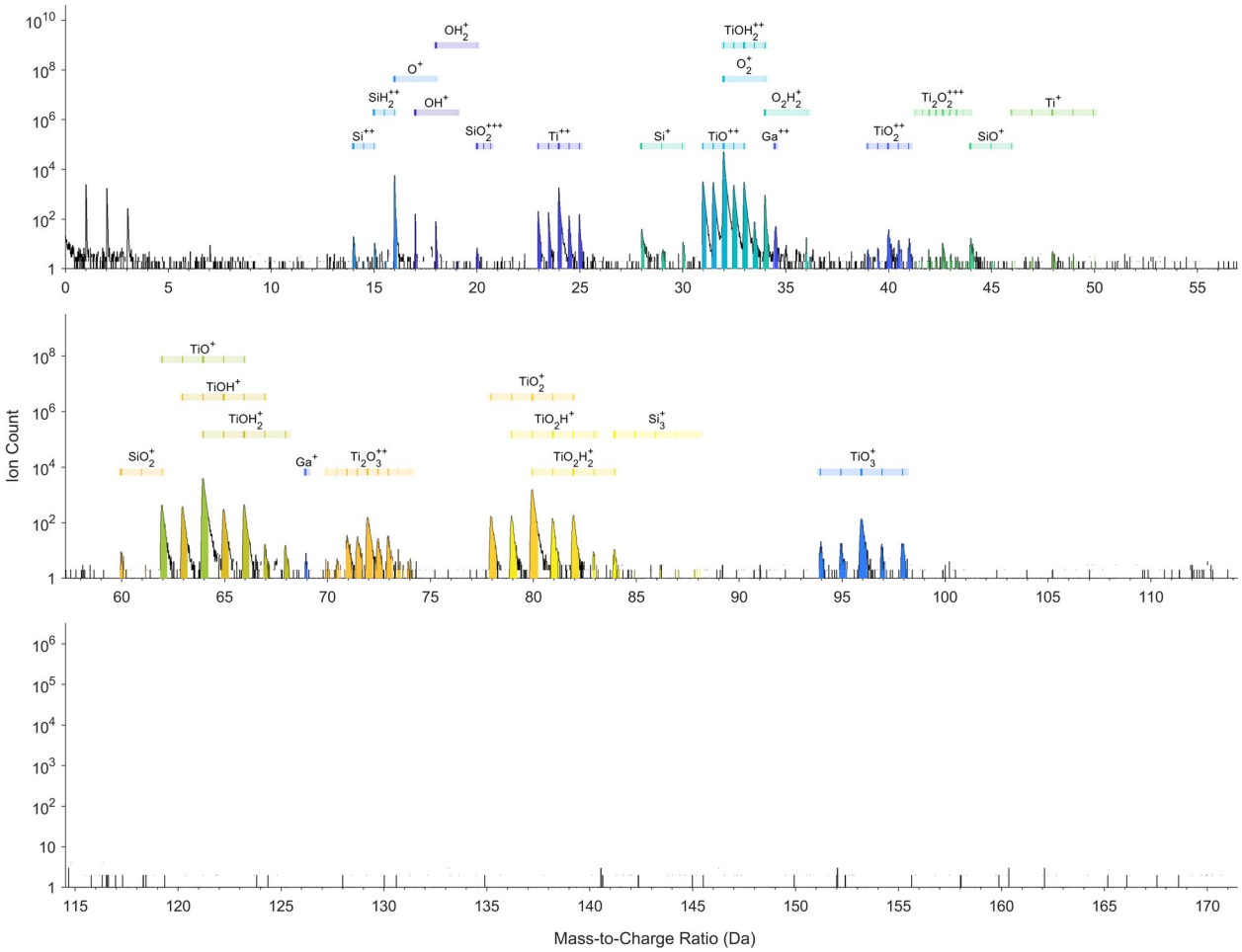

Figure 5.14: From the APT tip prepared from the oxide formed on Ti-0.8Si oxidized for 8 h (N_2-O_2, 800 °C), as shown in Figure 5.11a, the mass spectrum for a selected cylindrical volume across the grain boundary (along the blue arrow in Figure 5.11a). Labels show selected ions.

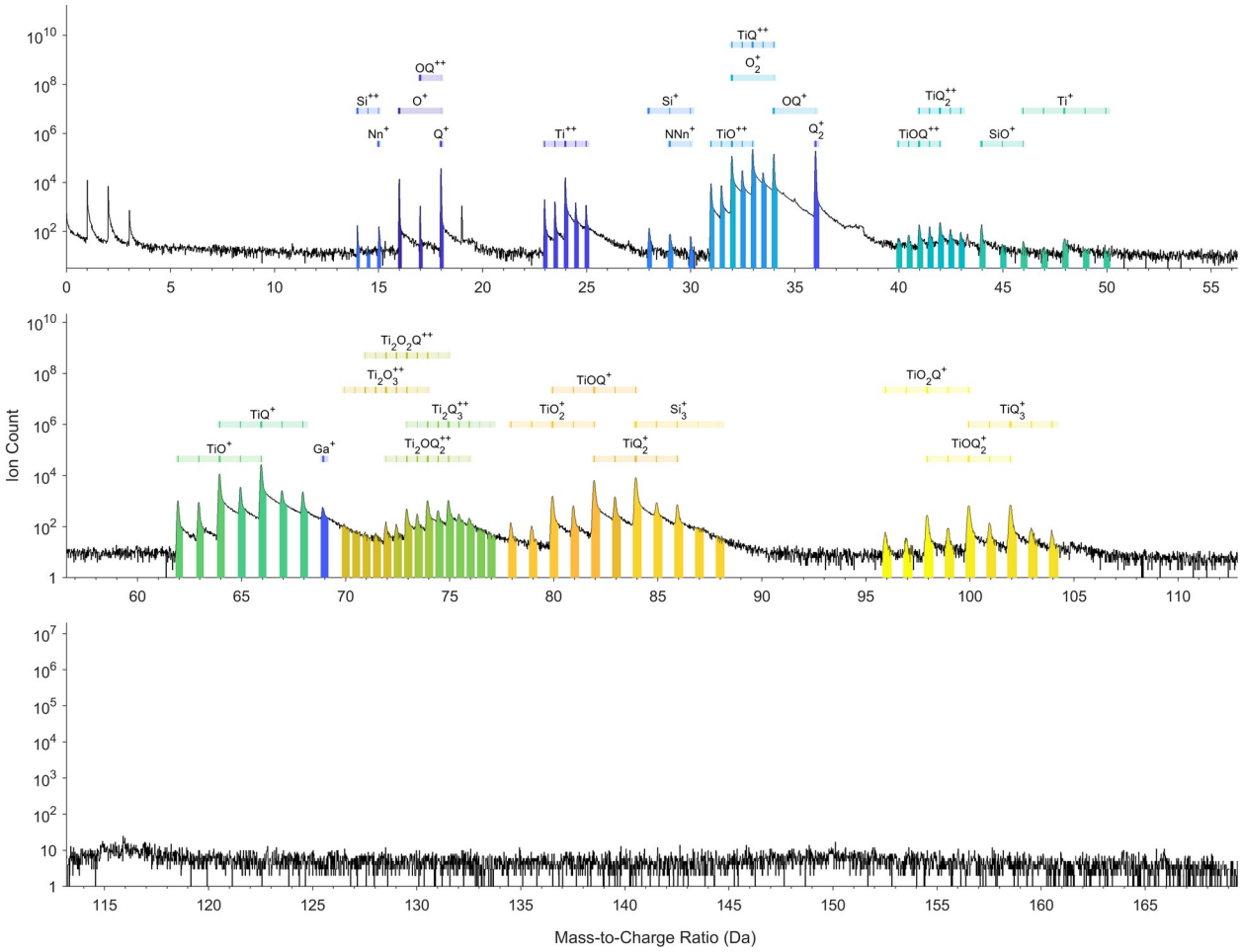

Figure 5.15: The mass spectrum of the APT tip prepared from the oxide formed on tracer-oxidized Ti-0.8Si (18 h in $^{15}N_2$-$^{18}O_2$ followed by 4 h in N_2-O_2, 800 °C), as shown in Figure 5.11b. Labels show selected ions, with "Nn" denoting ^{15}N and "Q" denoting ^{18}O.

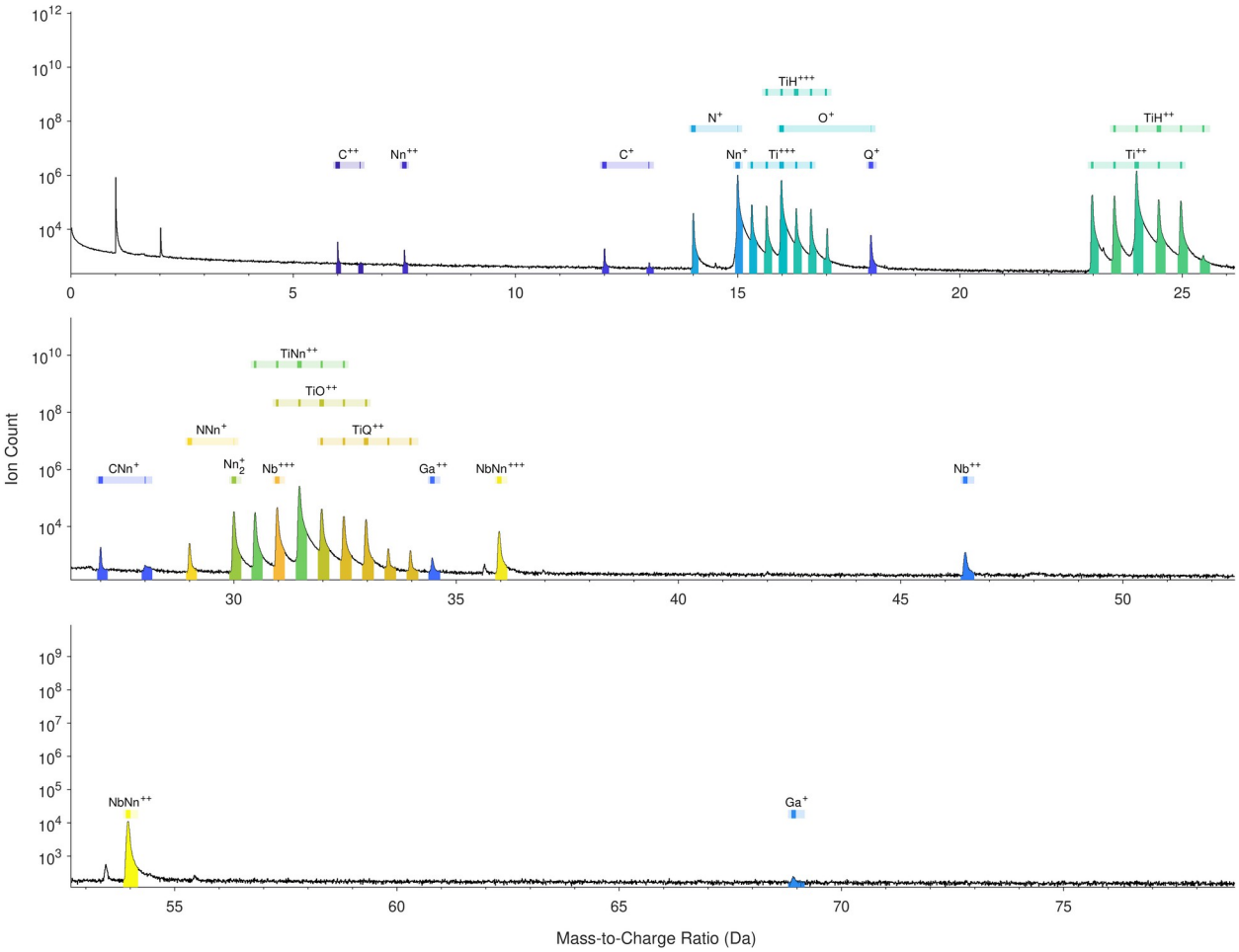

Figure 5.16: The mass spectrum of the APT tip prepared from the Ti_2N *nitride* phase near the nitride-metal interface on tracer-oxidized Ti-2Nb (18 h in $^{15}N_2$-$^{18}O_2$ followed by 4 h in N_2-O_2, 800 °C). Labels show selected ions, with "Nn" denoting ^{15}N and "Q" denoting ^{18}O. Smooth background, with no peaks, was detected up to 185 Da (not shown).

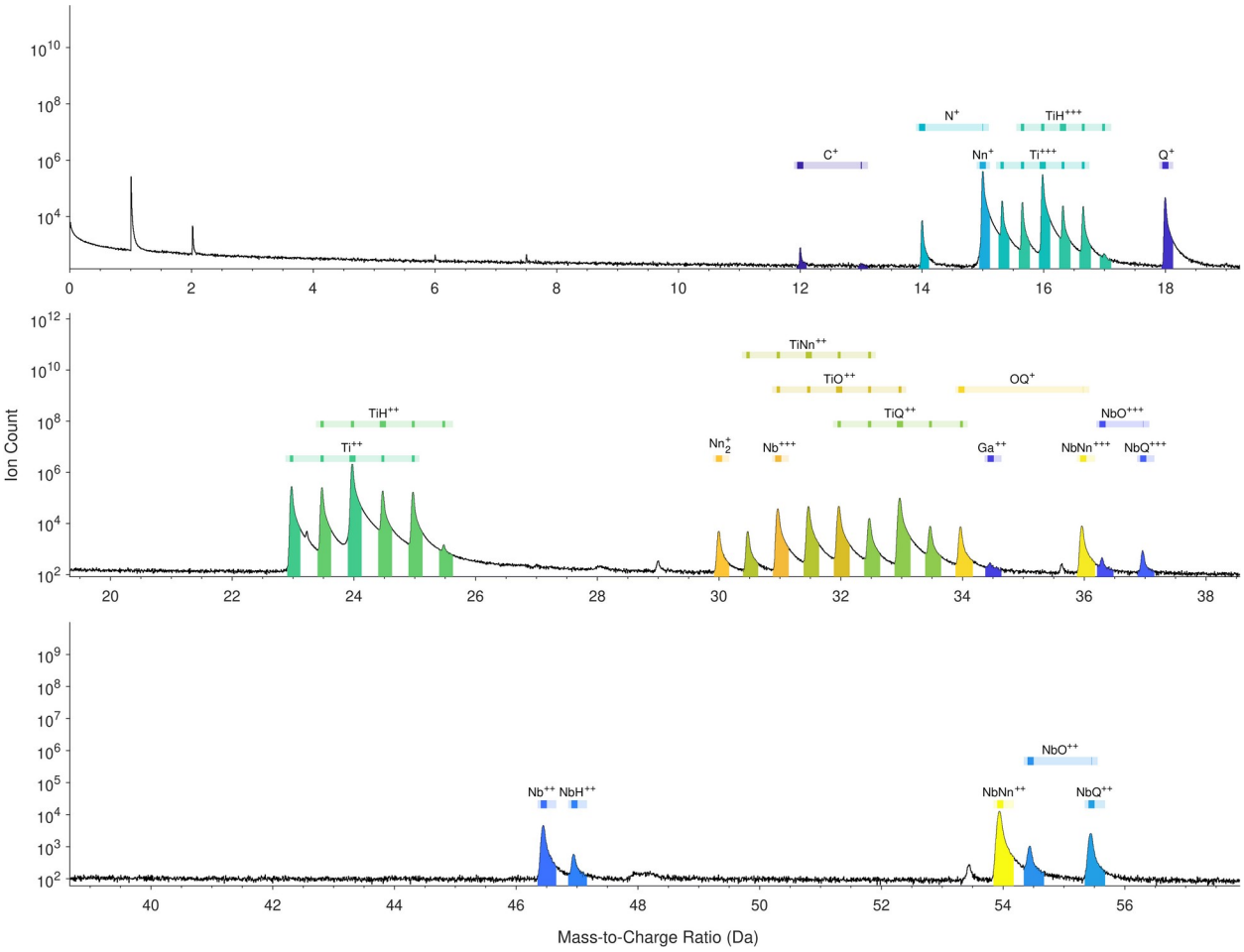

Figure 5.17: The mass spectrum of the APT tip prepared from the *metal* phase near the nitride-metal interface on tracer-oxidized Ti-2Nb (18 h in $^{15}N_2$-$^{18}O_2$ followed by 4 h in N_2-O_2, 800 °C). Labels show selected ions, with "Nn" denoting ^{15}N and "Q" denoting ^{18}O. Smooth background, with no peaks, was detected up to 220 Da (not shown).

5.6.2 Quantification parameters for STEM-EDS concentration profiles

Concentration profiles for oxygen and nitrogen dissolved near the surface of the metal were generated from STEM-EDS maps on cross-sectional lamellae. To improve the accuracy of data quantification, certain parameters were changed from the default values in the *Spectrum Image Quantification* panel in Velox 3.1 as follows:

- Pre-filtering ticked, using the recommended average filter
- Use absorption correction: Yes
- Sample thickness: 150 nm
- Density: 4.5 g/cm^3 (i.e. the density of α Ti)
- Use optimized spectrum fit: Yes

- Ionization cross-section model: Schreiber-Wims

The Schreiber-Wims ionization-cross section model was used rather than the default Brown-Powell model since it provides better accuracy for transition metals.

5.6.3 Additional WDS measurements correlated with nitride-layer thickness

Initial O concentration profiles were positioned without considering the thickness of the overlying nitride layer. Since the nitride layer exhibited dramatic local variations in thickness in pure Ti (especially at 100 h) and Ti-0.8Si (e.g. at 22 h in Figure 5.9d and at 100 h in Figure 5.6c), additional WDS measurements were collected to verify the initial data and to investigate potential correlations between the nitride-layer thickness and long-term O concentrations in the metal. On pure Ti and on Ti-0.8Si oxidized for 100 h, one concentration profile was collected where the nitride layer was thin (< 300 nm) and another where it was thick (~3 µm on pure Ti and ~4 µm on Ti-0.8Si). As shown in Figure 5.18, the profiles were identical in regions with thin and thick nitride layers and matched initial data collected from non-specific regions.

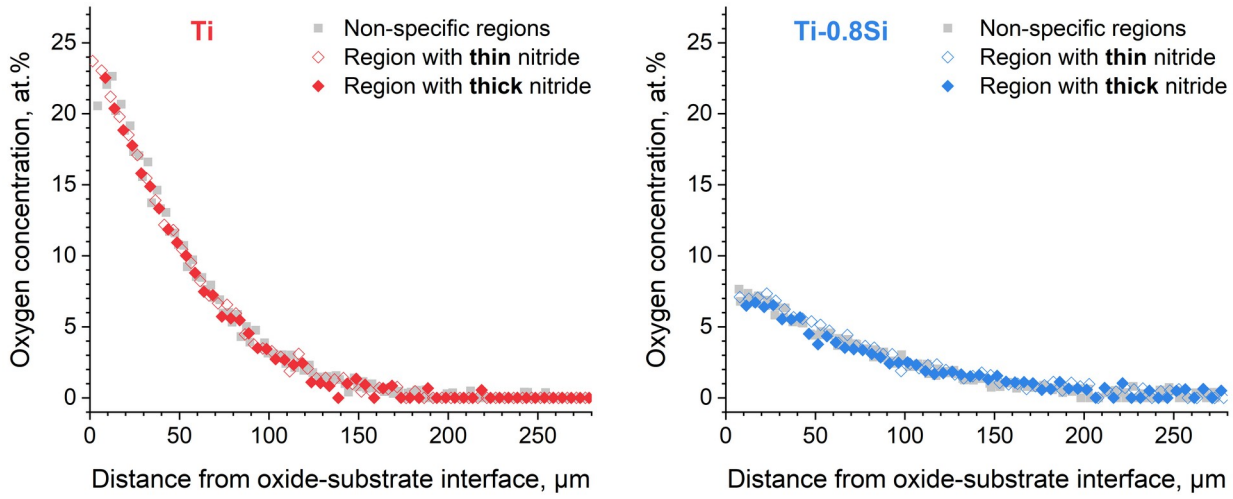

Figure 5.18: WDS measurements of oxygen concentrations in the metal for pure Ti (left) and Ti-0.8Si (right) oxidized for 100 h (800 °C, N_2-O_2) correlated with the nitride-layer thickness. The data from non-specific regions is the data shown for 100 h in Figure 5.8.

5.6.4 APT analyses in the nitride and metal on Ti-0.8Si oxidized for 100 h

A series of APT tips was prepared in the Ti_2N nitride and metal in the polished cross section of Ti-0.8Si oxidized for 100 h (800 °C, N_2-O_2). Nine specimens were created from a lift-out

spanning the nitride and metal. The lift-out was 18 μm long and oriented at 45° with respect to the oxide-substrate interface. Specimens were sharpened using the Ga FIB in a Thermo Fisher Scientific Helios 650 Nanolab SEM using standard techniques and then analyzed using a Cameca LEAP 5000 HR using a specimen temperature of 30 K, laser-assisted mode with a laser pulse energy of 15–25 pJ, and auto pulse-rate control with a minimum m/q range (Da) of 100–200. The detection rate was either fixed at 0.5% or controlled by constant field, with a field estimate of 26 V/nm and target areal evaporation of 80–130%/μm^2. Cameca AP Suite version 6.1.0.29 was used to reconstruct data and perform decomposition of peaks for improved accuracy of compositional analyses.

The analyses (Figure 5.19) agreed well with other results. Specifically, the approximate nitride composition, O and N concentrations near the nitride-metal interface, and trends in O and N concentrations in the metal were consistent with WDS (Figure 5.8), EDS (Figure 5.9), and APT (Figure 5.12). Additionally, the Si-rich precipitates previously noted in EDS maps (Figure 5.6) were identified as Ti_5Si_3 and Ti_3Si. Ti_5Si_3 (60 at.% Ti, 37 at.% Si) was detected in the nitride, and Ti_3Si (76% Ti, 24% Si) was detected in the metal. N concentration was moderate at 3.0 at.% in Ti_5Si_3 (in the nitride) and low at 0.3 at.% in Ti_3Si (in the metal). In both phases, O concentration phases was low at ~0.3 at.%. Si concentration in the nitride and metal excluding the precipitates was typically well below the nominal alloy content of 0.8 at.%, consistent with the precipitation reducing the Si concentration in solid solution.

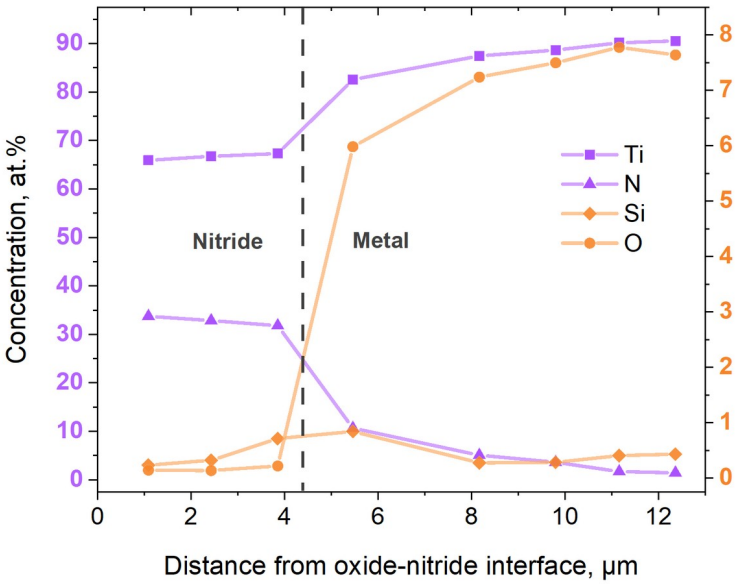

Figure 5.19: APT concentration profile in the Ti_2N nitride and metal located underneath the oxide scale formed on Ti-0.8Si oxidized for 100 h (800 °C, N_2-O_2). Each set of points at a given distance represents the bulk composition (excluding any precipitates) of a single APT specimen. Note that the connecting lines are included as a visual aid only. Estimates of atomic error are smaller than the symbols.

5.6.5 Additional Figures

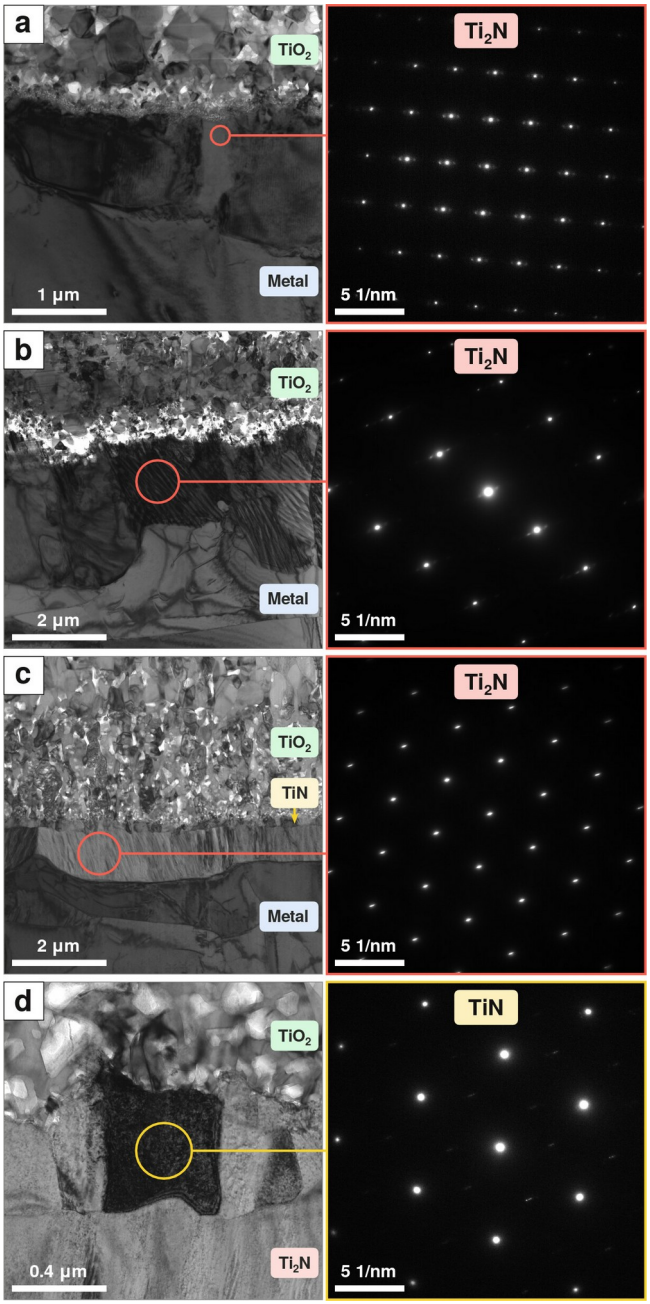

Figure 5.20: Bright-field TEM images (left) with corresponding selected-area TEM diffraction (right) on the nitride phases — Ti_2N ($P4_2/mnm$) or TiN ($Fm\bar{3}m$) — formed on (a) pure Ti oxidized for 100 h, (b) Ti-0.8Si oxidized for 32 h, and Ti-2Nb oxidized for (c) 8 h or (d) 32 h (N_2-O_2, 800 °C). Diffraction patterns were matched using SingleCrystal 4.1 (CrystalMaker Software Ltd.; Oxfordshire, UK) with physical distances, giving the zone axes (a) $[110]$, (b) $[\bar{1}\bar{4}3]$, (c) $[0\bar{1}0]$, and (d) $[111]$.

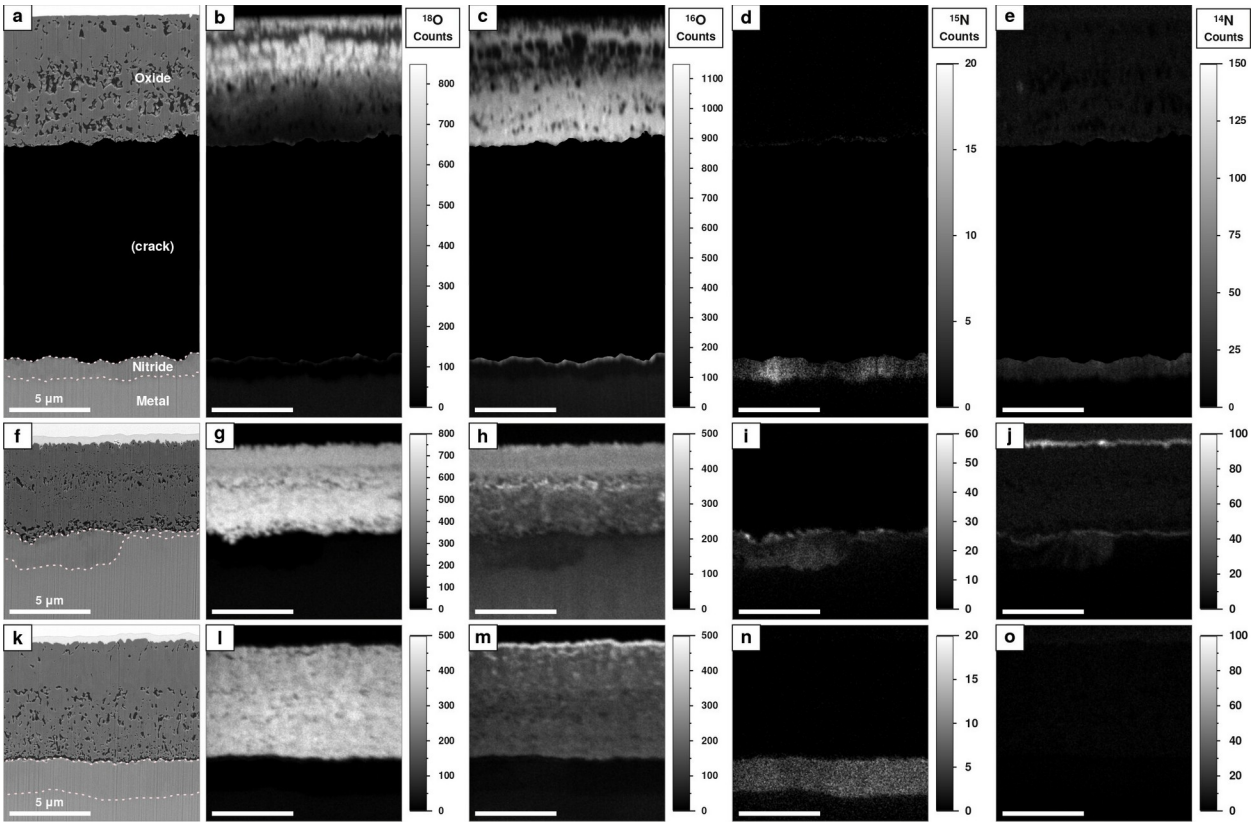

Figure 5.21: BSE-mode SEM (a, f, k) with corresponding nanoSIMS counts maps for cross sections of (a-e) pure Ti, (f-j) Ti-0.8Si, and (k-o) Ti-2Nb oxidized in two stages, first in $^{15}N_2$-$^{18}O_2$ and then in N_2-O_2 (800 °C). The first stage was 12 h for pure Ti and 18 h for Ti-0.8Si and Ti-2Nb, while the second stage was 4 h for all the materials. Columns are arranged with respect to the species and the oxidation stages, i.e. O from the first oxidation stage (b, g, i), O from the second stage (c, h, m), N from the first stage (d, i, n), and N from the second stage (e, j, o). ^{18}O, ^{16}O, ^{15}N, and ^{14}N were, respectively, detected as $^{18}O^-$, $^{16}O^-$, $^{12}C^{15}N^-$, and $^{12}C^{14}N^-$ ions. In (a-e), only the bottommost portion of the oxide scale is shown, and the crack between the oxide scale and substrate (shown at its true height of 13 μm here) is hidden. We note that, in (j), the high counts near the top corresponded to the Pt cap rather than the oxide.

Chapter 6: Summary and Future Directions

The motivation for this thesis was to develop a deeper understanding of how alloying additions and atmospheric nitrogen mechanistically influence the high-temperature oxidation response of titanium, as the current limited understanding is arguably hindering scientifically informed development of next-generation oxidation-resistant titanium alloys. This thesis investigated the role of two alloying elements known to be particularly beneficial to the oxidation behavior, Si and Nb, and the role of atmospheric nitrogen. We oxidized pure Ti, Ti-0.8Si, and Ti-2Nb in atmospheres with and without nitrogen at 800 °C for up to 100 h. Low concentrations of alloying additions were used to maintain single-phase α-titanium solid solution at the isothermal oxidation temperature of 800 °C. This temperature was selected because it is just below the α-to-β transformation temperature, thereby maximizing temperature while avoiding the temperature-induced phase transformation of the metal. Using multi-scale characterization techniques including thermogravimetry, SEM, TEM. STEM, EDS, WDS, nanoSIMS, and APT, we systematically compared the oxidation responses to understand the overall oxidation behavior, oxidized microstructures, local chemistry and phases, and ultimately the oxidation mechanisms. Notably, our two-stage oxidation experiments using isotopically labeled atmospheres and subsequent nanoSIMS analyses provided unparalleled insight into the scale-growth mechanisms and transport in the microstructures.

In the following discussion, we summarize the main chapters while underscoring the significance of key findings. Then we consider specific unresolved questions and potential experiments to address them. Finally, we discuss broader extensions of this work, focusing first on building foundational scientific knowledge and then on the industrial relevance.

In our investigation of the roles of Si and Nb alloying independent of nitrogen, we discredited many of the mechanisms proposed in the literature and identified two *new*, *distinct* mechanisms that were not previously identified. In these studies, we compared the oxidation responses of pure Ti, Ti-0.8Si, and Ti-2Nb at 800 °C in Ar-20% O_2 and in two-stage exposures of $^{16}O_2$ followed by $^{18}O_2$. Si and Nb additions reduced overall mass gains by reducing oxide

thickness rather than the amount of oxygen dissolved in the metal. Contrary to prior suggestions in the literature [9], [11], [14], [15], Si and Nb had no effect on oxygen diffusivity or solubility in the metal. Instead, they influenced the initial scale growth but via different mechanisms. For pure Ti, the initial compact oxide scale grew both outward and inward, as confirmed using isotopic oxygen. Alloying with Si (**Chapter 3**) initially suppressed inward oxide growth and led to a compact oxide scale growing only by outward Ti diffusion. The suppression of inward oxide growth was due to the formation of a continuous Ti_5Si_3 silicide layer between the oxide and metal. Eventual breakdown of the Ti_5Si_3 layer enabled fast inward oxide growth, ultimately resulting in a Si-containing lamellar oxide scale. In contrast to the effects of alloying with Si, alloying with Nb (**Chapter 4**) reduced outward growth of the initial compact scale. We attributed this benefit to Nb segregation to the (rutile TiO_2) oxide grain boundaries slowing outward Ti transport along the oxide grain boundaries. Nb segregation to oxide grain boundaries — especially by additionally limiting inward O transport as hypothesized — likely also contributed to the eventual formation of a Ti_2O suboxide layer at the scale-metal interface in Ti-2Nb, which was not observed in pure Ti. Although the possible benefits of doping of oxide grain boundaries is well known, particularly for Cr_2O_3- and Al_2O_3-forming alloys (i.e. the reactive-element effect [94], [106]), to our knowledge, this is the first report of a similar phenomenon in TiO_2-forming/titanium-based alloys. To the best of our knowledge, our use of isotopic oxygen for the first time unambiguously revealed that oxygen diffusion primarily takes place along TiO_2 *grain boundaries*. This finding is important because it is counter to the typical assumption of *lattice* transport dominating. Additionally, it suggests that the oft-purported benefits of Si^{4+} [11] or Nb^{5+} [14], [15], [16], [19] doping the oxide and reducing *lattice* O diffusivity are not relevant here.

In our investigation of the role of atmospheric nitrogen (**Chapter 5**), we conclusively demonstrated how nitrogen in the metal contributes to reducing oxygen concentrations in the metal, thereby clarifying long-standing confusion in the literature. Additionally, we showed that the synergy between alloying additions and nitrogen is mainly in keeping the oxide scales compact rather than by influencing the behavior of N or O in the metal. In this study, we oxidized pure Ti, Ti-0.8Si, and Ti-2Nb at 800 °C in N_2-20% O_2 or in sequential isotopically labeled N_2-20% O_2 atmospheres and then compared the behavior to that in nitrogen-free atmospheres. As in nitrogen-free atmospheres, the oxidation of the three materials in N_2-O_2 entailed growth of oxide scale and dissolution of oxygen in the metal. However, nitrogen brought

the addition of a nitride layer at the oxide-metal interface and nitrogen dissolution in the metal. As we demonstrated using thermodynamic calculations and diffusion simulations with Thermo-Calc, the presence of nitrogen in the metal near the nitride-metal interface plays a key role in reducing O concentrations throughout the metal. Nitrogen, which remains confined more closely to the surface of the metal than O due to its slower diffusion away into the metal, thermodynamically limits the O concentration near the surface and therefore throughout the metal. Additionally, simulations confirmed the experimentally observed uphill diffusion of O in the presence of a concentration gradient of N. Notably, the alloying additions did not significantly influence the behavior of N and O in the metal, in contrast to recent suggestions [107]. The null effect of alloying additions on the behavior in the metal of O, as also noted in Ar-O_2 atmospheres, and N is important because it suggests that dilute alloying is *not* an effective strategy for influencing O and N solubilities or diffusivities in the (α-phase) metal. Although atmospheric nitrogen had almost no effect on the oxidation rate of pure Ti, it greatly reduced the oxidation rates and mass gains of Ti-0.8Si and Ti-2Nb alloys. These reduced mass gains in the alloys initially reflected reductions in oxygen in the metal but, at longer oxidation times, mainly reflected reduced scale thicknesses. The synergy between alloying and nitrogen helped maintain compact oxide scales, preventing the formation of the lamellar scales observed during oxidation in nitrogen-free atmosphere and the oxidation of pure Ti regardless of atmosphere. In contrast to oxide grain boundaries being the primary pathway for inward O transport in the compact scales formed in Ar-O_2, the oxide lattice also facilitated O transport in the scales formed in N_2-O_2. Therefore, the aforementioned purported influence of Si^{4+} or Nb^{5+} doping on lattice O diffusion that was not relevant in Ar-O_2 may be relevant in N_2-O_2 and in other atmospheres. For alloy design, this finding underscores the need to consider the intended use atmosphere. For example, efforts to slow transport through the oxide scale by doping oxide grain boundaries would be rendered ineffective if, as influenced by the oxidation atmosphere, lattice diffusion dominates.

While this thesis brings many new findings regarding transport in the oxide during the high-temperature oxidation of titanium, some details on transport rates and transport pathways in the oxide and nitrides remain unconfirmed. In general, additional two-stage tracer oxidation experiments followed by nanoSIMS and/or APT analyses would be helpful to clarify these unknowns. Concerning transport rates in the oxide scales formed in Ar-O_2, it is important to determine the temperature at which lattice diffusion dominates, which is generally expected toward higher temperatures [71]. Additionally, further work is needed to confirm, as

hypothesized, if Si (noted in the oxide after breakdown of the silicide layer) influences Ti or O transport along oxide grain boundaries and if Nb slows inward O transport along oxide grain boundaries. Although similar questions pertain to the scales formed in N_2-O_2, additional tracer oxidation experiments and nanoSIMS analyses may not be informative because of the additional transport through the lattice complicating the interpretation. In N_2-O_2 atmospheres, it is also worth clarifying if doping of the bulk (rutile TiO_2) oxide with Si or Nb influences lattice Ti diffusivity or O diffusivity. To investigate the influence on O lattice diffusivity, we could compare the diffusion behavior of ^{18}O in single-crystal TiO_2, as a control, and Si- and Nb-doped TiO_2 after high-temperature exposure to N_2-$^{18}O_2$. Although we attempted to investigate the influence of Nb on O lattice diffusivity using such an experiment with an $^{18}O_2$ exposure atmosphere (Appendix 3), no clear differences with Nb doping were noted, contrary to expectations from the literature. Considering our observations of significant lattice O diffusion only with the presence of atmospheric nitrogen, it would be worthwhile to repeat these experiments using an exposure atmosphere of N_2-$^{18}O_2$ rather than $^{18}O_2$. Concerning transport pathways, further work is needed to confirm if Ti transport occurs along oxide grain boundaries, as presumed in scales formed in Ar-O_2, and/or through the lattice. For such investigations, the use of a Ti isotope in the starting material may be helpful. In the nitrides, the transport pathways of N and O require clarification. To investigate the lack of inward oxide growth despite enhanced lattice O diffusivity in the oxide scales noted for the alloys in N_2-O_2, additional experimental and computational work could help clarify if the presence of alloying elements, particularly Nb, in the titanium nitrides can slow their oxidation rates. Finally, additional research, especially using computational methods, is needed to better understand the mechanisms by which Nb segregation to oxide grain boundaries influences transport. As proposed for the reactive-element effect in Al_2O_3 scales, two potential mechanisms include site blocking [105] or altering the local bonding environment at the grain boundaries [111].

Toward expanding scientific knowledge, two natural extensions of this thesis include investigating the oxidation behavior and mechanisms in other binary titanium alloys and at higher temperatures. We cannot overemphasize the need to systematically investigate the effects of other minor alloying additions while accounting for atmospheric nitrogen, as we did for Si and Nb in this thesis. Particular elements of interest include those already known to be potentially beneficial to the oxidation behavior of titanium (e.g. Al, Cu, Mo, Ta, and W [8]) and those typically used in commercial near-α titanium alloys used at high temperatures (esp. Al, Mo, Sn,

and Zr [33]). The latter group is especially important for understanding the individual and synergistic roles of such elements in the oxidation responses of multi-component titanium-based alloys. We expect that many alloying additions can behave like Nb, segregating to the oxide grain boundaries and influencing transport along them. In particular, we hypothesize that Ta behaves this way and is beneficial like Nb, since small Ta additions to titanium have been shown to improve the oxidation behavior in oxygen atmospheres [20], [24]. More broadly, this phenomenon may also be relevant to the oxidation of other alloys that form rutile TiO_2 in the oxide scales, including the burgeoning family of refractory multi-principal-element alloys (e.g. equimolar WMoCrTiAl and NbMoCrTiAl [112]). From a scientific perspective, it would be interesting to explore the role of nitrogen at higher temperatures in β titanium, e.g. in pure Ti above the α-to-β transformation temperature of 882 °C. Because O and N ingress would stabilize a layer of α phase in the metal underneath the scale (as in [20], [113]), we hypothesize that the beneficial role of nitrogen in the metal described for α alloys in this thesis may be similar in β alloys.

This thesis raises many important considerations and potential research opportunities for the industrial use of titanium alloys as high-temperature structural materials. In general, there is a strong need for modeling the oxidation process in a way that holistically accounts for the microstructure, growth of the oxide scale and underlying nitride layer, O and N dissolution in the metal, transport mechanisms and rates, mechanical properties, complex sample geometries of real parts, and the evolution of stresses, especially with cyclic heating reflective of real-world use. While industrially relevant, such modeling would also be useful for advancing our understanding of the important contributions to lamellar scale growth and ultimately how to suppress it. As typical commercial alloys would have lower purity than the materials used in this thesis, investigations are needed to determine the sensitivity of the oxidation responses and oxidation mechanisms to alloying impurities. Such sensitivity to impurities is reasonably expected considering the literature on the reactive-element effect [106]. In light of the beneficial role of nitrogen in the metal in reducing oxygen concentrations, it is interesting to consider using nitrogen as an intentional alloying addition to help limit oxidation. Since both oxygen and nitrogen are solid solution strengtheners and up to ~1.2 at.% oxygen is used to enhance yield strength in commercially pure Ti alloys [2], replacing oxygen with nitrogen (e.g. 2 at.% as in [114]) may be an effective strategy for achieving a similar strengthening effect *while* improving oxidation behavior. While we emphasized the need to account for atmospheric nitrogen in this

thesis, atmospheric humidity can also influence the oxidation behavior of titanium alloys (e.g. [14], [15]) and requires further study.

In summary, this thesis makes significant and original contributions to the field of high-temperature oxidation of titanium. In our investigations on the role of alloying elements and atmospheric nitrogen, we discredited many mechanisms repeated throughout the literature, evidenced previously unidentified mechanisms by which Si and Nb influence scale growth, and conclusively demonstrated the beneficial role of nitrogen in the metal on reducing oxygen concentrations in the metal. For the first time in the titanium oxidation literature, we showed that oxygen transport through the (rutile TiO_2) oxide primarily takes place along oxide grain boundaries, rather than through the lattice as previously assumed. Such fundamental knowledge is critical for designing oxidation-resistant titanium alloys. Still, research opportunities abound. Our hope is that future studies address some of the research topics proposed here in our collective efforts to expand the oxidation resistance and high-temperature capability of structural titanium alloys.

Appendices

Appendix A: Microstructure of Specimens Before Oxidation

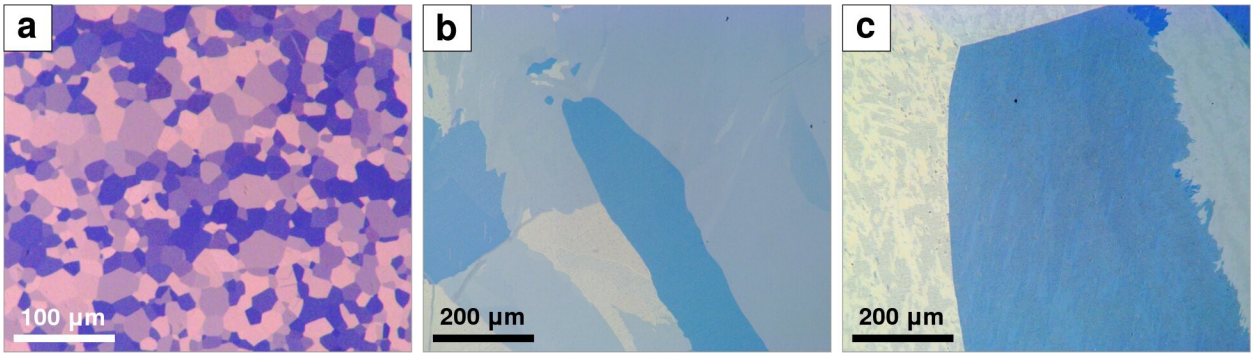

Appendix Figure A.1: Polarized-light microscopy of (a) pure Ti, (b) as-cast Ti-0.8Si, and (c) as-cast Ti-2Nb used for oxidation studies. Grains in pure Ti (a) were equiaxed and up to 50 µm in size. In contrast, grains in Ti-0.8Si and Ti-2Nb were irregular in shape and significantly larger, up to millimeters in size. Note that the heat-treated Ti-0.8Si and Ti-2Nb used for N_2-O_2 oxidation studies (**Chapter 5**) are not shown.

Appendix B: Grinding/Polishing Procedure for Specimens to be Oxidized

Specimens used for oxidation studies were small, typically about 1 mm thick and 3~10 mm in length and width. To help hold the small specimens during grinding/polishing and to achieve uniform surface finishes, a fixture was used. The fixture was prepared from high-purity (99.999%) Ti plate purchased from Alfa Aesar (Lot M31E035). A 15 x 20 x 6 mm piece was cut from the plate, and a hole approximately 8 mm in diameter and centered on the large face was drilled through the thickness. Finally, sharp corners and burrs were removed by grinding with coarse alumina papers. A specimen was mounted inside the hole in the fixture using Crystalbond 509 mounting adhesive using the following steps:

1. Preheat a hot plate to approximately 100 °C.
2. Place an aluminum crucible on the hot plate, filling it with sufficient mounting adhesive to fully encase the specimen when placed inside the hole in the fixture.
3. While the mounting adhesive is warming, coat one side of a glass microscope slide with PTFE mold release (Item 200-10015; Allied High Tech Products, Inc.; Rancho Dominguez, CA).
4. Once the mold release has dried, place the fixture on top of the coated slide and center the specimen inside the hole in the fixture, as shown in Appendix Figure B.1a.
5. Place the slide setup on the hot plate, leaving part of the slide overhanging the hotplate for use as a handle.
6. After letting the slide setup warm for about 1 minute, pour mounting adhesive into the hole, filling it about halfway.
7. Firmly push the specimen against the microscope slide using fine tipped tweezers and then slowly withdraw the tweezers. Note that withdrawing the tweezers too quickly or while the mounting adhesive is viscous may pull the specimen away from the slide. Confirm that the specimen is flat against the slide by briefly removing the slide setup from the hot plate and viewing the specimen from underneath. This step is intended to

make the surfaces of the specimen and polishing fixture coplanar and thereby minimize the grinding time needed after mounting.

8. Remove the slide setup from the hot plate, and allow it to cool to room temperature.
9. With the slide held flat against a stable surface, twist the fixture to detach it from the slide, as shown in Appendix Figure B.1b. The specimen should remain encased in mounting adhesive within the fixture.

Using a manual grinder/polisher with an 8" diameter platen, the mounted specimen was then ground with 360 grit alumina paper (Item ALO-500P8-100; Pace Technologies Inc.; Tucson, AZ) until all the specimen surface was exposed, i.e. not covered by mounting adhesive. This was followed by grinding with 600 grit alumina paper (Item ALO-1200P8-100, Pace Technologies Inc.) for 1 minute at 100 RPM and then polishing using 9 μm diamond products on a woven, silk cloth (Item 407448; Buehler; Lake Bluff, IL) for 10 minutes at 140 RPM. The cloth was initially charged with monocrystalline diamond paste (Item 406253; Buehler) and polycrystalline diamond suspension (Item 406633, Buehler) and then periodically doused with a few drops of the suspension every 15 seconds.

A similar polishing fixture was used to help prepare plate-shaped specimens used for thermogravimetric oxidation studies, as shown in Appendix Figure B.1c. While the fixture was not needed for preparing the two large faces in the manner described above because the specimens were large, it was used to prepare the four small faces. For this process, one of the large faces of the specimen was attached to the vertical side of the fixture using mounting adhesive. The specimen was positioned such that excess material to be removed hung below the bottom surface of the fixture, and the final position of the small face to be prepared was coplanar with the bottom surface of the fixture. During initial grinding with 360 grit alumina paper, the fixture was initially held above the platen, with only the specimen contacting the platen. Once most of the excess material was removed, both the specimen and fixture were pressed against the platen and ground until flat. This was followed by grinding with 600 grit alumina paper for 1 minute at 100 RPM. To prepare the other small faces, the fixture was heated to soften the mounting adhesive, the specimen was repositioned and then ground, and this process was repeated. Finally, the two large faces were ground and polished in the manner described in the previous paragraph.

The mounted specimen was sonicated in soapy water after each grinding/polishing step. To remove the specimen from the fixture, the setup was sonicated in acetone until the specimen was free. Then the specimen was sonicated separately for 5 minutes in new acetone. We note that multiple specimens could be mounted and ground/polished together, space permitting. However, to prevent possible cross contamination, specimens of different materials (pure Ti, Ti-0.8Si, and Ti-2Nb) were not prepared together. Additionally, each material was finally polished using a distinct cloth.

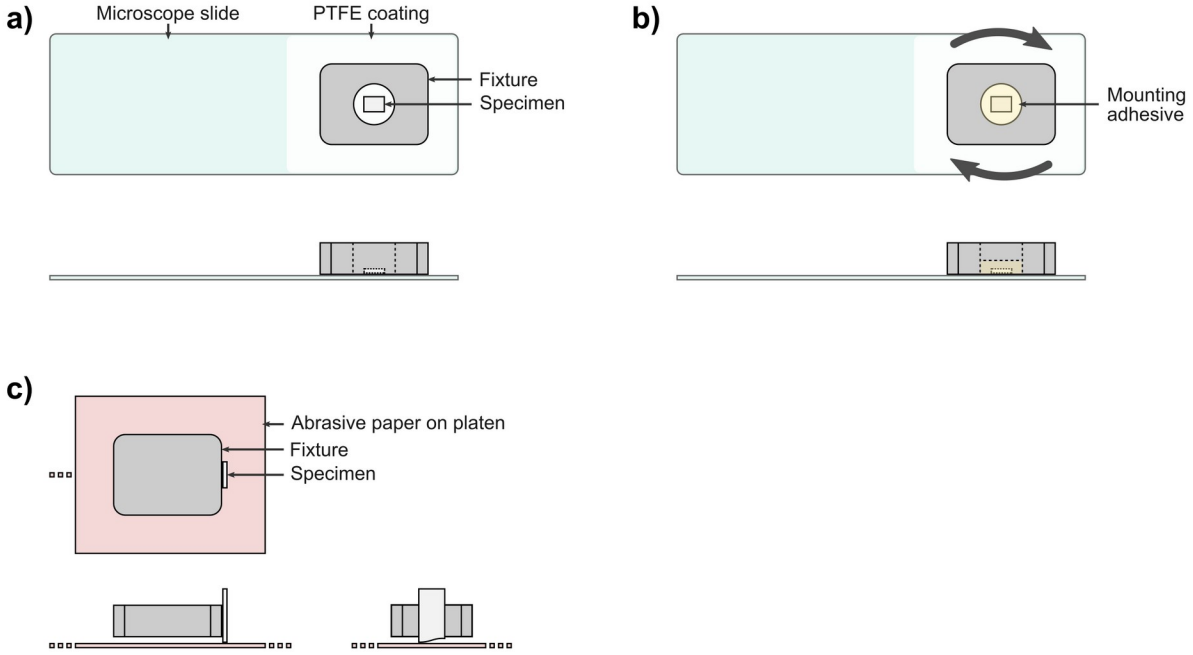

Appendix Figure B.1: Schematics showing how titanium grinding/polishing fixtures were used to hold specimens to be oxidized (top to bottom and then left to right: top view, front view, right-side view). Small specimens used for typical experiments were placed within a fixture (a) and secured using mounting adhesive (b). In (b), arrows indicate twisting to detach the mounted specimen from the slide. (c) Large, plate-shaped specimens used for thermogravimetric experiments were attached to the side of the fixture for shaping and preparing the four small faces.

Appendix C: Preparation of Bulk Oxidized Cross Sections

To prepare oxidized specimens for WDS analysis and microscopy on the bulk cross sections, specimens were mounted in epoxy and manually polished using a distinct procedure. There were four main steps: initial mounting, sectioning, remounting, and grinding and polishing.

Initial Mounting

1. Clean a 31 mm diameter mounting cup and base with an acetone-soaked wipe.
2. Install the base into the mounting cup and coat the interior with PTFE mold release (Item 200-10015; Allied High Tech Products, Inc.).
3. Place two small spacer bars parallel inside the cup. Aluminum bars with the dimensions 22 x 1 x 5 mm were used, with the 22 x 1 mm face contacting the base. Bars should be the exact same height (4 mm minimum) and at least 3 mm apart. The use of spacer bars helps to better surround the oxidized specimen with epoxy and thereby preserve the oxide scale on all the surfaces during subsequent sectioning.
4. Lay the specimen across the bars with the main surface of interest face down, as shown in Appendix Figure C.1a. Multiple specimens can be mounted together for convenience. In this case, positioning the surfaces of interest face down is especially convenient for WDS analysis and microscopy because it aligns all the surfaces of interest in the final prepared cross section (even when specimens have different thicknesses or nonparallel top and bottom surfaces).
5. Combine low-viscosity, low-shrinkage epoxy resin (Item 203453128, Buehler) with corresponding epoxy hardener (Item 203453032, Buehler) in a weigh boat. For the EpoKwick FC system used, suitable amounts were 8.8 g of resin and 2 g of hardener.
6. Gently stir the epoxy mixture for 2 minutes. Sufficient mixing is *critical* for proper curing. After sufficient mixing, initial faint streaks reflecting the separate resin and hardener components should disappear, and the mixture should become perceptibly

warm. Remove any bubbles by pulling them to the edge of the cup with the stirring stick. The presence of more than a few bubbles indicates improper stirring technique.

7. Slowly pour the epoxy mixture into the cup. If needed, adjust the positions of the spacer bars or specimen using the stirring stick or tweezers.
8. Allow the epoxy to cure for at least 24 hours before proceeding.

Sectioning

1. Gently remove the epoxy puck from the cup.
2. Using coarse abrasive paper, grind the top and bottom faces of the puck to flatten them and to reduce puck thickness to about 1 cm. Center the specimen in the thickness (Appendix Figure C.1b).
3. Using the same abrasive paper, grind two flat faces on the sides of the puck. Faces should be opposite each other and perpendicular to the bars, as shown in Appendix Figure C.1c. This step is needed so that the sectioned half of the puck can fit into the mounting cup during the remounting procedure.
4. Cut the puck on a low-speed diamond saw using a low-concentration, fine-grit diamond wafering blade (Item WB-0040LC, Pace Technologies Inc.). This type of blade is ideal for minimizing sectioning damage in brittle materials, i.e. the oxide scale and underlying metal. Position the puck with the oxidized surface of interest facing the blade (to put the oxide scale in compression during the cut), and center the blade in the gap between the two spacer bars (Appendix Figure C.1d). Typical cutting time is 1-2 hours. If cutting is slow, dress the blade to expose new abrasives and/or add more weight to increase the cutting force.
5. Rinse and then sonicate the sectioned halves for 2 minutes with methanol or isopropanol (*not* acetone, as it is too aggressive on the epoxy).
6. Allow the sectioned halves to dry overnight. Only one half is needed for the following remounting procedure.

Remounting

1. Clean a 31 mm diameter mounting cup and base with an acetone-soaked wipe.
2. Install the base into the mounting cup and coat the interior with the PTFE mold release.

3. Combine low-viscosity, low-shrinkage epoxy resin with corresponding epoxy hardener in a weigh boat. For the Buehler EpoKwick FC system used, suitable amounts were 8.8 g of resin and 2 g of hardener.
4. Gently stir the epoxy mixture for 2 minutes, removing any bubbles with a stirring stick.
5. Using the stirring stick, squeegee a small amount of epoxy mixture into the cut face of the sectioned half, wiping back and forth 3-5 times or more if bubbles continue coming out of the surface.
6. Stick the cut face onto the base of the mounting cup, centering the specimen in the cup. For WDS experiments, a piece of pure Ti was added to the cup for use as a standard reference material.
7. Slowly pour the epoxy mixture into the cup.
8. Allow the epoxy to cure for at least 24 hours before proceeding.

Grinding and Polishing

1. Gently remove the epoxy puck from the cup.
2. Using coarse abrasive paper, grind the top of the puck flat, removing the protrusion from the sectioned half.
3. Using a manual grinder/polisher with an 8” diameter platen, grind the face containing the specimen with 600 grit SiC paper at 100 RPM for 1 minute, with the oxidized surface of interest perpendicular to the grinding direction and in compression. Repeat this step using a new sheet of abrasive paper three more times. During this step, chips in the oxide scale and underlying metal created during sectioning gradually disappeared, as noted with periodic inspection using optical microscopy. *Between this step and the following grinding/polishing steps, sonicate the puck in soapy water for 1 minute.*
4. Grind the face with 800 grit SiC paper at 100 RPM for 2 minutes, rotating 180° after 1 minute. Repeat this step using a new sheet of abrasive paper two more times.
5. Grind the face with 1200 grit SiC paper at 100 RPM for 2 minutes, rotating 180° after 1 minute. Repeat this step using a new sheet of abrasive paper one more time.
6. Prepare a 10-15 g mixture of 10 wt.% 50% hydrogen peroxide (Item H341-500, Thermo Fisher Scientific) and 90 wt.% 0.03 μm colloidal silica (Item AP-345; Mager Scientific Inc.; Dexter, MI).

7. Polish the face using the colloidal-silica mixture on a soft, porous, foam pad (Item BC2-8008-SSMAG, Pace Technologies Inc.) for 25 minutes at 120-140 RPM, dousing the pad with a few drops of the mixture every 15 seconds and rotating the puck 90° every 5-10 minutes. To prevent colloidal silica from sticking to the surface, run water on the pad for the final 10 seconds of polishing, and then sonicate the puck for 10 minutes in soapy water.

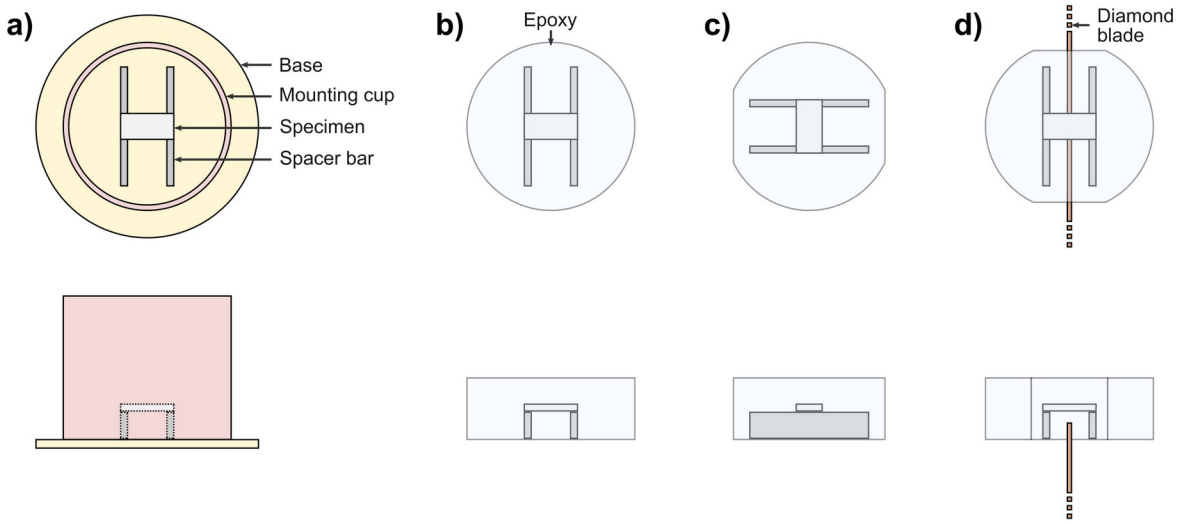

Appendix Figure C.1: For the preparation of bulk oxidized cross sections, schematics showing certain steps during initial mounting (a-c) and sectioning (d) procedures. These steps were followed by remounting one cut half from (d) and grinding and polishing. The top row and bottom row show the top and front views, respectively.

Appendix D: Setups and Procedures for Two-Stage Tracer Oxidation

D1: Introduction

The setups and procedures for two-stage tracer oxidation differed slightly for experiments conducted in O_2 atmospheres (in **Chapter 3** and **Chapter 4**) and in N_2-O_2 atmospheres (**Chapter 5**). For convenience, the schematics of those setups are reproduced here (Appendix Figures D.1 and D.2). Both setups used a quartz oxidation chamber, a tube furnace (Model TF55035A-1, Lindberg/Blue M, Thermo Fisher Scientific), a mass spectrometer (PrismaPro QMG 250 F1, 1–100 μ; Pfeiffer Vacuum GmbH) and supporting turbopump system (HiCube 80 Eco, Pfeiffer Vacuum GmbH) for monitoring gases in the oxidation chamber, a diaphragm vacuum pump (MD 1C; Vacuubrand Inc.) for evacuating the system, and gas sources. All tubing used was stainless steel. Changes between the initial setup, used with O_2 atmospheres, and the revised setup, used with N_2-O_2 atmospheres, were made mainly to allow for exchanging the atmosphere during oxidation by flowing gases. The approximate layout of the present system in the lab is shown in Appendix Figure D.3, along with detailed schematics of various components in Appendix Figures D.4, D.5, D.6 and D.7. This documentation is intended to serve as a detailed record of the experiments performed, as a guide for future users of this system, and as inspiration for those who may wish to design similar systems.

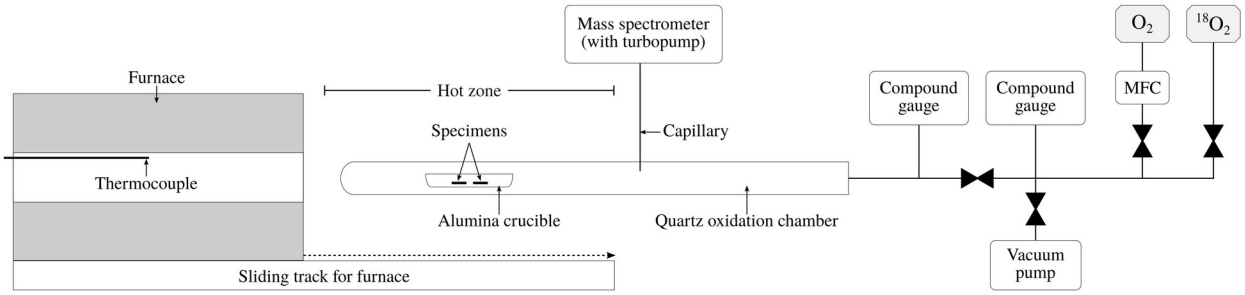

Appendix Figure D.1: Schematic of the experimental setup for two-stage tracer oxidation experiments in O_2 atmospheres.

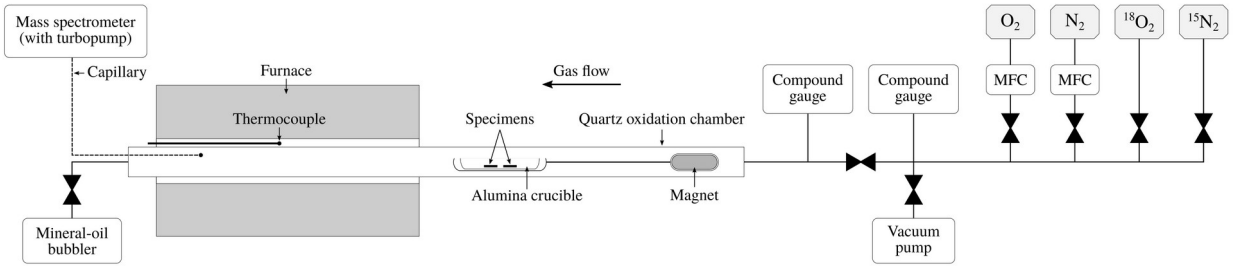

Appendix Figure D.2: Schematic of the experimental setup for two-stage tracer oxidation experiments in N_2-O_2 atmospheres.

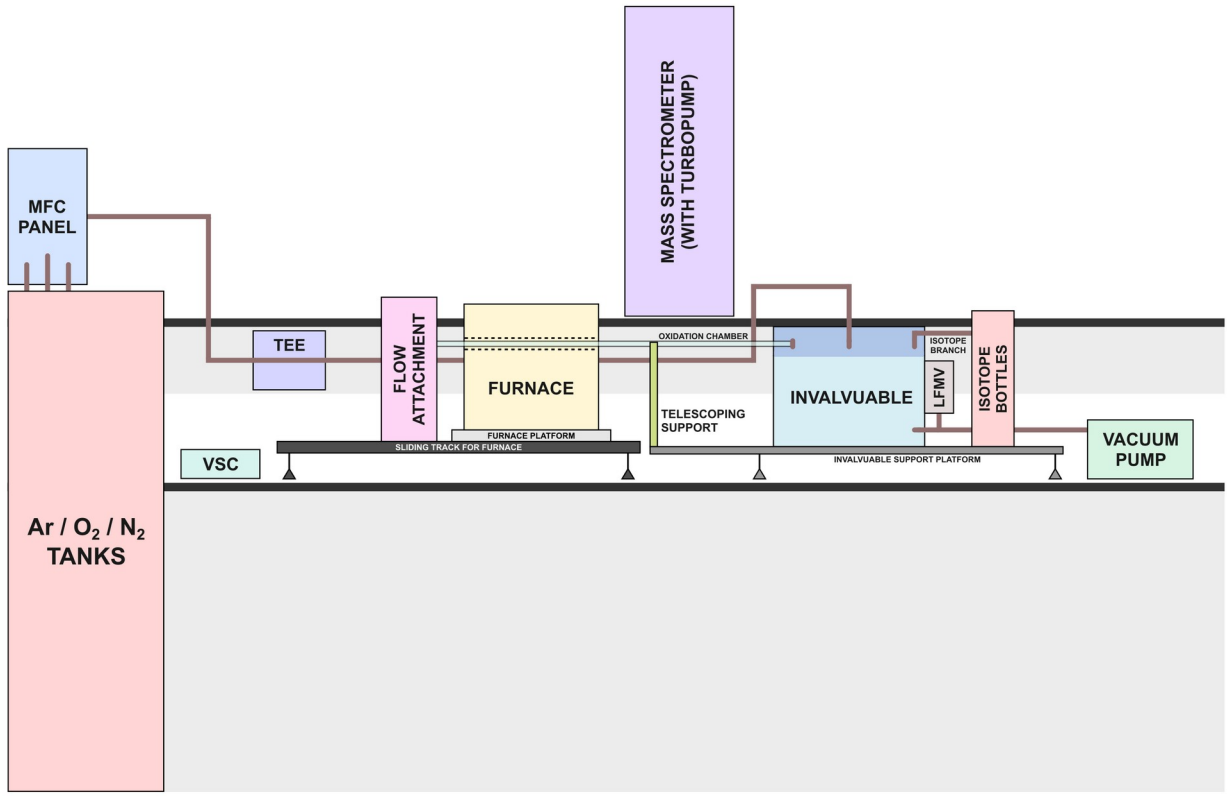

Appendix Figure D.3: Front-view schematic showing the layout of the tracer oxidation system in the laboratory (to scale). As shown, the system is configured with the ability to flow gases during oxidation, as it was configured for experiments using N_2-O_2 atmospheres. For experiments with O_2 atmospheres, the flow attachment was not used. Brown lines show the main gas connections (capillaries are not shown). The MFC panel, gas tee, main control panel ("Invalvuable"), and isotope branch are shown in more detail in Appendix Figures D.4, D.5, D.6, and D.7, respectively. VSC is the vacuum system controller. LFMV is the low-flow metering valve connected between the "HT Vacuum" port on Invalvuable and the vacuum pump, which was used to slow the vacuuming rate of hot gases.

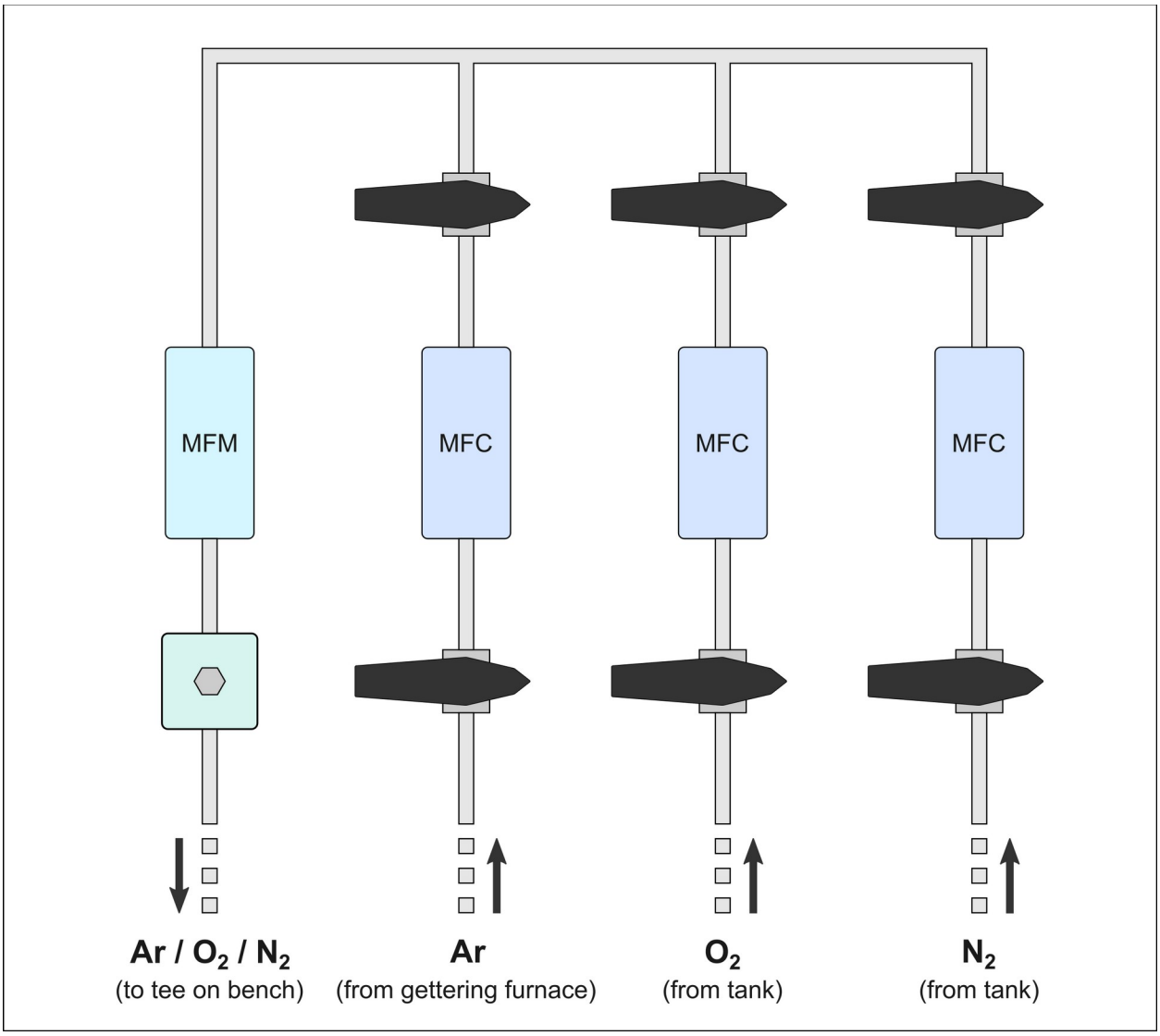

Appendix Figure D.4: Front-view schematic of the MFC panel, which contains connections to Ar, O_2, and N_2 gas supplies, mass flow controllers (MFCs), a mass flow meter (MFM), and valves. Each gas supply is controlled by an MFC and a pair of valves. Valves are shown in the closed position. The MFM, which measures all outflowing gas and is calibrated for Ar, is used for validation purposes. Cables (not shown) connect the MFCs and MFM to the vacuum system controller.

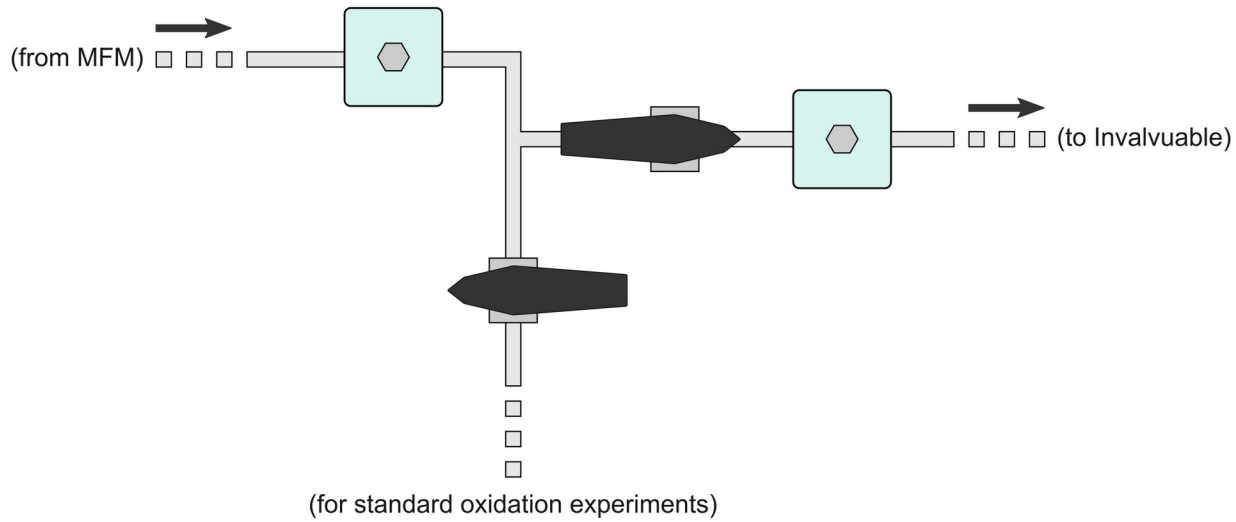

Appendix Figure D.5: Front-view schematic of the tee mounted on the bench used to direct standard gases (Ar, O_2, N_2) for oxidation experiments. For tracer oxidation experiments, the valves should be positioned as shown.

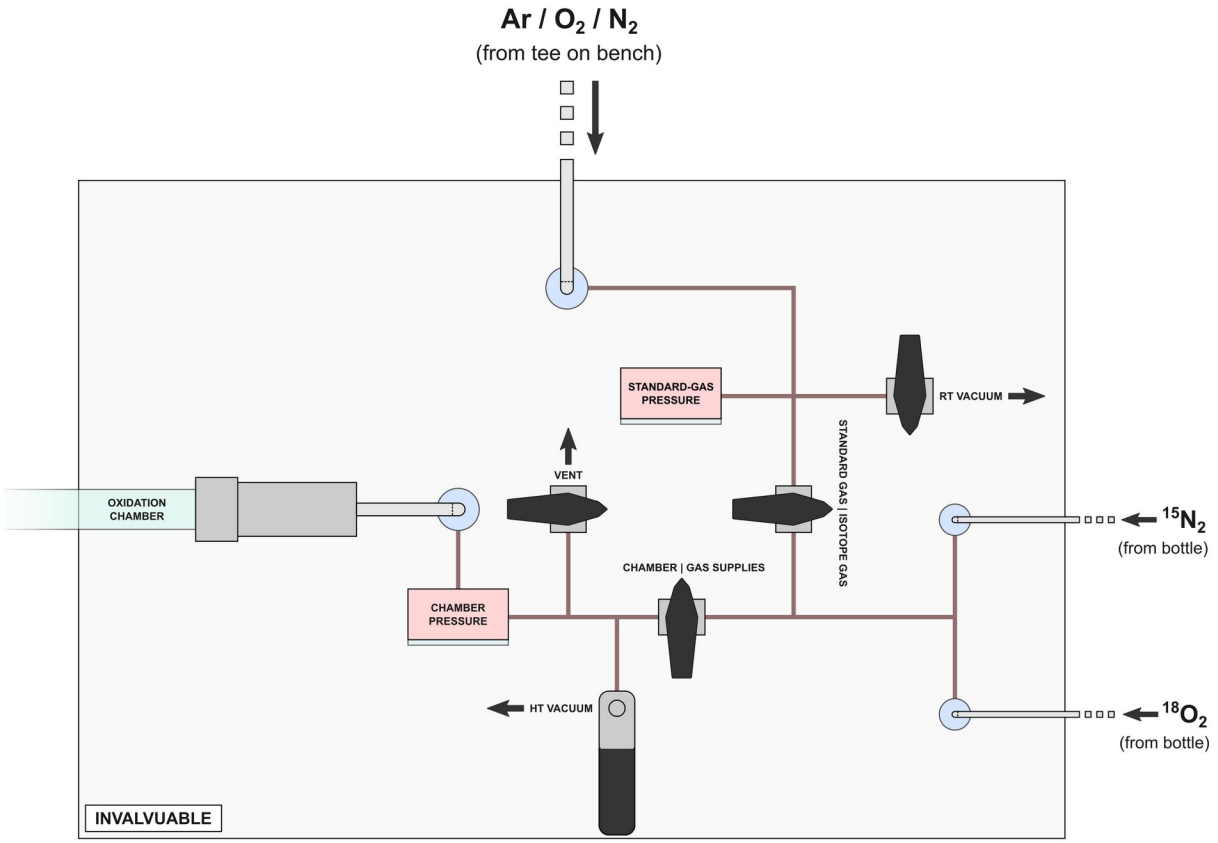

Appendix Figure D.6: Top-view schematic of the main control panel used for tracer oxidation experiments, named "Invalvuable." This panel connects all gas supplies to the oxidation chamber. Blue circles indicate where tubing connects to the panel. Brown lines show connections between components. The various valves allow for isolating parts of the system, connecting to the vacuum pump for evacuation, and venting to atmosphere. Compound gauges (in red) show the pressure in the oxidation chamber and in the standard-gas line.

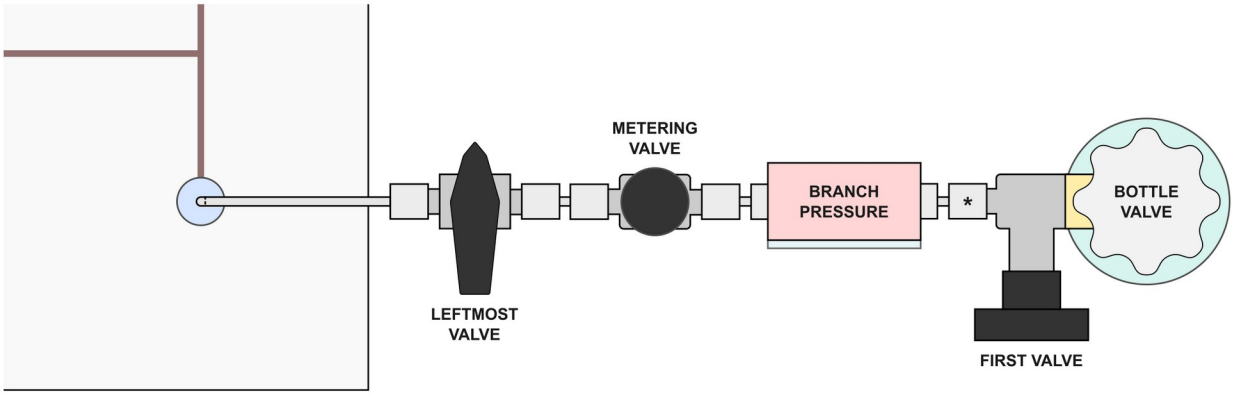

Appendix Figure D.7: Top-view schematic of the isotope branch, which is attached to the isotope bottle and suspended over Invalvuable. The asterisk denotes the nut to loosen when replacing the bottle.

D2: Preliminary Preparation

Safety Considerations

The two main safety considerations when using this system are volatilization and overpressure. The volatilization of the specimen or the oxides formed could harm the user and, upon condensing, permanently contaminate various parts of the system. While not a concern for titanium at the temperatures used, this possibility should in general be considered. Overpressure, which is most likely to result from user error during setup, could lead to the oxidation chamber popping out of its fitting or, in the extreme case, exploding. To minimize these risks, the system was designed with a check valve (Item SS-4CA-3; Swagelok Company; Solon, OH) in the segment containing the oxidation chamber. Note that the check valve has an internal O-ring seal and is therefore a potential leak source, as discussed later. The check valve is located directly under the "Chamber" gauge. Its cracking pressure, which is adjustable from 3-50 psi, should be set around 10 psi as a default. The cracking pressure can be verified and adjusted as follows:

1. Open and then close the "Vent" valve to vent the oxidation chamber to atmosphere.
2. Using a permanent marker, draw a line across the Swagelok Ultra-Torr fitting used to seal the oxidation chamber and the compression fitting attached to it. This is to mark the current tightened position of the compression fitting.
3. Using wrenches, remove the Swagelok Ultra-Torr fitting.
4. Seal the open tube with a cap (Item SS-400-C, Swagelok), tightening it by hand and then a 1/8 turn with a wrench to make a temporary seal. Note that this cap may leak if not sufficiently tightened, which may cause confusion during the following adjustment process.
5. On Invalvuable, open the "Standard Gas | Isotope Gas" and "Chamber | Gas Supplies" isolation valves.
6. Using a gas source such as N_2 at 100 SCCM, pressurize the system to 20 psi, and then turn off the gas flow. This may require increasing the outlet pressure on the regulator.
7. Using the "Standard-Gas" compound gauge, confirm that the pressure slowly decreases and then stabilizes around 10 psi. This indicates that the check valve is operating as intended. If the default cracking pressure of 10 psi is the desired cracking pressure, stop here. Otherwise, continue with the following steps to adjust the cracking pressure.
8. Open and then close the "Vent" valve.

9. Adjust the check valve to its lowest cracking pressure (3 psi). For additional details and helpful schematics, see documentation from Swagelok (https://www.swagelok.com/downloads/webcatalogs/en/ms-crd-0047.pdf).
    1. Insert a 5/32” hex wrench up into the open end of the check valve.
    2. Turn the wrench clockwise (as viewed from above) to loosen the locking screw.
    3. Slide the wrench further up through the adjusting screw.
    4. To set the cracking pressure to its minimum, turn the wrench clockwise until it cannot be turned further.
    5. Slide the wrench back down into the locking screw.
    6. Turn the wrench counterclockwise to tighten the locking screw.
10. Pressurize the system to 15 psi, and then turn off the gas flow. Confirm that the pressure slowly decreases and then stabilizes around 3 psi.
11. As desired, repeat steps 8-10 with necessary modifications to incrementally increase the set cracking pressure and then verify it. In step 9.4, increase the set cracking pressure by turning the wrench counterclockwise. In step 10, pressurize the system to 10 psi above the anticipated cracking pressure. Note that the cracking-pressure adjustment is very sensitive, with 1/8 to 3/8 turn of the adjusting screw potentially enough for 10 psi cracking pressure.
12. When finished with adjustments, open and then close the “Vent” valve.
13. Using wrenches, remove the cap and reattach the Ultra-Torr fitting. Tighten the Ultra-Torr fitting slightly past the previously marked position on the fitting body, at which point a significant increase in resistance should be felt.

Checking isotope gas supplies

Confirm that sufficient isotope gas is present in the lecture bottles. For a lecture bottle, the final pressure, P_{bf}, after filling the oxidation chamber can be estimated using

$$P_{bf} = \frac{P_{bi} V_b + V_c \left(P_{ci} - P_{cf} \right)}{V_b},$$

where P_{bi} is the initial bottle pressure, V_b is the bottle volume (0.45 L), V_c is the oxidation chamber volume, P_{ci} is the initial chamber pressure (0 if evacuated), and P_{cf} is the final chamber

pressure. The final bottle pressure, P_{bf}, must be greater than or equal to the final chamber pressure, P_{cf}, as a pressure difference is needed for the gas to flow. Note that this equation uses absolute pressures, with atmospheric pressure (1 atm) being about 14.70 psi.

To replace a lecture bottle, locate the first valve attached to the bottle, as shown in Appendix Figure D.7. Using a permanent marker, draw a line across the valve body and the nut (marked with an asterisk in Appendix Figure D.7) to mark the current tightened position of the nut relative to the valve body. While bracing the valve body with a wrench, loosen the nut and disconnect it. Support the hanging components just detached from the valve using a ring stand with a clamp. Slightly loosen the clamps securing the lecture bottle in its stand, and lift the bottle up and out. Transfer the first valve on the used bottle to the new bottle, using a new PTFE sealing washer and tightening the valve to the bottle first by hand and then slightly more using a wrench. To avoid interference with the bottle during this process, it may be necessary to temporarily remove the knob on the first valve (by loosening the set screw and pulling off the knob). Install the new bottle in the stand, and reconnect the compression fitting. Bracing the valve body with a wrench, tighten the nut slightly past the previously marked position on the valve body, at which point a significant increase in resistance should be felt. For more information on reassembly of compression fittings, refer to documentation from Swagelok (https://www.swagelok.com/downloads/webcatalogs/EN/MS-13-151.PDF).

Preparing the mass spectrometer for monitoring gases

If using the mass spectrometer to monitor gases, turn on the turbopump at least 72 h before the experiment. If the turbopump is not powered on and allowed to pump down sufficiently in advance, additional signals reflecting contaminants present in the vacuum chamber may be detected. To help the system achieve higher vacuum and better cleanliness, close the valve to the capillaries by bracing the valve body with one hand and pointing the valve handle toward the middle position, between the two capillaries. We note that two capillaries, a PEEK capillary and fused-silica capillary, were installed for use with the different setups.

Checking alignment of the oxidation chamber and furnace

Confirm that the oxidation chamber to be used is properly aligned with the furnace, particularly when planning to slide the furnace over the oxidation chamber during the experiment. For alignment, it is helpful to level both the oxidation chamber and furnace using a torpedo level.

After alignment, confirm that the (Swagelok Ultra-Torr) connections to the oxidation chamber are not unduly stressed, as this can cause the ends of the chamber to crack and interfere with the seal.

Inspecting connections to the oxidation chamber

Inspect the oxidation chamber for cracks, especially at the main opening and capillary port. Confirm that O-rings are damage free and clean. If needed, coat O-rings with a very thin layer of high-vacuum grease (Dow Corning; Midland, MI), wiping off excess grease using a clean glove.

Checking the system for leaks

The system should be periodically checked for leaks. First, configure the valves in Appendix Figures D.4 and D.5 as shown. On Invalvuable (Appendix Figure D.6), open the "Standard Gas | Isotope Gas" and "Chamber | Gas Supplies" isolation valves. For each lecture bottle, ensure that the built-in valve is closed, and then fully open all (3) subsequent valves (Appendix Figure D.7). If the flow attachment is installed, close the valve on it. Evacuate the system through the "RT Vacuum" valve on Invalvuable for 2 minutes. Then close all open valves on Invalvuable and the isotope branches to segment the system. Mark the pressure on the four compound gauges, two on Invalvuable and one on each isotope branch. Scotch Magic tape, with the indicating edge colored, is particularly useful for marking the gauges, as it can be reused indefinitely and leaves no residue. The following day, inspect gauges for any increases in pressure. If no changes are noted, incrementally open valves to connect a portion of the system to the relevant gauge and again check for a pressure change. This method is helpful for narrowing down the source of a leak. Likely sources of leaks include O-ring seals, any recently adjusted stainless-steel compression fittings, and the PTFE seal between the lecture bottle and first valve. These leaky connections can be fixed by cleaning or replacing the seals or with slight tightening. While the compression fittings between fixed components are not likely to leak and should not need adjustment, the various valves may require maintenance to prevent eventual leakage with use. For this, refer to documentation for valve packing adjustment from Swagelok.

D3: Procedure for Tracer Oxidation in O_2 Atmospheres

1. At least 72 h before the experiment, review Section D2, and complete necessary steps.
2. Turn on the vacuum system controller (MKS 946; MKS Instruments, Inc.; Andover, MA). The vacuum system controller and attached flow controllers and flow meter should be powered on at least 30 minutes before use for accurate performance.
3. Open the valves on the O_2 tank and regulator. On the MFC panel (Appendix Figure D.4), open the valve below the O_2 MFC, and close all others. On the bench tee, configure the valves as shown in Appendix Figure D.5.
4. On the mass-spectrometer setup, while bracing the body of the valve to the capillaries with one hand, point the handle toward the PEEK capillary. Because this step introduces a small burst of gas from the valve into the vacuum chamber, "Emission" should be off. Otherwise, the system as configured will automatically turn off "Emission" in response to the gas.
5. In the PV MassSpec software, turn on "Emission." Emission should be turned on about 30 minutes before use for accurate performance.
6. In PV MassSpec, start data collection using an appropriate recipe. To avoid interruption or loss of data, set data collection to continuous and pause updates on the PC to prevent it from rebooting during the experiment.
7. Load specimens into a clean alumina crucible.
8. Using the stainless-steel loading rod, push the crucible into the desired position in the oxidation chamber. Note that the notch at the end of the loading rod can be used to pull the crucible forward if needed. The oxidation chamber used was a tube, sealed at one end, with a 19 mm outer diameter, 17 mm inner diameter, and length of 915 mm. A short tube (40 mm length, 9.53 mm outer diameter, located about 500 mm away from the sealed end) was attached perpendicular to the chamber wall for use as a capillary port. The capillary port should be facing up.
9. Connect the oxidation chamber to the system.
    1. If necessary, relocate the tube furnace by loosening the two hand brake levers, sliding the furnace platform, and tightening the levers. For safety, the furnace should always be locked in place when not being moved.
    2. If necessary, adjust the height of the telescoping support.

3. Ease the chamber into the pipe clamp located on the top of the telescoping support, taking care not to jostle the specimens.
4. Remove the protective storage cap, knurled nut, sleeve, and O-ring from the (Swagelok Ultra-Torr) fitting on Invalvuable (Appendix Figure D.6), and install the knurled nut, sleeve, and O-ring onto the oxidation chamber. Note that the thin part of the sleeve should touch the O-ring.
5. Fully insert the oxidation chamber into the fitting and tighten the knurled nut by hand.
6. Slowly pull the oxidation chamber forward about 2 mm. This can help prevent the fitting from cracking the rim of the chamber.
7. Gently tighten the pipe clamp around the oxidation chamber.
8. Install the capillary fitting into the port in the same way that the oxidation chamber was installed. If the system pressure will exceed a few psi above atmospheric pressure, secure the fitting to the port (e.g. with packing tape) to prevent the fitting from popping off.

10. Install the thermocouple guide tube into the furnace. This quartz tube holds the thermocouple above the specimens and at the center of the furnace.
11. Confirm that the oxidation furnace can slide over the chamber without any interference. Check first with the furnace lid open and then with the lid closed and latched shut.
12. Install the thermocouple, plug both ends of the furnace with furnace wool, and preheat the furnace to 800 °C.
13. Purge the system with O_2.
    1. On Invalvuable, open the "Standard Gas | Isotope Gas" and "Chamber | Gas Supplies" isolation valves. Ensure that the (built-in) bottle valve on the $^{18}O_2$ bottle is closed, and then fully open all (3) subsequent valves on the isotope branch (Appendix Figure D.7).
    2. On Invalvuable, briefly open and then close the "Vent" valve, and confirm that the two compound gauges read atmospheric pressure. If not, mark true atmospheric pressure on the gauges using Scotch Magic tape.
    3. Turn on the diaphragm vacuum pump. Note that the vacuum pump should be connected to two barbs, one leading to the "RT Vacuum" valve and another to the "HT Vacuum" valve.

4. Open the “RT Vacuum” valve on Invalvuable, pull vacuum for 5 minutes, and close the valve.
5. Using the vacuum system controller, enable O_2 flow at 200 SCCM.
6. Open the valve above the O_2 MFC (Appendix Figure D.4). When the system reaches atmospheric pressure after about 1 minute, close the valve to stop gas flow.
7. Open the “RT Vacuum” valve, pull vacuum for 1 minute, and close the valve.
8. Repeat steps 6-7 two more times.
9. In PV MassSpec, confirm the presence of strong signals from ^{16}O species and weak signals from others, especially ^{14}N. With each purge cycle, the non-^{16}O signals should get progressively weaker. If non-^{16}O signals are particularly high, flow O_2 out through the “Vent” valve (e.g. at 500 SCCM for 10 minutes) to flush the O_2 regulator and line before repeating steps 4-8.

14. On the $^{18}O_2$ branch, close the leftmost valve (Appendix Figure D.7) to isolate the branch from Invalvuable. Open all other valves on the branch, and then briefly open and then close the bottle valve. This is to pressurize the branch and eliminate the possibility of air leaking into it.
15. Calibrate 0.2 atm on the “Chamber” gauge using the O_2 MFC.
    1. On the vacuum system controller, set O_2 flow to 50 SCCM.
    2. Open the valve above the O_2 MFC, measure the time to fill to atmospheric pressure, and close the valve.
    3. Open the “RT Vacuum” valve, pull vacuum for 1 minute, and close the valve.
    4. Open the valve above the O_2 MFC for 0.2 times the previously measured time to fill to atmospheric pressure, and then close the valve.
    5. Mark 0.2 atm on the “Chamber” gauge using Scotch Magic tape.
    6. Open the “RT Vacuum” valve, pull vacuum for 1 minute, and close the valve.
16. Turn off the vacuum pump.
17. Refill the system to the desired O_2 pressure.
    1. Open the valve above the O_2 MFC.
    2. At the desired pressure (or after the appropriate elapsed flow time), close the “Standard Gas | Isotope Gas” valve on Invalvuable.
    3. After the standard gas line pressurizes to about 10 psi, close the valve above the O_2 MFC. Pressurizing this line is helpful because the line can be used to add small

amounts of O_2 into the chamber if needed later during oxidation (by opening the "Chamber | Gas Supplies" isolation valve and slowly cracking open the "Standard Gas | Isotope Gas" valve).

4. On the vacuum system controller, turn off O_2 flow.
5. Close the "Chamber | Gas Supplies" valve on Invalvuable.

18. Remove the furnace wool from the right end of the furnace, slide the preheated furnace in place over the oxidation chamber, and replace the wool. Adjust the thermocouple as needed.
19. After 8 minutes for temperature equilibration, start the oxidation time.
20. After the desired time for the first oxidation stage, exchange the oxidation atmosphere.
    1. Turn on the vacuum pump.
    2. Fully open for 10 seconds and then close the low-flow metering valve (Item SS-SS4-VH, Swagelok) mounted underneath Invalvuable, taking care not to overtighten it to prevent damage. This metering valve connects to the "HT Vacuum" valve through a 1.5 m length of tubing. Note that the metering valve does not fully stop flow in the closed position.
    3. Open the "HT Vacuum" valve for 30 seconds and then close it. During this time, while watching the "Chamber" compound gauge, slowly open the metering valve to achieve a gradual decrease in chamber pressure. We note that motivation for using a metering valve, 1.5 m length of tubing, and special temperature-resistant "HT Vacuum" valve (Item SS-62PS4-5228, Swagelok) was to help cool the hot gas and regulate its extraction in order to prevent damaging components on Invalvuable and the vacuum pump.
    4. Open the "RT Vacuum," "Standard Gas | Isotope Gas," and "Chamber | Gas Supplies" valves in rapid sequence.
    5. After 30 seconds, close the "RT Vacuum" and "Standard Gas | Isotope Gas" valves.
    6. On the $^{18}O_2$ branch, open the bottle valve, close the low-flow metering valve (Item SS-SS2-VH, Swagelok), and open the leftmost valve.
    7. While watching the "Chamber" compound gauge, regulate the metering valve to slowly flow $^{18}O_2$ into the chamber and reach the desired pressure within 1 minute. Then close the leftmost valve on the branch, all other valves on the branch, and the bottle valve.

8. On Invalvuable, close the “Chamber | Gas Supplies” valve.

21. After the desired time for the second oxidation stage, remove the furnace wool from the right end of the furnace, slide the furnace off of the oxidation chamber, replace the wool, and power off the furnace.
22. Clean up.
    1. After the specimens have cooled to room temperature (~20 minutes), open the “Vent” valve, remove the specimens using the loading rod, reinstall the oxidation chamber (or replace it with the protective cap), and close the “Vent” valve.
    2. Open the “Standard Gas | Isotope Gas” and “Chamber | Gas Supplies” valves, evacuate the system through the “RT Vacuum” valve, and backfill with O_2.
    3. Close the valves on the O_2 tank and regulator.
    4. Confirm that O_2 flow is disabled on the O_2 MFC, power off the vacuum system controller, and close all valves on the MFC panel.
    5. On the mass-spectrometer setup, close the valve to the capillaries.
    6. In PV MassSpec, stop data collection and turn off “Emission.” To allow the filament to cool in high vacuum, wait until the following day to turn off the turbopump.

D4: Procedure for Tracer Oxidation in N_2-O_2 Atmospheres

1. At least 72 h before the experiment, review Section D2, and complete necessary steps.
2. Turn on the vacuum system controller (MKS 946; MKS Instruments, Inc.; Andover, MA). The vacuum system controller and attached flow controllers and flow meter should be powered on at least 30 minutes before use for accurate performance.
3. Open the valves on the Ar, O_2, and N_2 tanks and regulators. On the MFC panel (Appendix Figure D.4), open the valves below the Ar, O_2, and N_2 MFCs, and close all others. On the bench tee, configure the valves as shown in Appendix Figure D.5.
4. On the mass-spectrometer setup, while bracing the body of the valve to the capillaries with one hand, point the handle toward the fused-silica capillary. Because this step introduces a small burst of gas from the valve into the vacuum chamber, “Emission” should be off. Otherwise, the system as configured will automatically turn off “Emission” in response to the gas.
5. In the PV MassSpec software, turn on “Emission.” Emission should be turned on about 30 minutes before use for accurate performance.

6. In PV MassSpec, start data collection using an appropriate recipe. To avoid interruption or loss of data, set data collection to continuous and pause updates on the PC to prevent it from rebooting during the experiment.
7. Load specimens into a clean alumina crucible. Place this inside the magnetic loading rod.
8. Insert the magnetic loading road into the wide end of the oxidation chamber. The oxidation chamber used was a long, wide tube (19 mm outer diameter, 17 mm inner diameter, 915 mm length) that transitioned into a short, narrow tube (6.35 mm outer diameter, 150 mm length). As shown in Appendix Figure D.3, the wide end connects to Invalvuable (Appendix Figure D.6), while the narrow end connects to the flow attachment. The flow attachment consists of a (Swagelok Ultra-Torr) fitting through which the silica-capillary passes, a valve, and the mineral-oil bubbler (i.e. the left side in Appendix Figure D.2). Note that the narrow end functions both as the capillary port and as the exit for flowing gas.
9. Position the oxidation chamber, furnace, and thermocouple.
    1. If necessary, move the flow attachment out of the way.
    2. If necessary, relocate the tube furnace by loosening the two hand brake levers, sliding the furnace platform, and tightening the levers. For safety, the furnace should always be locked in place when not being moved.
    3. If necessary, adjust the height of the telescoping support.
    4. Ease the chamber into the pipe clamp located on the top of the telescoping support, taking care not to jostle the specimens.
    5. Remove the protective storage cap, knurled nut, sleeve, and O-ring from the (Swagelok Ultra-Torr) fitting on Invalvuable, and install the knurled nut, sleeve, and O-ring onto the oxidation chamber. Note that the thin part of the sleeve should touch the O-ring.
    6. Fully insert the oxidation chamber into the fitting and tighten the knurled nut by hand.
    7. Slowly pull the oxidation chamber forward about 2 mm. This can help prevent the fitting from cracking the rim of the chamber.
    8. Gently tighten the pipe clamp around the oxidation chamber.
    9. While supporting the open furnace lid, slide the furnace into position.
    10. Holding a magnet against the bottom of the chamber underneath the magnetic loading rod, move the specimens into the position that will be used during oxidation, and

confirm that the telescoping support does not interfere with the motion. Make a reference mark on the oxidation chamber for use later, and then retract the magnetic loading rod to the rightmost position.

11. Add furnace wool around the ends of the furnace.
12. Place the thermocouple in position, over the eventual specimen location.
13. Close and latch the furnace lid, confirming that doing so does not put undue stress on the oxidation chamber.

10. Position and connect the flow attachment.
    1. To the left of the furnace, secure the flow attachment to the sliding track with the four bolts, threaded but still loose, and move the flow about 30 cm away from the open end of the oxidation chamber.
    2. On the flow attachment, remove the cap protecting the delicate capillary. Feed the capillary into the end of the oxidation chamber while sliding the flow attachment to the right, into position.
    3. When the capillary fitting is about 3 cm away from the open end of the oxidation chamber, remove the knurled nut, sleeve, and O-ring from the fitting and transfer them over the capillary and onto the end of the oxidation chamber.
    4. Fine tune the alignment of the flow attachment.
        1. Tighten the four bolts securing the flow attachment to the sliding track.
        2. To adjust the vertical alignment of the capillary fitting with the chamber end, loosen the bolt on the plastic clamp tube support, shift the components up or down, and tighten the bolt.
        3. To adjust the horizontal alignment of the capillary fitting with the chamber end, slightly loosen the 3 bottom bolts on the T-shaped plate on either side of the base of the flow attachment, shift the components backward or forward, and tighten the bolts.
        4. Repeat steps 2-3 as needed.
    5. Loosen the four bolts securing the flow attachment to the sliding track. Gradually move the flow attachment into position while guiding the capillary fitting over the end of the oxidation chamber.
    6. Tighten the four bolts securing the flow attachment to the sliding track, confirming that this does not put undue stress on the end of the oxidation chamber.

7. Push the O-ring, sleeve, and knurled nut onto the capillary fitting, and tighten the nut by hand.

11. Purge the system with Ar.
    1. Close the valve on the flow attachment.
    2. Ensure that the bottle valve on each lecture bottle ($^{18}O_2$, $^{15}N_2$) is closed, and then fully open all (3) subsequent valves on each isotope branch (Appendix Figure D.7).
    3. On Invalvuable (Appendix Figure D.6), open the "Standard Gas | Isotope Gas" and "Chamber | Gas Supplies" isolation valves. Briefly open and then close the "Vent" valve, and confirm that the two compound gauges read atmospheric pressure. If not, mark true atmospheric pressure on the gauges using Scotch Magic tape.
    4. Turn on the diaphragm vacuum pump. Note that the vacuum pump should be connected to both the "RT Vacuum" and "HT Vacuum" valves.
    5. Open the "RT Vacuum" valve on Invalvuable, pull vacuum for 5 minutes, and close the valve.
    6. Using the vacuum system controller, enable Ar flow at 200 SCCM.
    7. Open the valve above the Ar MFC (Appendix Figure D.4) to start gas flow. When the system reaches atmospheric pressure after about 1 minute, close the valve above the Ar MFC to stop gas flow.
    8. Open the "RT Vacuum" valve, pull vacuum for 1 minute, and close the valve.
    9. Repeat steps 7-8 two more times.
    10. In PV MassSpec, confirm the presence of strong signals from Ar species and weak signals from others, especially ^{14}N. With each purge cycle, the non-Ar signals should get progressively weaker. If non-Ar signals are particularly high, flow Ar out through the flow attachment (e.g. at 500 SCCM for 10 minutes) to flush the Ar line and regulator before repeating steps 5-9.
12. On the $^{18}O_2$ and $^{15}N_2$ branches (Appendix Figure D.7), close the leftmost valve to isolate the branch from Invalvuable. Open all other valves on the branch.
13. As discussed in Section D2, confirm that the isotope bottles at their current pressures can be used to fill the chamber — i.e. using a pressure difference to drive flow — with 0.2 atm $^{18}O_2$ and then 0.8 atm $^{15}N_2$. Note that reversing the filling order is acceptable with modifications to the following steps as appropriate. *Failure to complete this step could waste costly isotope gases and contaminate the gas supplies in the lecture bottles.*

14. Calibrate 0.2 atm on the “Chamber” gauge using the Ar MFC.
    1. On the vacuum system controller, set Ar flow to 50 SCCM.
    2. Open the valve above the Ar MFC, measure the time to fill to atmospheric pressure, and close the valve.
    3. Open the “RT Vacuum” valve, pull vacuum for 1 minute, and close the valve.
    4. Open the valve above the Ar MFC for 0.2 times the previously measured time to fill to atmospheric pressure, and then close the valve.
    5. Mark 0.2 atm on the “Chamber” gauge using Scotch Magic tape.
    6. Open the “RT Vacuum” valve, pull vacuum for 1 minute, and close the valve.
15. Turn off the vacuum pump.
16. Fill the system with $^{15}N_2$-20% $^{18}O_2$.
    1. Close the “Standard Gas | Isotope Gas” valve on Invalvuable.
    2. On the $^{18}O_2$ branch, close the low-flow metering valve (Item SS-SS2-VH, Swagelok), and open the leftmost valve.
    3. While watching the “Chamber” compound gauge, regulate the metering valve to slowly flow $^{18}O_2$ into the chamber to 0.2 atm. Then close the leftmost valve on the branch, all other valves on the branch, and the bottle valve.
    4. On the $^{15}N_2$ branch, close the metering valve, and open the leftmost valve.
    5. While watching the “Chamber” compound gauge, regulate the metering valve to slowly flow 0.8 atm $^{15}N_2$ into the chamber, up to 1 atm. Then close the leftmost valve on the branch, all other valves on the branch, and the bottle valve.
17. On the mass-spectrometer setup, close the valve to the capillaries by pointing the valve handle toward the middle position. This step conserves the gases in the chamber during the 24 h waiting period needed for gases to thoroughly mix.
18. In PV MassSpec, turn off “Emission.” Note that data collection is still in progress.
19. After 24 h, point the handle of the valve to the capillaries toward the fused-silica capillary. Then turn on “Emission” in PV MassSpec. Confirm that the signals agree with expectations for a $^{15}N_2$-20% $^{18}O_2$ atmosphere.
20. On Invalvuable, close the “Chamber | Gas Supplies” valve.
21. Preheat the furnace to 800 °C for ~20 minutes.

22. Using a magnet, gently move the magnetic loading rod into the previously marked position, inserting the specimens into the furnace. After 8 minutes for temperature equilibration, start the oxidation time.
23. In preparation for the second oxidation stage, flush the O_2 and N_2 regulators and lines and backfill the standard-gas line with N_2-20% O_2.
    1. On the vacuum system controller, set O_2 and N_2 flow to 500 SCCM.
    2. Turn on the vacuum pump, and open the "RT Vacuum" valve.
    3. On the MFC panel, open the valves above the O_2 and N_2 MFCs to start flow. Close these valves after 10 minutes.
    4. On the vacuum system controller, set O_2 flow to 10 SCCM and N_2 flow to 40 SCCM.
    5. Close the "RT Vacuum" valve.
    6. As the pressure on the "Standard-Gas" gauge approaches atmosphere, close the valves above the O_2 and N_2 MFCs.
24. After the desired time for the first oxidation stage, start N_2-20% O_2 flow to exchange the oxidation atmosphere. *The following steps must be done in rapid sequence, ideally within 10 seconds, to avoid overpressurizing the oxidation chamber.*
    1. On the MFC panel, open the valves above the O_2 and N_2 MFCs simultaneously.
    2. On Invalvuable, open the "Standard Gas | Isotope Gas" and "Chamber | Gas Supplies" valves.
    3. On the flow attachment, open the valve.
25. After the desired time for the second oxidation stage, use the magnet to pull the magnetic loading rod to the rightmost position, removing the specimens from the furnace. Power off the furnace.
26. After the specimens have cooled to room temperature (~20 minutes), close the valves above the O_2 and N_2 MFCs to stop gas flow. Then close the valve on the flow attachment.
27. Immediate cleanup:
    1. Close the valves on the Ar, O_2, and N_2 tanks and regulators and on the MFC panel.
    2. Confirm that flows are disabled on the vacuum system controller, and power it off.
    3. On the mass-spectrometer setup, close the valve to the capillaries.
    4. In PV MassSpec, stop data collection and turn off "Emission." To allow the filament to cool in high vacuum, leave the turbopump on.
28. Cleanup the following day, after the furnace has cooled:

1. Turn off the turbopump.
2. On Invalvuable, open the “Vent” valve. Remove the oxidation chamber and specimens, and then reinstall the oxidation chamber (or replace it with the protective cap). Close the “Vent” valve.
3. Open the “Standard Gas | Isotope Gas” and “Chamber | Gas Supplies” valves, evacuate the system through the “RT Vacuum” valve, and backfill the system with Ar.

Appendix E: O Diffusion Experiments in Single-Crystal Rutile TiO_2

Experiments were conducted using single-crystal rutile TiO_2 with the goal of measuring O diffusivity and investigating any possible influence of pulling vacuum, as was done for tracer-oxidized specimens in Chapter 3 and Chapter 4, on the O diffusivity. Because Nb-doped TiO_2 was available and could be used to evaluate the first mechanism discussed in Section 2.4, we also evaluated the effect of Nb on O diffusivity in TiO_2.

Polished, single crystals of pure (001), (110), and (100) rutile TiO_2 and (100) rutile TiO_2 doped with 0.5 wt.% (1.15 at.%) Nb were purchased from MTI Corporation (Richmond, CA). Crystals were scored using a diamond scribe and broken into pieces. Four pieces, one from each crystal, were ultrasonically cleaned with methanol and sealed into the chamber of the tracer oxidation setup shown in Figure 3.1. The chamber was evacuated using the diaphragm vacuum pump, nominally rated to 2 mbar, and backfilled with O_2 to atmospheric pressure. This purging process was repeated three more times. After reaching 800 °C, the furnace was moved over the specimens, which then equilibrated in temperature for 8 minutes. At 800 °C, the chamber was evacuated for 10 minutes using the vacuum pump before backfilling with $^{18}O_2$ to atmospheric pressure. Specimens remained at 800 °C for 4 more hours and were then passively cooled to room temperature by removing the furnace. A set of control specimens not exposed to vacuum at high temperature was prepared in a similar way, except with Ar (rather than O_2) used to purge the chamber and $^{18}O_2$ (rather than O_2) used for the final backfill before the 4 h heat treatment at 800 °C. Nominal gas purity was 99.999% for Ar, 99.993% for O_2, and 99.0% for $^{18}O_2$. Isotopic purity was ≥ 99.00% for $^{18}O_2$ and presumably the natural abundance for O_2 (99.76% ^{16}O).

After the heat treatment, cross-sectional lamellae about 8 μm wide and 3 μm tall were prepared from carbon-coated specimens using the Ga FIB in a Thermo Fisher Scientific Helios 650 Nanolab SEM. Standard FIB procedures were used, including depositing a protective Pt cap and final cleaning at low voltage (5 kV). Lamellae were analyzed with nanoSIMS using a Cameca NanoSIMS 50 with a focused Cs^+ beam (0.2 pA current, ~50 nm spot size) at a mass-

resolving power of ~3000 (corrected after [89]). $^{16}O^-$, $^{18}O^-$, and (to distinguish the Pt cap) $^{12}C^-$ ions were detected simultaneously using pulse counting on electron multipliers.

Data was processed using Python, with the *sims* module (https://pypi.org/project/sims/) to help load and manipulate nanoSIMS datasets. Each dataset consisted of multiple frames of the mapped area. Datasets were processed using the same six-step procedure. First, all frames were rotated to align the oxide surface horizontally, with the Pt cap on top. Second, frames were cropped. Third, frames were aligned in the vertical direction using the maximum of ^{18}O counts. Fourth, for each vertical position, counts were summed along the horizontal direction to generate a profile of counts for ^{18}O and ^{16}O with depth into the surface. Fifth, ^{18}O isotopic concentration ($^{18}O/(^{16}O + {}^{18}O)$) was calculated and then normalized by dividing by the maximum value. Sixth, the normalized ^{18}O isotopic concentration, starting at the maximum value assumed to reflect the oxide surface, was fit to Equation 5 to calculate O diffusivity.

No strong differences in ^{18}O diffusion behavior were noted between the specimens. The calculated O diffusivity values were on the order of $1–3 \times 10^{-18}$ m^2/s and reasonably agreed with values previously estimated using the ^{18}O isotopic oxygen concentrations across oxide grain boundaries observed in nanoSIMS (e.g. in Figure 3.10). Therefore, these experiments did not help clarify if pulling vacuum or doping with Nb influences the lattice O diffusivity in TiO_2. Repeating these experiments with a longer heating time could be helpful to better distinguish potential effects on O diffusivity.

Bibliography

[1] J. D. Destefani, "Introduction to Titanium and Titanium Alloys," in *Properties and Selection: Nonferrous Alloys and Special-Purpose Materials*, ASM International, 1990, pp. 586–591. doi: 10.31399/asm.hb.v02.a0001080.

[2] G. Lütjering and J. C. Williams, *Titanium*. Berlin; New York: Springer, 2003. Accessed: Nov. 09, 2018. [Online]. Available: http://public.eblib.com/choice/publicfullrecord.aspx?p=3088489

[3] J. R. Davis, Ed., "Introduction and Overview of Titanium and Titanium Alloys," in *Metals Handbook Desk Edition*, ASM International, 1998, pp. 575–578. doi: 10.31399/asm.hb.mhde2.a0003140.

[4] A. E. Jenkins, "The oxidation of titanium at high temperatures in an atmosphere of pure oxygen," *J. Inst. Metals*, vol. 82, pp. 213–221, Jan. 1954.

[5] P. Kofstad, P. B. Anderson, and O. J. Krudtaa, "Oxidation of titanium in the temperature range 800–1200°C," *Journal of the Less Common Metals*, vol. 3, no. 2, pp. 89–97, Apr. 1961, doi: 10.1016/0022-5088(61)90001-7.

[6] J. Stringer, "The oxidation of titanium in oxygen at high temperatures," *Acta Metallurgica*, vol. 8, no. 11, pp. 758–766, Nov. 1960, doi: 10.1016/0001-6160(60)90170-X.

[7] G. R. Wallwork and A. E. Jenkins, "Oxidation of Titanium, Zirconium, and Hafnium," *J. Electrochem. Soc.*, vol. 106, no. 1, pp. 10–14, Jan. 1959, doi: 10.1149/1.2427248.

[8] H. W. Maynor, B. R. Barrett, and R. E. Swift, "Scaling of titanium and titanium alloys," Wright Air Development Center, WADC Tech. Rep. 54-109, 1955.

[9] C. J. Rosa, "Oxidation of Ti-1Si and Ti-5Si alloys," *Oxidation of Metals*, vol. 17, no. 5–6, pp. 359–369, Jun. 1982, doi: 10.1007/BF00742117.

[10] A. M. Chaze and C. Coddet, "The role of nitrogen in the oxidation behaviour of titanium and some binary alloys," *Journal of the Less Common Metals*, vol. 124, no. 1–2, pp. 73–84, Oct. 1986, doi: 10.1016/0022-5088(86)90478-9.

[11] A. M. Chaze and C. Coddet, "Influence of silicon on the oxidation of titanium between 550 and 700°C," *Oxidation of Metals*, vol. 27, no. 1, pp. 1–20, Feb. 1987, doi: 10.1007/BF00656726.

[12] D. Vojtěch, B. Bártová, and T. Kubatík, “High temperature oxidation of titanium–silicon alloys,” *Materials Science and Engineering: A*, vol. 361, no. 1–2, pp. 50–57, Nov. 2003, doi: 10.1016/S0921-5093(03)00564-1.

[13] D. Vojtěch, H. Čížová, K. Jurek, and J. Maixner, “Influence of silicon on high-temperature cyclic oxidation behaviour of titanium,” *Journal of Alloys and Compounds*, vol. 394, no. 1–2, pp. 240–249, May 2005, doi: 10.1016/j.jallcom.2004.11.019.

[14] P. Pérez, V. A. C. Haanappel, and M. F. Stroosnijder, “The effect of niobium on the oxidation behaviour of titanium in N_2/20% O_2 atmospheres,” *Materials Science and Engineering: A*, vol. 284, no. 1, pp. 126–137, May 2000, doi: 10.1016/S0921-5093(00)00754-1.

[15] P. Pérez, V. A. C. Haanappel, and M. F. Stroosnijder, “The Effect of Niobium on the Oxidation Behavior of Titanium in Ar/20% O_2 Atmospheres,” *Oxidation of Metals*, vol. 53, no. 5, pp. 481–506, Jun. 2000, doi: 10.1023/A:1004680909484.

[16] Y. S. Chen and C. J. Rosa, “High-temperature oxidation of Ti-4.32 wt.% Nb alloy,” *Oxidation of Metals*, vol. 14, no. 2, pp. 147–165, Apr. 1980, doi: 10.1007/BF00603991.

[17] B. E. Tegner, L. Zhu, C. Siemers, K. Saksl, and G. J. Ackland, “High temperature oxidation resistance in titanium–niobium alloys,” *Journal of Alloys and Compounds*, vol. 643, pp. 100–105, Sep. 2015, doi: 10.1016/j.jallcom.2015.04.115.

[18] M. Göbel, J. D. Sunderkötter, D. I. Mircea, H. Jenett, and M. F. Stroosnijder, “Study of the high-temperature oxidation behaviour of Ti and Ti4Nb with SNMS using tracers,” *Surface and Interface Analysis*, vol. 29, no. 5, pp. 321–324, 2000, doi: 10.1002/(SICI)1096-9918(200005)29:5<321::AID-SIA872>3.0.CO;2-Q.

[19] H. Jiang, M. Hirohasi, Y. Lu, and H. Imanari, “Effect of Nb on the high temperature oxidation of Ti–(0–50 at.%)Al,” *Scripta Materialia*, vol. 46, no. 9, pp. 639–643, May 2002, doi: 10.1016/S1359-6462(02)00042-8.

[20] R. J. Hanrahan and D. P. Butt, “The effects of nitrogen on the kinetics and mechanisms of oxidation of Titanium-Tantalum alloys,” *Oxid Met*, vol. 48, no. 1, pp. 41–58, Aug. 1997, doi: 10.1007/BF01675261.

[21] C. Dupressoire, A. Rouaix-Vande Put, P. Emile, C. Archambeau-Mirguet, R. Peraldi, and D. Monceau, “Effect of Nitrogen on the Kinetics of Oxide Scale Growth and of Oxygen Dissolution in the Ti6242S Titanium-Based Alloy,” *Oxidation of Metals*, vol. 87, no. 3–4, pp. 343–353, Apr. 2017, doi: 10.1007/s11085-017-9729-1.

[22] C. Dupressoire *et al.*, “The role of nitrogen in the oxidation behaviour of a Ti6242S alloy: a nanoscale investigation by atom probe tomography,” *Acta Materialia*, vol. 216, p. 117134, Sep. 2021, doi: 10.1016/j.actamat.2021.117134.

[23] I. Abdallah, C. Dupressoire, L. Laffont, D. Monceau, and A. Vande Put, “STEM-EELS identification of TiO_XN_Y, TiN, Ti_2N and O, N dissolution in the Ti2642S alloy oxidized in

synthetic air at 650 °C," *Corrosion Science*, vol. 153, pp. 191–199, Jun. 2019, doi: 10.1016/j.corsci.2019.03.037.

[24] Y. S. Chen and C. J. Rosa, "Oxidation characteristics of Ti-4.37 wt.% Ta alloy in the temperature range 1258–1473 K," *Oxidation of Metals*, vol. 14, no. 2, pp. 167–185, Apr. 1980, doi: 10.1007/BF00603992.

[25] R. L. Rawe and C. J. Rosa, "The effects of gaseous pretreatment and oxide sintering on oxidation of Ti-4.32 wt.%Nb alloy," *Oxidation of Metals*, vol. 14, no. 6, pp. 549–566, Dec. 1980, doi: 10.1007/BF00603479.

[26] V. Optasanu *et al.*, "Nitrogen quantification and tracking during high temperature oxidation in air of titanium using ^{15}N isotopic labelling," *Corrosion Science*, vol. 216, p. 111072, May 2023, doi: 10.1016/j.corsci.2023.111072.

[27] T. C. Valenza, P. Chao, P. K. Weber, O. K. Neill, and E. A. Marquis, "Protective role of silicon in the high-temperature oxidation of titanium," *Corrosion Science*, vol. 217, p. 111110, Jun. 2023, doi: 10.1016/j.corsci.2023.111110.

[28] T. C. Valenza, P. K. Weber, and E. A. Marquis, "Role of niobium in the high-temperature oxidation of titanium," *Corrosion Science*, vol. 225, p. 111603, Dec. 2023, doi: 10.1016/j.corsci.2023.111603.

[29] N. S. H. Gunda, B. Puchala, and A. Van der Ven, "Resolving phase stability in the Ti-O binary with first-principles statistical mechanics methods," *Physical Review Materials*, vol. 2, no. 3, Mar. 2018, doi: 10.1103/PhysRevMaterials.2.033604.

[30] N. S. H. Gunda and A. Van der Ven, "First-principles insights on phase stability of titanium interstitial alloys," *Phys. Rev. Materials*, vol. 2, no. 8, p. 083602, Aug. 2018, doi: 10.1103/PhysRevMaterials.2.083602.

[31] H. Okamoto, "O-Ti (Oxygen-Titanium)," *J. Phase Equilib. Diffus.*, vol. 32, no. 5, p. 473, Jul. 2011, doi: 10.1007/s11669-011-9935-5.

[32] H. Okamoto, "N-Ti (Nitrogen-Titanium)," *JPE*, vol. 14, no. 4, pp. 536–536, Aug. 1993, doi: 10.1007/BF02671982.

[33] J. C. Williams and R. R. Boyer, "Opportunities and Issues in the Application of Titanium Alloys for Aerospace Components," *Metals*, vol. 10, no. 6, Art. no. 6, Jun. 2020, doi: 10.3390/met10060705.

[34] S. C. Parida, N. K. Gupta, K. Krishnan, G. A. Rama Rao, and B. K. Sen, "High-Temperature Oxidation of β-NbTi Alloys," *Metallurgical and Materials Transactions A*, vol. 39, no. 9, pp. 2020–2025, Sep. 2008, doi: 10.1007/s11661-008-9548-8.

[35] M. Bönisch, M. Calin, J. van Humbeeck, W. Skrotzki, and J. Eckert, "Factors influencing the elastic moduli, reversible strains and hysteresis loops in martensitic Ti–Nb alloys," *Materials Science and Engineering: C*, vol. 48, pp. 511–520, Mar. 2015, doi: 10.1016/j.msec.2014.12.048.

[36] J. J. Gutiérrez Moreno, D. G. Papageorgiou, G. A. Evangelakis, and Ch. E. Lekka, “An ab initio study of the structural and mechanical alterations of Ti-Nb alloys,” *Journal of Applied Physics*, vol. 124, no. 24, p. 245102, Dec. 2018, doi: 10.1063/1.5025926.

[37] G. Venketaraman, A. G. Jackson, K. R. Teal, and F. H. Froes, “The influence of Nb addition on structure and properties of rapidly solidified intermetallics,” *Materials Science and Engineering*, vol. 98, pp. 257–263, Feb. 1988, doi: 10.1016/0025-5416(88)90165-6.

[38] T. K. Roy, R. Balasubramaniam, and A. Ghosh, “High-temperature oxidation of Ti_3Al-based titanium aluminides in oxygen,” *Metallurgical and Materials Transactions A*, vol. 27, no. 12, pp. 3993–4002, Dec. 1996, doi: 10.1007/BF02595648.

[39] Y. Ogawa and E. Miura-Fujiwara, “Effect of Nb Addition on Oxide Formation on Ti–xNb Alloys,” *Mater. Trans.*, vol. 60, no. 10, pp. 2204–2212, Oct. 2019, doi: 10.2320/matertrans.MT-M2019136.

[40] R. E. McMahon *et al.*, “A comparative study of the cytotoxicity and corrosion resistance of nickel–titanium and titanium–niobium shape memory alloys,” *Acta Biomaterialia*, vol. 8, no. 7, pp. 2863–2870, Jul. 2012, doi: 10.1016/j.actbio.2012.03.034.

[41] Y. Li, C. Yang, H. Zhao, S. Qu, X. Li, and Y. Li, “New Developments of Ti-Based Alloys for Biomedical Applications,” *Materials*, vol. 7, no. 3, Art. no. 3, Mar. 2014, doi: 10.3390/ma7031709.

[42] M. Bönisch *et al.*, “Thermal stability and latent heat of Nb–rich martensitic Ti-Nb alloys,” *Journal of Alloys and Compounds*, vol. 697, pp. 300–309, Mar. 2017, doi: 10.1016/j.jallcom.2016.12.108.

[43] S. Miyazaki and H. Y. Kim, “Basic characteristics of titanium–nickel (Ti–Ni)-based and titanium–niobium (Ti–Nb)-based alloys,” in *Shape Memory and Superelastic Alloys*, Elsevier, 2011, pp. 15–42. doi: 10.1533/9780857092625.1.15.

[44] X. Zhang, Y. Zhan, J. She, J. Hu, and Y. Du, “Effect of cyclic heat treatment on the microstructures and mechanical properties of Ti–Si alloys,” *IJMR*, vol. 101, no. 6, pp. 765–771, Jun. 2010, doi: 10.3139/146.110338.

[45] D. L. Moffat, “Phase Transformations in the Titanium-Niobium Binary Alloy System,” Ph.D., The University of Wisconsin - Madison, 1985. Accessed: Nov. 18, 2020. [Online]. Available: http://search.proquest.com/docview/303379917/abstract/BA7E03AC0A5040A0PQ/1

[46] Y. Zhang, H. Liu, and Z. Jin, “Thermodynamic assessment of the Nb-Ti system,” *Calphad*, vol. 25, no. 2, pp. 305–317, Jun. 2001, doi: 10.1016/S0364-5916(01)00051-7.

[47] H. Okamoto, “Nb-Ti (Niobium-Titanium),” *JPE*, vol. 23, no. 6, p. 553, Dec. 2002, doi: 10.1361/105497102770331325.

[48] V. M. Dyekanyenko and V. V. Vavilova, “Investigation of phase equilibria in the niobium-titanium-oxygen system and equilibrium diagram construction,” *Fazovye Ravnovesiya Met. Splavakh*, pp. 245–251, 1981.

[49] K. Frisk, L. Dumitrescu, M. Ekroth, B. Jansson, O. Kruse, and B. Sundman, "Development of a database for cemented carbides: Thermodynamic modeling and experiments," *J. Phase Equilib.*, vol. 22, no. 6, pp. 645–655, 2001.

[50] H. M. Flower, K. Lipscombe, and D. R. F. West, "The effect of silicon on the structure and mechanical properties of an α + β titanium alloy," *J Mater Sci*, vol. 17, no. 4, pp. 1221–1231, Apr. 1982, doi: 10.1007/BF00543544.

[51] N. E. Paton and M. W. Mahoney, "Creep of titanium-silicon alloys," *Metall Mater Trans A*, vol. 7, no. 11, pp. 1685–1694, Nov. 1976, doi: 10.1007/BF02817886.

[52] M. W. Mahoney and N. E. Paton, "Fatigue and fracture characteristics of silicon-bearing titanium alloys," *Metall Mater Trans A*, vol. 9, no. 10, pp. 1497–1501, Oct. 1978, doi: 10.1007/BF02661828.

[53] "Timetal Exhaust XT - Low Alloyed Titanium For Automotive & Motorcycle Applications." Titanium Metals Corporation, 2010. Accessed: Nov. 13, 2020. [Online]. Available: https://www.timet.com/assets/local/documents/datasheets/cpgrades/XT.pdf

[54] Y. Yang, B. P. Bewlay, and Y. A. Chang, "Thermodynamic modeling of the Hf–Ti–Si ternary system," *Intermetallics*, vol. 15, no. 2, pp. 168–176, Feb. 2007, doi: 10.1016/j.intermet.2006.05.002.

[55] R. Beyers, "Thermodynamic considerations in refractory metal-silicon-oxygen systems," *Journal of Applied Physics*, vol. 56, no. 1, pp. 147–152, Jul. 1984, doi: 10.1063/1.333738.

[56] R. Sinclair, "Study of Interfacial Reactions in Metal-Silicon and Related Systems by High-Resolution Electron Microscopy and Thermodynamic Analysis," *Materials Transactions, JIM*, vol. 31, no. 7, pp. 628–635, 1990, doi: 10.2320/matertrans1989.31.628.

[57] K. Chou, P.-W. Chu, and E. A. Marquis, "Early oxidation behavior of Si-coated titanium," *Corrosion Science*, vol. 140, pp. 297–306, Aug. 2018, doi: 10.1016/j.corsci.2018.05.035.

[58] C. Herzig, R. Willecke, and K. Vieregge, "Self-diffusion and fast cobalt impurity diffusion in the bulk and in grain boundaries of hexagonal titanium," *Philosophical Magazine A*, vol. 63, no. 5, pp. 949–958, May 1991, doi: 10.1080/01418619108213927.

[59] M. Köppers, Chr. Herzig, M. Friesel, and Y. Mishin, "Intrinsic self-diffusion and substitutional Al diffusion in α-Ti," *Acta Materialia*, vol. 45, no. 10, pp. 4181–4191, Oct. 1997, doi: 10.1016/S1359-6454(97)00078-5.

[60] Y. Mishin and Chr. Herzig, "Diffusion in the Ti–Al system," *Acta Materialia*, vol. 48, no. 3, pp. 589–623, Feb. 2000, doi: 10.1016/S1359-6454(99)00400-0.

[61] G. B. Gibbs, D. Graham, and D. H. Tomlin, "Diffusion in titanium and titanium—niobium alloys," *The Philosophical Magazine: A Journal of Theoretical Experimental and Applied Physics*, vol. 8, no. 92, pp. 1269–1282, Aug. 1963, doi: 10.1080/14786436308207292.

[62] U. Köhler and Ch. Herzig, “On the Anomalous Self-Diffusion in B.C.C. Titanium,” *physica status solidi (b)*, vol. 144, no. 1, pp. 243–251, Nov. 1987, doi: 10.1002/pssb.2221440122.

[63] A. E. Pontau and D. Lazarus, “Diffusion of titanium and niobium in bcc Ti-Nb alloys,” *Phys. Rev. B*, vol. 19, no. 8, pp. 4027–4037, Apr. 1979, doi: 10.1103/PhysRevB.19.4027.

[64] M. Köppers, D. Derdau, M. Friesel, and C. Herzig, “Self-Diffusion and Group III (Al, Ga, In) Solute Diffusion in hcp Titanium,” *Defect and Diffusion Forum*, vol. 143–147, pp. 43–48, Jan. 1997, doi: 10.4028/www.scientific.net/DDF.143-147.43.

[65] J. Räisänen and J. Keinonen, “Annealing behavior of Si in ion-implanted α-Ti,” *Appl. Phys. Lett.*, vol. 49, no. 13, pp. 773–775, Sep. 1986, doi: 10.1063/1.97543.

[66] Y. Iijima, S.-Y. Lee, and K.-I. Hirano, “Diffusion of silicon, germanium and tin in β-titanium,” *Philosophical Magazine A*, vol. 68, no. 5, pp. 901–914, Nov. 1993, doi: 10.1080/01418619308219375.

[67] R. F. Peart and D. H. Tomlin, “Diffusion of solute elements in beta-titanium,” *Acta Metallurgica*, vol. 10, no. 2, pp. 123–134, Feb. 1962, doi: 10.1016/0001-6160(62)90057-3.

[68] Z. Liu and G. Welsch, “Literature Survey on Diffusivities of Oxygen, Aluminum, and Vanadium in Alpha Titanium, Beta Titanium, and in Rutile,” *Metallurgical Transactions A*, vol. 19, no. 4, pp. 1121–1125, Apr. 1988, doi: 10.1007/BF02628396.

[69] A. Anttila, J. Räisänen, and J. Keinonen, “Diffusion of nitrogen in α-Ti,” *Applied Physics Letters*, vol. 42, no. 6, pp. 498–500, Mar. 1983, doi: 10.1063/1.93981.

[70] R. J. Wasilewski and G. L. Kehl, “Diffusion of nitrogen and oxygen in titanium,” *Journal of the Institute of Metals*, vol. 83, no. Part 3, pp. 94–104, 1954.

[71] P. Kofstad, *High temperature corrosion*. London ; New York: Elsevier, 1988.

[72] G. Bertrand, K. Jarraya, and J. M. Chaix, “Morphology of oxide scales formed on titanium,” *Oxidation of Metals*, vol. 21, no. 1–2, pp. 1–19, Feb. 1984, doi: 10.1007/BF00659464.

[73] P. H. Morton and W. M. Baldwin, “The scaling of titanium in air,” *Transactions of the American Society for Metals*, vol. 44, pp. 1004–1029, 1952.

[74] C. Coddet, J. F. Chretien, and G. Beranger, “Investigation on the fracture mechanism of oxide layers growing on titanium by acoustic emission,” *Titanium and titanium alloys: scientific and technological aspects*, vol. 2, pp. 1097–1105, 1982.

[75] J. E. L. Gomes and A. M. Huntz, “Correlation between the oxidation mechanism of titanium under a pure oxygen atmosphere, morphology of the oxide scale, and diffusional phenomena,” *Oxidation of Metals*, vol. 14, no. 3, pp. 249–261, Jun. 1980, doi: 10.1007/BF00604567.

[76] K. Chou, P.-W. Chu, C. G. Levi, and E. A. Marquis, “Influence of a silicon-bearing film on the early stage oxidation of pure titanium,” *Journal of Materials Science*, vol. 52, no. 16, pp. 9884–9894, Aug. 2017, doi: 10.1007/s10853-017-1143-1.

[77] K. E. Wiedemann, R. N. Shenoy, and J. Unnam, “Microhardness and lattice parameter calibrations of the oxygen solid solutions of unalloyed α-titanium and Ti-6Al-2Sn-4Zr-2Mo,” *MTA*, vol. 18, no. 8, pp. 1503–1510, Aug. 1987, doi: 10.1007/BF02646662.

[78] T. Hurlen, “Oxidation of Titanium,” *J. Inst. Met.*, vol. 89, pp. 128–136, 1961 1960.

[79] P. Kofstad, “High-temperature oxidation of titanium,” *Journal of the Less Common Metals*, vol. 12, no. 6, pp. 449–464, Jun. 1967, doi: 10.1016/0022-5088(67)90017-3.

[80] A. E. Jenkins, “A further study of the oxidation of titanium and its alloys at high temperatures,” *J. Inst. Metals*, vol. 84, Sep. 1955, Accessed: Nov. 18, 2019. [Online]. Available: https://www.osti.gov/biblio/4365615

[81] A. M. Chaze and C. Coddet, “Influence of alloying elements on the dissolution of oxygen in the metallic phase during the oxidation of titanium alloys,” *Journal of Materials Science*, vol. 22, no. 4, pp. 1206–1214, Apr. 1987, doi: 10.1007/BF01233110.

[82] G. M. Crosbie, “Chemical diffusivity and electrical conductivity in TiO_2 containing a submicron dispersion of SiO_2,” *Journal of Solid State Chemistry*, vol. 25, no. 4, pp. 367–378, Aug. 1978, doi: 10.1016/0022-4596(78)90122-6.

[83] N. Vaché and D. Monceau, “Oxygen Diffusion Modeling in Titanium Alloys: New Elements on the Analysis of Microhardness Profiles,” *Oxid Met*, vol. 93, no. 1, pp. 215–227, Feb. 2020, doi: 10.1007/s11085-020-09956-9.

[84] D. Vojtěch, T. Kubatík, K. Jurek, and J. Maixner, “Cyclic-Oxidation Resistance of Protective Silicide Layers on Titanium,” *Oxidation of Metals*, vol. 63, no. 5–6, pp. 305–323, Jun. 2005, doi: 10.1007/s11085-005-4385-2.

[85] D. Vojtěch, T. Kubatík, and H. Čížová, “Application of Silicon for a Protection of Titanium against High-Temperature Oxidation,” *Materials Science Forum*, vol. 482, pp. 243–246, Apr. 2005, doi: 10.4028/www.scientific.net/MSF.482.243.

[86] D. Vojtěch, P. Novák, P. Macháč, M. Morťaniková, and K. Jurek, “Surface protection of titanium by Ti_5Si_3 silicide layer prepared by combination of vapour phase siliconizing and heat treatment,” *Journal of Alloys and Compounds*, vol. 464, no. 1–2, pp. 179–184, Sep. 2008, doi: 10.1016/j.jallcom.2007.10.020.

[87] J. D. Majumdar, B. L. Mordike, S. K. Roy, and I. Manna, “High-Temperature Oxidation Behavior of Laser-Surface-Alloyed Ti with Si and SiCAl,” *Oxidation of Metals*, vol. 57, p. 26, 2002.

[88] J. Donovan, D. Snyder, and M. Rivers, “An Improved Interference Correction for Trace Element Analysis,” *Microbeam Analysis*, no. 2, pp. 23–28, 1993.

[89] J. Pett-Ridge and P. K. Weber, “NanoSIP: NanoSIMS Applications for Microbial Biology,” in *Microbial Systems Biology: Methods and Protocols*, A. Navid, Ed., in Methods in Molecular Biology. New York, NY: Springer US, 2022, pp. 91–136. doi: 10.1007/978-1-0716-1585-0_6.

[90] L. R. Nittler, “L’image.” Carnegie Institution of Washington, Washington, DC, Oct. 21, 2021. [Online]. Available: https://sites.google.com/carnegiescience.edu/limagesoftware/

[91] A. J. London, “AtomProbeLab.” Jul. 26, 2022. [Online]. Available: https://sourceforge.net/projects/atomprobelab/

[92] A. J. London, “Quantifying Uncertainty from Mass-Peak Overlaps in Atom Probe Microscopy,” *Microscopy and Microanalysis*, vol. 25, no. 2, pp. 378–388, Apr. 2019, doi: 10.1017/S1431927618016276.

[93] P. Pietrokowsky and P. Duwez, “Crystal Structure of Ti_5Si_3, Ti_5Ge_3, and Ti_5Sn_3,” *JOM*, vol. 3, no. 9, pp. 772–773, Sep. 1951, doi: 10.1007/BF03397370.

[94] T. L. Barth *et al.*, “Grain boundary transport through thermally grown alumina scales on NiAl,” *Corrosion Science*, vol. 209, p. 110798, Dec. 2022, doi: 10.1016/j.corsci.2022.110798.

[95] T. S. Lundy and W. A. Coghlan, “Processus de transport dans les oxydescation self diffusion in rutile,” *J. Phys. Colloques*, vol. 34, no. C9, pp. C9-302, Nov. 1973, doi: 10.1051/jphyscol:1973953.

[96] T. B. Gruenwald and G. Gordon, “Oxygen diffusion in single crystals of titanium dioxide,” *Journal of Inorganic and Nuclear Chemistry*, vol. 33, no. 4, pp. 1151–1155, Apr. 1971, doi: 10.1016/0022-1902(71)80184-7.

[97] J. I. Goldstein, S. K. Choi, F. J. J. Loo, G. F. Bastin, and R. Metselaar, “Solid-state Reactions and Phase Relations in the Ti-Si-O System at 1373 K,” *Journal of the American Ceramic Society*, vol. 78, no. 2, pp. 313–322, Feb. 1995, doi: 10.1111/j.1151-2916.1995.tb08802.x.

[98] Z. Tang, J. J. Williams, A. J. Thom, and M. Akinc, “High temperature oxidation behavior of Ti_5Si_3-based intermetallics,” *Intermetallics*, vol. 16, no. 9, pp. 1118–1124, Sep. 2008, doi: 10.1016/j.intermet.2008.06.013.

[99] H. J. Seifert, H. L. Lukas, and G. Petzow, “Thermodynamic Optimization of the Ti-Si System / Thermodynamische Optimierung des Systems Ti-Si,” *International Journal of Materials Research*, vol. 87, no. 1, pp. 2–13, Jan. 1996, doi: 10.1515/ijmr-1996-870102.

[100] R. Mitra and V. V. R. Rao, “Elevated-temperature oxidation behavior of titanium silicide and titanium silicide-based alloy and composite,” *Metall and Mat Trans A*, vol. 29, no. 6, pp. 1665–1675, Jun. 1998, doi: 10.1007/s11661-998-0089-y.

[101] A. Abba, A. Galerie, and M. Caillet, “High-temperature oxidation of titanium silicide coatings on titanium,” *Oxidation of Metals*, vol. 17, no. 1–2, pp. 43–54, Feb. 1982, doi: 10.1007/BF00606192.

[102] T. B. Reed, *Free energy of formation of binary compounds: an atlas of charts for high-temperature chemical calculations*. Cambridge, Mass.: MIT Press, 1971.

[103] M. R. Aldaz Cervantes, "Fundamentals of Titanium Interactions with Nitrogen and Oxygen," UC Santa Barbara, 2022. Accessed: Dec. 12, 2022. [Online]. Available: https://escholarship.org/uc/item/24j1b2cr

[104] B. A. Pint, A. J. Garratt-Reed, and L. W. Hobbs, "The reactive element effect in commercial ODS FeCrAI alloys," *Materials at High Temperatures*, vol. 13, no. 1, pp. 3–16, Jan. 1995, doi: 10.1080/09603409.1995.11689496.

[105] B. A. Pint and K. B. Alexander, "Grain Boundary Segregation of Cation Dopants in α-Al_2O_3 Scales," *J. Electrochem. Soc.*, vol. 145, no. 6, pp. 1819–1829, Jun. 1998, doi: 10.1149/1.1838563.

[106] J. Quadakkers and L. Singheiser, "Practical Aspects of the Reactive Element Effect," *MSF*, vol. 369–372, pp. 77–92, Oct. 2001, doi: 10.4028/www.scientific.net/MSF.369-372.77.

[107] V. Optasanu *et al.*, "Strong correlation between high temperature oxidation resistance and nitrogen mass gain during near alpha titanium alloys exposure in air," *Corrosion Science*, vol. 224, p. 111547, Nov. 2023, doi: 10.1016/j.corsci.2023.111547.

[108] A. M. Huntz, "Scale growth and stress development," *Materials Science and Technology*, vol. 4, no. 12, pp. 1079–1088, Dec. 1988, doi: 10.1179/mst.1988.4.12.1079.

[109] C. Coddet, A. M. Craze, and G. Beranger, "Measurements of the adhesion of thermal oxide films: application to the oxidation of titanium," *J Mater Sci*, vol. 22, no. 8, pp. 2969–2974, Aug. 1987, doi: 10.1007/BF01086499.

[110] A. M. Chaze and C. Coddet, "Influence of the nature of alloying elements on the adherence of oxide films formed on titanium alloys," *Oxid Met*, vol. 28, no. 1, pp. 61–71, Aug. 1987, doi: 10.1007/BF00666471.

[111] J. P. Buban *et al.*, "Grain Boundary Strengthening in Alumina by Rare Earth Impurities," *Science*, vol. 311, no. 5758, pp. 212–215, Jan. 2006, doi: 10.1126/science.1119839.

[112] B. Gorr, S. Schellert, F. Müller, H.-J. Christ, A. Kauffmann, and M. Heilmaier, "Current Status of Research on the Oxidation Behavior of Refractory High Entropy Alloys," *Advanced Engineering Materials*, vol. 23, no. 5, p. 2001047, 2021, doi: 10.1002/adem.202001047.

[113] R. J. Hanrahan and D. P. Butt, "Oxidation kinetics and mechanisms of Ti-Ta alloys," *Oxidation of Metals*, vol. 47, no. 3–4, pp. 317–353, Apr. 1997, doi: 10.1007/BF01668517.

[114] T. Ando, K. Nakashima, T. Tsuchiyama, and S. Takaki, "Microstructure and mechanical properties of a high nitrogen titanium alloy," *Materials Science and Engineering: A*, vol. 486, no. 1, pp. 228–234, Jul. 2008, doi: 10.1016/j.msea.2007.08.074.